



12-2010

# The Importance of Chain Connectivity in the Formation of Non-covalent Interactions between Polymers and Single-walled Carbon Nanotubes and its Impact on Dispersion

Dias Linton

*University of TN*, [dlinton1@utk.edu](mailto:dlinton1@utk.edu)

---

## Recommended Citation

Linton, Dias, "The Importance of Chain Connectivity in the Formation of Non-covalent Interactions between Polymers and Single-walled Carbon Nanotubes and its Impact on Dispersion." PhD diss., University of Tennessee, 2010.  
[https://trace.tennessee.edu/utk\\_graddiss/896](https://trace.tennessee.edu/utk_graddiss/896)

This Dissertation is brought to you for free and open access by the Graduate School at Trace: Tennessee Research and Creative Exchange. It has been accepted for inclusion in Doctoral Dissertations by an authorized administrator of Trace: Tennessee Research and Creative Exchange. For more information, please contact [trace@utk.edu](mailto:trace@utk.edu).

To the Graduate Council:

I am submitting herewith a dissertation written by Dias Linton entitled "The Importance of Chain Connectivity in the Formation of Non-covalent Interactions between Polymers and Single-walled Carbon Nanotubes and its Impact on Dispersion." I have examined the final electronic copy of this dissertation for form and content and recommend that it be accepted in partial fulfillment of the requirements for the degree of Doctor of Philosophy, with a major in Chemistry.

Mark D. Dadmun, Major Professor

We have read this dissertation and recommend its acceptance:

Jimmy Mays, Charles Feigerle, Bamin Khomami

Accepted for the Council:

Carolyn R. Hodges

Vice Provost and Dean of the Graduate School

(Original signatures are on file with official student records.)

---

To the Graduate Council:

I am submitting herewith a dissertation written by Dias Linton entitled “The Importance of Chain Connectivity in the Formation of Non-covalent Interactions between Polymers and Single-walled Carbon Nanotubes and its Impact on Dispersion.” I have examined the final electronic copy of this dissertation for form and content and recommend that it be accepted in partial fulfillment of the requirements for the degree of Doctor of Philosophy, with a major in Chemistry.

Mark D. Dadmun, Major Professor

We have read this dissertation  
and recommend its acceptance:

Jimmy Mays

Charles Feigerle

Bamin Khomami

Accepted for the Council:

Carolyn R. Hodges  
Vice Provost and Dean of the Graduate School

(Original signatures are on file with official student records.)

**THE IMPORTANCE OF CHAIN CONNECTIVITY IN THE FORMATION OF  
NON-COVALENT INTERACTIONS BETWEEN POLYMERS AND SINGLE-  
WALLED CARBON NANOTUBES AND ITS IMPACT ON DISPERSION**

A Dissertation

Presented for the

Doctor of Philosophy Degree

The University of Tennessee, Knoxville

Dias Linton

December 2010

**Copyright © 2010 by Dias Linton**

**All Rights Reserved.**

## DEDICATION

**To Mami, Didi, Wat, Ojack, and Jocelyn,**

*Thank you for your love throughout the years.*

*How else could I become what I've become?*

*All your plans and hopes and even fears,*

*Now come together in what I have done.*

*Know that I am grateful for your love.*

*Your hard work is mirrored now in mine.*

*On you all my accomplishments must shine.*

*Underneath my pride, your spirits move.*

*Nicholas Gordon*

## ACKNOWLEDGEMENT

This dissertation would not have been possible without the technical guidance and moral support from my advisor, Professor Mark Dadmun, who has trained me in both the “hard science” and “soft skill” aspects. For that, I will be forever indebted to him. I would also like to express my deepest gratitude to Professor Jimmy Mays, who has been very gracious in offering his constructive advice on the synthetic aspect of my research. I would like to thank Dr. Bobby Sumpter and Prof. Charles Feigerle for their close collaborations in my research and Prof. Bamin Khomami for his objective comments on my dissertation. To the past and present Dadmun group members, Dr. Rujul Mehta, Dr. Kevin Rice, Dr. Sudesh Kamath, Dr. Asif Rasheed, Dr. Deepali Kumar, Shraddha Deodhar, Dr. Earl Ashcraft, Nathan Henry, Chang-Uk Lee, Dana Algaier, Caleb Dyer, Brian Bachner, Lesley Thompson, Bradley Miller, Say Lee Teh, Mary Mutz, Onome Swader, Adam Imel, Dr. Wen Yin and Dr. Raghavendra Hegde, I sincerely appreciate their camaraderie throughout my graduate career. I am grateful for the research help from Professor David Bucknall (Georgia Tech) on wide angle neutron diffraction, Dr. Ilia Ivanov (ORNL) on Raman spectroscopy, Dr. Paraskevi Driva (U. of Athens, Greece) on anionic polymerization, Mr. Tom Malmgren (U. of TN) on polymer characterization, Dr. Joseph Spruiell (U. of TN) on small angle X-ray scattering and Dr. Ken Littrell (ORNL), Dr. William Heller (ORNL) and Dr. Silvia Imberti (ISIS) on data reduction. I am also indebted to many of the staff in the department, Arthur Pratt, Bill Gurley, Johnny Jones, Gary Wynn, Tim Free, Darrell Lay, Traymon Allen, Sharon Marshall, Gail Cox, Rhonda Wallace and Lisa Bonds. I would also like to offer my sincerest gratitude to everyone else that supported me in any respect during the completion of this dissertation. And finally,

to family...my mother, Jennifer Nanang, my father, Linton Albert, my brothers, Leslie Entigar Linton and Andin Linton and my sister-in-law, Jocelyn Wong...words would never be enough to thank you for your endearing love, confidence in my abilities and standing by me whether it be rain or shine. To the latest addition, Allyson Yot Linton, the second Miss Linton of the family, I am tremendously proud to have you as my niece.

Financial support for this work was provided by DOE (DE-AC05-00OR22725) and NSF (DMR-0706323, DMR-0241214).



## ABSTRACT

Polymer nanocomposites have garnered incredible promise in the field of material science due to the excellent mechanical strength, thermal and electrical conductivities of the nanoparticles and the extension of these properties to the processing flexibility inherent to plastics. However, practical realization of these nanoparticle-based materials has been hindered by the tendency of these nanoparticles to aggregate as a result of strong inter-particle forces. In this dissertation, we investigate the formation of non-covalent charge transfer interactions between polymers and single-walled carbon nanotubes (SWNTs) with the goal of optimizing interfacial adhesion and homogeneity of nanocomposites without modifying the SWNT native surface.

Nanocomposites of SWNTs and three sets of polymer matrices with varying composition of electron donating or electron accepting functional groups were prepared. In the first part of this dissertation, quantitative characterization by optical microscopy and Raman spectroscopy and qualitative results through thick film composite visualization show that the existence of a moderate amount of interacting moieties along the polymer chain results in an enhanced intermolecular interaction with SWNT, which translates to an optimum nanoparticle homogeneity.

Calculations from density functional theory and Flory-Huggins theory correlate with the experimental results, which illustrate that chain connectivity is critical in controlling the accessibility of the functional groups to form intermolecular interactions. Thus, controlling the amount of interacting functional groups throughout the polymer

chain such that an adequate distance between them is realized will direct the extent of charge transfer interaction, which enables tuning the SWNT dispersion.

The second part of this dissertation focuses on the elucidation of the morphology of these nanoparticle entities in a polymer matrix. The observance of microphase-separated peaks in the scattering patterns of polyacrylonitrile (PAN) nanocomposites indicate an ordering of the PAN polymer induced by the carbon nanotube cage, which could either be due to a thermodynamically bound layer around the SWNT or the occurrence of SWNT-induced PAN crystallization.

Finally, UV-Vis measurements were performed on SWNT-polymer suspension in order to comprehend the interactions that occur during nanocomposite fabrication. These results demonstrate that SWNT dispersions in pure N,N-dimethyl formamide (DMF) are stabilized by the adsorption of polymers onto the SWNTs.

## TABLE OF CONTENTS

<b>CHAPTER 1: INTRODUCTION.....</b>	<b>1</b>
1.1 Historical Background, Structure and Properties of Carbon Nanomaterials.....	1
1.2 Polymer Nanocomposite.....	9
A. Covalent vs Noncovalent Functionalization.....	9
B. Interfacial Adhesion.....	13
C. Morphology and Dispersion.....	19
1.3 Application of Flory-Huggins Theory to Polymer Nanocomposite.....	23
1.4 Conclusions and Proposed Experiments.....	27
 <b>CHAPTER 2: EXPERIMENTAL TECHNIQUES.....</b>	 <b>29</b>
2.1 Commercially Purchased Materials.....	29
A. Chemicals.....	29
B. Polymers.....	30
C. Carbon Materials.....	30
2.2 Purification of Reagents.....	30
A. Monomers.....	30
B. Copper (I) Bromide and Copper (I) Chloride.....	31
2.3 Synthesis of Polymers.....	31
A. Atom Transfer Radical Polymerization (ATRP).....	31
B. Free Radical Polymerization.....	41
C. Microwave Assisted Polymerization.....	46
2.4 Polymer Characterization.....	49

A.	$^1\text{H}$ NMR.....	49
B.	$^{13}\text{C}$ NMR.....	56
C.	Elemental Analysis.....	59
D.	Differential Scanning Calorimetry.....	60
E.	Gel Permeation Chromatography.....	60
F.	Intrinsic Viscometry.....	61
2.5	Preparation of Polymer Nanocomposite.....	62
A.	Raman Spectroscopy and Optical microscopy.....	62
B.	Small Angle Neutron/X-ray scattering/X-ray Diffraction.....	62
C.	UV-Vis Spectroscopy.....	63
D.	Wide Angle Neutron Diffraction Samples.....	64
2.6	Polymer Nanocomposite Characterization and Analysis.....	64
A.	Optical Microscopy and Image Analysis.....	64
B.	Raman Spectroscopy.....	65
C.	Small Angle-X-ray Scattering.....	66
D.	Small Angle Neutron Scattering.....	66
E.	UV-Vis Spectroscopy.....	67
F.	X-ray Diffraction (XRD).....	67
G.	Wide Angle Neutron Diffraction.....	67
 <b>CHAPTER 3: EVIDENCE OF CHARGE TRANSFER INTERACTION IN POLYMER NANOCOMPOSITES.....</b>		 70
3.1	Introduction.....	70
3.2	Materials.....	70

3.3	Results and Discussion.....	72
	A. Raman Spectroscopy.....	72
	B. Density Functional Theory Calculation.....	87
	C. Calculation of Free Energy of Mixing, $\Delta G$ .....	92
3.4	Conclusion.....	103

#### **CHAPTER 4: OPTIMIZATION OF NANOPARTICLE DISPERSION USING NON-COVALENT CHARGE TRANSFER INTERACTION.....105**

4.1	Introduction.....	105
4.2	Materials.....	106
4.3	Results and Discussion.....	106
	A. Dispersion Quality Determination by Thick Film Composite Visualization.....	106
	B. Optical Microscopy and Aggregate Size Analysis.....	110
	C. Nanotube Dispersion using Raman Spectroscopy.....	122
4.4	Conclusion.....	130

#### **CHAPTER 5: MORPHOLOGY OF POLYACRYLONITRILE NANOCOMPOSITES BY SMALL ANGLE NEUTRON SCATTERING.....131**

5.1	Motivation.....	131
5.2	Materials.....	132
5.3	Basics of Small Angle Neutron and X-ray Scattering.....	134
5.4	Results and Discussion: Real space Structure and Scattering Patterns of Polyacrylonitrile (PAN) composites.....	138
5.5	Conclusion.....	157

<b>CHAPTER 6: DISSOLUTION OF SINGLE-WALLED NANOTUBES BY POLYMERIC STERIC STABILIZATION.....</b>	<b>159</b>
6.1 Introduction.....	159
6.2 Materials.....	163
6.3 Basic Theory of Colloid Science.....	163
A. Strategies for Imparting Colloidal Stability.....	163
B. Polymer Solution Thermodynamics – Flory Huggins Theory.....	169
6.4 Results and Discussion.....	170
6.5 Conclusion.....	186
 <b>CHAPTER 7: CONCLUSIONS AND FUTURE WORK.....</b>	 <b>188</b>
7.1 Final Conclusion.....	188
7.2 Future Work.....	193
 <b>REFERENCES.....</b>	 <b>197</b>
 <b>APPENDIX A.....</b>	 <b>210</b>
A.1 Effect of Chain Flexibility on the Formation of Charge Transfer Interactions...	211
 <b>VITA.....</b>	 <b>219</b>

## LIST OF TABLES

Table	Page
<b>1.1</b> Characteristics of Traditional and Nanoscale Fillers: Shape, Size Properties, Dimensions and Uses.....	<b>7</b>
<b>2.1</b> SWNT manufacturer's specifications.....	<b>30</b>
<b>3.1</b> Characteristics of PMMA, PDMAEMA and MMA- <i>ran</i> -DMAEMA used in this study.....	<b>71</b>
<b>3.2</b> Characteristics of PS, PAN and styrene- <i>ran</i> -acrylonitrile polymers used in this study.....	<b>71</b>
<b>3.3</b> Characteristics of PS, PCNSt and styrene- <i>ran</i> -cyanostyrene polymers used in this study.....	<b>71</b>
<b>3.4</b> MMA- <i>ran</i> -DMAEMA polymer nanocomposite's (containing 1.0 wt% SWNT) Gibbs free energy of mixing $\Delta G$ , entropic contribution $\Delta S$ and Chi interaction parameter $\chi$ calculated from Flory-Huggins theory.....	<b>98</b>
<b>3.5</b> Styrene- <i>ran</i> -acrylonitrile polymer nanocomposite's (containing 1.0 wt% SWNT) Gibbs free energy of mixing $\Delta G$ , entropic contribution $\Delta S$ and Chi interaction parameter $\chi$ calculated from Flory-Huggins theory.....	<b>99</b>
<b>3.6</b> Styrene- <i>ran</i> -cyanostyrene polymer nanocomposite's (containing 1.0 wt% SWNT) Gibbs free energy of mixing $\Delta G$ , entropic contribution $\Delta S$ and Chi interaction parameter $\chi$ calculated from Flory-Huggins theory.....	<b>100</b>
<b>5.1</b> Thickness of nanoparticle diameter and bound polymer layer thickness ( $D + \Delta$ ) for polyacrylonitrile composites containing 0.1 wt% to 2.0 wt% SWNT.....	<b>150</b>
<b>A.1</b> Characteristic ratio of PMMA, PDMAEMA and MMA- <i>ran</i> -DMAEMA polymers used in this study.....	<b>216</b>
<b>A.2</b> Characteristic ratio of PS, PAN and styrene- <i>ran</i> -acrylonitrile polymers used in this study.....	<b>216</b>
<b>A.3</b> Characteristic ratio of PS, PCNSt and styrene- <i>ran</i> -cyanostyrene polymers used in this study.....	<b>216</b>

## LIST OF FIGURES

Figure	Page
1.1 Single walled- and multi walled-carbon nanotubes.....	4
1.1 The construction of unit cell in SWNT.....	5
1.2 Methods to achieve nanoparticle dispersion in polymer matrix. (a) $\pi$ - $\pi$ interactions (b) Non-covalent interactions (c) Covalent functionalization.....	10
2.1. Mole fraction of DMAEMA in copolymer as a function of DMAEMA mole fraction in comonomer feed.....	36
2.2 Polymerization setup for the copolymerization of styrene-ran-acrylonitrile.....	37
2.3 Mole fraction of AN in copolymer vs mole fraction of AN in comonomer feed.....	39
2.4 Mole fraction of CNSt in copolymer vs mole fraction of CNSt in comonomer feed.....	45
2.5 Mole fraction of MMA in copolymer as a function of MMA mole fraction in the comonomer feed.....	50
2.6 Typical $^1\text{H}$ NMR spectra of MMA-ran-DMAEMA.....	51
2.7 $^1\text{H}$ NMR spectra of colored polyacrylonitrile.....	53
2.8 $^1\text{H}$ NMR spectra of commercial PAN synthesized by free radical technique.....	54
2.9 $^1\text{H}$ NMR spectra of St-ran-MMA.....	57
2.10 NMR spectra of styrene-ran-cyanostyrene with 24 mol% cyanostyrene.....	58
2.11 X-ray diffraction pattern from $\text{C}_{60}$ , PAN polymer and PAN composites 5 wt% containing 6 wt% $\text{C}_{60}$ .....	68
3.2 Schematic of the (a) G band atomic vibrations along the nanotube circumference and along the nanotube axis and (b) RBM vibrational mode, attributed to the symmetric movement of all carbon atoms in the radial direction.....	77
3.3 Estimated and experimental $\text{D}^*$ band peak shift for DMAEMA nanocomposites as a function of % DMAEMA.....	82
3.4 Estimated and experimental $\text{D}^*$ band peak shift for SAN nanocomposites as a function of % AN.....	84



<b>3.5</b>	Estimated and experimental D* band peak shift for cyanostrene nanocomposites as a function of % CNSt.....	86
<b>3.6</b>	Optimized geometries for DMAEMA, AN, and CNSt monomers interacting with an (8,0) semiconducting SWNT with binding energies given in parenthesis as determined by density functional theory (DFT).....	88
<b>3.7</b>	Optimized binding orientation between cyanostyrene trimer and (8,0) semiconducting SWNT as determined by DFT calculation.....	91
<b>3.8</b>	Gibbs free energy of mixing (J/mol) as a function of molecular unit entities in SWNT, M <sub>A</sub> .....	94
<b>4.1</b>	Photographs of (a) PMMA, (b) PDMAEMA and (c) DMA30 thick film composites with 0.1 wt % content of SWNT.....	107
<b>4.2</b>	Photographs of (a) PS, (b) PAN and (c) SAN45 thick film composites with 0.1 wt% SWNT.....	109
<b>4.3</b>	Photographs of SWNT nanocomposites with (a) polystyrene (b) CNSt23.6 and (c) PCNSt as the matrix containing 0.1wt% SWNT.....	111
<b>4.4</b>	Optical micrographs of (a) DMA30 (b) DMA10 (c) PMMA and (d) PDMAEMA nanocomposites with 1.0 wt% SWNT loading at 10x magnification.....	112
<b>4.5</b>	Diameter of aggregates in 1% SWNT nanocomposites as a function of mol% DMAEMA in copolymer.....	114
<b>4.6</b>	Area of aggregates in 1% SWNT nanocomposites as a function of mol% DMAEMA in copolymer.....	115
<b>4.7</b>	Optical micrographs of (a) SAN29.5 (b) SAN 45 (c) SAN 56.2 (d) PAN nanocomposites.....	117
<b>4.8</b>	The integrated area under the G-band (left) along the horizontal line shown on the right for PAN nanocomposite.....	118
<b>4.9</b>	The integrated area under the G-band (left) along the horizontal line shown on the right for PS nanocomposite.....	119
<b>4.10</b>	Optical Micrographs of (a) CNSt 12.6 (b) CNSt 23.6 (c) CNSt 40.2 and (d) CNSt 50.0.....	120
<b>4.11</b>	Color-coded map of the integrated area under the G-band for CNSt24 micrograph.....	121

<b>4.12</b>	Variation of G band intensities for the corresponding clear (diamond symbol) and aggregated (circle symbol) regions of optical micrograph taken at 50x magnifications.....	123
<b>4.13</b>	Ratio of the Intensity of G band in the clear region to that in the aggregated region, which is a measure of the dispersion of the SWNT in the nanocomposite as a function of % DMAEMA in matrix copolymer.....	125
<b>4.14</b>	Ratio of the Intensity of G band in the clear region to that in the aggregated region, which is a measure of the dispersion of the SWNT in the nanocomposite as a function of % AN in matrix copolymer.....	128
<b>5.1</b>	Illustration of scattering experiment and relationship between wavevectors and momentum transfers.....	134
<b>5.2</b>	Small angle neutron scattering patterns of polyacrylonitrile thick film composite with varying SWNT loading, 0.1-2.0 wt% SWNT.....	139
<b>5.3</b>	Schematic of the wrapping of a “bound-polymer” layer around SWNT aggregates.....	141
<b>5.4</b>	Illustrations of four states of particle organization in a dense polymer melt, (I) contact aggregation, (II) steric stabilization, (III) local bridging attraction, and (IV) longer range ‘tele-bridging’ attraction.....	142
<b>5.5</b>	Schematic representation of structural changes that alter the dimensionless isothermal compressibility $I(Q=0)$ for (a) unperturbed polymer chain(b) a nanocomposite with low filler concentration and (c) a nanocomposite with high filler volume fraction.....	146
<b>5.6</b>	Scattering intensity at the lowest measurable $Q$ , $I(Q_{low})$ as a function of mass % SWNT.....	147
<b>5.7</b>	$Q$ at $I(Q)_{max}$ as a function of % SWNT in polyacrylonitrile thick film composite.....	149
<b>5.8</b>	Maximum scattering intensity ( $I(Q)_{max}$ ) at $x_{center}$ of the observed correlation peak in the scattering of PAN nanocomposite.....	151
<b>5.9</b>	Schematic representation of three methods that the presence of a nanoparticle can induce/modify polymer crystallization. (a) nanohybrid shish kebabs (b) Nanoplate-induced polymer crystallization, (c) nanoparticle-decorated polymer single crystals.....	153
<b>6.1</b>	Schematic of sample preparation process for polymer nanocomposites.....	160

<b>6.2</b>	Diagram representing the origin of electrostatic stabilization for negatively charged particles.....	164
<b>6.3</b>	Schematic representation of (I) depletion and (II) steric stabilization.....	167
<b>6.4</b>	Schematic representation of the steric stabilization of a SWNT particle by an amphiphatic block copolymer.....	174
<b>6.5</b>	Absorbance at 500 nm of the SWNT material in suspension.....	177
<b>6.6</b>	SWNT concentration (mg/L) in suspension after centrifugation.....	178
<b>6.7</b>	Schematic representation of two sterically stabilized particles with (a) thicker and (b) thinner bound polymer layers.....	181
<b>6.8</b>	Effective nanoparticle diameter (in nanometer) in suspension from dynamic light scattering (DLS).....	183
<b>6.9</b>	SWNT concentration x particle size in suspension as a function of percent acrylonitrile in SAN copolymer.....	184
<b>A.1</b>	Structures of (a) PDMAEMA, (b) poly(ethyl butyl) methacrylate, (c) PCNSt and (d) poly ( $\alpha$ -methyl styrene).....	215

## CHAPTER 1: INTRODUCTION

### 1.1 Historical Background, Structure and Properties of Carbon Nanomaterials

Carbon-related materials have been used in art and technology since ancient times. Charcoal, graphite and carbon black, all of which are a pure form of soot have long been used as drawing, printing and writing materials and coal has been a vital source of energy for centuries.<sup>1</sup> Perhaps the inception of active carbon fiber research came in the 1950s, stimulated by the needs for stiff light-weight fibers that could be used in the space and aircraft industries. Great advances in the preparation of continuous carbon fibers based on polymer precursors, for instance, polyacrylonitrile (PAN), and mesophase pitch-based fibers were attained.<sup>2</sup> The commercially available mesophase pitch-based fibers are exploited for their extremely high bulk modulus and high thermal conductivity, while PAN fibers are widely used for their high tensile strength.<sup>2</sup> The high modulus of the mesophase pitch fibers is due to the high degree of c-axis orientation (i.e. mean angle with respect to fiber axis) of the sheets, which is typically less than 3°. The high strength of PAN-based fibers is related to the defects in the structure, which inhibit the slippage of adjacent graphene planes relative to each other. Typical diameters for these individual commercial fibers are ~7  $\mu\text{m}$  and they can be very long; therefore are typically woven into bundles called tows and wound up as a continuous yarn on a spool.

In the 1960s and 1970s, efforts to develop new bulk synthetic carbon materials with properties approaching single crystal graphite led to the development of highly oriented pyrolytic graphite (HOPG) by Moore and coworkers.<sup>3,4</sup> When methane or other

hydrocarbon vapors are cracked onto a hot surface, the carbon formed nucleates and grows as a compact deposited layer and not in the gas phase as soot. In the temperature range of 1900 to 2300 °C, the deposits are highly graphitized, with the c-axis of the crystallites roughly normal to the heated substrate.<sup>5</sup> However, it was soon realized that new research directions were needed to reduce fiber defects and make progress towards perfecting the structure of synthetic filamentary carbon materials. This led to the development of vapor phase grown carbon fibers (VGCF)<sup>6,7</sup> by a catalytic chemical vapor deposition process (CVD). Studies by high resolution electron microscopy reveal the VGCF structure to be a hollow tube with diameter ranging from 20 Å to 500 Å. They are arranged in a concentric sheet fashion resembling the “annual ring structure of a tree”, with the innermost hollow tube behaving like carbon nanotubes.<sup>7</sup>

During experiments aimed at understanding the mechanisms by which long-chain carbon molecules are formed, the remarkable discovery of Buckminster fullerene, a stable cluster consisting of 60 carbon atoms by Kroto and Smalley occurred in 1985.<sup>8,9</sup> This 60-carbon atom structure resembles a truncated icosahedron soccerball, which consists of a polygon with 60 vertices and 32 faces, 12 of which are pentagonal and 20 hexagonal. However, the real breakthrough that stimulated the spur of nanotechnology came in 1991 when multi-walled carbon nanotubes (MWNT) was discovered by Sumio Ijima.<sup>10</sup> The first synthesis of MWNT involved an arc-evaporation method, where graphite electrodes were held at a short distance apart during arcing. The carbon, which evaporated from the anode recondensed as a hard cylindrical deposit on the cathodic rod and was found to contain both nanotubes and nanoparticles.<sup>11</sup> Two years later, Ijima and

Toshinari of NEC<sup>12</sup> and Bethune et al.<sup>13</sup> of IBM Almaden Research Center in California independently reported the synthesis of single-walled carbon nanotubes (SWNT). These were produced using the same synthetic method as the MWNTs discovered earlier but with ferromagnetic transition metal-impregnated electrodes.<sup>12,13</sup> In 1995, Smalley and coworkers reported the laser evaporation method of SWNTs, where a cylindrical graphite target doped with small amounts of metal catalyst (typically 0.5-1.0 % each of Co and Ni) is vaporized by a Nd: YAG laser. Nevertheless, synthesis by CVD technique has become an increasingly favored commercial method for SWNT synthesis due to its scalability, simple apparatus and production of tubes that are of equal or higher structural quality than arc-evaporated tubes. For MWNTs however, the arc-evaporation technique remains the best method for the synthesis of high quality tubes.

Structurally, a SWNT is a hollow cylinder formed by rolling a graphite sheet whereas a MWNT is a group of coaxial SWNTs (Figure 1.1). A perfect SWNT has essentially  $sp^2$  bonding between the carbon atoms. Due to the highly-curved nature of a SWNT,  $\sigma$ - $\pi$  rehybridization occurs, where three  $\sigma$  bonds distort slightly out of plane causing the  $\pi$  orbital to be more delocalized outside the tube. For this reason, nanotubes are mechanically stronger, electrically and thermally more conductive and chemically and biologically more active than graphite.<sup>14</sup> As shown in Figure 1.2, a SWNT can be uniquely characterized in terms of a chiral vector,  $C$ , joining two crystallographically equivalent points on the original 2-dimensional graphene lattice. Mathematically, chiral vector  $C$  is composed of a set of two integers  $(n,m)$  corresponding to graphite vectors  $a_1$  and  $a_2$  where:<sup>14</sup>

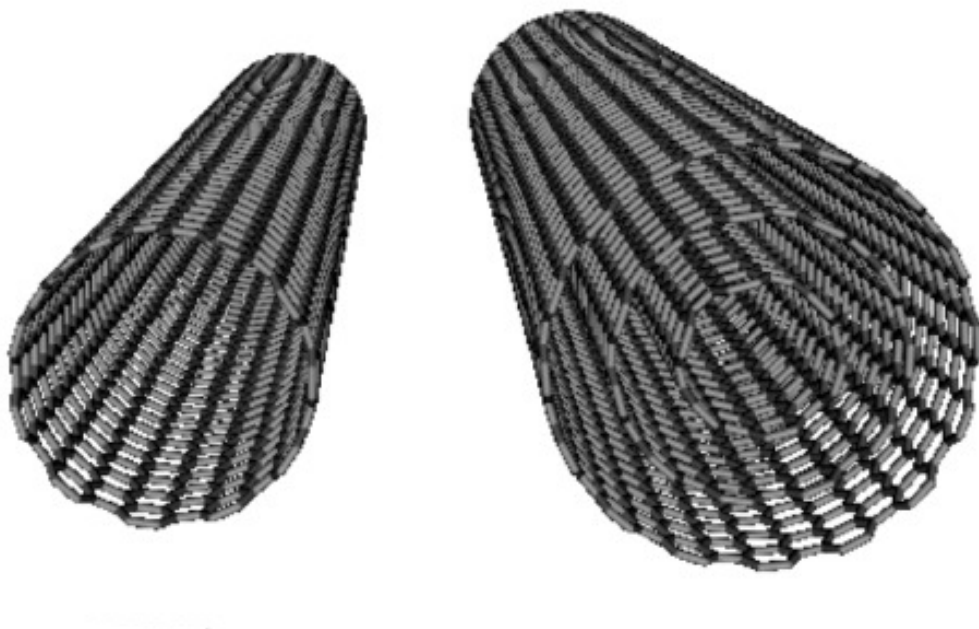


**Figure 3.1.** Single walled- and multi walled-carbon nanotubes

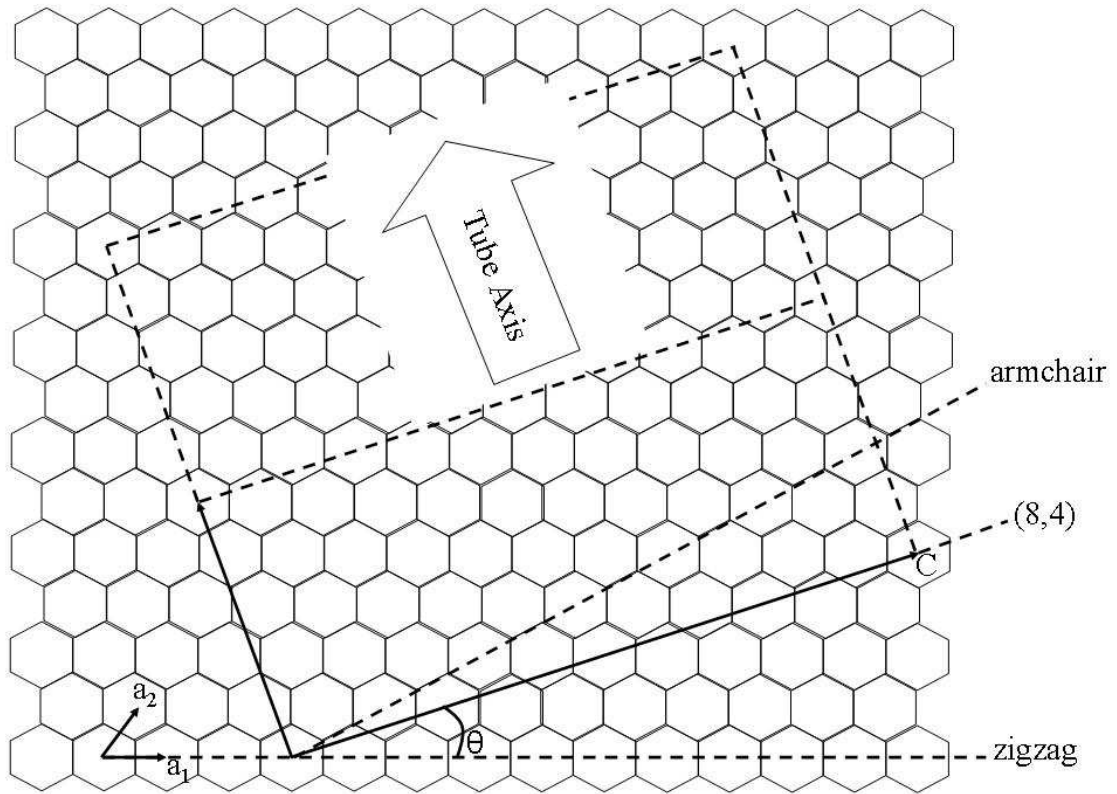


**Figure 1.4.** The construction of unit cell in SWNT



$$C = na_1 + ma_2 \quad (\text{Equation 1.1})$$

The diameter of the (n,m) SWNT is given by:

$$d_t = \frac{|C|}{\pi} = \frac{a\sqrt{n^2 + nm + m^2}}{\pi} \quad (\text{Equation 1.2})$$

where  $a=|a_1|=|a_2|=0.246$  nm is the lattice constant of the graphite, as determined experimentally and theoretically.<sup>14</sup> Three distinct types of nanotube structures can be generated by rolling up the graphene sheet into a cylinder, as shown in Figure 1.2. The zigzag and armchair tubes correspond to  $\theta=0^\circ$  and  $\theta=30^\circ$  respectively and chiral tubes correspond to  $0^\circ < \theta < 30^\circ$ . The chiral angle  $\theta$  is defined as:<sup>15</sup>

$$\theta = \tan^{-1} \left[ \frac{\sqrt{3}m}{m + 2n} \right] \quad (\text{Equation 1.3})$$

In the (n,m) notation from Equation 1.1, the vectors (n,0) or (0,m) denote zigzag nanotubes, vectors (n,n) denote armchair nanotubes and all other vectors (n,m) correspond to chiral nanotubes. Both armchair and zigzag tubes have a mirror plane and are therefore considered as achiral. In principle, the electronic structure of nanotubes is strongly dependent on their chiral angle and a SWNT is metallic when  $(n-m) = 3q$ , where  $q$  is an integer, and is semiconducting otherwise.

Table 1.1<sup>16</sup> compares the size, shape, properties and application of traditional fillers and newer cutting-edge nanoscale fillers. Although conventional fillers such as carbon fiber and carbon graphite have good elastic moduli as well as beneficial electrical

**Table 2.1.** Characteristics of traditional and nanoscale fillers: Shape, size, properties, dimensions and uses

	Approximate Shape <sup>a</sup>	Smallest Dimension (nm) <sup>a</sup>	Aspect Ratio <sup>b</sup>	Elastic Modulus (GPa)	Electrical Conductivity (S/cm)	Thermal Conductivity (W/m K)	Commercial Uses
<b>Traditional Fillers</b>							
Carbon black	agglomerate of spheres	10-100	1-5	...	10-100	0.1-0.4	tires, hoses, shoes, elastomers
Carbon fiber	rods	5,000-20,000	10-50	300-800	0.1-10	100-1000	aerospace, automotive, marine, sporting, medical
Carbon graphite	plate	250-500	15-50	500-600	1-10	100-500	gaskets, seals
E-glass	rods	10,000-20,000	20-30	75	...	...	marine, automotive, construction, filtration
Mineral: CaCO <sub>3</sub>	sphere	45-70	~1	35	...	3-5	paper, paint, rubber, plastics
	platelet	600-4,000	1-30				
Mineral: silica	agglomerate of spheres	8,000-30,000	5-10	30-200	...	1-10	reinforced plastics, thermal insulator, paint, rubber
							reinforcing agent
Mineral: talc, china clay	platelet	5,000-20,000	5-10	1-70	...	1-10	paper, consumer goods, construction
<b>Nanoscale Fillers</b>							
Carbon nanofiber	rod	50-100	50-200	500	700-1000	10-20	hoses, aerospace, ESD/EMI shielding, adhesives
Carbon MWNT	rod	5-50	100-10,000	1,000	500-10,000	100-1000	automotive, sporting, ESD/EMI shielding
Carbon SWNT	rod	0.6-1.8	100-10,000	1,500	1000-10,000	1000	filters, ESD/EMI shielding
Aluminosilicate nanoclay	plate	1-10	50-1000	200-250	...	1-10	automotive, packaging, sporting
							tires, aerospace
Nano-TiO <sub>2</sub>	sphere	10-40	~1	230,000	10 <sup>-11</sup> -10 <sup>-12</sup>	12	photocatalysis, gas sensors, paint
Nano-Al <sub>2</sub> O <sub>3</sub>	sphere	300	~1	50	10 <sup>-14</sup>	20-30	seal rings, furnace liner tubes, gas laser tubes, wear pads

conductivity, they are mediocre compared to carbon nanotubes. More specifically, traditional carbon filler have elastic modulus on the order of 300-800 GPa whereas the elastic modulus of SWNT, which is independent of tube chirality but dependent on tube diameter, can reach as high as 1 TPa for 1-2 nm diameter tube, owing to its nanoscale features and ultrahigh surface-to volume ratio. MWNT's Young's modulus is higher (~1.1-1.3 TPa) since it will acquire the modulus of the highest value of a SWNT plus contributions from coaxial intertube coupling or van der Waals force. While most hard materials fail with a strain of 1% or less, CNT can sustain up to 15% tensile strain before fracture due to elastic buckling through which high stress can be released.<sup>14</sup> Although the electrical conductivity of carbon fiber or graphite can reach up to ~10 S/cm, it is inferior compared to the electrical conductivity of SWNT/MWNT, which is on the order of ~10,000 S/cm (100 times greater than copper).<sup>17</sup> Furthermore, the CNT also has exceptional thermal conductivity (~6000 W m<sup>-1</sup> K<sup>-1</sup>, exceeding diamond), thereby providing tremendous promise for their potential applications. In fact, great progress has been made towards their applications in chemical and biological separation, energy storage such as fuel cells and lithium batteries, composites for coating, filling and structural materials, probes, sensors and field emission devices.<sup>14</sup> The 'ideal' structure of SWNTs has allowed it to gain an edge over existing filler materials in research and incorporation in advanced materials with targeted properties.

## **1.2 Polymer Nanocomposite**

### **A. Covalent vs Noncovalent Functionalization**

The outstanding properties of SWNT outlined above can be effectively exploited by incorporating the nanotubes into a matrix. Their incorporation in polymer nanocomposites can extend the function and utility of these carbon based nanoparticles while maintaining the manufacturing and processing flexibility inherent to plastics, thermosets and resins. However, practical realization of nanotube-based materials has been hindered by a number of problems, such as the need to separate the carbon nanotubes (CNT) from the bundles formed during processing,<sup>18</sup> the underlying problems that researchers encounter during purification processes or characterization,<sup>19</sup> and the existence of strong interparticle forces between the CNT that impede uniform dispersion of these nanofillers. Polymer-based nanocomposites are one avenue that has been extensively investigated in an attempt to achieve particle spatial dispersion, where intermolecular interactions between polymer matrices and CNTs can be achieved either by covalent attachment of polymers onto CNTs<sup>20,21</sup> or non-covalent interactions between polymers and CNTs such as charge transfer,<sup>22</sup> adsorption of polymers with large  $\pi$  systems<sup>23</sup> or nonspecific CH- $\pi$  interaction.<sup>24</sup> Figure 1.3 is a schematic showing the methods commonly used to chemically modify the surfaces of carbon nanotubes in order to achieve solubility.

Covalent attachment of polymers to functionalize the CNT surface can increase the degree of interfacial adhesion relative to that of unfunctionalized CNTs. For instance,

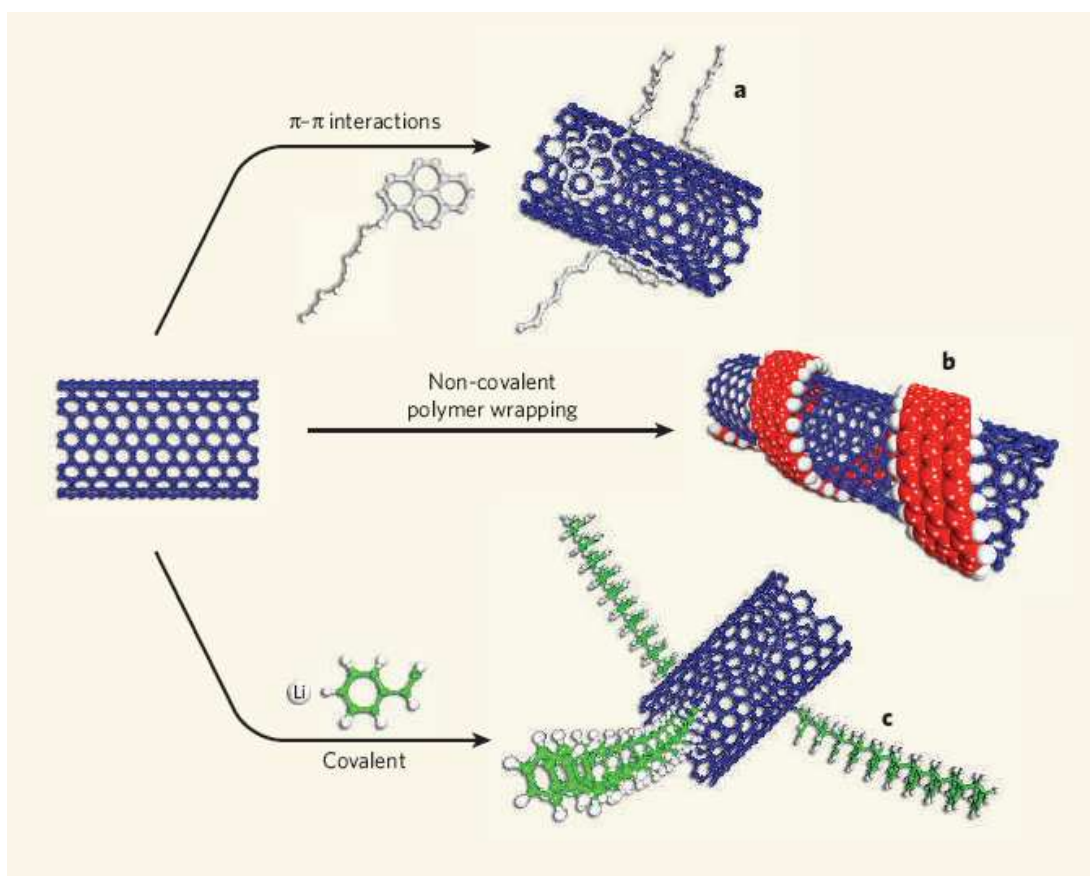


**Figure 1.5.** Methods to achieve nanoparticle dispersion in polymer matrix. (a)  $\pi$ - $\pi$  interactions (b) Non-covalent interactions (c) Covalent functionalization. Figure adapted from Reference 26.

polystyrene (PS) nanocomposites with PS-functionalized single-walled nanotubes (SWNTs) form a percolated filler network structure with 1.5 wt% SWNT whereas pristine SWNTs, when mixed with the same polystyrene matrix, do not exhibit the formation of a network superstructure for loadings as high as 3 wt%.<sup>25</sup> McIntosh et al. synthesized benzoyl peroxide initiated, in situ functionalized SWNT with polypropylene (PP) and the resulting composite, which were spun into 2.5, 5.0, 7.5 and 10.0 wt% SWNT/PP fibers demonstrated improved mechanical properties, in tensile strength by 82.9, 89.8, 72.3 and 173.1 percent respectively whereas the elastic modulus increased by 69.2, 99.7, 137.2 and 133.7 percent respectively, over that of the neat polypropylene fibers.<sup>26</sup> In addition, Zhu and coworkers have noted significant improvement in the mechanical properties of epoxy polymer composites that has been covalently bound to the SWNTs.<sup>27</sup> Such improvement in mechanical behavior is also in agreement in theory. For example, molecular dynamics and statics simulation of nanotubes functionalized with hydrocarbon chains show an increase in the local stiffness of the functionalized SWNT with respect to the nonfunctionalized form. The mechanical strength is also found to increase with the increase in the number of chemical attachments.<sup>28</sup> These results indicate improved compatibility between functionalized SWNT and polymer matrix and the resulting better dispersion of SWNT, and consequently better mechanical properties of the polymer nanocomposite.

However, the oxidative treatment of SWNTs during covalent functionalization results in shortened tubes and a more detrimental effect is the increase in the number of structural defects. The introduction of  $sp^3$ -hybridized defects in the graphitic framework

of the nanotube walls is detrimental to the thermal and electronic properties of the CNT due to the disruption of the  $\pi$ -conjugated system of the nanotube network. This drawback has been reported by Bergeret and coworkers, whereby spectroscopic evidence from x-ray photoelectron spectroscopy and Raman spectroscopy suggests the loss of CNT's metallic character upon covalent functionalization via nitric acid purification.<sup>29</sup> In addition, Bahr et al. also observed the disappearance of the features in the UV/vis/NIR absorption spectra of derivatized tube via electrochemical reduction of a variety of aryl diazonium salts when compared to the pristine SWNT.<sup>30</sup> The features found in the spectrum of pristine SWNT are due to the singularities in the density of states and are attributed to the band gap transitions in the nanotubes. Similarly, the featureless NIR spectrum of SWNTs functionalized based on the 1,3-dipolar cycloaddition of azomethine ylides, generated by condensation of  $\alpha$ -amino acid and aldehyde,<sup>31</sup> and a separate experiment based on diazonium functionalized SWNT<sup>32</sup> also indicates significant electronic perturbation of the nanotubes and disruption of the extended  $\pi$  network. These authors also claim that these reactions can be thermally reversed, cleaving the functional groups from the SWNT sidewalls, thereby restoring the properties of the pristine metallic or semiconducting nanotubes.<sup>31,32</sup> This postulation was made based on the similarity of the disorder induced D band from Raman spectroscopy of pristine SWNT and thermally annealed functionalized-SWNT. This band represents the conversion of  $sp^2$  to  $sp^3$  character due to the introduction of defect during functionalization.<sup>30-33</sup> However, to the best of our knowledge, experimental investigations that compare the electronic properties

of non-functionalized SWNT and thermally annealed functionalized-SWNT have not been fully studied nor understood.

As such, in many cases, non-covalent modification is a more preferable route for achieving CNT spatial uniformity in polymer matrices. Poly(methyl methacrylate),<sup>34</sup> aromatic/aliphatic polyimides,<sup>35,36</sup> conjugated polymers such as poly(arylene ethynylenes),<sup>23</sup> nonconjugated poly(acrylic acid),<sup>37</sup> polystyrene and poly(ethylene oxide) dimethyl ether<sup>38</sup> are a few host polymer matrices among the plethora of studies that have adopted a non-covalent approach as a pathway to achieve CNT dispersion. We have taken this approach in our investigation and quantify the extent of non-covalent interfacial interaction and correlate it to dispersion in polymer-based nanocomposites in order to reproducibly tune the material properties, understand the interfacial phenomenon in polymer nanocomposites and most importantly, preserve the intrinsic properties of the carbon nanotubes.

## **B. Interfacial Adhesion**

It has been well-established that the performance of a polymer nanocomposite depends critically on the interfacial adhesion between the nanofiller and the matrix material.<sup>16,22,24,39-52</sup> Nanofillers such as CNTs, fullerenes and graphenes offer great advantage in comparison with traditional micron-sized fillers due to its small size and the accompanying increase in surface area. Since the polymer chains in close proximity to the filler is perturbed with respect to those in the bulk, the importance of polymer-particle interactions is amplified in polymer nanocomposite. In other words, due to the existence



of a large fraction of polymers in the interface for nanoscale fillers, the strength of interaction between the filler surface and polymer matrix dominate the macroscopic properties and it is imperative to understand the impact of interface on the ultimate macroscopic properties of polymer nanocomposites. As an example to reiterate this further, for a mixture of a mere 1 vol% of a spherical nanoparticle (radius  $\sim 2$  nm) with a polymer matrix (interfacial thickness  $\sim 6$  nm), the volume fraction occupied by the interfacial region is  $\sim 63$  vol%, where more than half of the composite is affected by the presence of the second-phase particles.<sup>16</sup>

Before attempting to determine the macroscopic properties of polymer nanocomposites, one of the most difficult challenges that needs to be overcome is the quantitative assessment of the extent and efficiency of adhesion through the interface between nanotubes and polymers. Devising an experiment for this study is difficult due to the heterogeneity of CNT diameter and chirality as well as the limited reproducibility of polymer nanocomposite's behavior. Thus, molecular modeling or simulations serves as an invaluable tool to investigate the extent of interfacial interaction in these multi-component systems.

A combination of an atomistic molecular dynamics computer simulation<sup>53</sup> and experimental work<sup>54</sup> has been performed to elucidate the nature of SWNT and conjugated poly(*m*-phenylenevinylene-*co*-2,5-dioctyloxy-*p*-phenylenevinylene) (PmPV) interaction. Simulation suggests that the polymer backbone provides the strongest binding (123 kJ/mol per PmPV repeat unit) to the SWNT and not the octyloxy side groups. At a binding energy of 36 kJ/mol per PmPV repeat unit, the side chains have a

greater freedom of movement to wrap around the nanotube in an ordered fashion. These results were supported by TEM results showing a SWNT network coated in PmPV, consisting of a large amount of intertwined PmPV-coated ropes. Furthermore, the absorption spectrum of the composite indicates a significant reduction in electron delocalization relative to the pure PmPV, suggesting significant alteration of chain conformation due to nanotube interaction.

The influence of nanotube chirality, temperature and chemical modification on the interfacial adhesion of SWNT with polyphenylacetylene (PPA) has also been investigated theoretically.<sup>55</sup> The influence of temperature on the interaction energy between the SWNT and PPA is considered negligible while chirality plays an important role in the interaction, with the armchair tube having the best structure to interact with PPA. PPA also stretches and wraps around unmodified and methyl- and phenyl-functionalized SWNT but not around tubes with hydroxyl- and fluorine- moieties. The authors suggest that the reason for the preferential interaction is due to the similarity of methyl and phenyl electronic structures to that of PPA.

A single nanotube fragmentation under tensile stresses within a nanotube-containing thin polymeric film has also been observed in an effort to probe the efficiency and quality of the polymer-SWNT interface.<sup>56</sup> Assuming that the applied stress is transferred to the nanotube via a nanotube-matrix interfacial shear mechanism at the molecular level, a force balance of the SWNT-polymer system is expanded from the classical version of the Kelly-Tyson model, proposed for a fiber-polymer system.<sup>57</sup> These calculation results by Wagner et al. suggests that interfacial shear strength values are

influenced by nanotube diameter and tensile strength of a nanotube segment. In addition, they found that the presence of defects in the tube decrease the tube strength and consequently results in a variability of interfacial strength. In another set of experiments, Liao and Li used molecular mechanics to simulate a pull-out test using a SWNT and polystyrene. These studies predict an interfacial shear stress value of about 160 MPa. These computer studies, calculations, simulations and modeling provide an important tool for the prediction of filler-matrix interaction, which is a key in designing effective polymer nanocomposites.

Experimentally, charge transfer interaction between functional groups on a polymer chain and SWNT has been detected by noticeable shifts in the vibrational spectra of SWNTs and/or polymers. For instance, in SWNT-nitrile functionalized polyimide nanocomposite, a  $4\text{ cm}^{-1}$  upshift in the tangential G band signature of SWNT is observed by Raman spectroscopy and a downshift of  $\sim 2\text{ cm}^{-1}$  in the nitrile stretching mode ( $\sim 2232\text{ cm}^{-1}$ ) is detected by Infrared spectroscopy.<sup>36</sup> In addition, the transparent films containing nanotubes were deep green in color while pristine films were pale yellow. These quantitative and qualitative observations were attributed to the formation of electron donor-acceptor complex between SWNTs and the polymer matrix via the 2,6-bis(3-aminophenoxy) benzonitrile monomers, which acted as Lewis acids (withdrawing electron density from SWNT). Small molecules<sup>58,59</sup> and alkali<sup>60</sup> have also been employed as donor or acceptor groups. Collins and coworkers demonstrated that exposure of SWNT to air or oxygen dramatically influences the nanotubes' electrical resistance, thermoelectric power and local density of states as determined by transport

measurements and scanning tunneling spectroscopy. This oxygen-induced charge transfer in SWNTs could indicate the presence of on-tube defects, making oxygen sensitivity an ideal way to determine the concentration of defects in CNTs.<sup>58</sup> Charge transfer interaction between gaseous molecules such as electron accepting NO<sub>2</sub> and electron donating NH<sub>3</sub> have also been reported to dramatically increase or decrease the electrical resistance of a semiconducting SWNT. In addition, Claye et al. observed an 8 cm<sup>-1</sup> downshift in the tangential G mode of SWNT doped with K- and Li-doped SWNTs.<sup>60</sup>

Although Raman spectroscopy has been extensively used to study the extent of charge transfer interaction in polymer nanocomposite systems, these studies are limited to the measurement of an ensemble of heterogenous SWNTs. Shim et al.<sup>61</sup> utilized resonant microRaman measurements to examine the charge transfer interaction of polyethyleneimine adsorption onto SWNT. This characterization technique is exploited to ensure that only one SWNT contributes to the observed signal. They observed an upshift in both the lower and higher frequency tangential G bands (G<sup>-</sup> and G<sup>+</sup>) upon PEI doping, consistent with C-C bond length expansion in the SWNT upon electron injection and as observed in alkali metal doping of nanotube and graphite systems. Furthermore, there is a strong diameter dependence of the magnitude of the downshift for both peaks. An investigation by Wood and coworkers demonstrates upshifts in the frequency of the second order disorder-induced D\* band of SWNTs when molecular pressure is applied to the nanotube's sidewalls by immersing them in various liquids of varying cohesive energy density (CED) or macroscopic pressure that is applied by a diamond anvil cell.<sup>62-</sup>

<sup>66</sup> The authors have systematically attributed the positive peak shift of the D\* band

frequency of carbon nanotubes embedded in a polymer matrix relative to that of the pure SWNTs to (I) CED or internal pressure of a polymer phase,<sup>62,64-68</sup> (II) compression of SWNT C-C bonds from the shrinkage of polymer matrix,<sup>69</sup> (III) the temperature dependence of SWNT structure in air<sup>68</sup> and (IV) the shift produced by the stress induced from the temperature dependence of cohesive energy density.<sup>70</sup> The aforementioned factors were eliminated as the cause for variation in the magnitude of D\* peak shift observed in our Raman spectra and will be discussed in greater detail in Chapter 3. In our study, the shift is interpreted to originate from the variation of compressive stress due to polymer-SWNT interactions. It is worth noting that for these spectroscopic techniques, it is important to ensure that measurements are taken at the interface of polymer and particle and not on the bundled nanoparticle.

Thus far, research work to understand the role of the structure of the polymer-nanoparticle interface as a vehicle to optimize the properties of polymer nanocomposite has been mostly focused on qualitative investigations.<sup>16,22,24,41-54</sup> In this dissertation, we will move beyond the qualitative investigation and quantitatively determine the relationship between intermolecular charge transfer interactions (i.e. electron donor-acceptor interactions) and SWNT dispersion in polymer nanocomposites. In this study, the amount of electron donating 2-(dimethylamino)ethyl methacrylate (DMAEMA) or electron accepting acrylonitrile (AN) and cyanostyrene (CNSt) moieties in three sets of copolymers was varied between ~10 and 50 mol% to control the extent of electron donor-acceptor complex formation with the SWNT and the resulting particle dispersion in the

polymer nanocomposites were characterized by Raman spectroscopy and optical microscopy.

### **C. Morphology and Dispersion**

Due to the emergence of increasingly complex functional materials in nanoscience, control over particle spatial dispersion in polymer matrix and development of practical approaches for characterizing their structures needs to be rigorously explored. Having this knowledge is a prerequisite for further understanding the structure-property-function relationships. Examples include nanoparticles embedded in polymer matrix,<sup>16,22,24,41-54</sup> species encapsulated in mesoporous hosts<sup>71,72</sup> and bulk crystals with intrinsic nanoscale order.<sup>73,74</sup> For the case of crystals, x-ray diffraction is a robust and quantitative method to retrieve the average atomic positions in the sample. For amorphous polymer nanocomposite however, an x-ray diffractometer generates a broad and continuous intensity distribution that is not amenable to a crystallographic solution.<sup>74</sup>

In attempts to solve this problem, imaging and spectroscopic techniques have been commonly used to determine the dispersion of carbon nanotube in polymer matrices.<sup>75-77</sup> However, it needs to be emphasized that structure elucidation is not a trivial challenge due to the complexity of the nanostructure that display multiple size scales on length scales ranging from Angstroms to millimeters. Foster and coworkers utilized atomic force microscopy (AFM) to study the nanoscale distribution of SWNT in polyurethane composite films. Although the authors claimed that the diameter of the bundled tubes measured were on the order of 7.17 nm, it was questionable as to whether

they were measuring SWNT bundles or excess polymer around a single SWNT.<sup>76</sup> Another disadvantage of this technique is that lateral dimensions measured are often overestimated due to the limited sharpness of the AFM tip and its mathematical convolution with surface features during imaging.<sup>76</sup> Transmission electron microscopy (TEM) has also been utilized to study the nanoparticle dispersion in polyimide nanocomposites, revealing fine features with 0.34 nm spacing in the bundle contrast regions. This is thinner than the average diameter of the 1.4 nm individual tubes and the authors stated that reason is unclear. It needs to be pointed out that structure elucidation of a polymer nanocomposite by TEM is a complex task due to the extremely low contrast between SWNT and polymer matrix<sup>78</sup> and is also dependent on nonstructural factors such as sample thickness, lens aberrations and imaging conditions.<sup>74</sup> In addition, the requirement of ultra-thin sectioning of bulk samples by microtome to obtain morphology of “as-processed” samples adds ambiguity to the interpretation of 3-D organization of filler in polymer matrices because the size of the 3-D structure exceeds the thickness of ultrathin sections.

Small angle x-ray, neutron or light scattering techniques have also been proven to be a valuable tool for quantitative measures of SWNT dispersion in suspensions<sup>79-82</sup> and polymer matrices<sup>83-85</sup> for wave vectors  $Q \sim 10^{-4}$ - $10^{-1} \text{ \AA}^{-1}$ , which corresponds to a real space length scale of 1-1000 nm. In a scattering event, the term  $Q$  correlates the scattering event to the spatial properties of the scattering sample and is inversely proportional to the real space length scale. A more in depth discussion on the basics of a scattering experiment is presented in Chapter 5. The concept of “fractal dimension” or

self-similarity, which stems from a purely mathematical sense from the study of certain geometrical objects, can be applied SWNTs.<sup>86-89</sup> To illustrate this in a physical sense, consider a stretched string, which clearly resembles a one-dimensional object. When this string is placed on a surface and looped back and forth so it covers the surface completely, a two-dimensional object is obtained, and if it is folded up in a tight ball, it begins to look three-dimensional. Since this is a continuous process, the dimensionality of the object evolves continuously from 1 to 3. Similarly, in the case of SWNTs, it would be expected that the scattered intensity from isolated rigid rods with diameter  $D$  and length  $L$  follows a  $Q^{-1}$  law for wave vectors  $2\pi/L < Q < 2\pi/D$ , where the exponent -1 corresponds to fractal dimension of 1. Although rare, isolated SWNT has been observed in the scattering pattern of dilute suspensions of purified SWNTs in  $D_2O$  with added sodium dodecylbenzene sulfonate ionic surfactant.<sup>82</sup> Most studies however observed a fractal dimension between 2 and 3, characteristic of a network of carbon “ropes”, which is interpreted to be side-by-side aggregates of SWNTs.<sup>90</sup> Schaefer and coworkers determined the morphology of SWNT suspension in polyelectrolyte solutions using a combination of small- and ultrasmall-angle X-ray scattering and light scattering.<sup>81</sup> The scattering curve consists of three power-law regimes separated by breaks, which fix the relevant length scales and the intervening power laws that reveal the morphology of the nanoparticle entities. The slope of -2.2 over an extensive region of the largest length scale (0.22-28  $\mu m$ ) corresponds to the mean radius of the swollen ropes. The slope of -4 over the length scale of 722 Å and 0.22  $\mu m$  was interpreted to arise from the smooth surface of the ropes whereas the third power law regime (60 Å – 722 Å) with a power-law exponent



of -2.1 is interpreted to arise from the small-scale mesh-like network present inside the highly swollen ropes. The swollen morphology implies that the suspended ropes were close to full dispersion and when sonication was performed on the suspension, rod-like morphology was gradually observed at a length scale of 5000 Å -30000 Å.

Raman spectroscopy is another valuable probe of the local structure of composite material. Utilizing this spectroscopic technique, Rasheed et al.<sup>51,52</sup> developed a method to quantify SWNT dispersion by using the ratio of average-G band intensity in the clear region ( $I_{clear}^G$ ) of the composite to the average G-band intensity in the aggregated region ( $I_{agg}^G$ ). A homogeneously dispersed sample exhibits a ratio of  $I_{clear}^G / I_{agg}^G$  approaching 1, whereas poorly dispersed SWNTs will exhibit an  $I_{clear}^G / I_{agg}^G$  that will approach 0. In the Raman spectra of a SWNT, the G band is derived from the graphite-like in-plane mode, and therefore can be readily used to determine the local relative concentration of SWNT in nanocomposite samples. Similarly, Du et al. utilized the Raman imaging method to quantitatively characterize the SWNT dispersion in a PMMA matrix by obtaining a Raman mapping intensity map over a 40 µm x 40 µm domain.<sup>47</sup> The quantitative dispersion level of the composite was characterized by the mean standard deviation of the Raman scattering intensity. In another experimental study, utilizing similar concept, laser scanning confocal microscopy (LSCM) has been utilized to evaluate the degree of mixing of MWNT in a polystyrene matrix on the meso and micrometer scales. This method requires the presence of a fluorescent dye, Nile blue A perchlorate (NB), in the polymer nanocomposite, where low fluorescence correspond to the MWNT particles as a result of quenching by the tube. The corresponding intensity-versus-distance profile, taken from

the data along the horizontal center line in each image, gives a quantitative indication of the level of particle distribution in each sample.<sup>91</sup>

### **1.3. Application of Flory-Huggins Theory to Polymer Nanocomposite**

It is the premise of this dissertation that, in order to gain full insight into the interfacial properties in polymer nanocomposites, a fundamental understanding of the factors that control the material behavior must be obtained. One must therefore take a closer look at the basic thermodynamics of polymer blends developed by Josiah Gibbs in 1875, generally defined by the Gibbs free energy of mixing,  $\Delta G_m$ :

$$\Delta G_m = \Delta H - T\Delta S \quad (\text{Equation 1.4})$$

which consists of both the enthalpic component,  $\Delta H$  and entropic component,  $\Delta S$ .

Polymer blending is a convenient route for the development of new polymeric materials, which combines the excellent properties of more than one existing polymer.<sup>92-</sup>

<sup>95</sup> Generally speaking, in homogenous blends, both blend components lose part of their identity and the final properties are usually the arithmetical average of both blend components whereas in heterogenous blends, the properties of all blend components are present. Therefore, the advantage of this strategy is the attainment of a wide range of material properties by simply changing the blend composition. In addition, it is usually a cheaper and less time consuming method than the development of new monomers or polymerization routes as the basis for an entirely new polymeric material.<sup>96</sup>

In order for a multicomponent system to be miscible, a negative free energy change of mixing (Equation 1.4) is necessary. However, most polymer pairs phase separate when mixed due to the low entropy of mixing two polymer chains and the fact that enthalpy of mixing is often positive. Due to the degree of disorder in a long polymer chain, the addition of a second component does not produce a substantial gain in entropy. It is therefore crucial to achieve efficient intermolecular interaction between the two components in the system to attain a favorable enthalpic interaction and consequently a negative free energy of mixing. These interactions may range from strongly ionic to weak and nonbonding interactions, such as hydrogen bonding, ion-dipole, dipole-dipole and donor-acceptor interactions.

From Flory-Huggins theory, a natural extension of regular solution theory to the case where at least one of the components is polymeric, the free energy of mixing can be written as:

$$\frac{\Delta G_m}{RT} = \frac{\Phi_A}{N_A} \ln \Phi_A + \frac{\Phi_B}{N_B} \ln \Phi_B + \chi_{AB} \Phi_A \Phi_B \quad (\text{Equation 1.5})$$

where  $\Phi_A, \Phi_B$  and  $N_A$  and  $N_B$  are the volume fractions and number of molecular units in component A and component B respectively, R the gas constant, T the temperature in Kelvin and  $\chi_{AB}$  is the Flory-Huggins interaction parameter. The first two terms in Equation 1.5 denotes the configurational entropy of mixing the two components and the third term denotes the enthalpic component. As the combinatorial entropy term is negligible for polymeric systems, the free energy of mixing, and thus the miscibility is

dominated by the enthalpy of mixing. Strictly speaking, SWNTs are not polymers in the conventional sense and the question arises whether this theory, which is conventionally used to predict miscibility behavior of polymer blends, can be applied analogously to polymer nanocomposite systems. Although the discussion presented was focused solely on the physical interpretation of this theory to polymer blend system, its application mathematically to our multi-component system is discussed in detail in Section 3.3C.

Due to the remarkable simplicity of the Flory Huggins theory, it remains widely popular among investigators dealing with experimental data treatment. However, as evidenced experimentally in subsequent chapters and discussed briefly here, this theory falls short in providing an adequate explanation for a number of experimental results.<sup>97,98</sup> Geometrical constraint due to polymer chain connectivity is a crucial parameter that is not taken into account in this theory. This entropic parameter controls the formation of non-covalent interactions in polymeric mixtures<sup>97-100</sup> because the mobility of a given functional group along a chain is influenced by its proximity to other functional groups. More specifically, the participation of one functional group in an intermolecular interaction will inhibit the mobility of a neighboring group and limit its ability to access and orient itself correctly to form an additional interfacial interaction. This effect is mitigated if the functional groups are adequately spaced out along the polymer chain, so that they are dynamically independent and the formation of one intermolecular interaction does not inhibit the formation of an additional interaction with the SWNT. Therefore, this exemplifies the importance of the interplay between chain connectivity

effects, steric shielding and spacing between specific interaction sites, which limit the number of inter-component bonding formation.

In fact, this has been thoroughly investigated in polymer blends and solutions. For instance, examination of the extent of hydrogen bonding<sup>101</sup> in blends of 2,3-dimethylbutadiene-*stat*-4-vinylphenol (DMBVPh) and ethylene-*stat*-vinyl acetate (EVA) copolymers of varying compositions<sup>100</sup>, and a separate study on solutions of 4-ethylphenol (Eph) and poly(n-alkyl methacrylate)s (PAMA) of varying alkyl side chain lengths<sup>99</sup> provide insight into the formation of intermolecular interactions in polymer blends. In these studies, the inter-association equilibrium constant,  $K_A^{Std}$ , determined from infrared spectroscopy by Coleman and Painter quantifies the extent of intermolecular hydrogen bonding between ester or acetoxy carbonyl group on EVA or PAMA and the phenolic hydroxyl group on DMBVPh or Eph.<sup>97,98</sup> The authors interpreted their results as a direct consequence of chain connectivity on the formation of intermolecular hydrogen bonds, whereby the formation of one hydrogen bond restricts the mobility of a nearby functional group to form an intermolecular interaction with the corresponding group, a consequence of rotational bond angle restrictions found in polymer chains. These effects are insignificant however, if the amount of interacting phenol or carbonyl groups in the copolymer is so low such that the intermolecular interaction cannot be formed. Therefore, there exists a certain composition of the copolymer whereby optimal intermolecular adhesion occurs.

## 1.4 Conclusions and Proposed Experiments

This dissertation focuses on developing a protocol to improve the dispersion of SWNT in polymers while keeping the native surface of single-walled carbon nanotube (SWNT) intact. Our previous experience in this area<sup>51,52,101</sup> is exploited to explore the effect of controlling the extent of intermolecular charge transfer interactions (electron donor-acceptor interactions) on the extent of SWNT spatial uniformity, by systematically varying the composition of the copolymer matrix. In these studies, the amount of electron donating 2-(dimethylamino) ethyl methacrylate (DMAEMA) or electron accepting acrylonitrile (AN) and cyanostyrene (CNSt) moieties in three sets of copolymers were varied between ~10 to 50 mol% to control the extent of electron-donor-acceptor complex formation with the SWNT. Density functional theory (DFT) calculations were completed to provide additional insight into the extent of molecular interaction between an interacting monomeric or oligomeric unit and SWNTs as well as the optimized geometries for the formation of the underlying interactions. The results were found to correlate very well with our experimental data and clearly indicate that controlling the extent of intermolecular electron-donor-acceptor complex formation between a polymer matrix and SWNT, which is governed by chain connectivity, provides a method to optimize the SWNT spatial dispersion.

In Chapter 3, the use of Raman spectroscopy to understand and obtain a measure of the level of charge transfer between the copolymers and SWNTs is described. Density functional theory (DFT) calculations are also presented to provide additional insight into the extent of molecular interaction between an interacting monomeric or oligomeric unit and

SWNTs as well as the optimized geometries for the formation of the underlying interactions. The discussion in Chapter 4 focuses on the quantification of dispersion of these polymer nanocomposites by optical microscopy and Raman spectroscopy. In Chapter 5, the utilization of small angle neutron scattering technique to evaluate the morphology of nanoadditive in the composite materials is presented. In Chapter 6, we seek to understand the system parameters that govern SWNT particle dispersion in suspension in the context of colloid science.

## CHAPTER 2: EXPERIMENTAL TECHNIQUES

The purpose of this chapter is to describe the reaction procedures and experimental details used in this study, including chemical purification, polymer synthesis, nanocomposite preparation and characterization of the composites. The characterization results of the polymers used for every experimental technique are presented in the following chapters preceding the results and discussion.

### 2.1 Commercially Purchased Materials

#### A. Chemicals

Methyl methacrylate (MMA), 4-cyanostyrene (CNSt) and styrene (St) monomers were purchased from Acros Organics and 2-(dimethylamino) ethyl methacrylate (DMAEMA) from Sigma Aldrich. Deuterated styrene (d-St) and deuterated acrylonitrile (d-AN) were purchased from Polymer Source Inc. and Cambridge Isotope Laboratories Inc. respectively. p-toluenesulfonyl chloride (p-TsCl), 2,2'-bipyridine (bpy), copper(I) chloride (CuCl), copper (I) bromide (CuBr), dimethyl formamide (DMF), N,N-dimethylacetamide (anhydrous, 99.8%) (DMAc), tetrahydrofuran (THF), methanol, anhydrous anisole, anhydrous p-xylene, anhydrous ethylene carbonate, 1-methyl-2-pyrrolidinone (NMP, Chromasolv Plus HPLC grade, >99%), 2,2'-azobisisobutyronitrile (AIBN), 2-bromopropionitrile (BPN), 4,4'-Dinonyl-2,2'-dipyridyl (dnBpy) and ethyl  $\alpha$ -bromoisobutyrate (Ebib) were purchased from Sigma Aldrich. n-hexane (99.7% purity, HPLC grade) and glacial acetic acid were purchased from Fisher Scientific. Propylene glycol monomethyl ether acetate hexamethyldisilazane (commercial name: Microprime Primer P-20) was purchased from Shin-Etsu MicroSi Inc.



## B. Polymers

Poly-2-(dimethylamino) ethyl methacrylate (PDMAEMA), polystyrene (PS) and polyacrylonitrile (PAN) were obtained from Scientific Polymer Products, Inc. Styrene-*ran*-acrylonitrile (SAN) copolymers with 29.5, 36.8, 45.0, 48.8, 56.2 mol% AN were obtained from an industrial source.

## C. Carbon Materials

The single-walled nanotubes (SWNTs) were used without further treatment and were purchased from Bucky USA for MMA-*ran*-DMAEMA Raman composites and Nano-C Inc. (purified by nitric acid treatment) for all others. Hydrochloric acid treated SWNT, purchased from Nano-C Inc. was utilized in the preparation of composite suspension for UV-Vis spectroscopy measurement. The manufacturer's specifications of the single walled carbon nanotubes are listed in Table 2.1.

**Table 2.1.** SWNT manufacturer's specifications

SWNT Supplier	Bucky USA	Nano-C (HNO <sub>3</sub> treatment)	Nano-C (HCl treatment)
Length	0.5-4.0 $\mu$ m	500-700 nm	700-900 nm
Diameter	1-2 nm	0.9-1.3 nm	
Purity	>95%	>95.5%	>93%
Iron metal residue		2.19%	3.34%

## 2.2 Purification of Reagents

### A. Monomers

The monomers were passed through a column of activated aluminum oxide (Neutral, Brockmann I, standard grade, ~150 meshes, 58 Å, Sigma Aldrich)

gravimetrically before use to remove impurities such as water and inhibitor. Inhibitors include 4-methoxyphenol in deuterated acrylonitrile monomer, 3,5-di-*tert*-4-butylhydroxytoluene (BHT) in deuterated styrene, monomethyl ether hydroquinone (MEHQ) in acrylonitrile and para *tert*-butyl catechol in styrene. Each has methoxy and/or hydroxyl group that have selective affinities for the oxide group on the alumina, thus allowing the purification of the monomers through an absorption process.

#### **B. Copper (I) Bromide and Copper (I) Chloride**

Copper (I) bromide and copper (I) chloride were purified by stirring over glacial acetic acid for 4 hours, followed by filtration. The remaining solid on the filter paper was washed twice with diethyl ether before drying in the vacuum oven for 1 day.<sup>102</sup> The CuBr and CuCl prepared is a light green, almost white crystalline powder that remains unchanged for an indefinite period if kept dry. Moist air converts it into a dark-green material and can be re-purified by grinding the material with sulfuric acid into a paste-like mixture, followed by washing and drying as outlined above.<sup>103</sup>

### **2.3 Synthesis of Polymers**

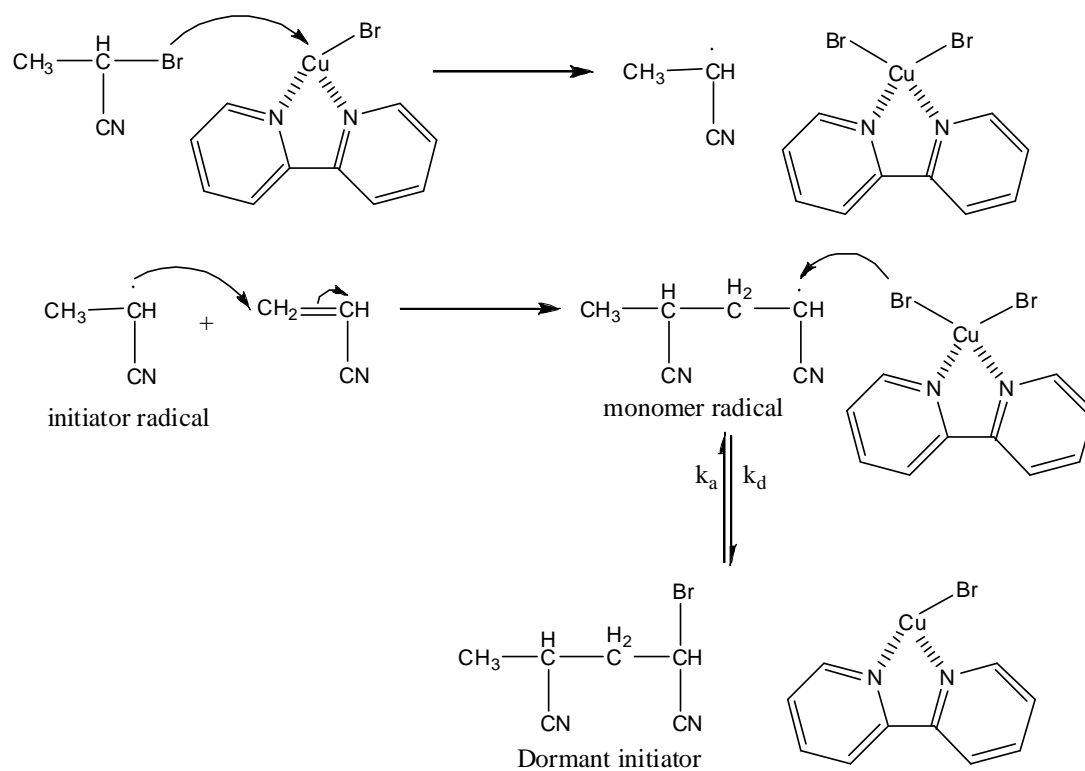
#### **A. Atom Transfer Radical Polymerization (ATRP)**

The production of well-defined functional polymers with controlled architecture, molecular weight distribution and composition has long been of interest to polymer chemists. While living polymerization techniques such as anionic and cationic techniques have the advantage of tailoring polymers with these desirable architectures, room for improvement still exists mainly due to their laborious synthetic procedures and sensitivity

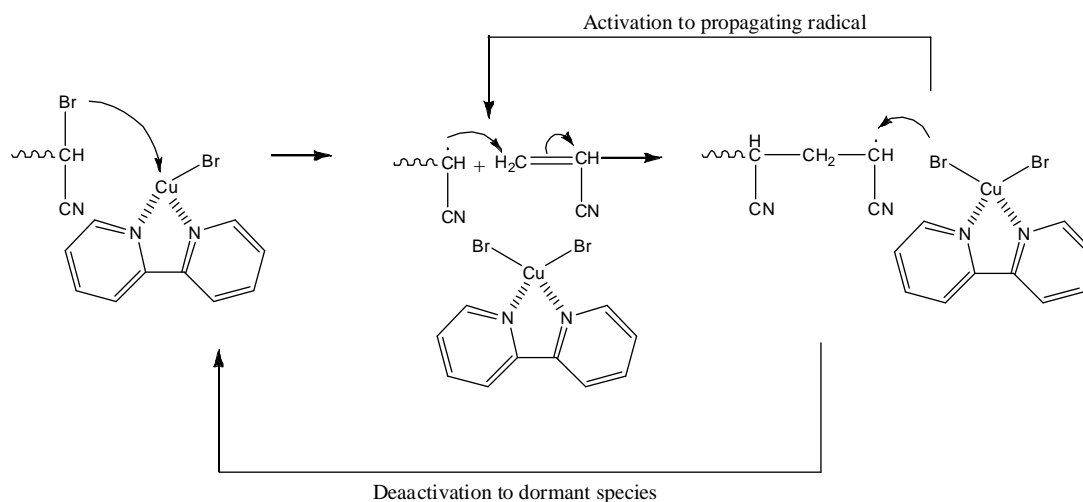
to impurities. The development of a “living” radical technique, atom transfer radical polymerization (ATRP), in the early 90’s proved to be a significant advancement in polymer synthesis because of its tolerance to proton species and less stringent reaction conditions while still retaining the advantage of the ability to produce well-defined polymers.

For the purpose of describing the reaction mechanism of ATRP, the polymerization of polyacrylonitrile (PAN) via this technique is outlined below. ATRP is a multicomponent system which consists of the monomer/s, an initiator with transferrable pseudohalogen and a catalyst which consists of a transition metal species with an appropriate ligand. In some cases however, additives can be included to accelerate the reaction. The reaction schemes for the initiation and propagation of PAN homopolymerization are shown in Schemes 2.1 and 2.2 respectively. The initiation mechanism involves the transfer of a bromide atom from the 2-bromopropionitrile initiator to the copper bromide/2,2’-bipyridine transition metal complex generating an initiator radical. This initiator radical is able to initiate the vinyl monomer, in this case, acrylonitrile, to produce a monomer radical. The radicals, or the active species, are generated through a reversible redox process catalyzed by the transition metal complex, which undergoes a one-electron oxidation with an accompanying abstraction of a pseudohalogen atom from the dormant species.

The propagation mechanism is also facilitated by the copper bromide/2,2’-bipyridine complex, which can activate the dormant initiator to generate growing chain radicals. To obtain well-defined polymers with narrow molecular weight distributions,



**Scheme 2.1.** Schematic of the initiation mechanism of PAN polymerization



**Scheme 2.2.** Schematic of the initiation mechanism of PAN polymerization

the transfer of halide must occur back and forth rapidly between the transition-metal catalyst complex and the growing chain ends to keep the concentration of radicals low while keeping the concentration of growing chains much higher. The generated free radicals propagate and terminate, as in conventional free radical polymerization through radical coupling and disproportionation. However, even though terminations occur, their contribution is small. Therefore, the control over ATRP are due to (II) fast initiation, thereby providing a constant concentration of growing polymer chains and (II) persistent radical effect, where rapid and reversible deactivation of propagating radicals allow low concentration of radicals, which minimizes termination.<sup>104</sup>

For a successful ATRP synthesis, the proper choice of monomers, initiators, catalysts, solvents temperature and additives is important. However, the choice of ligand is of utmost importance in ATRP synthesis since equilibrium of the radical and dormant species and solubility of the transition metal complex in the reaction medium is governed by the ligand.

### (I) Random Copolymer of MMA and DMAEMA

MMA and four MMA-*ran*-DMAEMA polymers (Table 3.1, Chapter 3) were synthesized by atom transfer radical polymerizations<sup>105,106</sup> using CuCl complexed by bipyridine (bpy) as the catalyst and p-TsCl as the initiator. The monomers ([M]: 6.0 M), bpy, p-xylene and p-TsCl were introduced, in this order, into a 250 ml 2-necked round-bottom flask that was equipped with a reflux condenser and a stir bar. The molar ratio of p-TsCl initiator, CuCl, and bpy ligand used was 1:6:12. The mixture was immediately degassed by three freeze-pump-thaw cycles to remove trace impurities. The flask was heated in an oil bath at 90 °C for 18 hours under nitrogen flow with continuous stirring. The resulting copolymers and homopolymer was diluted with tetrahydrofuran (THF) and passed through an alumina column twice to eliminate copper residues before it was precipitated in a ten-fold excess of cold n-hexane. These samples were then dried under vacuum at 70 °C for 2 days. Hereinafter, DMA(x) denotes MMA-*ran*-DMAEMA copolymer with x mol% of DMAEMA. The plot of mole fraction of DMAEMA in the copolymer,  $F_{\text{DMAEMA}}$  as a function of mole fraction of DMAEMA in comonomer feed,  $f_{\text{DMAEMA}}$  is shown in Figure 2.1.

### (II) Random Copolymer of Styrene and Acrylonitrile

The specially-constructed setup for the polymerization of styrene-*ran*-acrylonitrile (SAN) is illustrated in Figure 2.2. In a typical polymerization procedure for SAN consisting of 23.7 mol% acrylonitrile, the ligand 4,4'-Dinonyl-2,2'-dipyridyl (dnBpy) (0.417 g, 1.024 mmol) and anisole were charged into a Schlenk flask that is equipped with a flow adapter.<sup>107</sup> The contents were then stirred until a homogenous solution is achieved, followed by the addition of styrene (10.954 g, 0.105 mol),

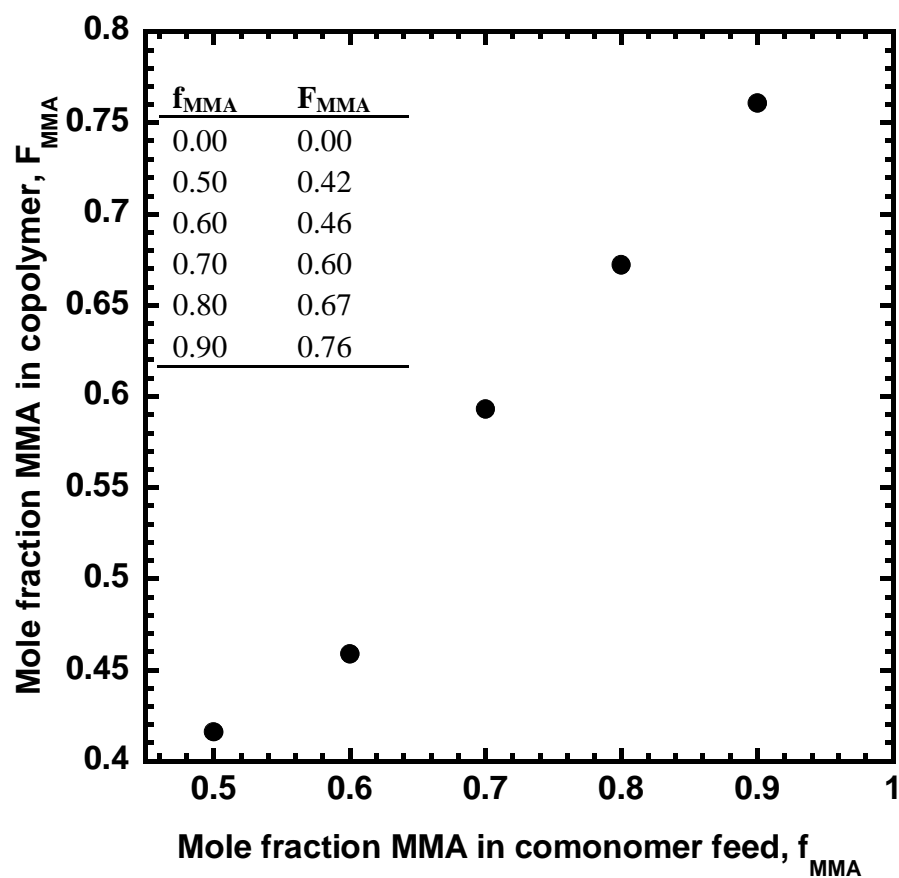


**Figure 2.1.** Mole fraction of DMAEMA in copolymer as a function of DMAEMA mole fraction in comonomer feed

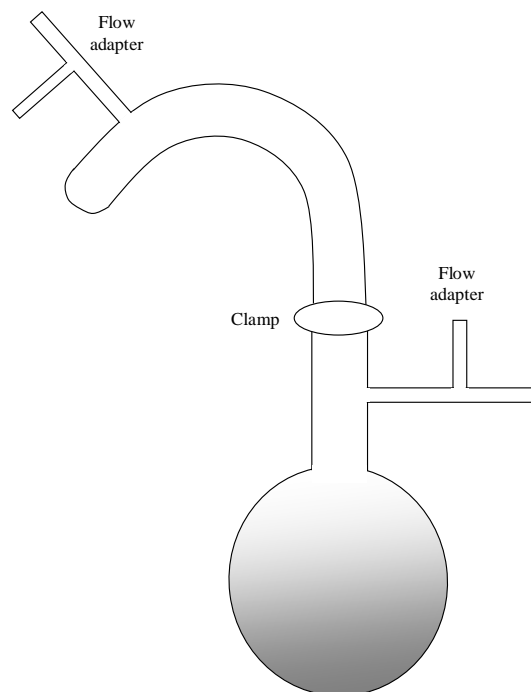


**Figure 2.2.** Polymerization setup for the copolymerization of styrene-ran-acrylonitrile

\



acrylonitrile (1.143 g, 0.022 mol) and ethyl  $\alpha$ -bromoisobutyrate (Ebib) initiator (0.0365 g, 0.128 mmol). The total monomer concentration was 5.5 M and the ratio of [EbiB]: [CuBr]: [dnBpy] was 1:4:8. The entire solution was subjected to three freeze-pump-thaw cycles and immersed in liquid nitrogen again until frozen. While frozen, the seal between the Schlenk flask and flow adapter was carefully opened and 0.512 mmol (0.0753 g) CuBr was added before pumping it again for another hour. After filling it with nitrogen, the reaction was thawed and the sealed flask was placed in an oil bath at 80 °C for 51 hours. The polymerization was terminated by opening the flask and exposing the catalyst to air. The resulting copolymers were diluted with THF and passed through an alumina column twice to eliminate copper residues before it was precipitated in an excess of cold methanol. These samples were then dried under vacuum at 70 °C for 2 days. For simplicity, SAN copolymer with x mol% AN will be referred to as SAN(x). The plot of mole fraction of AN in copolymer,  $F_{AN}$  as a function of mole fraction of AN in the comonomer feed,  $f_{AN}$  is shown in Figure 2.3.

### (III) Polyacrylonitrile

A typical synthetic procedure for polyacrylonitrile uses a free radical technique, although polymers with predefined molecular weights and narrow polydispersities are difficult to achieve using this method. Therefore, we have adopted the atom transfer radical polymerization (ATRP), a controlled/ “living” radical technique, to take advantage of the tolerance to water, impurities and convenience of temperature range (~0 to 100 °C) while still having control over the polymer structure.

Although narrow polydispersities were achieved, the polymerization of PAN via ATRP has a molecular weight limit of 30,000 g.mol<sup>-1</sup>. During reaction, it can be observed

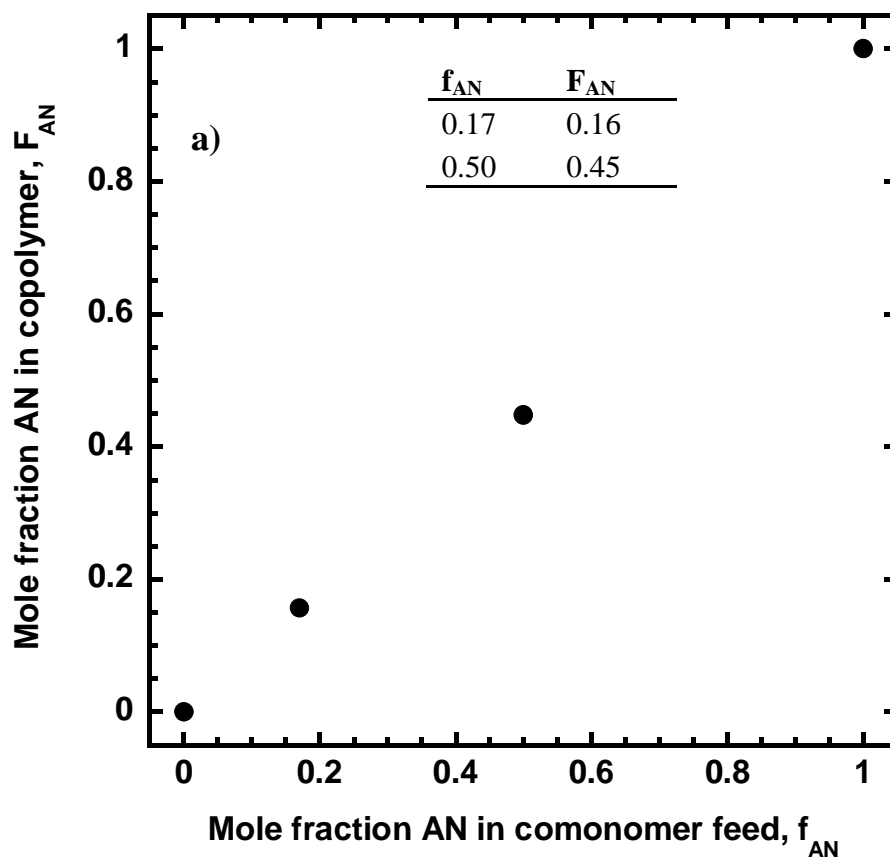
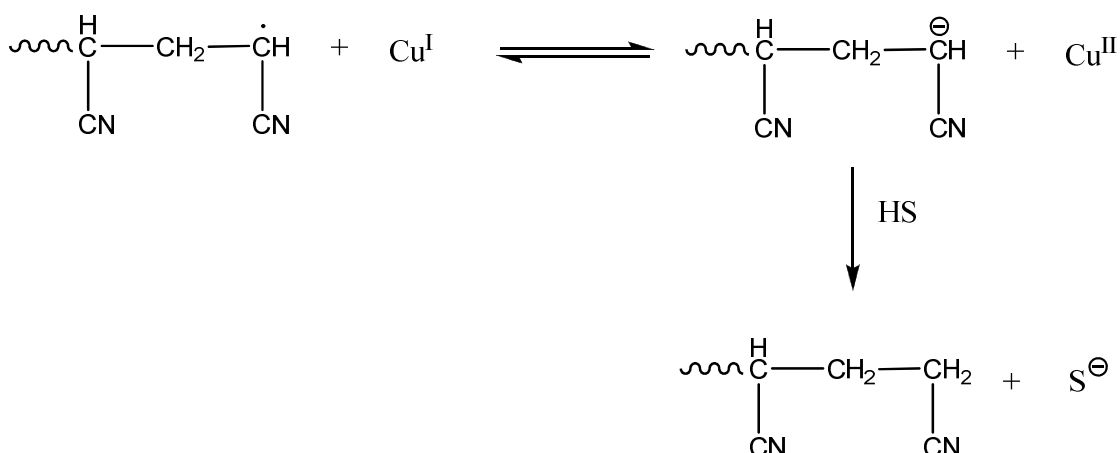


**Figure 2.3.** Mole fraction of AN in copolymer vs mole fraction of AN in comonomer feed

that the reaction steadily turns green indicating the generation of the deactivating Cu II species. Although several reasons for this behavior has been proposed by Matyjaszewski et al.,<sup>108</sup> the most probable is the reduction of the radical by Cu I to form an anion and Cu II species (Scheme 2.3). Therefore, the presence of any proton source such as water will terminate the reaction.



**Scheme 2.3.** Proposed mechanism of the reduction of a radical by Cu I to form Cu II species

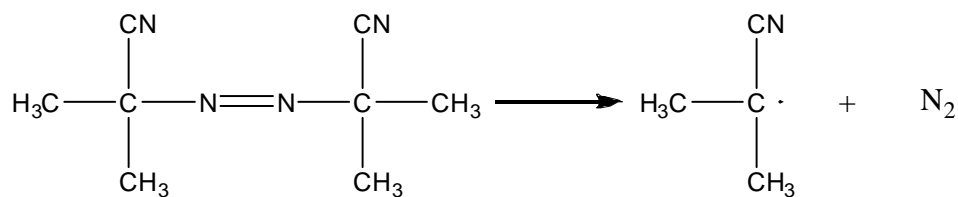
The polymerization procedure for polyacrylonitrile is as follows:<sup>108</sup> CuBr (0.087 mmol), ethylene carbonate (solid at room temperature), acrylonitrile (0.081 mol) and 2-bromopropionitrile (BPN) initiator (0.115 mmol) were added into a Schlenk flask. The total monomer concentration was 6.4 M. The entire reaction was frozen, pumped and thawed once. It was then subjected to a liquid nitrogen bath again and bpy ligand was added before pumping the reaction mixture for another one hour. After filling it with nitrogen, the reaction mixture was thawed and the sealed flask was placed in an oil bath at 45 °C for 22 hours. The resulting homopolymer was diluted with DMF, purified by passing through alumina column to remove copper residue, concentrated, and precipitated

in an excess of cold methanol. After filtration of the polymer, the samples were dried under vacuum without heat for 2 days.

## **B. Free Radical Polymerization**

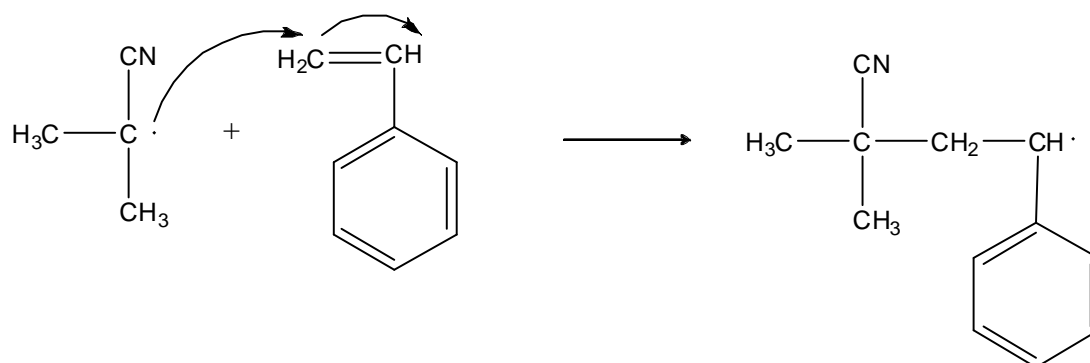
Free radical polymerization is an important technique due to its versatility with respect to reaction conditions and its compatibility with many monomers. However, there is little or no control over chain topology, tacticity or molar mass distribution. High-molecular-weight polymers are formed immediately since the production of a radical center adds many monomer units in a chain reaction and grow rapidly to a large size. As the polymerization proceeds, the monomer concentration decreases and the concentration of high-molecular weight polymers increase. In commercial application, the reaction is typically carried out to high or complete conversion. Therefore, polymerization processes often involve the addition of multiple charges of initiator and/or monomer during the course of reaction to minimize the molecular weight broadening due to high or complete conversion reaction.<sup>109</sup>

For the purpose of describing the reaction mechanism of free radical polymerization, the polymerization of styrene via this technique is outlined below. The polymerization consists of a sequence of three steps – initiation, propagation and termination. The first part of the initiation step is the homolytic dissociation of the AIBN initiator species, yielding a pair of 2-cyanopropyl radicals and nitrogen (Scheme 2.4). AIBN is a common free radical thermal initiator that is commonly used at 50-70°C.



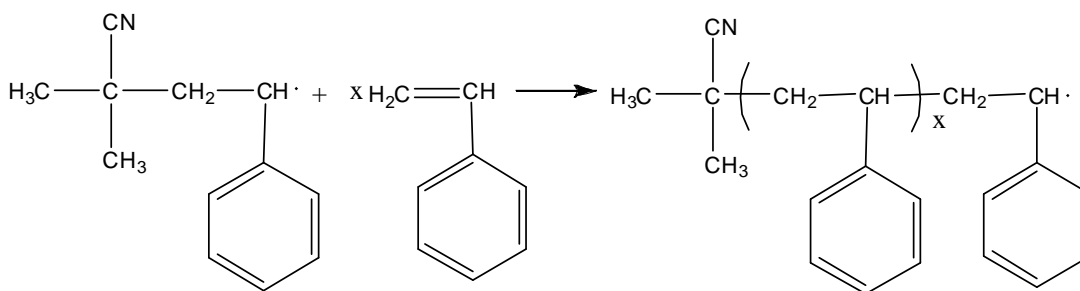
**Scheme 2.4.** Dissociation of AIBN

The second part of the initiation involves the initiation of a styrene monomer by the 2-cyanopropyl initiator radical to produce the chain initiating species, shown in Scheme 2.5. Once the radical initiator is produced, the polymer chain grows rapidly to high molar mass. Therefore, as the polymerization progresses, the molecular weight is relatively constant while the percent conversion increases.



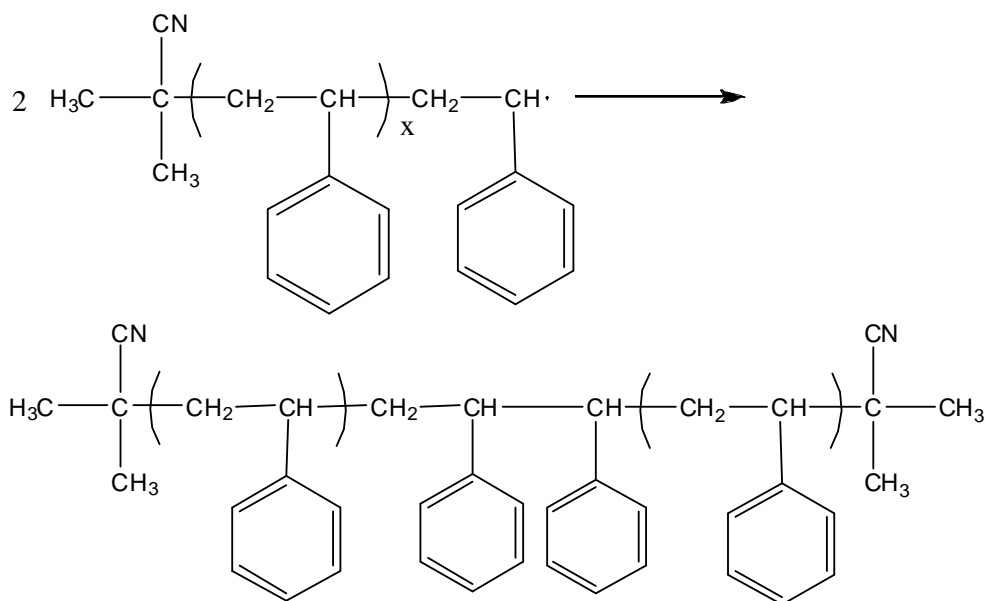
**Scheme 2.5.** Initiation of monomer by 2-cyanopropyl radical

In the propagation step, a chain initiating species adds itself to another monomer and this successive addition continues until termination occurs (Scheme 2.6).

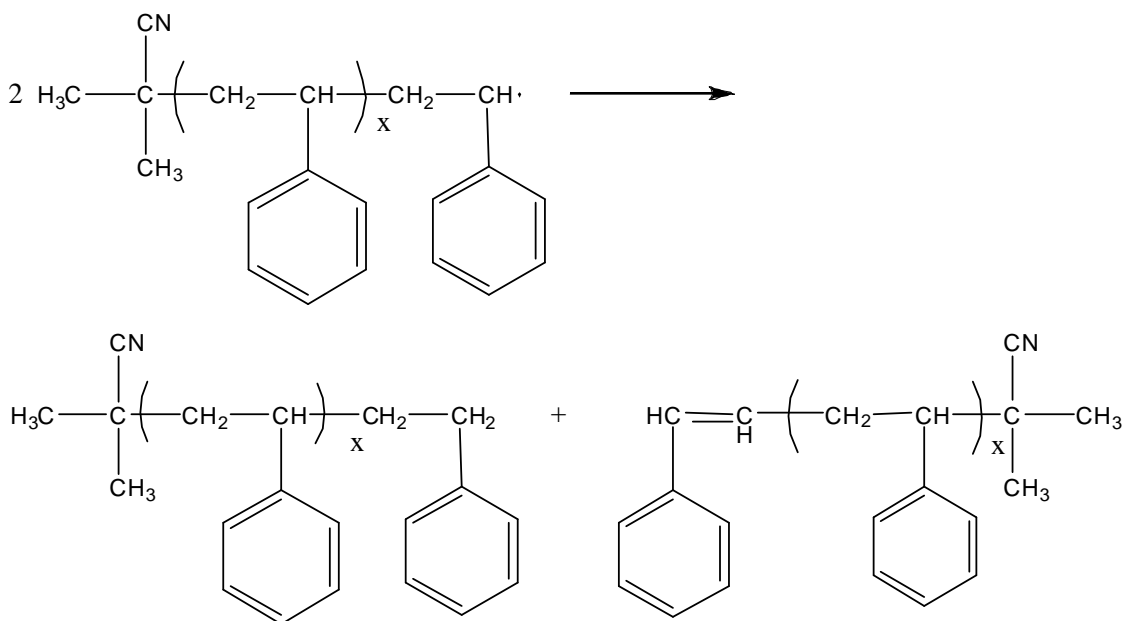


**Scheme 2.6.** Propagation step of polystyrene reaction

Termination occurs either by a more common coupling reaction (Scheme 2.7) or disproportionation (Scheme 2.8), in which a hydrogen radical that is  $\beta$  to one radical center is transferred to another radical center, resulting in the formation of one saturated and one unsaturated polymer molecule.



**Scheme 2.7.** Termination by coupling for polystyryl radical



**Scheme 2.8.** Termination by disproportionation of polystyryl radicals

### (I) Random Copolymer of Styrene and Cyanostyrene

Five copolymers of St and CNSt were synthesized by free radical polymerization.<sup>110,111</sup> In a typical polymerization procedure, St, CNSt (total monomer concentration: 4.5 M), DMA and AIBN initiator were introduced into a 100 ml 2-necked round-bottom flask equipped with a reflux condenser and a stir bar. This was subjected to three freeze-pump-thaw cycles and heated in an oil bath at 65 °C for 20 hours with continuous stirring and nitrogen flow. The resultant polymers were precipitated in a ten-fold excess of cold methanol and dried in the vacuum oven at 75 °C for 2 days. For simplicity, St-*ran*-CNSt with x mol% CNSt would be referred to as CNSt(x). The plot of cyanostyrene mole fraction in the random copolymer,  $F_{\text{CNSt}}$  as a function of cyanostyrene mole fraction in the comonomer feed,  $f_{\text{CNSt}}$  is shown in Figure 2.4. The experimental

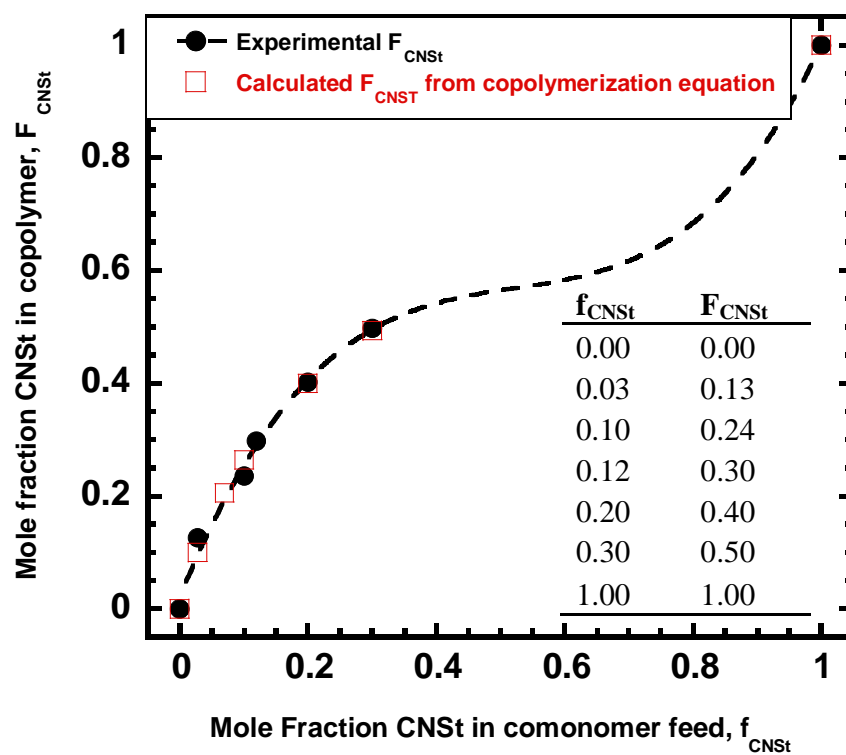


**Figure 2.4.** Mole fraction of CNSt in copolymer vs mole fraction of CNSt in comonomer feed



$F_{\text{CNSI}}$  was found to agree well the calculated  $F_{\text{CNSI}}$ , which was determined from copolymerization equation and reactivity ratios of  $r_{\text{CNSI}}=1.2$ ;  $r_{\text{SI}}=0.19$ .<sup>111</sup>

### C. Microwave Assisted Polymerization

The fundamentals of microwave radiation and literature survey of polymer synthesis can be found in the cited review articles.<sup>112-115</sup> In this section, a brief overview of the interaction of microwave radiation with chemical components and their benefits is discussed.

The utilization of microwave radiation as opposed to conventional heating in polymer chemistry is a rapidly growing field of research. Some of the advantages of microwave-assisted polymerizations are (I) non-contact heating (reduction of over heating of material surfaces), (II) penetrative radiation, enabling energy transfer directly to the reactive species, (III) material selective and (IV) rapid thermal and cooling effect, eliminating thermal degradation.<sup>116</sup> This technique has rendered itself attractive to chemists mainly due to a significant reduction of reaction time.

Microwave radiation, which is a form of electromagnetic energy, is composed of magnetic and electric fields. In chemical synthesis however, magnetic field interactions do not commonly occur. The electric field component causes molecular motion either by (I) dipole rotation, where polar molecules try to align themselves with the rapidly changing microwave electric field or (II) ionic conduction, where energy is transferred through free ions or ionic species in the heated substance. Since the reaction vessel wall is transparent to the microwave energy, dipolar or ionic chemical components experience instantaneous, homogenous and localized heating, resulting in the reduction of side

reactions. Thus, the choice of chemical constituents with high microwave energy absorbance level, i.e. high polarity or ionic conduction, is a crucial parameter before attempting a reaction. On the other hand, thermal heating is inefficient because transfer of energy is dependent upon the thermal conductivity of the bulk materials. The achievement of thermal equilibrium in this case is a very slow process, which can cause polymerization within the same vessel to start at different times, increasing the molecular weight distribution.

The field of microwave-assisted polymerizations is still in its infancy and rapid growth of investigations is expected. Nevertheless, the ability to perform uniform processing with commercial microwave reactors currently available has proven to be a potential benefit to neutron scatters that take advantage of the deuterium labeling, where polymers with similar characteristics (e.g. molecular weight and tacticity) but varying chemical isotopes are needed.

#### **(I) Free Radical Polymerization of Styrene-*ran*-cyanostyrene**

Random copolymers of styrene and cyanostyrene were polymerized by microwave assisted polymerization using a CEM MARS Microwave. A typical polymerization procedure is as follows: Styrene, cyanostyrene (total monomer concentration: 4.5 M), DMA and AIBN initiator were introduced into 100 ml CEM GreenChem glass vessel equipped with a stir bar. The vessel was then sealed tightly with a rubber stopper and the reaction mixture was subjected to three freeze-pump-thaw cycles through a needle injected into the rubber stopper. After removing the rubber stopper while in a glove box that is purged with nitrogen, the glass vessel was attached to the vessel holder that allows an airtight closure on the vessel. This reaction mixture was then

subjected to microwave radiation for 30 minutes at a temperature of 63°C and power of 300 Watts. The microwave reactor is equipped with built-in magnetic stirrers, fiber-optic temperature sensor and continuous feed-back control, which avoids thermal runaways. The resultant polymers were precipitated in an excess of cold methanol and dried in the vacuum oven.

## **(II) ATRP of St and MMA Random Copolymer**

Microwave-assisted polymerization was also used to synthesize random copolymers of styrene and methyl methacrylate of varying compositions. For a typical bulk polymerization, copper (I) chloride (0.253 g, 2.55 mmol) and 2,2'-bipyridine (1.20 g, 7.66 mmol) were introduced into a 100 ml CEM GreenChem glass vessel and the solids were stirred to achieve homogeneity. Then, styrene monomer (18.2 g, 0.175 mol), MMA monomer (17.5 g, 0.175 mol) and p-TsCl initiator (0.244 g, 1.27 mmol) were added. The vessel was then sealed tightly with a rubber stopper and the reaction mixture was subjected to three freeze-pump-thaw cycles through a needle injected into the rubber stopper. After removing the rubber stopper while in a glove box that is purged with nitrogen, the glass vessel was attached to the vessel holder that allows an airtight closure on the vessel. This reaction mixture was then subjected to microwave radiation for 45 minutes at a temperature of 95 °C and power of 600 Watts (5 reaction vessels). The molar ratios of [p-TsCl]: [CuCl]: [2,2'-bipyridine] were 1:2:6. The microwave reactor (CEM MARS Microwave) is equipped with built-in magnetic stirrers, fiber-optic temperature sensor and continuous feed-back control, which eliminates thermal runaways. The resultant polymers were precipitated in an excess of cold methanol and dried in the

vacuum oven. The plot of mole fraction of the MMA in copolymer,  $F_{\text{MMA}}$  as a function of mole fraction of MMA in the comonomer feed,  $f_{\text{MMA}}$  is shown in Figure 2.5.

## 2.4 Polymer Characterization

### A. $^1\text{H}$ NMR

#### (I) Random Copolymer of MMA and DMAEMA

The incorporation of monomers and copolymer composition for MMA-*ran*-DMAEMA copolymers were determined by  $^1\text{H}$  NMR Spectroscopy (Varian 300 MHz). Sample concentrations were 7 mg/ml in deuterated chloroform and the chemical shift scale was referenced to the tetramethylsilane peak at 0 ppm. The composition in MMA-*ran*-DMAEMA copolymers were calculated by integrating the three methoxy protons of the MMA units ( $\delta=3.6$  ppm) and the aliphatic protons of the six dimethylamino protons of DMAEMA units ( $\delta=2.3$  ppm). A typical  $^1\text{H}$  NMR spectrum of MMA-*ran*-DMAEMA is depicted in Figure 2.6. More specifically, the area per proton of the methoxy group corresponding to MMA is given by:

$$A_{\text{methoxy}} = \frac{\text{Area peak } a(1.18)}{3 \text{ protons}} = 0.39$$

The normalized area per proton of the DMAEMA units is determined as:

$$A_{\text{DMAEMA}} = \frac{\text{Area peak } d(1.00)}{6 \text{ protons}} = 0.17$$

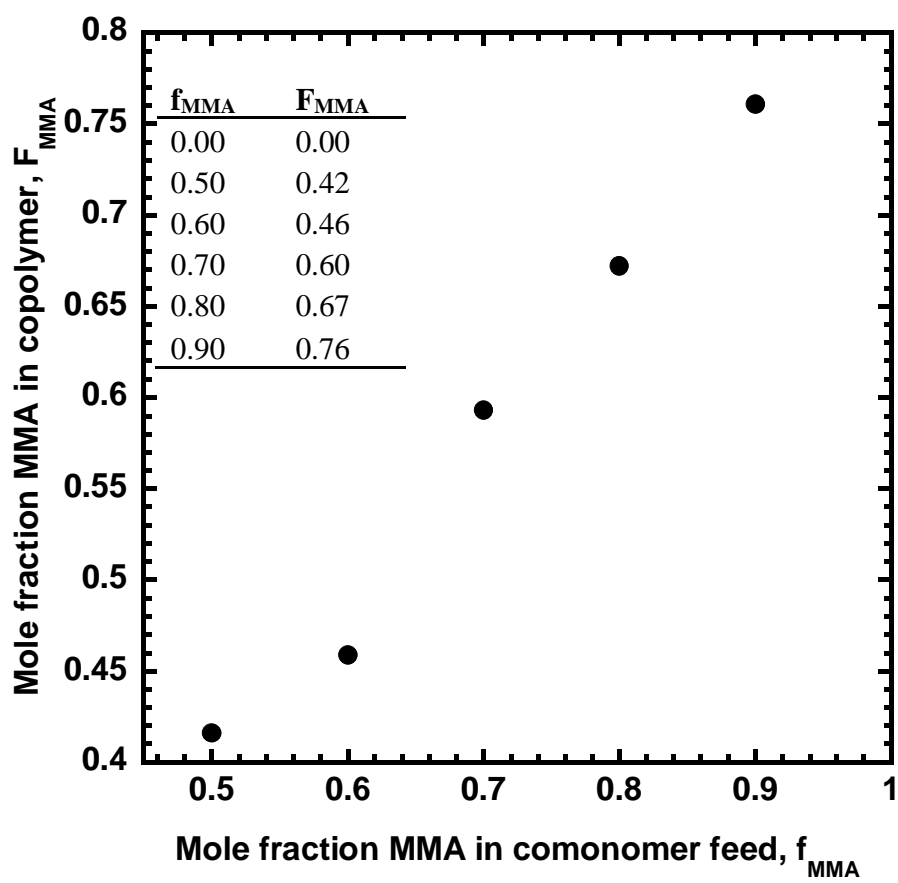


**Figure 2.5.** Mole fraction of MMA in copolymer as a function of MMA mole fraction in the comonomer feed

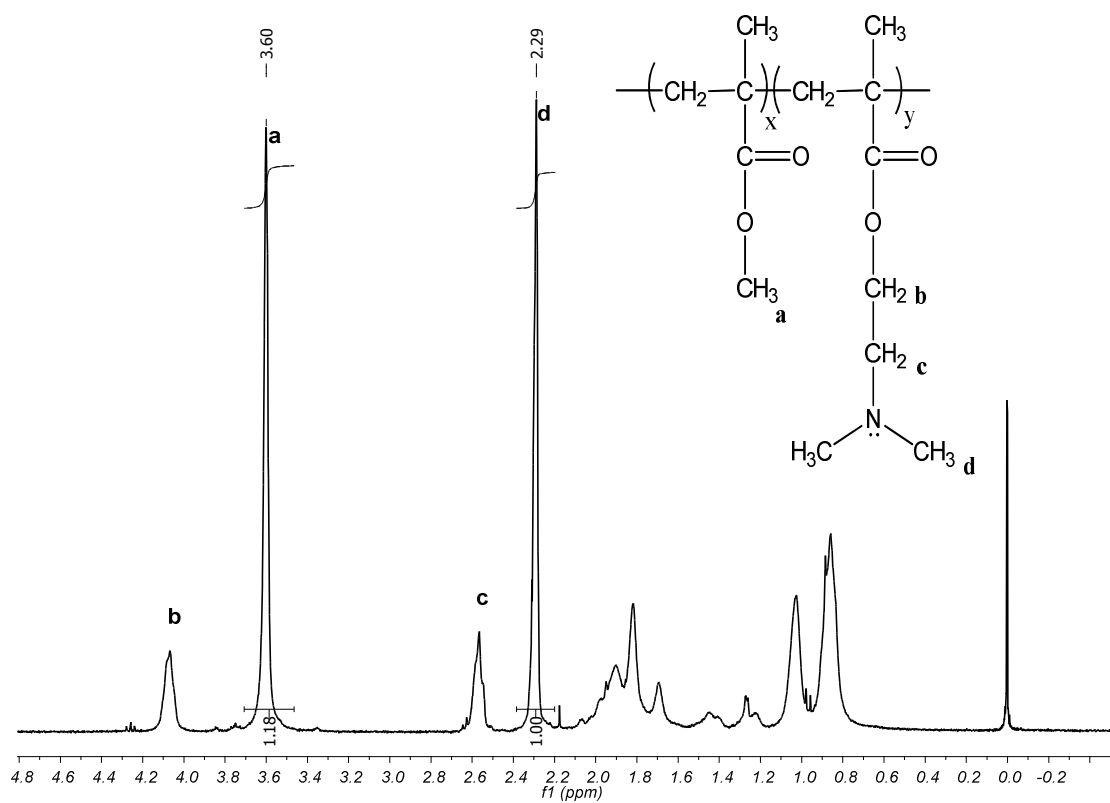


**Figure 2.6.** Typical  $^1\text{H}$  NMR spectra of MMA-ran-DMAEMA

Therefore, the mole percentage of DMAEMA monomer units in the random copolymer is calculated as:

$$\text{mol\% DMAEMA} = \frac{A_{\text{DMAEMA}}(0.17)}{A_{\text{methoxy}} + A_{\text{DMAEMA}}(0.17 + 0.39)} \times 100\% = 30.36\%$$

## (II) Polyacrylonitrile (PAN)

Structures of synthesized PAN were verified by  $^1\text{H}$  NMR Spectroscopy (Varian 300 MHz). Sample concentrations were 7 mg/ml in deuterated dimethyl sulfoxide ( $d_6$ -DMSO) and the chemical shift scale was referenced to the tetramethylsilane (TMS) peak at 0 ppm. The yellow, orange or brown coloration that was observed in some of the synthesized polyacrylonitrile could either be induced by exposure to heat during synthesis or drying or it may be a result of polymerization in a high dielectric constant solvent, in this instance, DMF.<sup>117</sup> Figure 2.7 illustrates a  $^1\text{H}$  NMR spectrum of a colored (i.e. orange) PAN. Peaks at 2.1 ppm and 3.2 ppm correspond to  $\beta$ -methylene and  $\alpha$ -methine protons respectively. The extra peak at 2.7 ppm in colored PAN, but absent in commercial free radical synthesized PAN (Figure 2.8) might be attributed to  $\text{H}^{\text{a'}}$  and  $\text{H}^{\text{b'}}$  in branched and/or cyclized structures (Scheme 2.9) that are proposed by Verneker et al.<sup>117</sup>

The methine protons (marked b') on both the branched and cyclized structure are more shielded and move upfield while the methylene (marked a') move downfield due to deshielding therefore giving rise to a single peak at 2.7 ppm. If this hypothesis is valid, the amount of intracyclization or branching that contributes to the coloration of the polyacrylonitrile is only 0.68 mol% as determined from the integration of the methylene

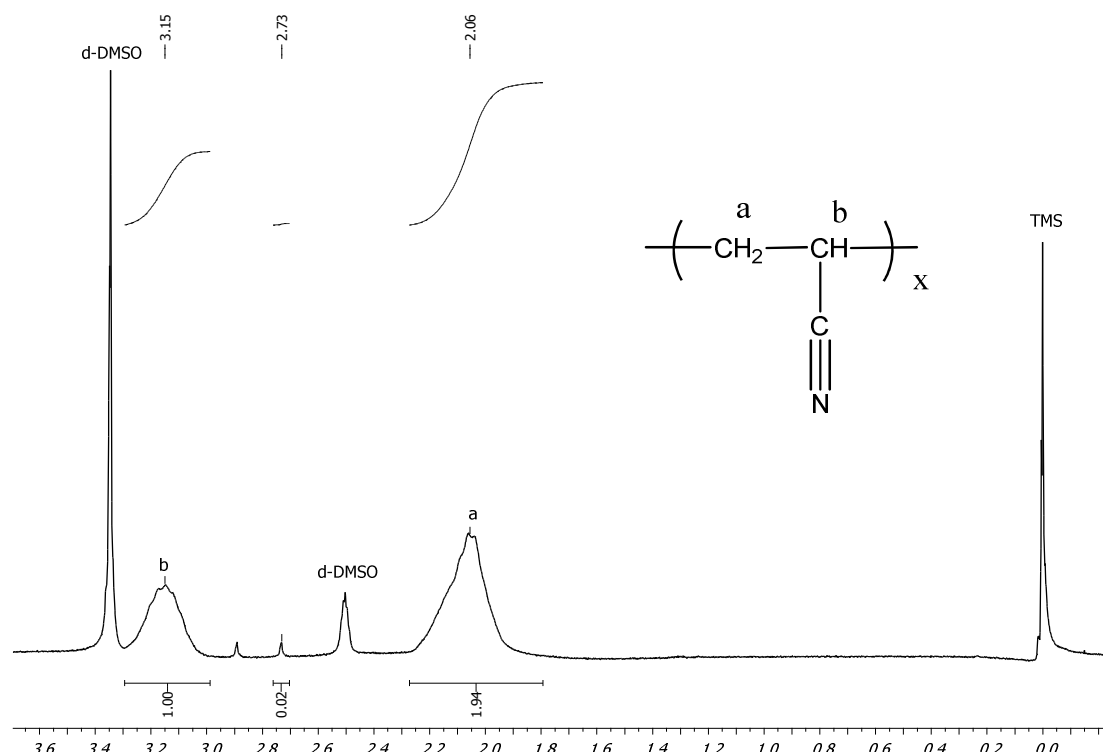


**Figure 2.7.**  $^1\text{H}$  NMR spectra of colored polyacrylonitrile



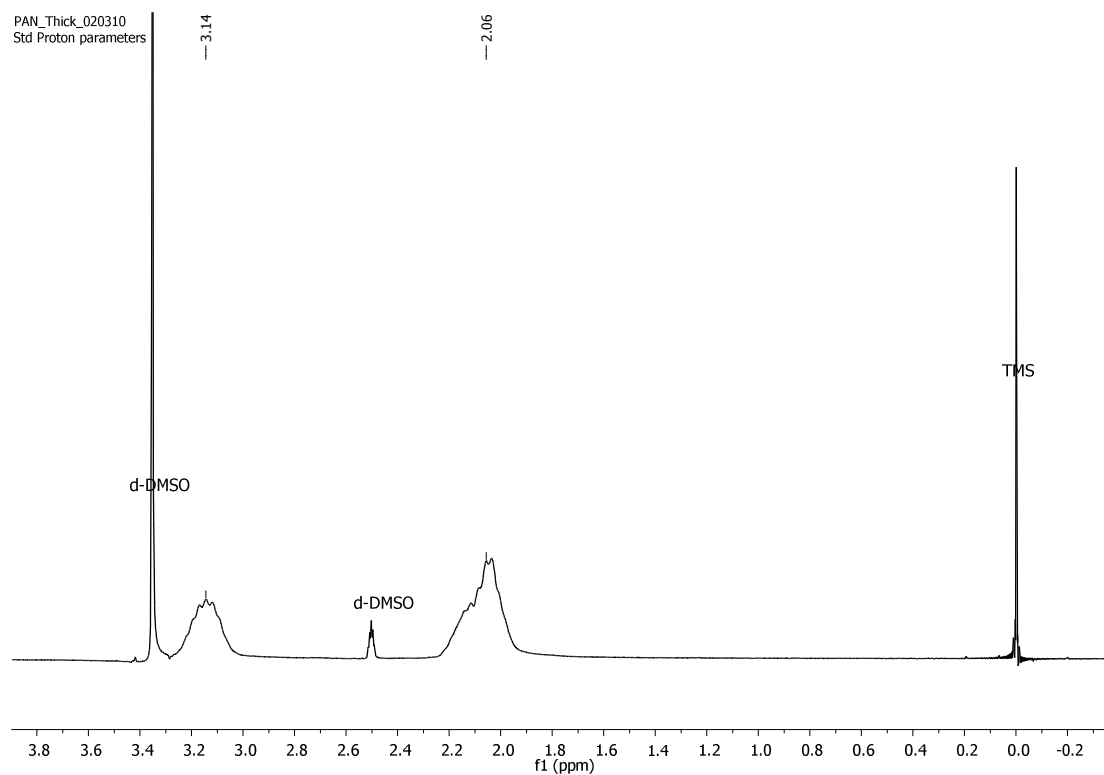
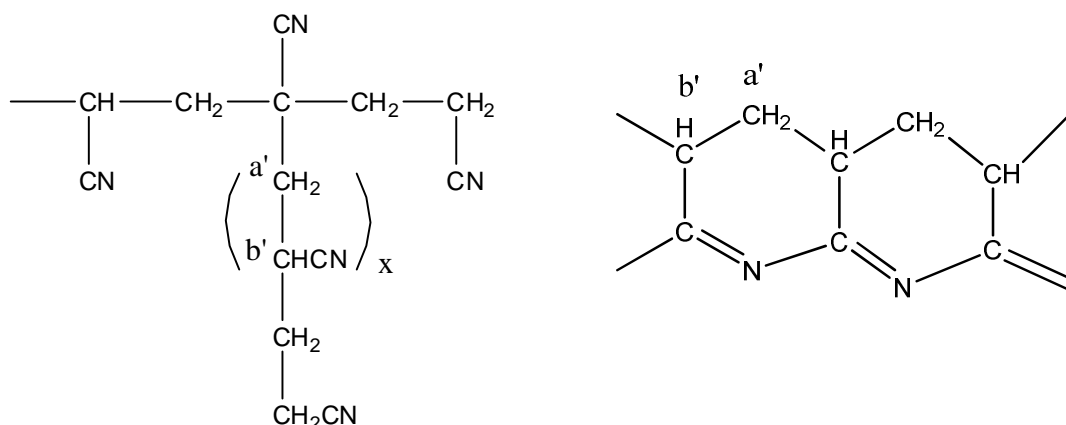


**Figure 2.8.**  $^1\text{H}$  NMR spectra of commercial PAN synthesized by free radical technique



**Scheme 2.9.** Branched or cyclized structures of PAN

protons (peak a) of linear PAN and protons in the cyclized/branched structure ( $\delta=2.7$  ppm).

### (III) Random Copolymer of Styrene and MMA

The copolymer composition for styrene-*ran*-MMA copolymers were determined by  $^1\text{H}$  NMR Spectroscopy (Varian 300 MHz). Sample concentrations were 7 mg/ml in deuterated chloroform and the chemical shift scale was referenced to the tetramethylsilane (TMS) peak at 0 ppm. The average mole fraction of styrene ( $F_{\text{St}}$ ) and molar ratio of styrene to MMA ( $F$ ) incorporated into the random copolymer can be calculated by the following equations, where  $A_{\text{St}(1\text{H})}$  represents the area per proton of styrene monomer and  $A_{\text{MMA}(1\text{H})}$  represents the area per proton corresponding to MMA unit.

$$F_{\text{St}} = \frac{A_{\text{St}(1\text{H})}}{A_{\text{St}(1\text{H})} + A_{\text{MMA}(1\text{H})}} \quad (\text{Equation 2.1})$$

$$F = \frac{F_{St(1H)}}{F_{MMA(1H)}} = \frac{A_{St(1H)}}{A_{MMA(1H)}} \quad (\text{Equation 2.2})$$

where:

$$A_{MMA(1H)} = \frac{\left[ A_{0.4-3.7} - \left( \frac{3}{5} \right) \times A_{6.5-7.0} \right]}{8} \quad (\text{Equation 2.3})$$

$$A_{St(1H)} = \frac{(A_{6.5-7.0})}{5} \quad (\text{Equation 2.4})$$

The peaks between  $\delta=0.4$  and 3.7 ppm corresponds to the protons in the MMA unit (protons d-f depicted in Figure 2.9) and the methylene and methyne groups on the styrene monomer (protons b and c). Therefore, the 3/5 term in Equation 2.3 denotes the relative number of styrene protons that appear in the 0.4 to 3.7 ppm region to those appearing at the chemical shift range other than 0.4–3.4 ppm. The number 5 in Equation 2.4 indicates the number of aromatic protons that appear in the chemical shift between 6.5-7.0 ppm.

## B. $^{13}\text{C}$ NMR

### (I) Random Copolymer of Styrene and Cyanostyrene

$^{13}\text{C}$  NMR spectroscopy was performed on St-*ran*-CNSt samples to confirm the incorporation of the nitrile group ( $\delta=119.1$  ppm, Figure 2.10) into the copolymer. Sample concentrations were 7 mg/ml in deuterated chloroform and the chemical shift scale was referenced to the tetramethylsilane peak at 0 ppm.

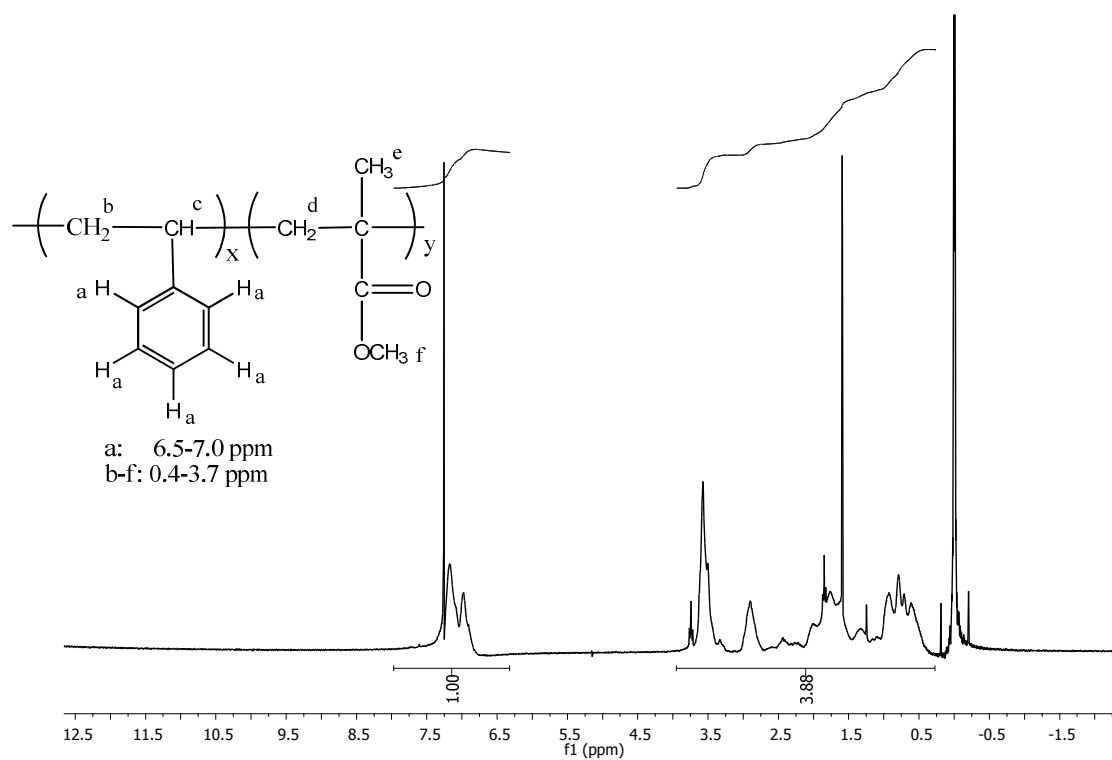


**Figure 2.9.** <sup>1</sup>H NMR spectra of St-ran-MMA

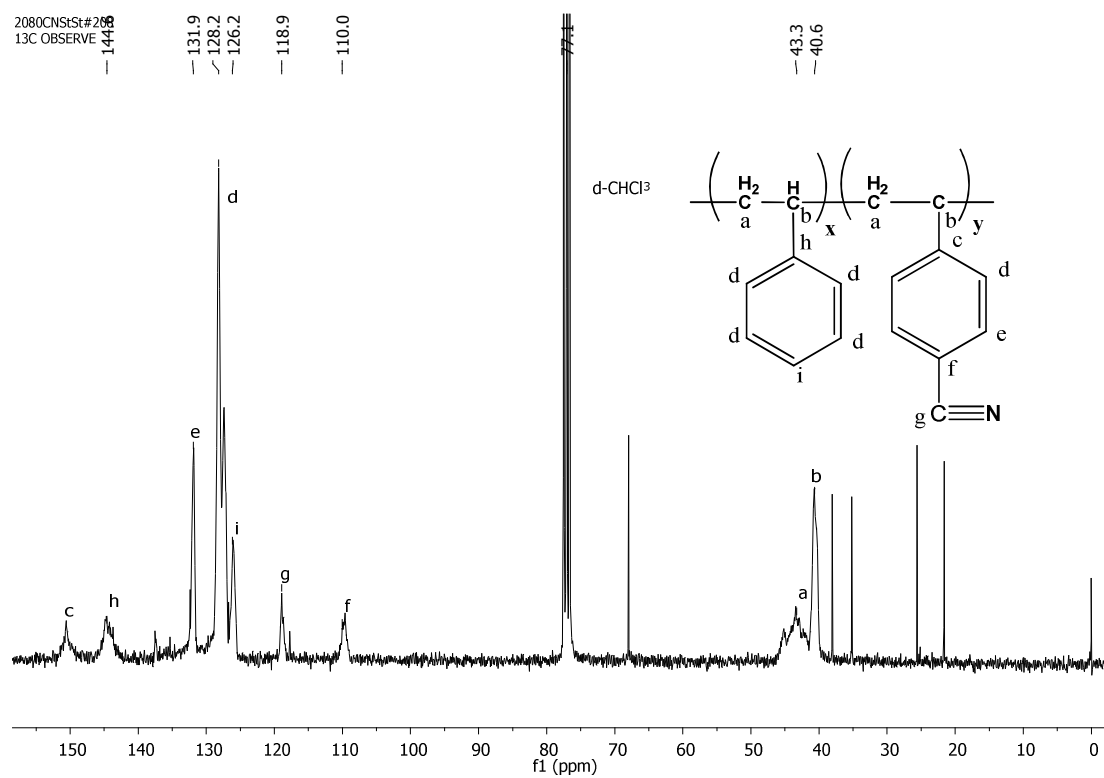


**Figure 2.10.** <sup>13</sup>C NMR spectra of styrene-*ran*-cyanostyrene with 24 mol% cyanostyrene

### C. Elemental Analysis

The composition of St-*ran*-CNSt and St-*ran*-AN copolymers were determined by elemental analysis, completed by Atlantic Microlab Incorporated, Norcross GA. The C, H, N analyses were performed by combustion using automatic analyzers and the values obtained are percent by weight determinations with an error limit of  $\pm 0.3\%$  for both accuracy and precision. A sample calculation of mol % nitrile in St-*ran*-CNSt is determined as follows:

If,  $a$ : % nitrile/cyanostyrene in copolymer

$b$ : % nitrogen in copolymer (determined from elemental analysis)

Average molecular weight monomer in copolymer,  $MW_{ave} = a \times MW_{CNSt} + (1 - a) MW_{St}$

$$b = \frac{\text{Atomic mass nitrogen} \times a}{MW_{ave}}$$

Therefore, mol % cyanostyrene in the random copolymer,  $a$ , is determined as:

$$\frac{b \times MW_{ave}}{\text{atomic mass nitrogen}}$$

From error analysis, an error limit of  $\pm 0.3$  mass% of nitrogen can translate up to an error of  $\pm 3.5$  mol% of nitrile.

#### **D. Differential Scanning Calorimetry**

DSC (Mettler Toledo DSC 821<sup>°</sup>) measurements were carried out to determine the thermal properties of the polymers and were run at a rate of 10 °C/min and nitrogen flow rate of 200 ml/min. In order to ensure complete removal of the samples' thermal history, the midpoint of the heat capacity change of the second consecutively identical measurement was recorded as the glass transition temperature.

#### **E. Gel Permeation Chromatography**

GPC analyses for MMA-*ran*-DMAEMA, commercially purchased St-*ran*-AN and St-*ran*-CNSt were performed at room temperature (20 °C) with a flow rate of 1 ml/min to determine the molecular weights and molecular weight distributions of polymer samples with respect to polystyrene standards. Measurements were carried out on a Polymer Labs GPC-20 instrument equipped with two 300 mm x 7.5 mm Polymer Labs 5 µm Mixed C columns and a 50 mm x 7.5 mm Polymer Labs 5 µm guard column and a Knauer K-2301 differential refractometer as a detector. Samples (filtered through a 0.45 µm syringe filter prior to injection) were at 1 mg/ml concentration and HPLC grade THF (100 ppm BHT stabilized) was used as the mobile phase.

GPC analysis for PCNSt, synthesized by our collaborator, was carried out at ambient temperature using a PL-GPC 50 Plus (Polymer Laboratories, Inc) with a differential refractive index detector, one PSS GRAL guard column (50 x 8 mm, 10 µm particles, Polymer Standards Service-USA, Inc.), and two PSS GRAL linear columns (each 300 x 8 mm, 10 µm, molecular weight range from 500 to 1,000,000 according to

Polymer Standards Service-USA, Inc.). DMF was used as the carrier solvent at a flow rate of 1.0 mL/min.

GPC analyses for the synthesized SAN and PAN polymers were carried out on a Waters GPC system consisting of a Waters model 510 pump, a Rheodyne model 7725 (i) manual injector with a 200  $\mu$ l loop, and a Knauer Smartline model 2300 differential refractive index detector. Measurements were performed at room temperature (20°C) with DMF+0.1 M LiBr as the mobile phase, toluene as a flow rate marker and flow rate of 1 ml/min. The columns, four PSS (Polymer Standards Service) GRAM; 8x300 mm; 10  $\mu$ m, 100, 1000, and 3000 Å along with an 8x50, 10  $\mu$ m guard, were calibrated with a set of polystyrene standards in the molecular weight range of 600 to 7,500,000 Daltons prior to use.

#### **F. Intrinsic Viscometry**

The molecular weight of SAN and PAN polymers obtained from GPC measurement gave an abnormally high molecular weight due to dipole-dipole interaction between nitrile groups along the polymer chains. Therefore, to further clarify their molecular weight, intrinsic viscometry measurements were performed on a Schott Instruments ViscoSystems AVS 370 dilute solution viscometer. The initial concentrated polymer solution (10 mg/ml) in DMF was placed in the viscometer and series dilutions were completed automatically utilizing the Dilut 4.0 software. The capillary of type 531-10 (overall length: 290 m, 0.64 mm capillary) was used. The viscometer is equipped with optical sensors for starting and stopping the timer, a heater/cooling bath for temperature regulation, a built-in magnetic stirrer to assure homogeneity of the solution and an



automatic burette for solvent dispensing accuracy. Measurements were carried out at 30 °C ( $t_0$  DMF: 84.77 seconds) and 25 °C ( $t_0$  DMF: 89.3 seconds) for SAN and PAN polymers respectively. The viscosity average molecular weights,  $M_v$  of the polymers were calculated using the following equation:

$$\log [\eta] = a \log M_v + \log K$$

$[\eta]$ : intrinsic viscosity in dl/g

To obtain viscosity average molecular weight,  $M_v$ , polydispersity index (PDI) information obtained from GPC measurement was utilized ( $PDI = M_w/M_n$ ).  $K$  and  $a$  values for SAN and PAN were as follows:<sup>118</sup>

$$K_{SAN}: 17.2 \times 10^{-5} \text{ dl/g} \quad a_{SAN}: 0.73$$

$$K_{PAN}: 39.2 \times 10^{-5} \text{ dl/g} \quad a_{PAN}: 0.75$$

## **2.5 Preparation of Polymer Nanocomposite**

### **A. Raman Spectroscopy and Optical microscopy**

SWNT (2.5 mg, 1 wt %) in DMF was sonicated for 1 hour in a sonicator bath (Branson 3510, 40 kHz). Appropriate amount of polymer was added to the DMF/SWNT suspension and stirred above  $T_g$  until the solution was reduced in volume, and was sonicated again for 15 minutes before spin-coating the polymer/SWNT/DMF dispersion on a glass substrate (10 sec at 300 rpm and 90 sec at 500 rpm). For CNSt samples, the glass substrate was coated with a primer before spin coating the polymer/SWNT/DMF

suspension to limit dewetting. The samples were kept above  $T_g$  under vacuum for 15 hours to remove traces of solvent and to thermally anneal the sample.

#### **B. Small Angle Neutron/X-ray Scattering/X-ray Diffraction**

In a typical preparation procedure, SWNT (0.625 mg, 0.1 wt%) was sonicated in 5 ml DMF for 1 hour in a Cole Parmer 8891 sonicator (47 kHz). Homopolymer/copolymer (0.624 g) was added to the SWNT/DMF suspension and concentrated down to 2.5 ml at a temperature above the polymer's  $T_g$ . The solution was stirred and a steady flow of air is blown at the rims of the vials to aid in concentrating the solution. Thereafter, this thick suspension is solution cast into a Teflon mold (1cm x 3cm x 1cm) and put in the vacuum oven for 3-5 days, slowly ramping it up to above the  $T_g$  of the polymer in a period of a couple of hours. The dry film is removed from the Teflon mold and compression molded on an aluminum mold (1 cm x 3cm x 0.1 cm) with Kapton sheets sandwiching the plate. These samples are compression molded above the  $T_g$  of the polymer at a pressure of ~10,000 lbs for a duration of about 5 minutes.

#### **C. UV-Vis Spectroscopy**

SWNT (6.8 mg, 1.0 wt%) was sonicated in 5.0 ml DMF for one hour. Appropriate amounts of polymer (i.e. SAN of varying nitrile content, PS and PAN) was added and further sonicated for two additional hours. The suspensions were then stirred with heat (100 °C) for one hour and transferred to 50 ml- centrifuge tubes (Thermo Scientific\* Nalgene\* Oak Ridge High-Speed FEP) that contain 25 ml DMF. The empty vial containing the suspension was rinsed with 5 ml DMF and the contents were transferred to the 50 ml centrifuge tubes. The final suspensions were shaken continuously for ~10

minutes to ensure homogeneity and allow the formation of charge transfer complex. This is centrifuged for 30 minutes at 6000 rpm. The supernatant was poured off carefully to avoid disturbing the excess free SWNTs at the bottom of the centrifuge. UV-Visible spectroscopic measurement of the supernatant was then performed.

#### **D. Wide Angle Neutron Diffraction Samples**

Appropriate amount of Buckminster fullerene,  $C_{60}$  (41.6 mg, 4.0 wt%) was sonicated in anisole (concentration: 5.6 mg/ml) for two hours. In a separate vial, appropriate amount of polymer (1.0 grams) was dissolved in NMP. The concentration of polystyrene, SAN20 and SAN45 in NMP was 0.15 g/ml while polyacrylonitrile has a concentration of 0.1 g/ml (Note: PAN was dissolved with the aid of heat). While under sonication, the fullerene-anisole solution was then added dropwise to polymer-NMP suspension followed by sonication for another hour. This is followed by precipitation of the solution in 250 ml cold diethyl ether for PAN and SAN45, and 250 ml cold methanol for PS and SAN20 with consistent stirring. After residing in the freezer overnight (~12 hours), the solution is filtered using a Millipore FHL type 0.45  $\mu$ m filter membrane. The brown powdered composites were then dried under vacuum at room temperature for 12 hours.

### **2.6 Polymer Nanocomposite Characterization and Analysis**

#### **A. Optical Microscopy and Image Analysis**

Optical microscopy (Nikon Microphot-FXA Microscope) was performed using 10x objectives to visualize the microscopic features of the composite films. Each image

has a domain size of 750  $\mu\text{m}$  x 1000  $\mu\text{m}$ . SIMAGIS Research 3.0, an image analysis program was utilized to quantify the average area and diameter of the aggregates. All visible aggregated regions on the nanocomposite film are included in the calculation of the average area of aggregates and the maximum distance within each aggregate is used as the diameter of aggregates. The results presented in this study are averaged over five optical micrographs.

## **B. Raman Spectroscopy**

To monitor the extent of polymer interaction between carbon nanotube and polymer matrix, Raman spectroscopy was performed using a JY-Horiba T64000 spectrometer with 514.5 nm edge filter, 600 gr/mm grating, 514.5 nm laser excitation and CCD detector. Laser output power is kept low ( $\sim 1$  mW, measured at the sample position) and constant to avoid sample degradation and peak frequency downshift due to increasing laser power.<sup>119,120</sup> The incident laser beam was focused onto the specimen surface through an 80x long working distance objective forming a laser spot size of  $\sim 1.0$   $\mu\text{m}$ . For each sample, ten spectra with 20 seconds acquisition and 10 accumulations were collected and the D\* band shift presented in Chapter 3 are averaged over 10 spectra. The resolution of the spectrometer is  $\sim 2$   $\text{cm}^{-1}$ .

Raman mapping was performed on a Renishaw 1000 spectrometer with 632.8 nm excitation wavelength, 50x long objective for composite visualization and a laser spot size of 2.0  $\mu\text{m}$ . About 100 spectral acquisitions are acquired for each nanocomposite sample in the Raman mapping analysis and intensities of the G band are averaged. The

Raman peak values stated throughout this dissertation were derived by fitting the raw data obtained from the spectrometer to a Lorentzian.

### **C. Small Angle X-ray Scattering**

The SAXS patterns for the thick film composites were recorded on a Molecular Metrology small angle x-ray machine using Cu K $\alpha$  radiation ( $\lambda=1.5418$  Å) equipped with a two-dimensional position sensitive proportional detector of circular shape (radius = 2.5 cm). A monochromatic x-ray source from the x-ray sealed tube is focused by a pair of Kirkpatrick-Baez microfocusing mirrors. The sample to detector distance was 1.5 m with the q range 0.01 Å<sup>-1</sup> to 0.15 Å<sup>-1</sup>. The x-ray operating voltage was 45 kV with a current of 0.66 mA. The exposure time for measuring each sample was 1 hour.

### **D. Small Angle Neutron Scattering**

Small angle neutron scattering experiments were also performed on the thick film composites to determine their structure and attempt to study the bound-layer conformation of the polymer surrounding the SWNT. Experiments were conducted using the General-Purpose SANS Diffractometer (CG-2) at the High Flux Isotope Reactor (HFIR) in Oak Ridge National Laboratory (ORNL). For the SANS measurements, a cold neutron wavelength of  $\lambda= 6$  Å and sample to detector positions of 0.3 m and 6 m were used ( $0.01 \text{ Å}^{-1} < q < 0.3 \text{ Å}^{-1}$ ). Scattered intensities were reduced and corrected for transmission, background and detector efficiency and converted to an absolute scale by calibration with a known standard using Igor Pro 5.0 (Wavemetrics, Inc.).

### **E. UV-Vis Spectroscopy**

UV-Vis absorption spectroscopy (Evolution 600 Thermo Scientific) was utilized to determine the concentration of SWNT in solution, recovered using the method stated in Section 2.5C. The absorption spectra were subtracted from absorbance of the solvent. From Beer's Law, the absorbance of the suspension can be written as:

$$A = \epsilon l c$$

where  $\epsilon$  is the molar absorptivity,  $l$  is the cell path length and  $c$  the SWNT concentration. From a previously determined value,  $\epsilon$  at 500 nm is  $0.0286 \text{ L}\cdot\text{cm}^{-1}\text{mg}^{-1}$ <sup>121</sup> allowing the determination of SWNT concentration in the SWNT-polymer complex.

### **F. X-ray Diffraction (XRD)**

Diffacted X-rays from the polymers and composites were collected using an XRD Instrument (Rigaku Inc.) to evaluate the solubility limit of  $\text{C}_{60}$  in the polymer. The x-ray source is a Bede Scientific Instruments Limited Microsource X-ray Generator, operated at 45kV and 0.66 mA. From Figure 2.11, The XRD pattern from the pure  $\text{C}_{60}$  clearly shows peaks at  $2\theta = 11.0, 17.9, 21.1, 21.9, 27.5, 28.3, 31.1, 33.1^\circ$  and the pure PAN polymer shows peaks at  $16.9, 17.6, 23.9, 26.7, 29.6^\circ$ . PAN composite with  $\geq 5 \text{ wt}\%$   $\text{C}_{60}$  show distinct diffraction peak at  $11.0^\circ$ , consistent with peaks for pure  $\text{C}_{60}$ . We therefore estimate the solubility limit of  $\text{C}_{60}$  in PAN polymer to be  $\sim 4 \text{ wt}\%$ .

### **G. Wide Angle Neutron Diffraction**

Diffraction data of the fullerene-polymer composites were collected on the small angle neutron diffractometer for liquids and amorphous samples (SANDALS) instrument

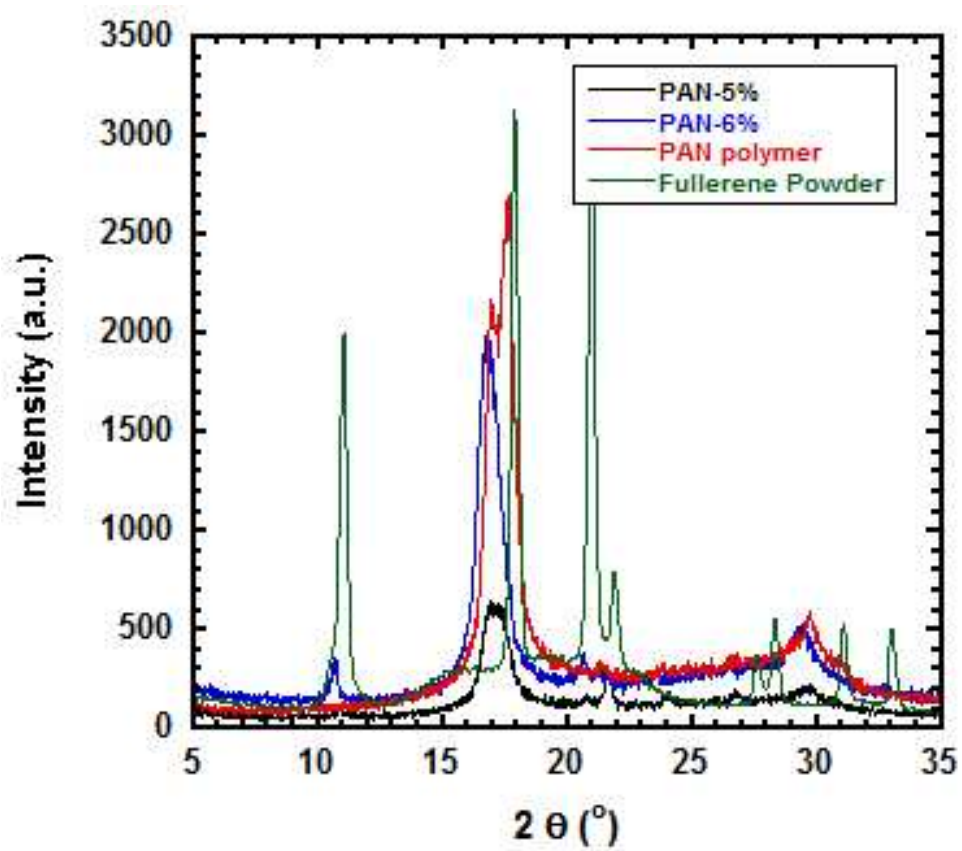


**Figure 2.11.** X-ray diffraction pattern from C<sub>60</sub>, PAN polymer and PAN composites containing 5 wt% and 6 wt% C<sub>60</sub>

at the ISIS spallation neutron source, Rutherford Appleton Laboratory, U.K. The composites were loaded into a flat plate titanium/zirconium null scatterer cell that has an internal sample thickness of 2 mm and wall thickness of 1 mm. Scattering data was also obtained for an incoherent scatterer vanadium slab (5.0 cm x 5.0 cm) of thickness 3.48 mm for data normalization. Data reduction and correction for background, multiple scattering, absorption and normalization was performed using GudrunGUI program (Release date: 20 Oct 2009) to give total static structure factors,  $S(Q)$ . Fourier Transformation of  $S(Q)$  generate pair distribution functions,  $g(r)$  that provide an insight into the intra- and inter-molecular relative density distributions of the system.



## CHAPTER 3: EVIDENCE OF CHARGE TRANSFER INTERACTION IN POLYMER NANOCOMPOSITES

### 3.1 Introduction

The work presented in this chapter seeks to understand and obtain a measure of the level of charge transfer between the copolymers and SWNTs utilizing Raman spectroscopy, discussed in Section 3.3.A. Density functional theory (DFT) calculations, described in Section 3.3.B, also provides additional insight into the extent of molecular interaction between an interacting monomeric or oligomeric unit and SWNTs as well as the optimized geometries for the formation of the underlying interactions. In addition, the chi ( $\chi$ ) interaction parameter between the polymer matrix and SWNT was calculated from Flory-Huggins theory (Section 3.3.C) to verify that the polymer chain connectivity plays a very fundamental role in controlling the extent of intermolecular charge transfer interaction.

### 3.2 Materials

Tables 3.1, 3.2 and 3.3 list all the polymers used in this study along with pertinent functional group composition (i.e. DMAEMA, acrylonitrile and cyanostyrene) and molecular weight characteristics. The MMA-*ran*-DMAEMA and styrene-*ran*-cyanostyrene copolymers were synthesized as outlined in Section 2.3.A.I and Section 2.3.B.I respectively. All the nanocomposite samples for Raman spectroscopy were prepared according to the procedure described in Section 2.5A.

**Table 3.1.** Characteristics of PMMA, PDMAEMA and MMA-*ran*-DMAEMA polymers used in this study

Polymer	mol% DMAEMA <sup>a</sup>	M <sub>n</sub> (g/mol)	PDI
PMMA	0	61,000	1.27
DMA10	12.2	44,000	1.52
DMA20	26.3	54,000	1.15
DMA30	30.4	46,000	1.08
DMA50	49.2	49,000	1.12
PDMAEMA	100	39,000	1.35

a: determined from <sup>1</sup>H NMR

**Table 3.2.** Characteristics of PS, PAN and styrene-*ran*-acrylonitrile polymers used in this study

Polymer	mol% acrylonitrile <sup>a</sup>	M <sub>n</sub> (g/mol)	PDI
PS	0.0	43,000	1.04
SAN30	29.5	83,000	2.28
SAN37	36.8	79,000	2.35
SAN45	45.0	55,000	2.04
SAN49	48.8	67,000	2.12
SAN56	56.2	55,000	2.37
PAN	100.0	39,000	1.35

a: determined by elemental analysis

**Table 3.3.** Characteristics of PS, PCNSt and styrene-*ran*-cyanostyrene polymers used in this study

Polymer	mol% cyanostyrene <sup>a</sup>	M <sub>n</sub> (g/mol)	PDI
PS	0.0	41,000	1.07
CNSt13	12.6	46,000	1.70
CNSt24	23.6	58,000	1.62
CNSt30	29.8	55,000	1.73
CNSt40	40.2	72,000	2.15
CNSt50	49.8	60,000	2.00
PCNSt	100.0 <sup>b</sup>	59,000	1.05

a: determined by elemental analysis

b: synthesized by our collaborator, Paraskevi Driva<sup>122</sup>

### **3.3 Results and Discussion**

#### **A. Raman Spectroscopy**

##### **(I) Origin of Raman Scattering and its Application to SWNT**

Since the discovery of the Raman effect by Sir C.V. Raman in 1928,<sup>123,124</sup> Raman spectroscopy has become a powerful tool for molecular structure determination. In these studies, it was demonstrated that when light is scattered by molecules in dust-free liquids or gases, a diffuse radiation that is the same wavelength as the incident beam is accompanied by a modified scattered radiation of degraded frequency, called the Raman scattering. In Raman spectroscopy technique, a sample is irradiated with a powerful laser source of visible or near-infrared monochromatic radiation and the scattered light is typically observed perpendicular to the incident beam. The scattered light results from elastic Rayleigh scattering, characteristic of scattering from particles much smaller than the incident beam wavelength, and inelastic Raman scattering, which is very weak ( $10^{-5}$  of the incident beam).<sup>125</sup>

The origin of Rayleigh and Raman scattering is illustrated in Figure 3.1.<sup>126</sup> When a molecule interacts with a photon from a laser source, the increase in its energy is equal to the energy of the photon  $h\nu$ , represented by Figure 3.1 (a), where  $h$  is Planck's constant and  $\nu$  is the frequency of the electromagnetic radiation. Since this process is not quantized, the energy of the molecule can fall in any of the virtual states, between the ground state and the first electronic excited state shown in the upper part of Figure 3.1.

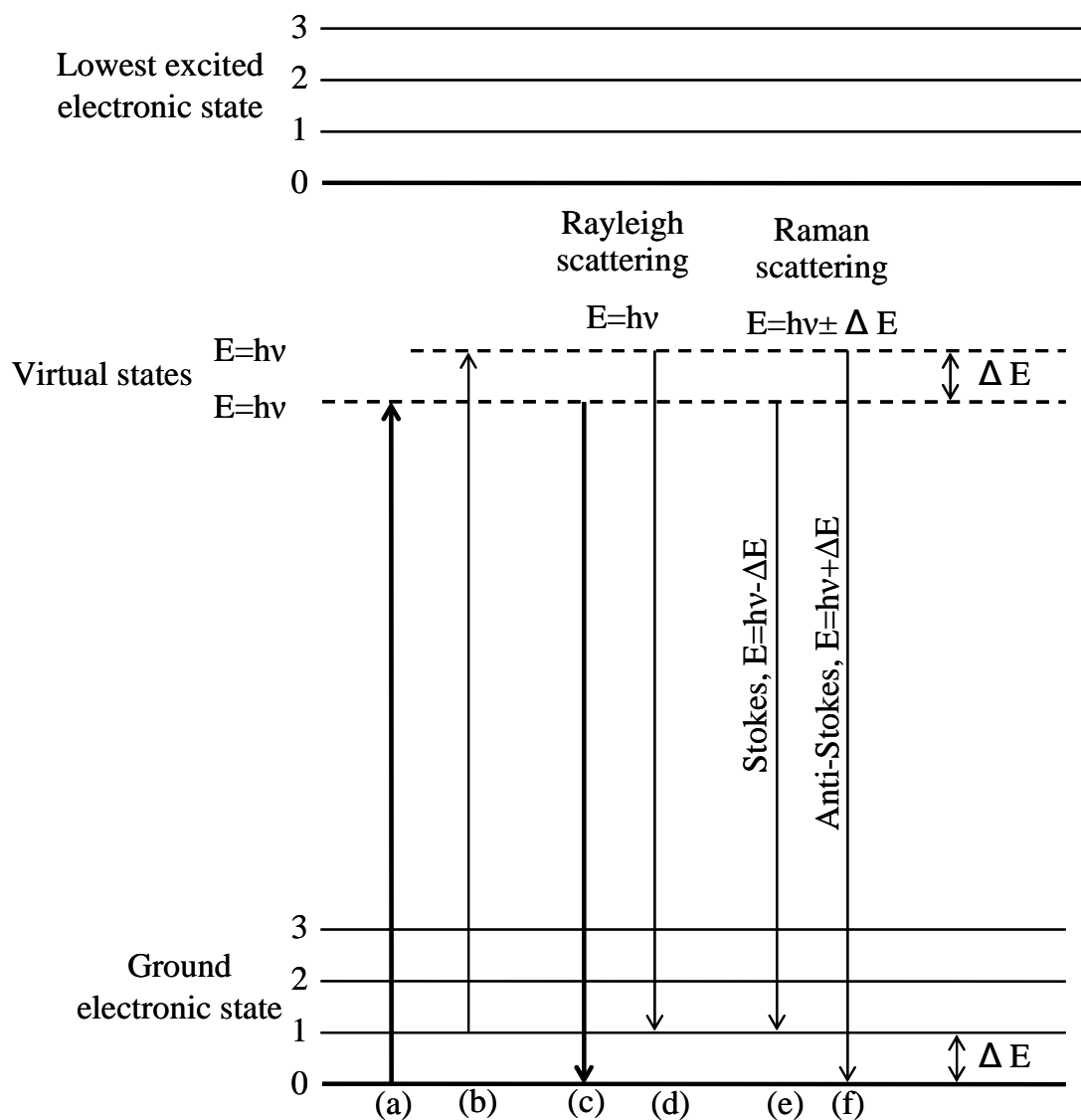


**Figure 3.1.** Origin of Rayleigh and Raman scattering

Figure 3.1 (b) shows the energy change if the molecule that is impinged by the photon resides in the first vibrational level of the electronic ground state. At room temperature, transition (a) occurs in greater abundance than transition (b) since the ground state abundance is higher than the excited state. As depicted by arrows (c) and (d), no loss of energy occur in Rayleigh scattering. Raman scattering, depicted by arrows (e) and (f), consists of Stokes and anti-Stokes scattering. Stokes emission occur when molecules re-emit a photon of energy  $E=h\nu-\Delta E$  and anti-stokes when energy re-emitted is  $h\nu+\Delta E$ . The lower-frequency Stokes scattering is more commonly used than the higher-frequency anti-Stokes scattering since it gives a more intense signal. However, in instances where fluorescing samples are encountered, the less-interfered anti-Stokes shift can be used despite its lower intensity. Another way to reduce fluorescence is to take advantage of higher wavelength lasers that are not energetic enough to produce fluorescence-producing excited electronic energy states in most molecules.<sup>126</sup> It is important to note that Stokes, anti-Stokes and Rayleigh lines all appear in a Raman spectrum even though the Stokes part of the spectrum is usually generated.<sup>126</sup>

Despite being similar in application to infrared spectroscopy (IR), Raman spectroscopy offers unique advantages that chemists can benefit from. In general, chemical species with covalent bonds have strong Raman signatures. It also offers a great platform for biological research since water is a weak Raman scatterer. Aqueous samples can be probed without major interference from water vibrations. In addition, molecular vibrations of hygroscopic and air-sensitive compounds can be conveniently measured using Raman spectroscopy since they can be placed in a sealed glass tube. In IR however, the glass tube absorbs the IR radiation. Some of the disadvantages of Raman

spectroscopy are the possibility of the sample's local heating, occurrence of fluorescence in some compounds, and the cost of the spectrometer.<sup>125</sup>

Since the discovery of carbon nanotubes, as multi-walled nanotubes in 1991<sup>11</sup> and as single-walled nanotubes in 1993,<sup>127</sup> Raman spectroscopy has been used to identify the properties (e.g. diameter, chirality) of nanotubes,<sup>128,129</sup> probe the quality of dispersion<sup>51,52</sup> and evaluate polymer matrix-nanotube interactions.<sup>62-67,130</sup> However, the power of Raman spectroscopy for characterizing carbon nanotubes was not fully appreciated until 1997 when Rao first showed that the Raman excitation frequency can be chosen to selectively excite nanotubes of particular diameter for study.<sup>131</sup> One year later, Pimenta demonstrated that metallic and semiconducting carbon nanotubes can be differentiated from the resonant behavior of the Raman modes.<sup>132</sup>

In the Raman spectra of SWNT, a prominent feature is the radial breathing mode (RBM), appearing between 120 cm<sup>-1</sup> and 250 cm<sup>-1</sup> wavenumber, attributed to the symmetric movement of all carbon atoms in the radial direction. A number of studies have yielded results for assigning RBM modes to specific (n,m) indices, which allow the determination of diameter and chirality of an isolated SWNT.<sup>129</sup> From the relationship  $\omega_{\text{RBM}} = A/d_t + B$ , where  $A = 234 \text{ cm}^{-1}$  and  $B = 10 \text{ cm}^{-1}$ , the diameter distribution,  $d_t$  for the Nano-CPT tubes used in this study that is in resonance with the laser line is between 0.9 to 1.3 nm.<sup>133</sup> The D Raman band of SWNTs, which is observed between 1250 and 1450 cm<sup>-1</sup> wavenumber, is due to the defects which lower the crystalline symmetry of the quasi-infinite lattice. Therefore, the intensity of the D mode peak gives a direct correlation to the degree of disorder in SWNTs. The peak in the region 1500-1605 cm<sup>-1</sup> is denoted the tangential G band. In isolated semiconducting nanotubes, two prominent

Lorentzian features of this band are the higher frequency  $G^+$  ( $\omega_G^+$ ) band, which is associated with atomic C-C stretching displacements along the nanotube axis and the lower frequency  $G^-$  ( $\omega_G^-$ ) band attributed to vibrations along the circumferential direction. In contrast, metallic tubes also have two dominant components with similar origins, but the lower frequency  $\omega_G^-$  is a broad Breit-Wigner Fano lineshape.<sup>134</sup> Since the G band is derived from the graphite-like in-plane mode, the intensity of the G band can readily be used to determine the relative concentration of SWNT in nanocomposite samples, regardless of whether the nanotube bundles are visually obvious with a microscope or not. Figure 3.2 is a schematic showing the G and RBM mode atomic vibrations. The second-order overtone of the D band, the  $D^*$  band occurs in the region of 2550-2800  $\text{cm}^{-1}$ . This mode is sensitive to any perturbation to the electronic structure of SWNT, such as from charge transfer effects.<sup>135,136</sup> Therefore, shifts in the frequency of the  $D^*$  band can be monitored to experimentally detect the presence of charge transfer processes.

## **(II) Polymer-SWNT Interaction Probed Using Raman spectroscopy**

In our study, the extent of intermolecular interaction within the nanocomposite is quantified by monitoring the frequency of the  $D^*$  band in a Raman spectrum, which provides a measure of the compressive or tensile forces imposed by the polymer matrix onto the nanotubes. As the diameter of the laser is  $\sim 1 \mu\text{m}$ , which is three orders of magnitude larger than the diameter of the nanotubes, the Raman signal that is analyzed is an average response from a population of SWNTs that exist in the Raman beam. Therefore, the  $D^*$  band is a very practical peak to be analyzed since this mode is weakly dependent on nanotube diameter variation.<sup>62</sup>

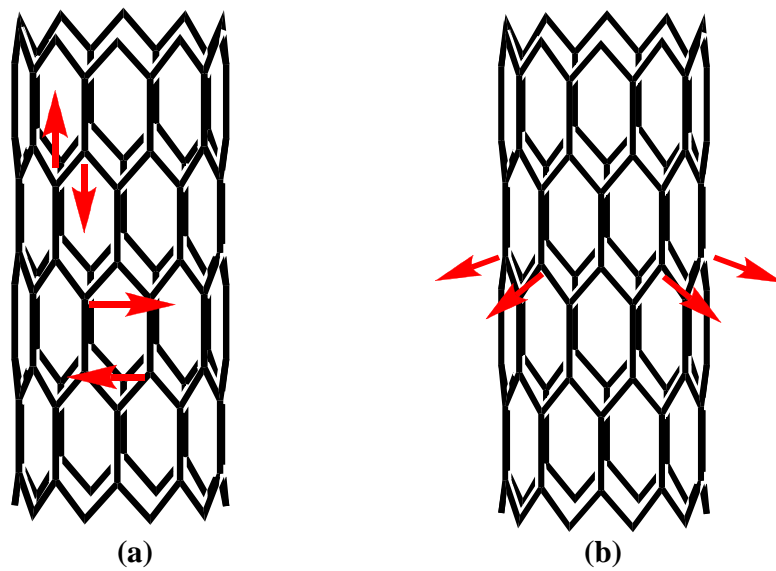


**Figure 3.2.** Schematic of the (a) G band atomic vibrations along the nanotube circumference and along the nanotube axis and (b) RBM vibrational mode, attributed to the symmetric movement of all carbon atoms in the radial direction



This analysis builds off of a previous investigation by Wood and coworkers that demonstrated upshifts in the frequency of the  $D^*$  band of SWNTs when molecular pressure is applied to the nanotube's sidewalls by immersing them in various liquids of varying cohesive energy density (CED) or macroscopic pressure that is applied by a diamond anvil cell.<sup>62</sup> In this study, the authors conclude that a positive peak shift of the  $D^*$  band frequency of carbon nanotubes embedded in a polymer matrix relative to that of the pure SWNTs arises due to (I) CED or internal pressure of a polymer phase,<sup>62,64-68</sup> (II) compression of SWNT C-C bonds from the shrinkage of polymer matrix,<sup>69</sup> (III) the temperature dependence of SWNT structure in air, which is small and considered negligible<sup>68</sup> and (IV) the shift produced by the stress induced from the temperature dependence of cohesive energy density, which is also considered negligible since it has been shown that for sufficiently long polymer chains, the change in CED with temperature is negligible.<sup>70</sup> Therefore, we focus on the first and second factors that contribute to the upshift in the  $D^*$  band in our nanocomposites.

In condensed liquid or solid phases, the cohesive energy,  $E_{\text{coh}}$ , of a substance is defined as the increase in internal energy,  $U$ , per mole if all the intermolecular forces are eliminated:<sup>137</sup>

$$E_{\text{coh}} = \Delta U \text{ (J/mol)} \quad \text{(Equation 3.1)}$$

On the molecular level, the cohesive energy inherently provides a measure of the attractive forces holding the presumably non-interacting molecules together. In a two-phase system however, the presence of a second minor phase, SWNT aggregates in our case, interferes with the balance of attractive and repulsive molecular forces in the matrix and thus generates compressive stresses from the surrounding medium to the nanofiller.

If the matrix is a liquid, the magnitude of this stress can be experimentally obtained from the relationship:

$$CED = \frac{E_{coh}}{V} = \delta^2 = \frac{\Delta U_{vap}}{V} \approx \frac{\Delta H_{vap} - RT}{V} \quad (\text{Equation 3.2})$$

where  $\delta$  is the solubility parameter  $((\text{J}/\text{cm}^3)^{1/2})$ ,  $V$  the molecular volume ( $\text{cm}^3/\text{mol}$ ),  $\Delta H_{vap}$  the enthalpy of vaporization ( $\text{J}/\text{mol}$ ),  $R$  the universal gas constant ( $\text{J}/\text{mol K}$ ) and  $T$  is the temperature ( $\text{K}$ ). For polymers however, indirect methods must be used for the determination of the CED as they do not vaporize. Using the group contribution method developed by Small, such that;

$$CED = \delta^2 = \frac{F^2}{V^2} \quad (\text{Equation 3.3})$$

where  $F$  is Small's molar attraction constant,<sup>137</sup> the CED of the polymers used in this study were calculated. For example, from Equation 3.3, PMMA and PDMAEMA have a CED of 357.1 MPa and 306.2 MPa respectively and therefore, DMA50 has a CED of 331.6 MPa.

With this value of the CED of the MMA-*ran*-DMAEMA polymer matrix, Wood's results estimate that the expected shift in the  $D^*$  band will be  $13.8 \text{ cm}^{-1}$ . This value is determined for all MMA-*ran*-DMAEMA copolymers and presented in Figure 3.2, which shows the expected shift in the  $D^*$  band as a function of % DMAEMA from the compressive force of the surrounding polymer matrix, as well as the experimentally determined  $D^*$  shift of our nanocomposites. Figure 3.2 clearly demonstrates that the  $D^*$  shift obtained in our studies is higher (except DMA30 nanocomposite, discussed later) than the shifts that would be expected from the CED of the polymer, i.e. the shift that would be expected if the interaction between polymer and nanotube is due solely to the

internal pressure of non-interacting polymers. As there is very little correlation between these two data sets, there must exist other factors that contribute to the observed upshift in the D\* band in the DMA polymer-nanocomposites.

Lourie et al. also used Raman spectroscopy to monitor the cooling-induced compressive deformation of carbon nanotubes embedded in an epoxy matrix,<sup>69</sup> a second factor that must be considered in interpreting our D\* band frequency shifts. When the epoxy-SWNT composite is cooled, the epoxy resin contracts, and the transfer of compressive and thermal stresses from the surrounding polymer to the SWNT results in a shortening of the C-C bond length in the nanotube shell, and an upshift in the D\* band. Based on a concentric cylinder model for a long tube embedded into an isotropic matrix, Wagner demonstrates that the axial tube stress due to cooling can be calculated theoretically and is directly proportional to the difference in the thermal expansion coefficients of the matrix and the nanotube, if the temperature gradient (i.e. difference between  $T_g$  of polymer and ambient temperature), volume fraction and Young's moduli of the tube and matrix are constant, which is true in our case.<sup>69,138</sup> Therefore, any contribution of polymer's contraction upon cooling to the D\* band upshift is expected to be constant for all DMA copolymer nanocomposites studied. The thermal histories of all the samples are also identical, therefore eliminating transfer of thermal stress to nanotube as the cause of the variation in D\* band upshift with copolymer composition. The variation in the magnitude of the D\* peak shift observed in these Raman spectra is thus interpreted to originate from the variation of compressive stress due to polymer-SWNT interactions.

One issue that also needs to be addressed here is the effect of molecular weight on the level of dispersion. The molecular weight of the polymers used in this study ranges from 39,000 to 83,000 g.mol<sup>-1</sup>. While molecular weight does play a role in the reinforcing effect of polymer nanocomposites, Winey et. al conclude that the molecular weight of an amorphous polymer matrix has no significant effect on SWNT dispersion in their investigation of PMMA nanocomposites with polymer molecular weight ranging from 25K and 100K.<sup>139</sup>

As shown in Figure 3.3, the PMMA and DMA10 composites have a D\* peak upshift of 16.1 cm<sup>-1</sup> and 16.8 cm<sup>-1</sup> respectively, indicating a very high molecular pressure induced upon the nanotube sidewalls and an absence of significant complex formation. This implies that at only 10 mol% DMAEMA, the extent of EDA complex formation between SWNTs and the tertiary amino group is insufficient to overcome the Van der Waals attraction between adjacent tubes. The magnitude of the D\* band upshift decreases as the % DMAEMA in the copolymer increases, an indication that charge transfer formation increases, thereby, relieving the internal pressure within the SWNT. This increases the inter-tube spacing, relieving the packing between the SWNTs, and can consequently improve dispersion. Among this series, the DMA30 composite has the smallest positive shift of 9.7 cm<sup>-1</sup>, implying that the DMA30 copolymer minimally compresses the nanotube, subsequently providing the most optimum charge transfer interaction between the copolymer and nanofiller, among its series. When the mol% DMAEMA in the copolymer increases further, the D\* band shift increases, up to 18.5 cm<sup>-1</sup> for the neat PDMAEMA homopolymer composite. This indicates that the degree of

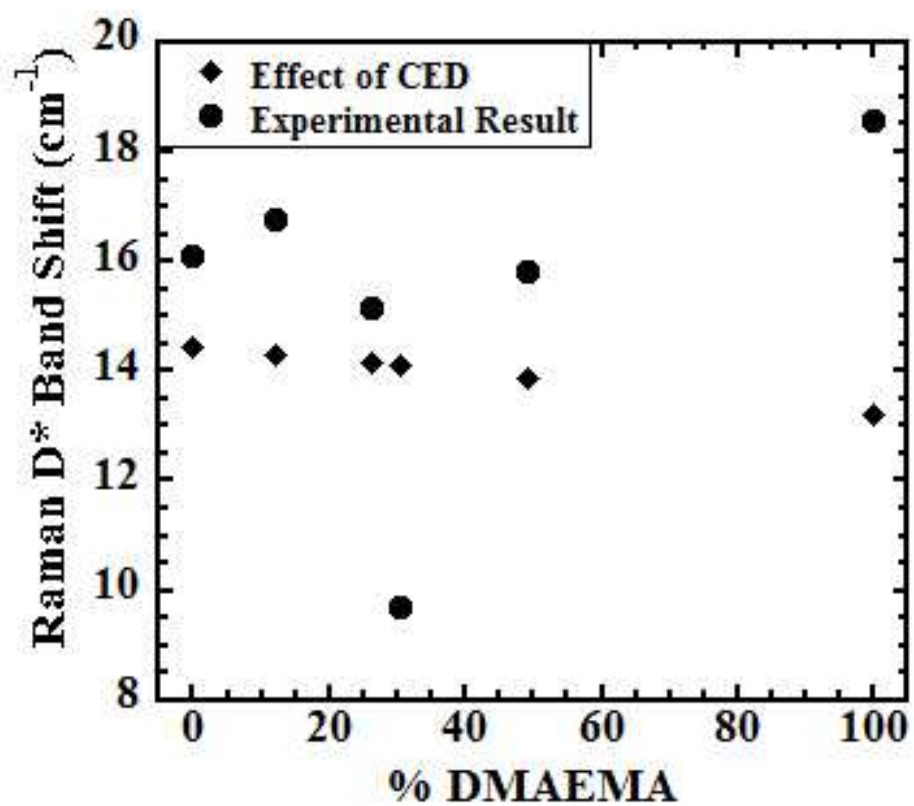


**Figure 3.3.** Estimated and experimental D\* band peak shift for DMAEMA nanocomposites as a function of % DMAEMA

compressive forces induced upon the SWNT is large, causing a decrease of tube-tube spacing, and potentially causing SWNT kinking, flattening or deformation.<sup>140</sup>

In order to provide insight into the extent of EDA interaction between the SWNT and SAN copolymers, the shift in the frequency of the D\* band was also monitored. As shown in Figure 3.4, the composites exhibit negative D\* peak shifts, in sharp contrast to the positive D\* band shifts of the MMA-*ran*-DMAEMA nanocomposites. Kao and coworkers have investigated the effect of strain applied to SWNT-epoxy composites and observed positive D\* band shifts in compression and a slight shift to lower wavenumbers in tension.<sup>120</sup> Ajayan and coworkers performed similar studies, and also found similar downshift in the D\* band with tension, but no significant shifts under compression. They argue that the D\* downshift in tension is a result of a reduction in the radial stresses due to debundling of the nanotubes, which causes an increase in the inter-tube spacing within the nanocomposite.<sup>141</sup> It is unclear however, whether these carbon nanotubes exist as isolates.

In our results, an upshift in the D\* band, as exhibited in the MMA-*ran*-DMAEMA composites, is interpreted as compressive forces that are transferred from the polymer to the SWNTs while negative shifts, as obtained for SAN composites indicate that the internal pressure within the carbon nanotube bundles is relieved by the formation of EDA complex between SAN copolymer and SWNT. Figure 3.4 shows the comparison between the Raman D\* shift obtained in our studies and the D\* band shifts that would be expected from purely CED forces by correlation to Wood's results, as discussed in the DMA results above. If the Raman shift obtained in this study were due to only the cohesive forces existing between the non-interacting polymer matrix and SWNT, a

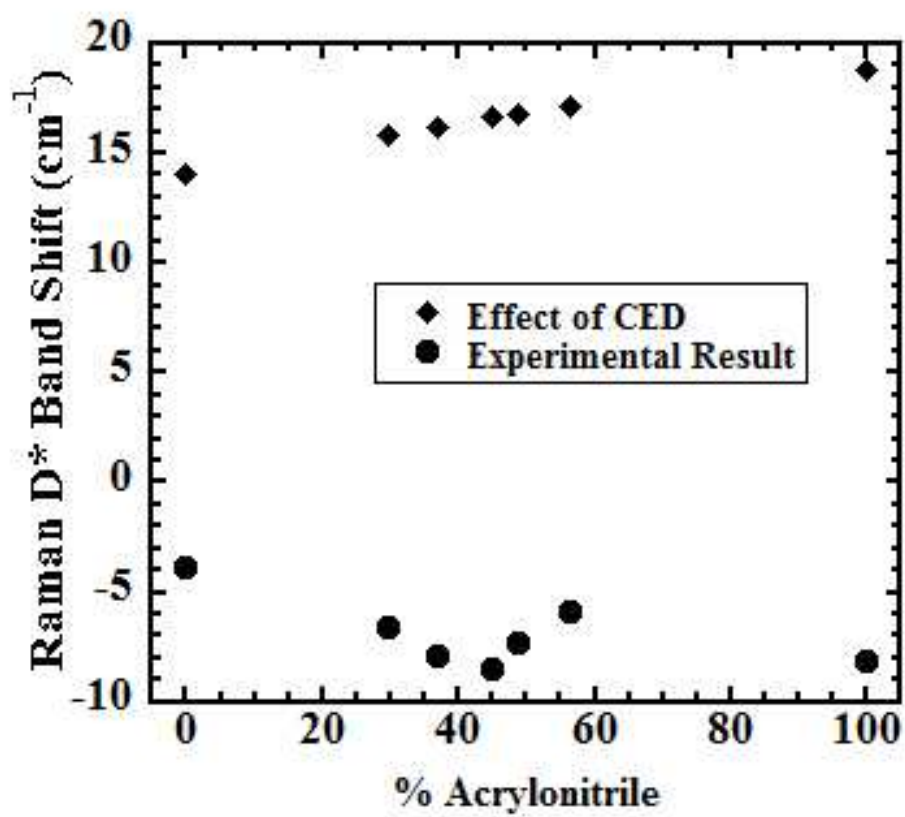


**Figure 3.4.** Estimated and experimental D\* band peak shift for SAN nanocomposites as a function of % AN

positive Raman shift similar to the DMA copolymers should be observed. However, clearly the D\* band peak shift is not due to the compressive stress induced upon SWNT, but is a result of forces that can result in SWNT debundling.

As shown in Figure 3.4, the polystyrene composite shows the smallest negative shift of  $\sim 3.8 \text{ cm}^{-1}$ , suggesting that polystyrene has a weak interaction with SWNTs, in the form of  $\pi$ - $\pi$  interactions between the aromatic rings on polystyrene and the nanotube surface. As AN is incorporated into the copolymer, stronger interfacial cohesion or EDA interaction is realized as evidenced by a larger negative shift, to a maximum value of  $\sim -8.5 \text{ cm}^{-1}$  for the 45% AN. However, as the percent AN increases further, the extent of the D\* band shift decreases. This may be explained as due to the proximity between AN moieties along the polymer chain, leading to the retardation of AN accessibility to form EDA interaction with the SWNT. Surprisingly, the PAN composite has a negative D\* shift of  $\sim 8.1 \text{ cm}^{-1}$ , comparable to that of SAN45, which is the best copolymer in this system. This anomaly will be discussed more fully in Section 3.3.B.

Similar experiments were performed on St-*ran*-CNSt nanocomposite to provide insight into the intermolecular charge transfer phenomena occurring between these polymer matrices and SWNT. The D\* peak shift relative to that of pure SWNT in air is monitored and shown in Figure 3.5. As was found for the SAN composites, CNSt composites also show a negative D\* shift suggesting that the internal pressure within the carbon nanotube is relieved by the formation of EDA complexes between CNSt copolymer and SWNT. As expected, the shift attained by PS is relatively small ( $\sim 3.8 \text{ cm}^{-1}$ ) owing to the weak  $\pi$ - $\pi$  interaction between polymer and tubes. As the incorporation of CNSt increases from 12.6 mol% to 23.6 mol%, the extent of D\* band shift increases



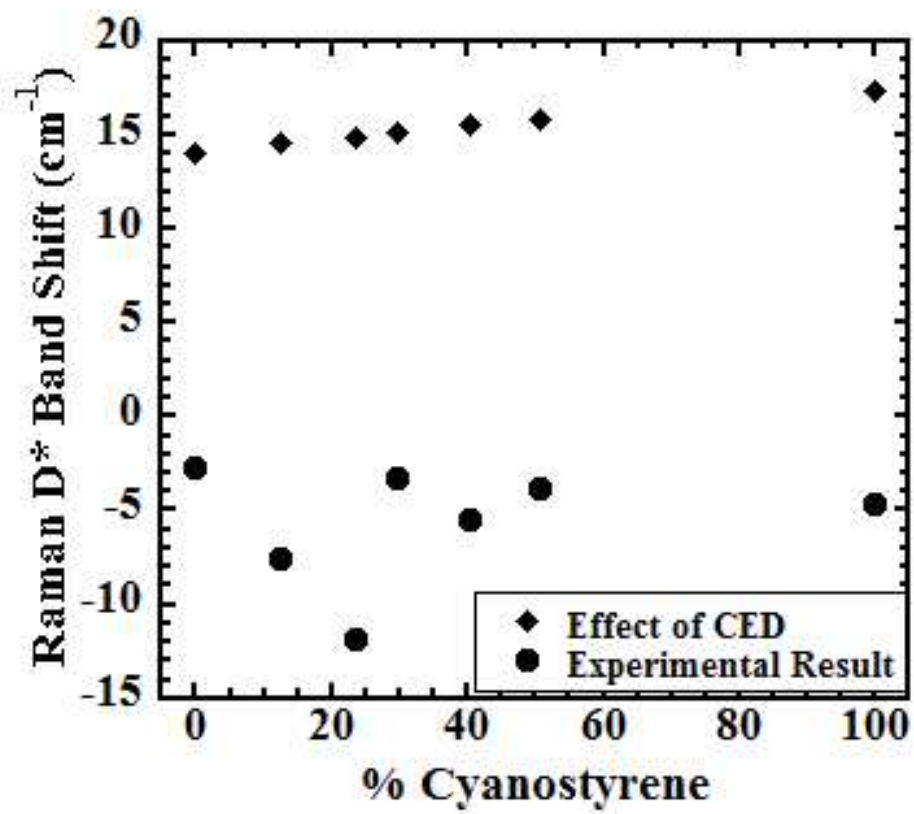
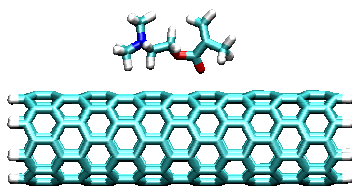


**Figure 3.5.** Estimated and experimental D\* band peak shift for cyanostyrene nanocomposites as a function of % CNSt

from negative  $\sim 7.6 \text{ cm}^{-1}$  to a maximum of negative  $\sim 11.8 \text{ cm}^{-1}$ , an indication that CNSt23 has the highest extent of intermolecular charge transfer among all three copolymer systems. A mere increase of 6.2 mol% of CNSt (CNSt 30) content above the optimum composition (CNSt 23) indicates a dramatic decrease of intermolecular interaction, where a negative shift of only  $\sim 3.3 \text{ cm}^{-1}$  is observed. CNSt 40 and CNSt 50 show larger negative shifts than CNSt30, but the extent of this downshift is small relative to CNSt 23. The neat homopolymer PCNSt has a positive D\* band shift of  $4.1 \text{ cm}^{-1}$ , indicating relatively poor interfacial interaction between the matrix and SWNT. Taken as a whole, these results indicate that the *St-ran*-CNSt copolymer forms the most robust charge transfer interaction with the nanofillers, followed by *St-ran*-AN and *MMA-ran*-DMAEMA.

## **B. Density Functional Theory Calculations (DFT)**

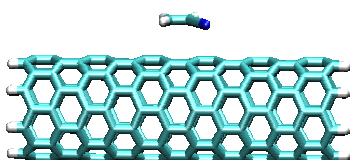
Density functional theory was used to provide insight into the formation of EDA interactions between monomers and SWNT and investigate the role of chain connectivity on the formation of EDA interactions. The optimized geometries for the monomer-SWNT systems and the binding energies were obtained from the DFT calculations completed by Dr. Bobby Sumpter,<sup>142</sup> and are illustrated in Figure 3.6. For the sake of completion, the details of the simulation are briefly discussed here. Three different single-walled carbon nanotubes (SWNTs) were considered: (8,0) semi-conducting and (9,0) quasi-metallic zigzag nanotubes and a (5,5) metallic armchair nanotube. For each case, the length of the nanotubes was at least 20 Å and the ends were passivated with hydrogen. All-electron density functional theory (DFT) calculations of the hydrogen



**DMAEMA**

(0.31 kcal/mole)

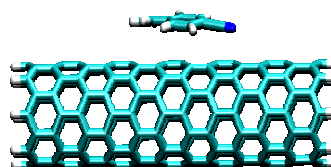
*Dispersed*



**Acrylonitrile**

(4.5 kcal /mol)

*Well-Dispersed*



**Cyanostyrene**

(10 kcal /mol)

*Most-Dispersed*

**Figure 3.6.** Optimized geometries for DMAEMA, AN, and CNSt monomers interacting with an (8,0) semiconducting SWNT with binding energies given in parentheses as determined by density functional theory (DFT)

terminated SWNTs interacting with monomers and small oligomers (up to 12 monomers were considered) were performed using NWChem<sup>143</sup> with the local density approximation (LDA) and generalized gradient approximation (GGA). The atom centered, contracted Gaussian basis sets, 3-21G<sup>144</sup> and 6-31 + G\*<sup>145</sup> were used during the calculation of the self-consistent solution. The initial geometries for the different nanotube-based systems were obtained by first optimizing the geometry of the nanotube-monomer/oligomers using molecular mechanics and the MM3 potential.<sup>146</sup> From these MM3 optimized geometries, full geometry optimization using DFT (LDA) with the 3-21G basis set was used to generate the final geometry.<sup>144,147</sup> In order to validate the relative strength and trends of the intermolecular interactions as computed from DFT-LDA, the addition of a damped, empirical dispersion term, DFT-D method was utilized in this study.

These results from the DFT calculations agree with our experimental results, where CNSt has the highest binding energy, 10 kcal/mol, which results in the highest extent of interfacial adhesion with SWNT, as discussed in Section 3.3.A.II. Due to the aromatic structure of CNSt, the preferred orientation of the CNSt monomer interacting with SWNT lies flat, with its  $sp^2$  resonance facing the  $\pi$  network structure of SWNT. Acrylonitrile has an intermolecular binding energy of 4.5 kcal/mole, half that of CNSt. This information qualitatively agrees with the experimental shifts of the D\* band, indicating that the extent of intermolecular interaction of SAN copolymers with SWNT is not as great as that of the CNSt copolymers. A small intermolecular binding energy of only 0.31 kcal/mol for the DMAEMA monomer implies a weak charge transfer interaction with SWNTs.

The binding energies of the monomers, illustrated in Figure 3.6 elucidates the extent of interaction achieved by *St-ran*-CNSt, *St-ran*-AN, and *MMA-ran*-DMAEMA, but it does not however, explain the occurrence of an optimal EDA interaction when the minority of the monomers are the interacting functional groups in the matrix (i.e. DMA30, SAN45, CNSt23). The optimized geometry of a cyanostyrene trimer as determined by DFT provides some additional insight into this result. Figure 3.7 shows an optimized geometry of a cyanostyrene trimer in the presence of an (8,0) semi-conducting single walled nanotube. This illustrates how the polymer must adopt a conformation that differs from the monomer optimized geometry in Figure 3.6 due to chain connectivity. In this system, the middle cyanostyrene monomer does not interact with the SWNT, while the monomers at the ends contribute a binding energy of 2.72 kcal/mol each (total binding energy of 5.44 kcal/mole for the trimer).

In polymer-nanocomposite systems, geometrical constraints are very important parameters that limit the formation of non-covalent interactions by polymers on the walls of nanotubes. For example, Yang and coworkers has performed a molecular dynamics (MD) simulation, which demonstrates that the plane of the aromatic rings of a PS homopolymer tends to be vertical to the surface of the SWNT. Parallel alignment of the aromatic rings on PS chain is more energetically favorable, however, not entropically, possibly due to chain connectivity effects (significant twisting of bonds occur if aromatic rings of PS were to align along SWNT surface), causing the aromatic rings to rotate away from the SWNT surface and align parallel to each other to optimize their mutual interaction.<sup>148</sup>

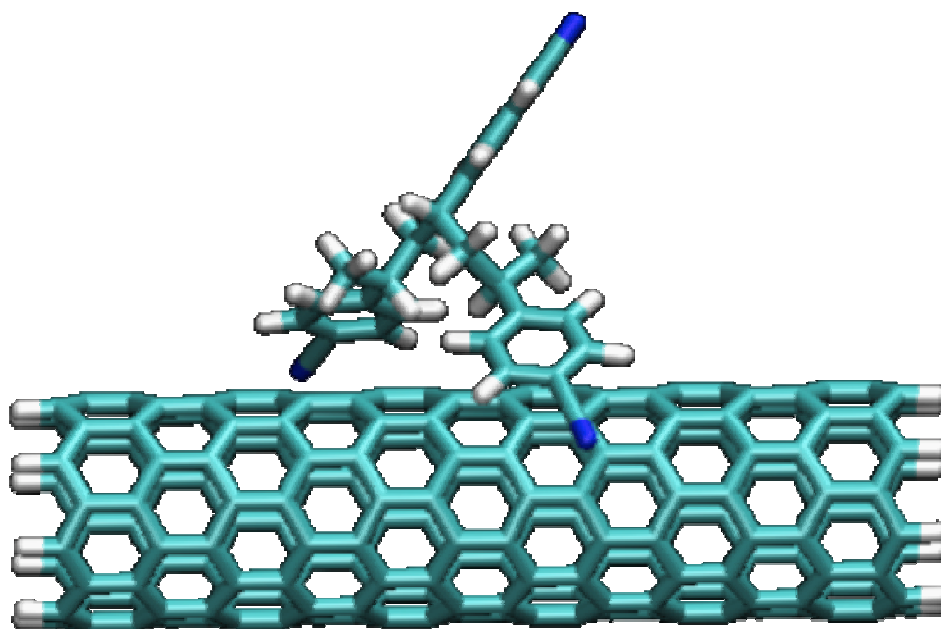


**Figure 3.7.** Optimized binding orientation between cyanostyrene trimer and (8,0) semiconducting SWNT as determined by DFT calculation

By the same token, polymer chain flexibility also plays a role in the formation of non-covalent interaction since this affects the ability of a polymer chain to conform itself favorably to the curved nanotube surface. MD simulations show that the intermolecular interaction between a polymer and SWNT changes by ~100% for the more flexible PS and ~50% for a stiff poly(p-phenylenevinylene) (PPV) polymer chain when the SWNT diameter increases.<sup>148</sup> This helps to explain why polyacrylonitrile shows anomalously good intermolecular interaction. The loss of the aromatic rings of the styrene leads to a significantly more flexible chain that can wrap more easily around the SWNT, creating more nitrile-SWNT EDA interactions.

In the case of a copolymer-SWNT system, the formation of the nitrile-SWNT interaction is not as trivial, as our results show that an increase in the distance between interacting functional groups along a polymer chain leads to higher occurrence of intermolecular charge transfer interaction with the SWNTs. This allows efficient formation of EDA complex since rotational freedom of the various interacting functional groups are increased as they are separated along the copolymer chain. However, too large of a separation of functional groups in a polymer chain is also unfavorable since intermolecular interaction would be hindered by the limited amount of interacting functional moiety.

### **C. Calculation of Free Energy of Mixing, $\Delta G$**

To provide further insight into the role of chain connectivity in governing the extent of interaction in nanotube-polymer composites, Flory-Huggins theory is applied to these systems. Flory-Huggins theory is a well-known extension of the regular solutions

theory to both polymer solutions and blends<sup>149</sup> and provides a useful expression for the change of Gibbs free energy of mixing for binary components A and B:

$$\frac{\Delta G_m}{RT} = \frac{\Phi_A}{N_A} \ln \Phi_A + \frac{\Phi_B}{N_B} \ln \Phi_B + \chi_{AB} \Phi_A \Phi_B \quad (\text{Equation 3.4})$$

where, in this case,  $\Phi_A$ ,  $\Phi_B$  and  $N_A$  and  $N_B$  are the volume fractions and number of molecular units in SWNT and polymer respectively,  $R$  the gas constant,  $T$  the temperature in Kelvin and  $\chi_{AB}$  is the Flory-Huggins interaction parameter. The first two terms in Equation 3.4 denotes the configurational entropy of mixing for the two components. For long chain polymers, the entropy of mixing,  $\Delta S$ , is quantitatively negative and small ( $N_A$  is large). Hence, unlike low molecular weight materials, the entropy of mixing does not contribute significantly to the overall Gibbs free energy of mixing,  $\Delta G$  to promote miscibility. Strictly speaking, SWNTs are not polymers in the conventional sense and therefore, the number of molecular units in SWNT,  $N_A$  has never been theoretically or experimentally determined. Nevertheless, in our attempt to use the Flory-Huggins theory in this polymer-nanocomposite system, we have taken a value of 5000 as the  $M_A$ . This arbitrary value was taken from the horizontal asymptote in the plot of Gibbs free energy of mixing (J/mol) vs the number of repeat units in SWNT,  $M_A$  in Figure 3.8.

To justify the usage of this arbitrary number, a PMMA molecule with molecular weight of 50,000 g/mol, which will have a degree of polymerization of 500, is considered. The radius of gyration, mass-weighted average distance of all the monomers from the center of mass, is a measure of the polymer size.<sup>150</sup> It can be calculated as follows:



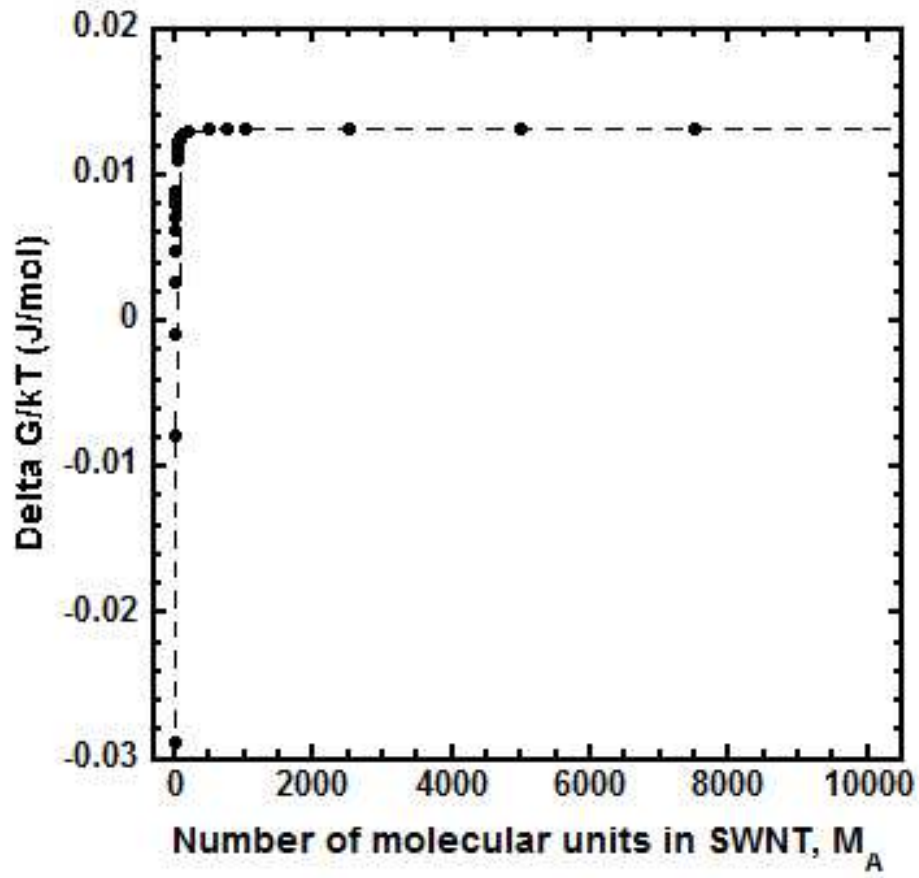


**Figure 3.8.** Gibbs free energy of mixing (J/mol) as a function of molecular unit entities in SWNT,  $M_A$ . Assumptions: (I) Chi interaction parameter,  $\chi=1.5$  and (II) polymer degree of polymerization,  $M_B = 500$

$$R_g = \left[ \frac{\langle h^2 \rangle_o}{6} \right]^{1/2}$$

where  $\langle h^2 \rangle_o$  denotes the mean-square end-to-end distance of the unperturbed polymer chain. From the experimentally determined chain dimension by small angle neutron scattering,  $\langle h^2 \rangle_o / M$  for PMMA is  $0.425 \text{ \AA}^2 \cdot \text{mol/g}$ .<sup>151</sup> Therefore, for a PMMA chain with chain length of 50,000 g/mol,

$$R_g = \left[ \frac{0.425 \times 50,000}{6} \right]^{1/2} = 59.5 \text{ \AA}$$

On the other hand, the length of a SWNT rod utilized in this study ranges from 500 nm to 4  $\mu\text{m}$ , which are orders of magnitude longer than a polymer chain. Thus, a choice of the number of SWNT molecular units,  $M_A$  as 5000, is reasonable as it is an order of magnitude larger than the polymer's degree of polymerization.

The last term in Equation 3.4 denotes the material-specific enthalpic contribution to the free energy of mixing and consists of the Flory Huggins parameter,  $\chi$ . In 1997, Groot and Warren<sup>152</sup> established useful parameter ranges for the particle-based Dissipative Particle Dynamics (DPD) simulation of mesoscopic systems and made a link between those parameters and  $\chi$ -parameters in Flory-Huggins model. Based on their theoretical work,  $\chi$  can be calculated using the following equation:<sup>152,153</sup>

$$\chi_{AB} = \frac{V_A}{kT} (\delta_B - \delta_A)^2 \quad (\text{Equation 3.5})$$

where  $V_A$  denotes the polymer molar volume and  $\delta_A$  and  $\delta_B$  represents the solubility parameter of SWNT and polymer respectively. In general terms,  $\chi$  is the fraction of thermal energy ( $kT$ ) needed to extract molecule A and B from their pure state, and then exchanging them. When A and B components do not favor contact, the  $\chi_{AB}$  value is

positive and when they favor each other over AA and BB contacts,  $\chi_{AB}$  is negative. The solubility parameters of the polymers can be calculated using the additive group contribution theory as outlined in Section 3.3A, Equation 3.3. The solubility parameter for carbon nanotube utilized in this study, which has an average diameter of 1.1 nm was taken as  $22.5 \text{ (J/cm}^3\text{)}^{1/2}$ , from Maiti's<sup>153</sup> particle-based dissipative particle dynamics simulation (DPD). In the simulation, the cohesive energy density (CED), which is the square of the solubility parameter, was obtained from the debundling energy of the close-packed CNT bundles, i.e. the energy cost of isolating a CNT from a bundle. The above approach for calculating  $\chi$  works reasonable well for non-polar interactions, and does not work in mixtures with strong polar or specific interactions, such as hydrogen bonds.

The question that arises however, as to whether this theory, which is conventionally used to predict miscibility behavior of polymer blends, can be applied analogously to polymer nanocomposite systems. Several efforts have been made to apply this theory to a variety of multi-component systems. Usrey et al. have experimentally determined SWNT solubility after covalent functionalization with aryl carboxylic acid or aryl hydroxyl groups in aqueous solution by using UV-vis-nIR photoabsorption spectroscopy and compared it to the calculated solubility parameter from polymer solubility theory. It was found that the solubility parameter calculated from the Maiti-RSP model<sup>153</sup> best describes the increasing solubility with increasing functionalization. In this model, the  $\chi$  interaction parameter is calculated using the solubility parameter that takes into account the polar group effects and hydrogen bonding, in addition to the dispersion interactions between molecules.<sup>154</sup> Maiti et al. have also mapped out the solubility parameter of carbon nanotubes (CNT) as a function of the CNT diameter,

which has provided a tool for predicting polymer-CNT solubility.<sup>153</sup> In conjunction with this, their simulation results have been further justified by an experimental study by Dalton et al., where poly(m-phenylenevinylene) (PmPV,  $\delta \sim 18.5 \text{ (J/cm}^3)^{1/2}$ ) polymers have selective affinity to CNTs of diameters ranging from 1.35 nm to 1.55 nm, which has similar solubility parameter to PmPV, determined from Maiti's dissipative particle dynamics simulation.<sup>155</sup> It is worth noting that components with similar solubility parameters generate miscibility whereas disparate solubility parameters yield limited miscibility. One major challenge that hampers the efforts to establish the applicability of Flory-Huggins theory to polymer nanocomposites is that the state of equilibrium, which is required for this thermodynamic analysis, is always questionable for multicomponent systems such as polymer nanocomposites. However, studies in the development of Flory-Huggins theory to polymer nanocomposite system can still provide guidelines to rationally design miscible systems.

In our effort to apply this mean-field, lattice model theory to our system, we have calculated the configurational entropy of mixing,  $\Delta S$  of the polymer-SWNT blend and the  $\chi$  interaction parameter that contribute to the overall change in Gibbs free energy of mixing,  $\Delta G$  of the nanocomposite. These values are shown in Tables 3.4, 3.5 and 3.6 for MMA-*ran*-DMAEMA, styrene-*ran*-acrylonitrile and styrene-*ran*-cyanostyrene nanocomposite, respectively. As expected, the entropy of mixing for all sets of nanocomposites is similar and quantitatively small and negative, indicating its negligible contribution to the overall free energy of mixing of the polymer nanocomposite. Therefore, we focus our attention to the enthalpic contribution to the free energy of mixing in the form of  $\chi$  interaction parameter. In general, the values of the interaction

**Table 3.4.** MMA-*ran*-DMAEMA polymer nanocomposite's (containing 1.0 wt% SWNT) Gibbs free energy of mixing  $\Delta G$ , entropic contribution  $\Delta S$  and Chi interaction parameter  $\chi$  calculated from Flory-Huggins theory

Polymer	mol % DMAEMA	Density (g/cm <sup>3</sup> )	Avg monomer molar mass (g/mol)	MW polymer (g/mol)	Molar Volume (cm <sup>3</sup> )	Solubility, $\delta$ (J <sup>1/2</sup> /cm <sup>3/2</sup> )	$\Delta G/kT$ (J/mol)	$\Delta S/kT$ ( J/mol)	Chi
PMMA	0.00	1.19	100.12	61000	1.40E-22	14.86	0.017	-0.00002	1.97
DMA12	0.12	1.18	107.09	44000	1.51E-22	14.91	0.019	-0.00003	2.10
DMA26	0.26	1.16	115.14	54000	1.65E-22	14.96	0.020	-0.00003	2.26
DMA30	0.30	1.15	117.48	46000	1.69E-22	14.98	0.020	-0.00003	2.31
DMA49	0.49	1.13	128.21	49000	1.88E-22	15.05	0.022	-0.00003	2.52
PDMAEMA	1.00	1.07	157.22	39000	2.44E-22	15.24	0.027	-0.00004	3.10

**Table 3.5.** Styrene-*ran*-acrylonitrile polymer nanocomposite's (containing 1.0 wt% SWNT) Gibbs free energy of mixing  $\Delta G$ , entropic contribution  $\Delta S$  and Chi interaction parameter  $\chi$  calculated from Flory-Huggins theory

Polymer	mol % AN	Density (g/cm <sup>3</sup> )	Avg monomer molar mass (g/mol)	MW Polymer (g/mol)	Molar Volume (cm <sup>3</sup> )	Solubility, $\delta$ (J <sup>1/2</sup> /cm <sup>3/2</sup> )	$\Delta G/kT$ (J/mol)	$\Delta S/kT$ (J/mol)	Chi
PS	0.00	1.05	104.15	43000	1.65E-22	15.96	0.015	-0.00003	1.70
SAN30	0.30	1.09	89.08	83000	1.36E-22	16.51	0.010	-0.00002	1.18
SAN37	0.37	1.10	85.35	79000	1.29E-22	16.65	0.009	-0.00002	1.07
SAN45	0.45	1.11	81.16	55000	1.22E-22	16.80	0.008	-0.00002	0.95
SAN49	0.49	1.11	79.22	67000	1.18E-22	16.87	0.008	-0.00002	0.90
SAN56	0.56	1.12	75.44	55000	1.12E-22	16.92	0.007	-0.00002	0.84
PAN	1.00	1.18	53.06	39000	7.47E-23	17.83	0.003	-0.00002	0.39

**Table 3.6.** Styrene-*ran*-cyanostyrene polymer nanocomposite's (containing 1.0 wt% SWNT) Gibbs free energy of mixing  $\Delta G$ , entropic contribution  $\Delta S$  and Chi interaction parameter  $\chi$  calculated from Flory-Huggins theory

Polymer	mol % CNST	Density (g/cm <sup>3</sup> )	Avg monomer molar mass (g/mol)	MW Polymer (g/mol)	Molar Volume (cm <sup>3</sup> )	Solubility, $\delta$ (J <sup>1/2</sup> /cm <sup>3/2</sup> )	$\Delta G/kT$ (J/mol)	$\Delta S/kT$ (J/mol)	Chi
PS	0.00	1.05	104.15	43000	1.65E-22	15.96	0.015	-0.00003	1.70
CNSt13	0.13	1.06	107.30	46000	1.68E-22	16.32	0.014	-0.00003	1.55
CNSt24	0.24	1.07	110.05	58000	1.71E-22	16.63	0.013	-0.00003	1.43
CNSt30	0.30	1.07	111.60	55000	1.73E-22	16.80	0.012	-0.00003	1.36
CNSt40	0.40	1.08	114.20	72000	1.76E-22	17.09	0.011	-0.00002	1.24
CNSt51	0.51	1.09	116.78	60000	1.79E-22	17.38	0.010	-0.00003	1.13
PCNSt	1.00	1.12	129.16	59000	1.91E-22	18.78	0.006	-0.00003	0.64

parameters order as  $\chi_{\text{DMAEMA}} > \chi_{\text{SAN}} \approx \chi_{\text{CNSt}}$ , which indicates preferential enthalpic interaction between styrene-*ran*-acrylonitrile or styrene-*ran*-cyanostyrene and the SWNTs relative to MMA-*ran*-DMAEMA with SWNTs, corroborating the aforementioned Raman spectroscopy data. However, the  $\chi$  parameters within each copolymer series vary monotonically with copolymer composition, and do not correlate with our experimental evidence that indicates that the existence of a minority of interacting functional group within a polymer chain leads to an optimum interfacial adhesion. For example, within SAN composites, (Table 3.5) the  $\chi$  parameter decreases as the nitrile content in the copolymer increases, suggesting that interfacial adhesion between the polymer matrix and SWNT increases. However, our Raman spectroscopy results shows that the extent of charge transfer interaction between the matrix and nanoparticle is the highest for PAN, followed by SAN45, SAN37, SAN49, SAN30, SAN56 and PS, which clearly does not correlate with this computational result.

The discrepancy between our experimental results and the calculation presented above, which indicates that the extent of EDA interaction will vary monotonically with the composition of interacting functional groups along the polymer chain, implies that the extent of intermolecular interaction is modified by a parameter that is not included in the calculation of free energy of mixing from Flory-Huggins theory. In fact, this effect has previously been investigated by Coleman and Painter in the prediction of the phase behavior of hydrogen bonded polymer blends.<sup>97,98</sup> In these studies, the experimentally determined fraction of hydrogen-bonded carbonyl groups,  $f_{HB}^{C=O}$ , from infrared spectroscopy can be used to determine  $K_A^{\text{Std}}$ , which quantifies the extent of intermolecular hydrogen bonding. The authors found that the extent of hydrogen bonding



in blends of polyvinyl phenol (PVPh) and phenol-*stat*-ethyl methacrylate (PEMA) is far less than their low molecular weight analogues. The observance of a higher extent of hydrogen bonding in the lower molecular weight analogue led the authors to conclude that due to polymer chain connectivity, the polymer chains in a blend, PVPh/PEMA mixture, has more steric restrictions on its backbone bond rotations, thereby limiting their ability to orient themselves appropriately for efficient hydrogen bonding formation. Therefore, the hydrogen-bonding functional groups need to be ‘spaced’ with non-hydrogen-bonding functional groups in order to efficiently enable the interacting moiety to orient themselves appropriately to form a hydrogen bond with another functional group.

To account for this entropic factor, the authors proposed to add a term of  $\Delta G_H/RT$  to the classic Flory-Huggins equation to account for the free energy of hydrogen bonding formation:

$$\frac{\Delta G_m}{RT} = \left( \frac{\Phi_A}{M_A} \ln \Phi_A + \frac{\Phi_B}{M_B} \ln \Phi_B \right) + \Phi_A \Phi_B \chi + \frac{\Delta G_H}{RT} \quad (\text{Equation 3.6})$$

where  $\Phi_A$ ,  $\Phi_B$ , and  $M_A$ ,  $M_B$  are the volume fractions and degrees of polymerization of components A and B, respectively. The first two terms are the combinatorial entropy whereas the third term represents the contribution from ‘physical’ or nonspecific forces and contains the classic Flory parameter  $\chi$ . The final term is the contribution from ‘chemical’ forces representing the ordering of hydrogen bond formation in the mixture relative to the pure state of the two components. The ‘physical’ force can be calculated from solubility parameters (Equation 3.5) and  $\Delta G_H$  may be determined by  $K_A^{\text{Std}}$  from the infrared analysis. By taking this entropic effect into consideration, they have successfully

predicted the miscibility maps of the overall phase behavior for blends of two copolymers in which the copolymer composition is systematically varied in both.<sup>156</sup> In addition, a separate experiment by Rasheed et al. has also shown that a moderate amount of vinyl phenol content along a polymer chain allows the most optimum hydrogen bonding formation with a carboxyl-functionalized SWNT.<sup>51,52,157</sup> Therefore, these previous studies further validate our claim that polymer chain connectivity is an additional and crucial entropic parameter, not taken into consideration in the classic Flory-Huggins theory, that governs the extent of intermolecular electron-donor-acceptor (EDA) complex formation between a polymer matrix and SWNT.

### **3.4 Conclusion**

Experimental and theoretical studies indicate that polymer chain connectivity governs the susceptibility of individual functional groups on a polymer chain to form electron donor-acceptor interactions with the SWNT and that the extent of this interaction can be systematically controlled by varying copolymer composition. The formation of the interaction is optimal when a minority of interacting functional groups is present in a copolymer matrix, as supported by Raman spectroscopy D\* band shift. Among the DMAEMA series, the smallest positive D\* band shift was obtained for the DMA30 nanocomposite, suggesting that the least compressive forces are exerted by the DMA30 polymer matrix onto the SWNT. In contrast, negative D\* band shifts indicate a level of debundling of the carbon nanotubes for SAN and St-CNSSt systems, with SAN45, PAN and CNSSt23 being the most efficient at relieving the internal pressure induced upon the carbon nanotubes. Good interfacial adhesion between PAN and SWNT also indicates that the effect of spacing along the polymer chain on the extent of intermolecular interaction

is less significant if the polymer chain is flexible. Binding energies of the interacting monomers with SWNT obtained from density functional theory calculations corroborates our experimental data, by demonstrating that cyanostyrene forms the strongest intermolecular interaction with the SWNT, followed by acrylonitrile and DMAEMA. In addition, the fully optimized structure of a cyanostyrene trimer interacting with a SWNT provides direct evidence that only a fraction of these interacting moieties along a polymer chain form an electron-donor-acceptor complex with the SWNT due to chain connectivity. Calculations of  $\chi$  interaction parameter from Flory-Huggins theory is also consistent with this interpretation. These results suggest that spacing the interacting functional groups along a polymer chain improves the efficiency of electron-donor-acceptor complex formation with the carbon nanotubes. The present study therefore proposes a pathway by which desired material properties can be achieved by reproducibly controlling the extent of intermolecular interaction and dispersion in polymer nanocomposites.

## CHAPTER 4: OPTIMIZATION OF NANOPARTICLE DISPERSION USING NON-COVALENT CHARGE TRANSFER INTERACTION

### 4.1 Introduction

Raman spectroscopy results ( $D^*$  Band shifts), density functional theory (DFT) calculation and calculation of the chi interaction parameter,  $\chi$  from Flory Huggins Theory presented in Chapter 3 provide evidence of the impact of altering the copolymer composition on the extent of intermolecular electron donor-acceptor complex formation between a polymer matrix and SWNT. Through this work, it was found that chain connectivity is a crucial parameter that governs the extent of interfacial adhesion between the SWNT nanoparticle and polymer matrix. However, one underlying question that still pervades and becomes the central theme of this chapter is: Does an optimum charge transfer interaction translate to improved SWNT nanoparticle spatial dispersion?

In our group's previous work, a systematic study investigating the extent of miscibility between a liquid crystalline polyurethane and an amorphous polymer, poly(styrene-*ran*-vinylphenol) blend was performed.<sup>158</sup> By varying the composition of vinyl phenol in the copolymer, the extent of intermolecular interaction, i.e. hydrogen bonding between the two polymers can be finely tuned to develop materials with improved dispersion. The concept of optimizing the intermolecular hydrogen bonding between two polymers has proven effective in increasing the miscibility window of this system. Would the same concept be applicable to the current study of polymer nanocomposites? In other words, can the extent of interaction and dispersion of single-walled nanotubes be systematically controlled by tuning the extent of electron-donor acceptor interaction through varying the copolymer composition in the copolymer

system? Section 4.3A describes a qualitative initial assessment of this study through visualization of thick film composites. To gain insight into the dispersion level of these polymer nanocomposites quantitatively, optical microscopy and Raman spectroscopy was utilized, as addressed in Section 4.3.B and 4.3.C respectively.

## **4.2 Materials**

The polymers used in this study are listed in Tables 3.1, 3.2 and 3.3 (Chapter 3). The MMA-*ran*-DMAEMA and styrene-*ran*-cyanostyrene copolymers were synthesized as outlined in Section 2.3.A.I and Section 2.3.B.1 respectively. All the polymer nanocomposite samples for optical microscopy and Raman spectroscopy were prepared as described in Section 2.5.A whereas the thick film composites were made as outlined in Section 2.5.B. Aggregate analysis was performed using SIMAGIS 3.0 Research software according to the procedure outlined in Section 2.6.B.

## **4.3 Results and Discussion**

### **A. Dispersion Quality Determination by Thick Film Composite Visualization**

As a first assessment in this study, thick films of 0.1 wt% SWNT nanocomposites containing polymers with varying copolymer composition were made to qualitatively visualize the range of dispersions obtained. As can be seen in Figure 4.1, a variation of dispersion quality can be readily observed, as in the thick film composites of PMMA, PDMAEMA and DMA30 nanocomposites. It is clearly evident that the DMA30 nanocomposite attains optical homogeneity and transparency throughout the entire film, indicative of good dispersion and interfacial adhesion between DMA30 copolymer and

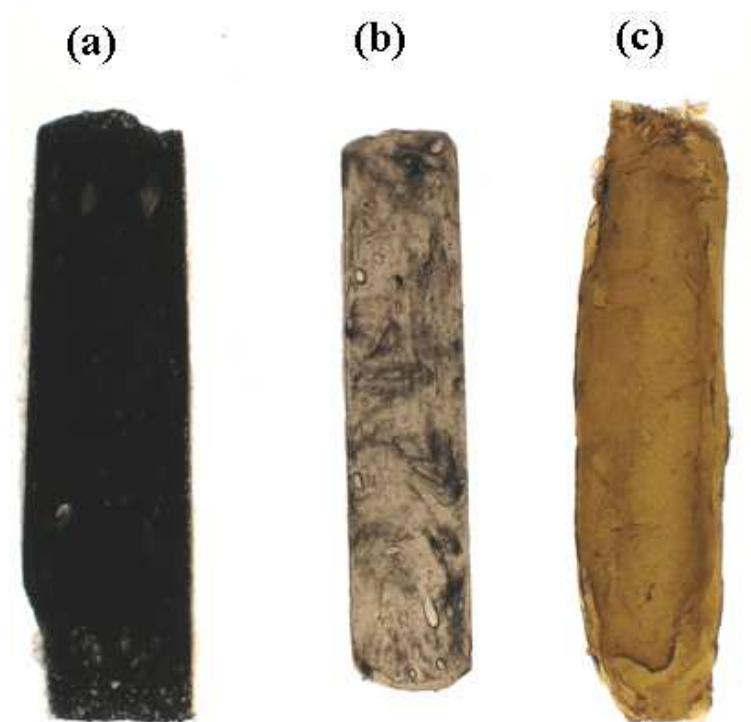


**Figure 4.1.** Photographs of (a) PMMA, (b) PDMAEMA and (c) DMA30 thick film composites with 0.1 wt % content of SWNT

SWNT. Although some variation in the DMA30 composite film exists, this is primarily due to the difference in the local thickness of the film. On the other hand, the PMMA nanocomposite appears dark and opaque indicating poor dispersion, attributed to the minimal interaction realized between the ester moieties on PMMA chains and SWNTs. Even though PDMAEMA has an abundance of tertiary amino interacting moieties compared to DMA30, the dispersion of SWNT in PDMAEMA nanocomposite is far more heterogeneous than the composite containing 30 mol% DMAEMA, implying that controlling the amount of non-covalent interaction between a copolymer and an anisotropic filler through the variation of copolymer composition provides a mechanism to improve SWNT dispersion.

In order to assess the effect of an electron withdrawing acrylonitrile (AN) on the formation of electron donor acceptor interactions and its correlation to the dispersion of SWNT in a polymer matrix, the same evaluation was performed on the thick film composites of *St-ran-AN*. Photographs of PS, PAN and SAN45 thick film composites with 0.1 wt% SWNT are shown in Figure 4.2. Qualitatively, it is evident that PS composite lacks homogeneity, indicated by the marble-like feature throughout the sample. The fact that poor dispersion is visually apparent for the PS composite indicates that the non-covalent  $\pi$ - $\pi$  interactions between polystyrene and SWNT<sup>43</sup> are insufficient to overcome the strong interparticle forces that exist between the nanotubes. When the electron withdrawing acrylonitrile moiety is incorporated into the polymer matrix however, a dramatic enhancement of the nanocomposites dispersion is observed, as shown in Figure 4.2.

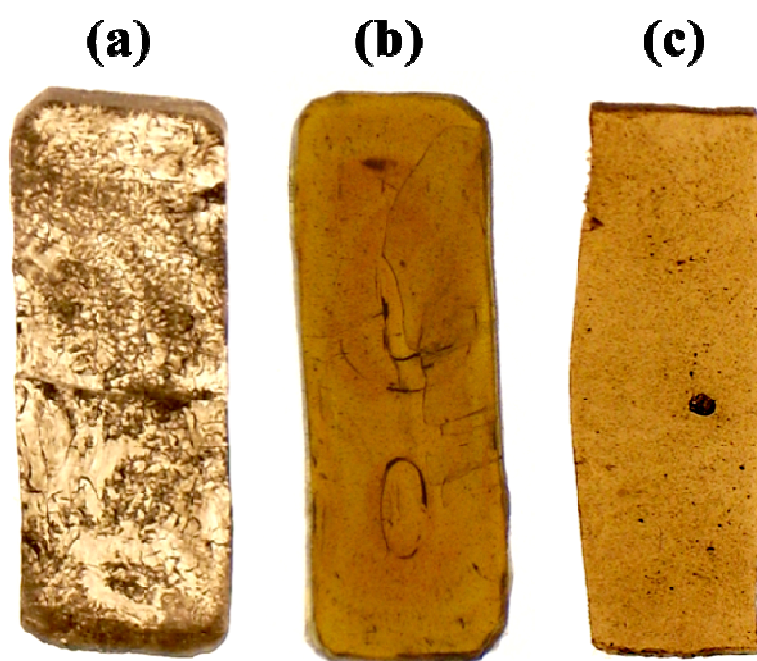


**Figure 4.2.** Photographs of (a) PS, (b) PAN and (c) SAN45 thick film composites with 0.1 wt% SWNT



A similar evaluation was performed on composites of *St-ran*-CNSt copolymers to investigate more fully the ability to tune the non-covalent interaction and its impact on dispersion by modifying the chemical structure of the functional monomer. The cyanostyrene monomer has a nitrile functional group in the para position of the phenyl ring, which should allow the distribution of electrons across a larger area, providing a stronger interaction. Thick film composites of PS and CNSt 23 with 0.1% SWNT depicted in Figure 4.3 shows that the *St-ran*-CNSt copolymers are excellent matrices for SWNT dispersion. This is presumably due to the existence of aromatic rings on both St and CNSt monomeric moieties allowing  $\pi$ - $\pi$  interactions with SWNTs as well as the formation of EDA interactions between the nitrile group and SWNT. Even though these thick film composites give qualitative visualization of the level of dispersion, quantitative analysis is needed to provide additional insight into the effect of copolymer composition on the extent of dispersion for all three systems studied.

## **B. Optical Microscopy and Aggregate Size Analysis**

The combination of optical microscopy and image analysis provides a tool by which material homogeneity can be quantified on the micron level. This approach provides insight into how the spatial dispersion of the SWNT in the polymer matrix changes with the variation of copolymer composition.<sup>52</sup> Therefore, optical microscopy was used to examine the SWNT dispersion in DMA10, DMA30, PMMA and PDMAEMA nanocomposites with 1.0 wt% SWNT loading, as shown in Figure 4.4, where these images show numerous large agglomerates on the nanocomposite film. It is worth noting that these images are representative of all the images acquired for each sample. The transparent areas on the film correspond to that of the neat polymer matrix,

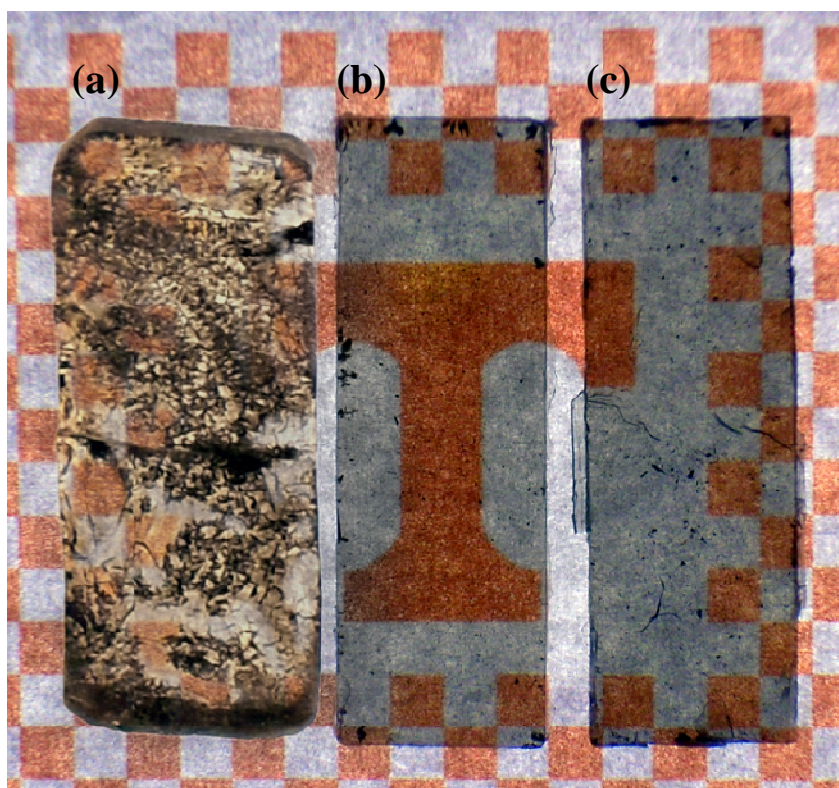


**Figure 4.3.** Photograph of SWNT nanocomposites with (a) polystyrene (b) CNST23.6 and (c) PCNSt as the matrix containing 0.1wt% SWNT

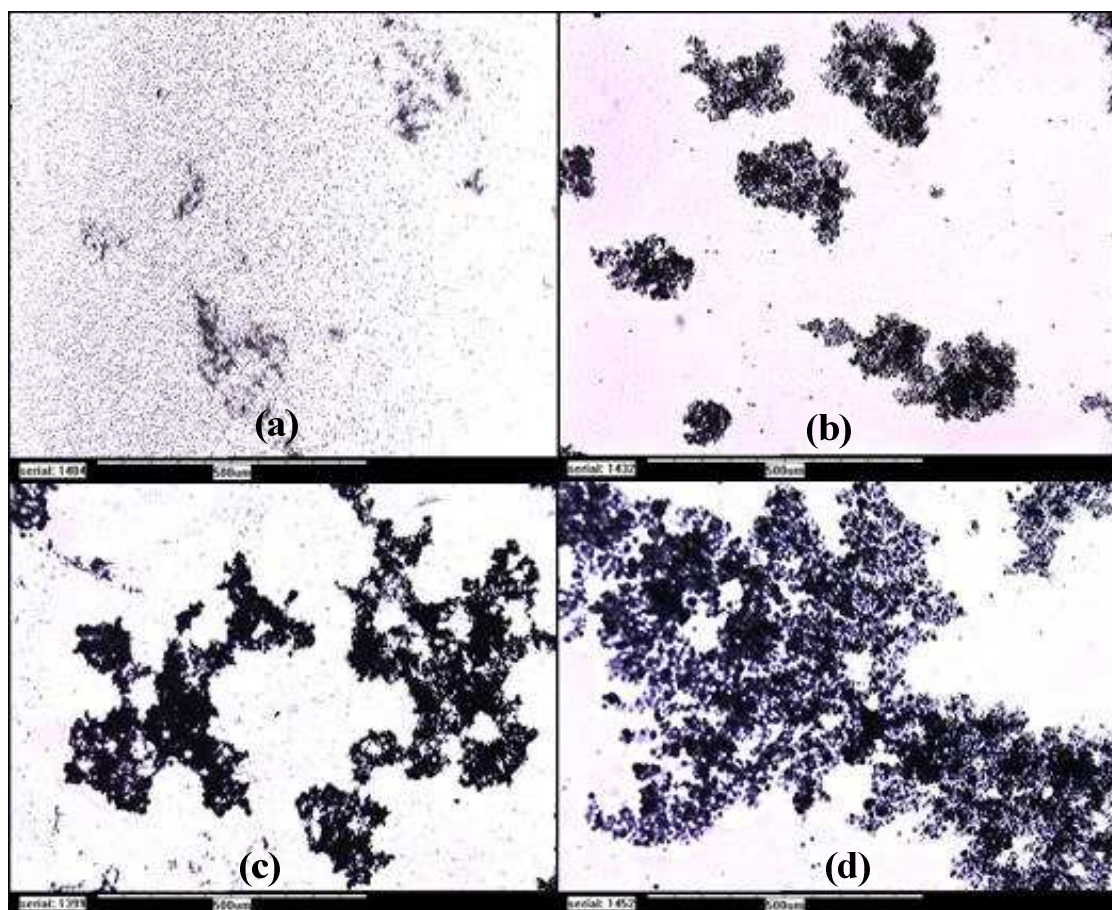


**Figure 4.4.** Optical micrographs of (a) DMA30 (b) DMA10 (c) PMMA and (d) PDMAEMA nanocomposites with 1.0 wt% SWNT loading at 10x magnification. Scale bar scale shown is 500  $\mu\text{m}$

as verified by Raman spectroscopy, discussed below. Qualitatively, one can visually observe that the PMMA and PDMAEMA homopolymer composites have significantly larger aggregates than the DMA10 and DMA30 composites. To quantify this data and the spatial distribution of aggregates on the films, the average diameter and area of aggregates are determined and are plotted in Figure 4.5 and Figure 4.6 as a function of mol % DMAEMA in the copolymer. The average area of aggregates for the PMMA nanocomposite is  $\sim 461 \mu\text{m}^2$ . The corresponding value for the diameter of agglomerates in the PMMA composite is  $6.0 \mu\text{m}$ , providing additional information on the quantitative uniformity of SWNT bundles within the nanocomposite. The aggregate area decreases to  $357 \mu\text{m}^2$  (diameter  $\sim 5.5 \mu\text{m}$ ) as the composition of DMAEMA increases to 10%. As the composition of DMAEMA increases further, there is a significant increase in the level of dispersion, as demonstrated by the decrease of area and diameter of aggregates for the DMA10, DMA20 and DMA30 nanocomposites. Among this series, the DMA30 composite has the smallest bundle size, where the aggregate area ( $37 \mu\text{m}^2$ ) decreases by a factor of  $\sim 10$  and the aggregate size ( $3.2 \mu\text{m}$ ) decreases by a factor of  $\sim 2$  relative to the neat homopolymer composites. However, as the composition of DMAEMA increases even further, the agglomerate size increases, as shown by the DMA50 nanocomposite with aggregate area of  $\sim 267 \mu\text{m}^2$  and diameter of  $\sim 5.1 \mu\text{m}$ . The extent of dispersion is even poorer for the PDMAEMA nanocomposite. This clearly demonstrates that the presence of more interacting moieties on the polymer chain does not correspond to improved dispersion in the polymer nanocomposite.

Optical microscopy was also used to visualize the local structure of the 1.0 wt%

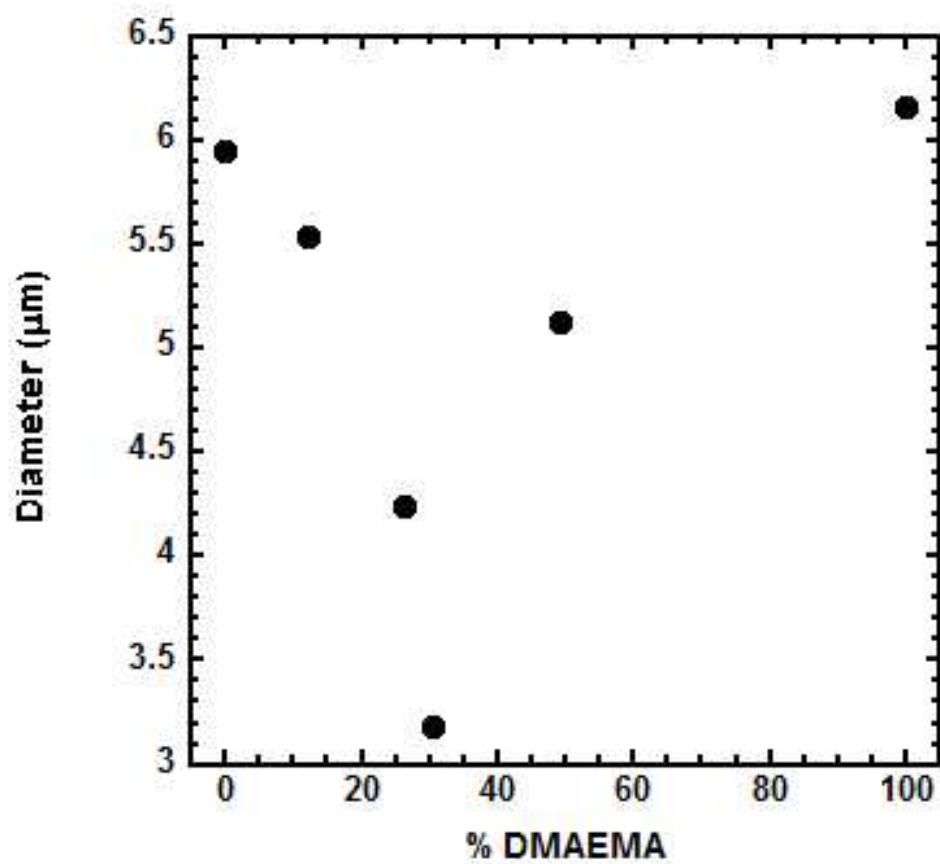


**Figure 4.5.** Diameter of aggregates in 1% SWNT nanocomposites as a function of mol% DMAEMA in copolymer

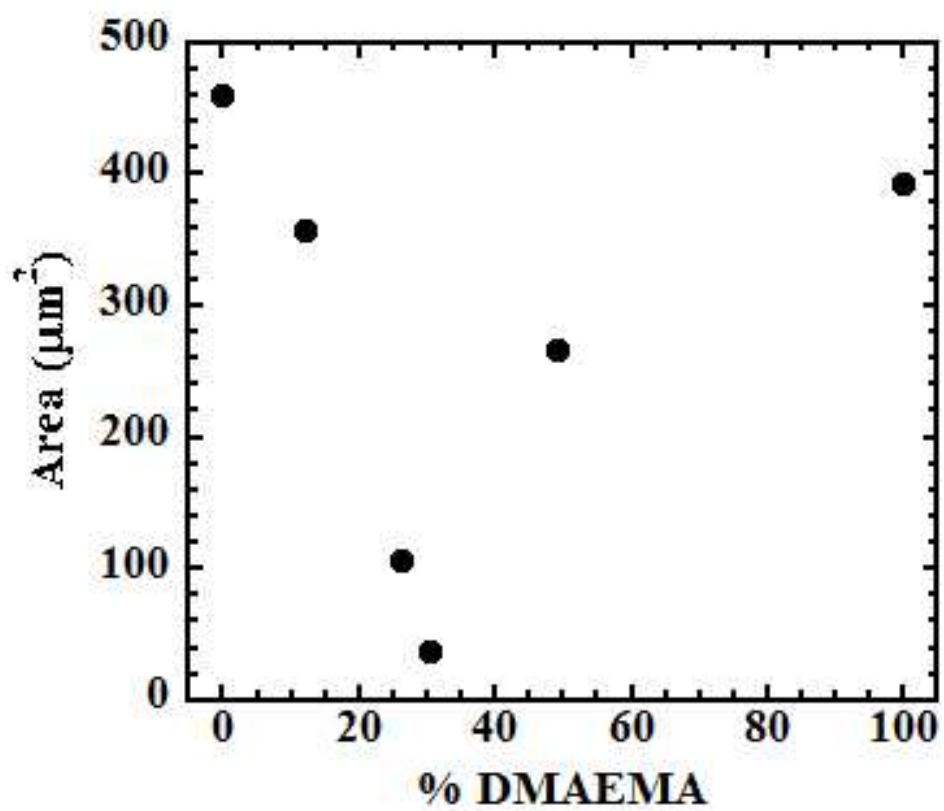


**Figure 4.6.** Area of aggregates in 1% SWNT nanocomposites as a function of mol% DMAEMA in copolymer

SWNT composites of all SAN and PAN polymers. From the optical micrographs in Figure 4.7, only minimal nanotube aggregates are observed, demonstrating that the SAN composites are well dispersed. The extent of dispersion is confirmed by Raman spectroscopy, where, Raman imaging scans were taken with a step size of 1  $\mu\text{m}$  and every spectrum shows clear SWNT signatures, indicating that tubes exist throughout the samples, even in optically clear regions. This is clearly exemplified in Figure 4.8, which shows that the integrated area under the G-band is relatively consistent along the horizontal line of the PAN composite, indicating homogeneously dispersed SWNT. In contrast, the PS composite shows broad variation in the integrated area under the G-band (Figure 4.9), consistent with poor nanoparticle dispersion. Note that the thick black horizontal streaks in the micrographs in Figures 4.8 and 4.9 are flaws originating from the microscope.

Similar to the SAN composites, the CNSt composites were also so well dispersed (Figure 4.10) that the resolution of the optical microscopy was not able to differentiate the level of dispersion of the nanocomposites of the different copolymers. In fact, optical microscopy does not show any SWNT aggregates, as Raman spectroscopy indicates that the dark spots in Figure 4.10 are defects, not SWNT aggregates. This observation indicates that the CNSt samples are more homogeneously mixed than either the DMA or SAN nanocomposites. Figure 4.11, which shows a color-coded map of the integrated area under the G-band for the CNSt24 micrograph exemplifies the homogeneity that is observed for the CNSt samples.

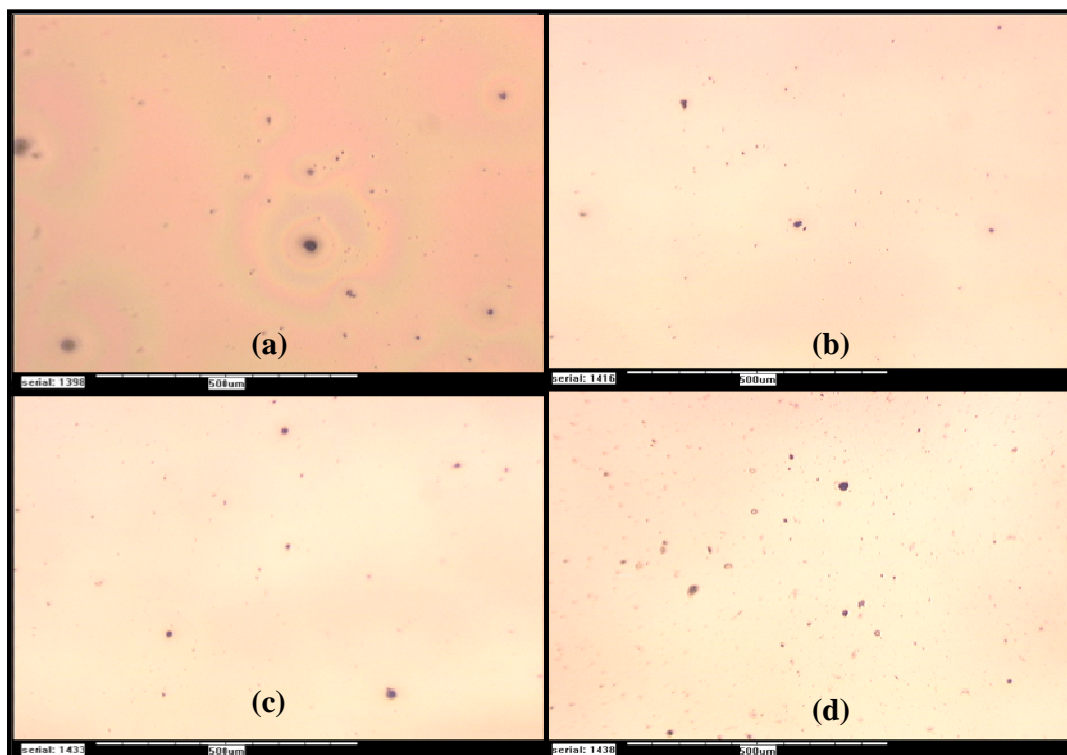


**Figure 4.7.** Optical micrographs of (a) SAN29.5 (b) SAN 45 (c) SAN 56.2 (d) PAN nanocomposites. Scale bar is 500  $\mu\text{m}$



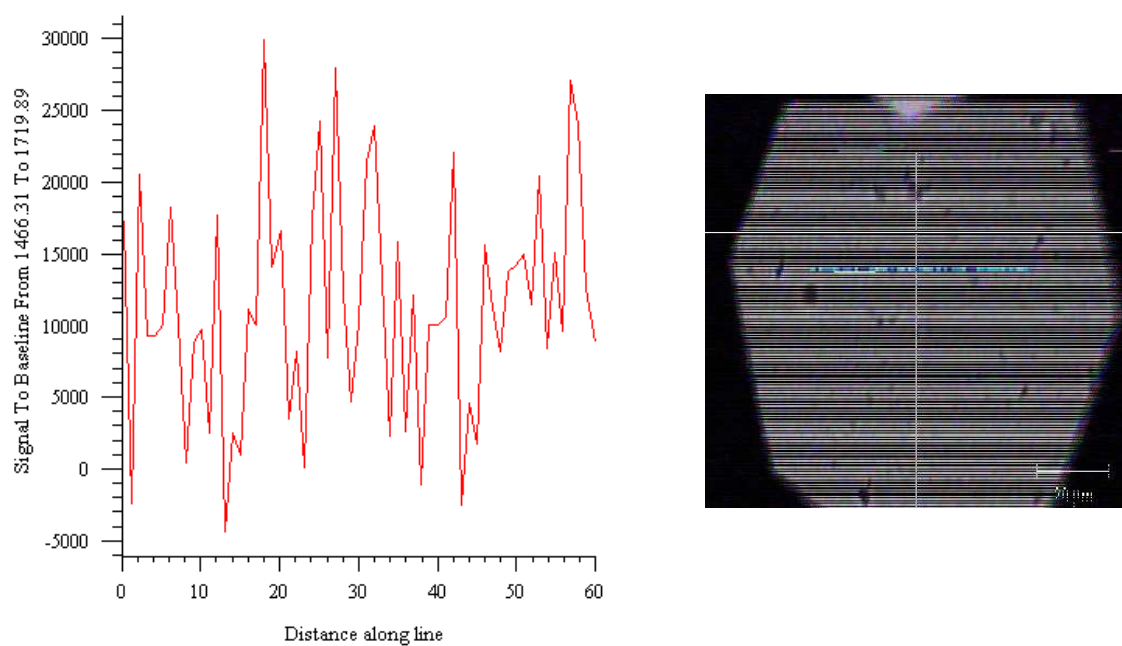


**Figure 4.8.** The integrated area under the G-band (left) along the horizontal line shown on the right for PAN nanocomposite

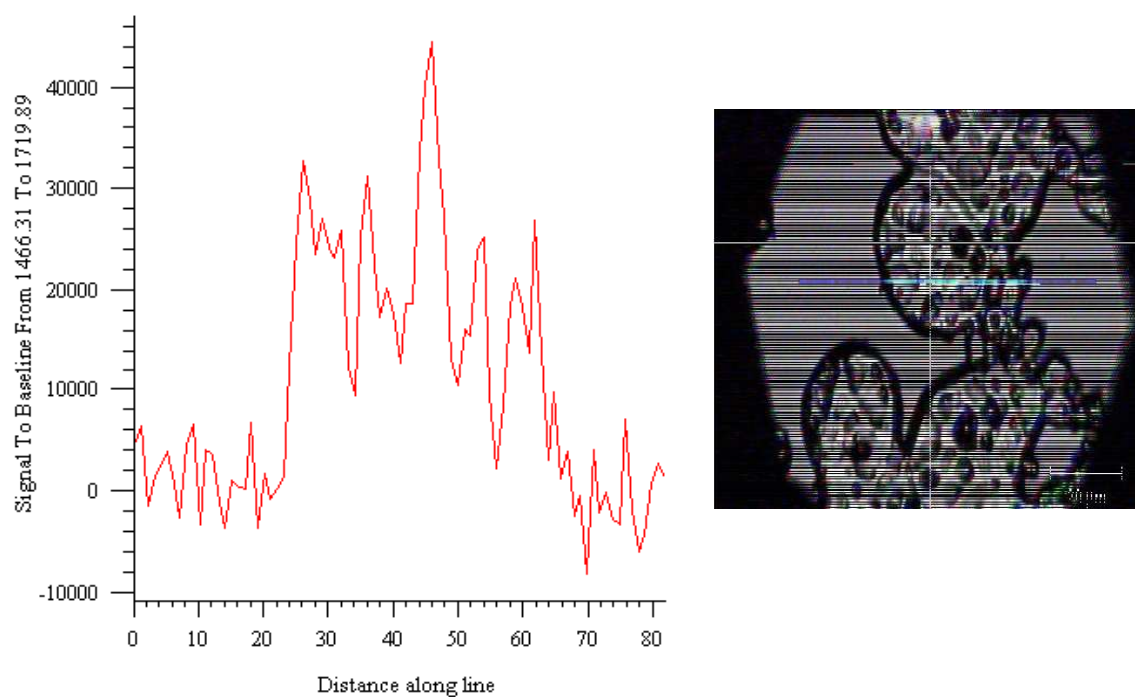


**Figure 4.9.** The integrated area under the G-band (left) along the horizontal line shown on the right for PS nanocomposite

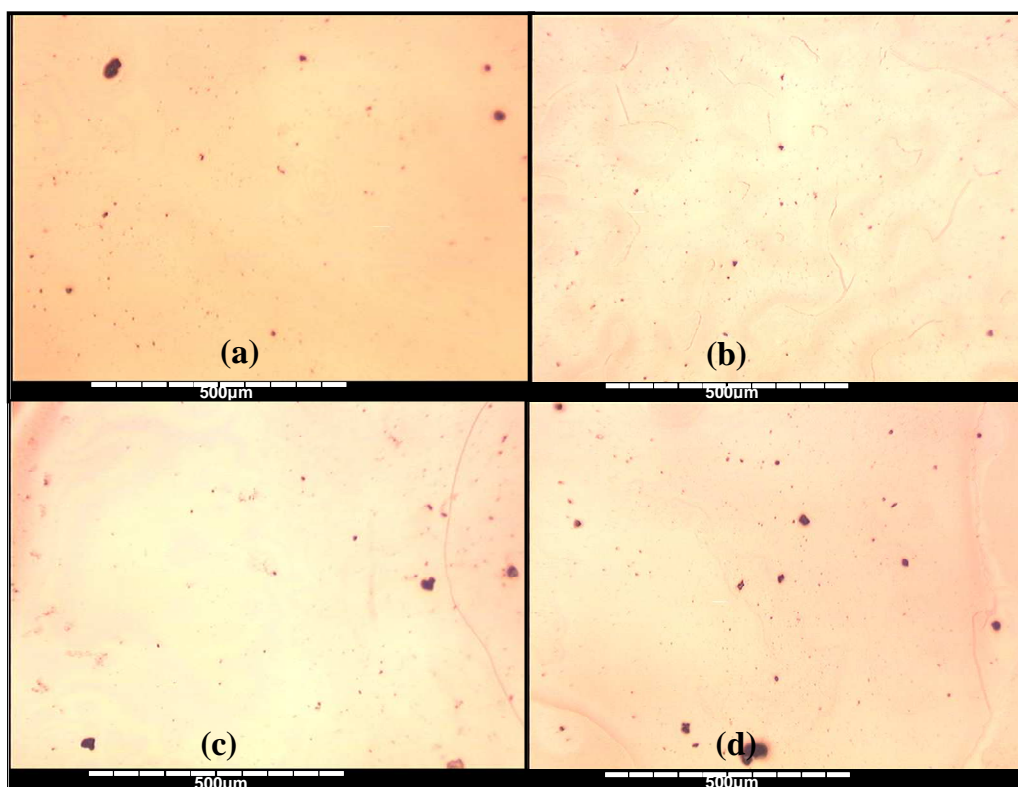


**Figure 4.10.** Optical Micrographs of (a) CNSt 12.6 (b) CNSt 23.6 (c) CNSt 40.2 and (d) CNSt 50.0

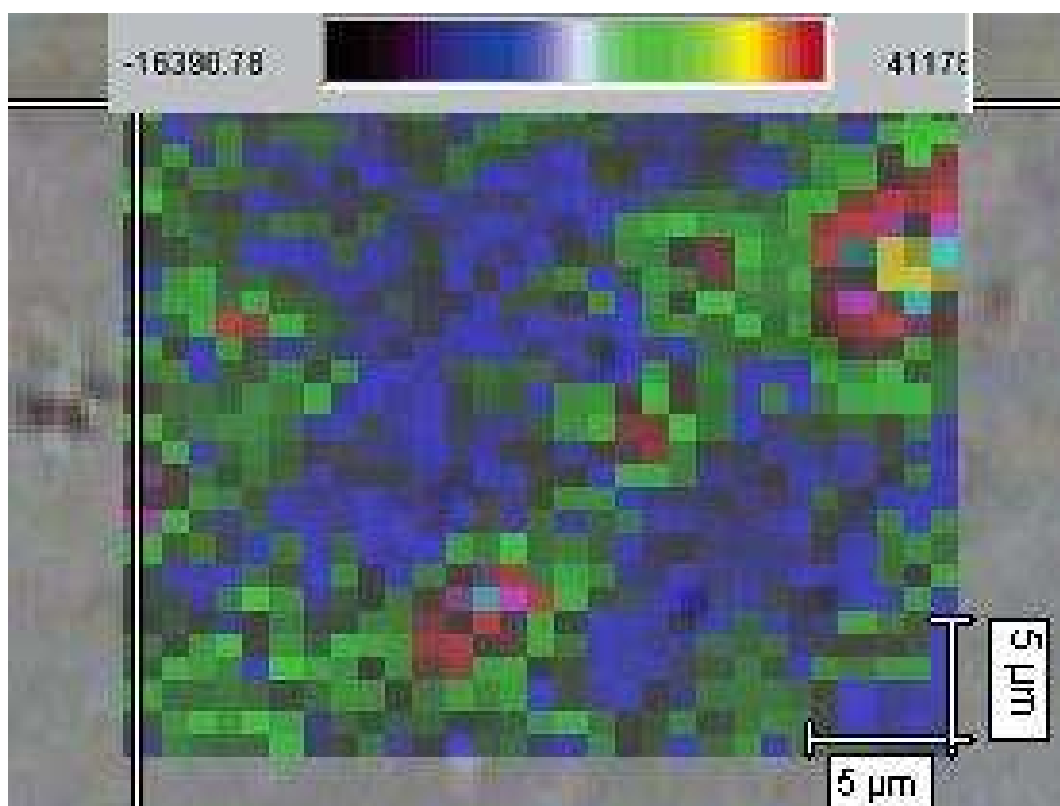


**Figure 4.11.** Color-coded map of the integrated area under the G-band for CNSt24 micrograph. The dark area corresponds to low SWNT content whereas the red area corresponds to the highest SWNT content

### C. Nanotube Dispersion using Raman Spectroscopy

In addition to optical microscopy, Raman mapping is an effective technique to quantify the level of dispersion among the copolymers at smaller length scales ( $\sim 2 \mu\text{m}$ ). As shown earlier, an optical microscopy image of the DMA SWNT nanocomposites shows areas where nanotube aggregates exist surrounded by areas that are optically clear. However, the resolution of the optical microscope does not indicate whether SWNTs exist in the optically clear region, and if they do, if they are individual tubes or small aggregates. Raman mapping can be used to quantify the distribution of the SWNT in the matrix, down to a resolution of  $\sim 2 \mu\text{m}$ . To explain this procedure, Figure 4.12 shows an optical micrograph and the typical Raman spectra near the G band of an area of the micrograph that clearly contains an aggregate and an area of the micrograph that is optically clear. The aggregated region undoubtedly consists of SWNT, and therefore there exists a strong G band peak at  $1500\text{-}1620 \text{ cm}^{-1}$ . In the optically clear region, however, the presence of the G band peak is indicative of SWNT that reside in the region that are not visible optically. Therefore, the variation of the G band intensities spatially throughout a nanocomposite sample provides a method to quantify the dispersion of nanotubes in the sample. To provide a quantification of this dispersion, the G band intensity of optically clear ( $I_{clear}^G$ ) sections of the sample is measured over  $\sim 50$  spots, as is the G band intensity of 50 spots within the aggregated ( $I_{agg}^G$ ) regions. The ratio of  $I_{clear}^G$  to  $I_{agg}^G$  is then determined to quantify the dispersion quality for every nanocomposite sample. In this analysis, nanotubes that are homogeneously dispersed in the polymer matrix will result in the ratio of  $I_{clear}^G / I_{agg}^G$  approaching 1, whereas poorly dispersed

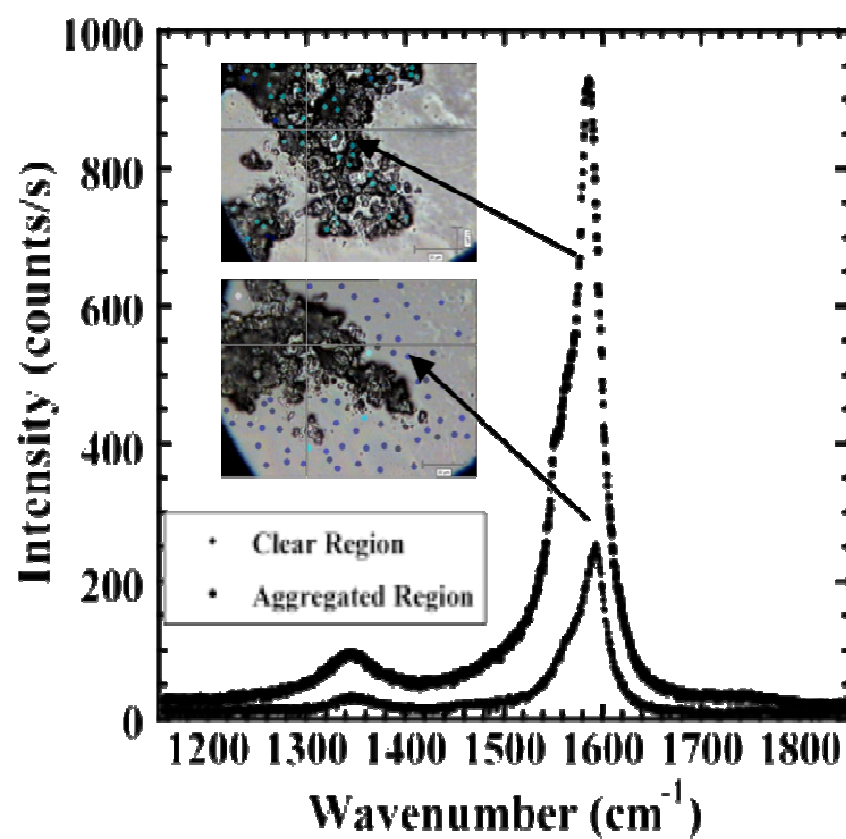


**Figure 4.12.** Variation of G band intensities for the corresponding clear (diamond symbol) and aggregated (circle symbol) regions of optical micrograph taken at 50x magnifications

SWNTs will exhibit an  $I_{clear}^G / I_{agg}^G$  that will approach 0. Thickness variation in these samples have been determined by ellipsometry and atomic force microscopy (% variation <15%) as well as by normalization of the  $I_G$  by the intensity of the D Band ( $I_D$ ), all of which verify that the quantification and interpretation of the reported results are not impacted by any thickness variation within the samples.

For consistency, each Raman spectra is baseline-corrected, smoothed by a 2-point adjacent-average method, fitted to two Lorentzian functions, and the G band intensity at  $x_{center}$  of the second Lorentzian curve ( $\omega_{G^+}$  band) is averaged for about 50 regions of the micrograph. The use of  $\omega_{G^+}$  for this analysis is most practical since this peak can be easily fitted with a Lorentzian line shape, unlike the broadened  $\omega_{G^-}$  feature, which is usually fitted using a Breit-Wigner-Fano lineshape.<sup>159</sup>

Figure 4.13 is a plot of  $I_{clear}^G / I_{agg}^G$  as a function of mol% DMAEMA in the DMAEMA nanocomposites. Carbon nanotubes and PMMA homopolymer is very immiscible, affirmed by a ratio of  $I_{clear}^G / I_{agg}^G \sim 0.09$ . As the percentage of interacting moiety DMAEMA increases to 10 mol%, the ratio increases to 0.14, indicating better dispersion between the polymer matrix and SWNT. At 30 mol% DMAEMA, the ratio of  $I_{clear}^G / I_{agg}^G$  increases to an optimal value of 0.31. However, this trend does not continue beyond DMA30 composite, where the 50 mol% DMAEMA and PDMAEMA composites show  $I_{clear}^G / I_{agg}^G$  that decrease to 0.13 and 0.15 respectively, indicating poor dispersion.

The trend observed in this Raman mapping analysis correlates very well with both optical microscopy (Section 4.3B) and Raman D\* band shift results (Chapter 3) and can be explained at the molecular level by the impact of chain connectivity on the formation

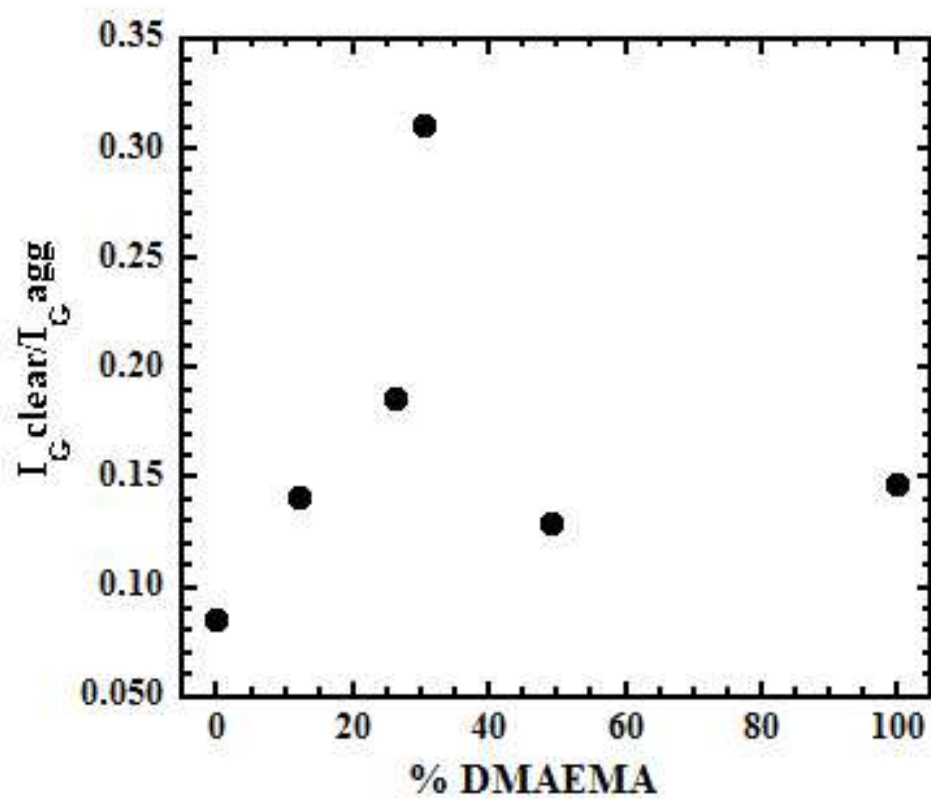


**Figure 4.13.** Ratio of the Intensity of G band in the clear region to that in the aggregated region, which is a measure of the dispersion of the SWNT in the nanocomposite as a function of % DMAEMA in matrix copolymer



of attractive electron donor-acceptor interactions between the polymer chain and the SWNT.<sup>158</sup> When an electron-donating tertiary amino group of DMAEMA on a polymer chain is in close proximity to the carbon cage of SWNT, an EDA complex can be formed. As more DMAEMA moieties are added randomly onto the polymer chain, an increase in interfacial cohesion can occur as a result of the formation of more intermolecular interactions between the polymer matrix and SWNT, leading to improved SWNT dispersion. However, once an optimal amount of DMAEMA groups has been incorporated into the copolymer matrix, our results show that further increasing the DMAEMA concentration results in a decrease of the degree of interfacial adhesion and dispersion of SWNT in a polymer matrix dramatically. The fundamental reason for this is that the mobility of a given  $-NR_3$  group on the MMA-*ran*-DMAEMA chain is influenced by its proximity to other  $-NR_3$  functional groups. More specifically, an  $-NR_3$  group that is participating in an EDA interaction will inhibit the mobility of neighboring  $-NR_3$  groups and limit its ability to access and orient itself correctly at the carbon nanotube sidewalls to optimally form an additional non-covalent interaction. This effect is mitigated if the  $-NR_3$  functional groups are adequately spaced out along the polymer chain, so that they are dynamically independent and the formation of one EDA interaction does not inhibit the formation of an additional interaction with the SWNT. Therefore, these results exemplify the importance of chain connectivity on the optimization of this EDA interaction.

The exact mechanism by which the inclusion of EDA interactions improves the SWNT dispersion in these polymer matrices remains an open question. Numerous investigations have been conducted to determine the importance of controlling interfacial

tension as a method to improve the dispersion in multi-component polymer systems, but have been mainly dedicated to polymer blend systems.<sup>160-162</sup> The applicability of this concept to polymer nanocomposites is much less well understood. However, based on our interpretation of our results, a reduction of interfacial tension could be the reason for the observed increase in dispersion. This would be true if the interfacial adhesion/binding between an interacting functional group (i.e. (2-(dimethyl aminoethyl) methacrylate, acrylonitrile and cyanostyrene) and SWNT leads to a polymer chain conforming itself to the nanotube sidewalls to increase enthalpic interactions, creating more SWNT-polymer interactions, thereby reducing interfacial tension.

However, without further investigation, this interpretation cannot be verified, as in polymer blends it has been shown that the presence of a copolymer at the polymer/polymer interface does not reduce the droplet size by reducing the interfacial tension, which would promote smaller droplets, since the size is unaffected when the volume fraction of the minority component is low. Rather, the copolymer is known to sterically stabilize droplets and inhibit droplet coalescence.<sup>163</sup> Additionally, the presence of electron donor-acceptor interaction in our system results in a slight charging of the SWNTs, which induces an electrostatic repulsive interaction between tubes, further aiding in their dispersion. Therefore, whether the dominant mechanism for improvement of dispersion is steric stabilization, lower interfacial tension, or electrostatic repulsion is a detail that will require further study.

Raman mapping was also performed on SAN composites to further quantify the dispersion of these samples. Figure 4.14 is a plot of  $I_{clear}^G / I_{agg}^G$  as a function of %

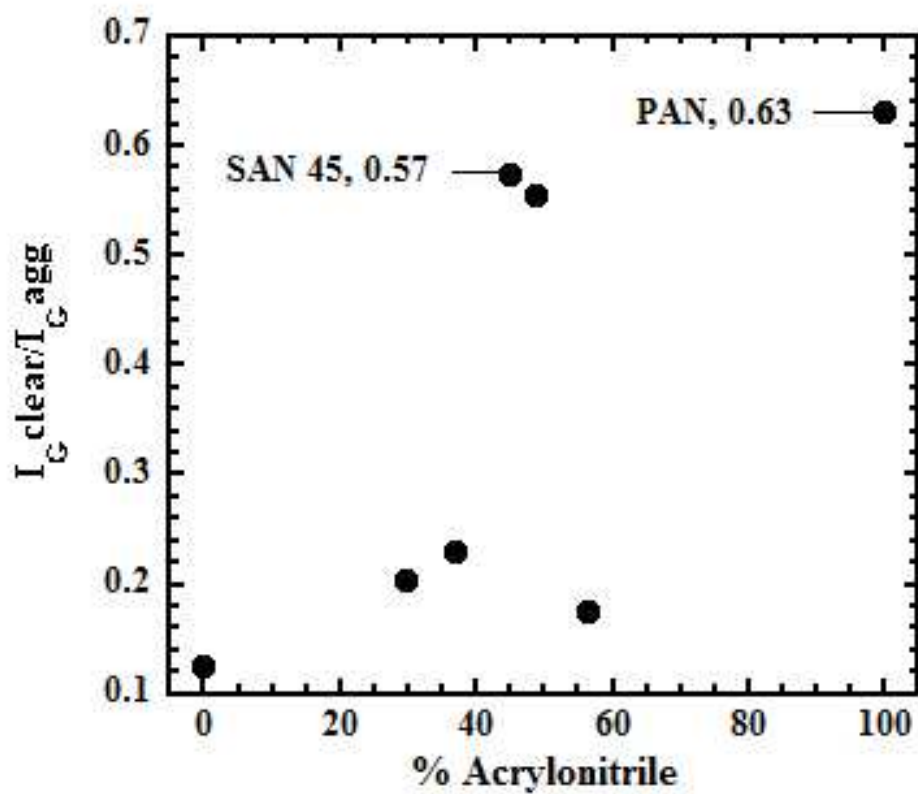


**Figure 4.14.** Ratio of the Intensity of G band in the clear region to that in the aggregated region, which is a measure of the dispersion of the SWNT in the nanocomposite as a function of % AN in matrix copolymer

acrylonitrile in the SAN copolymer. Inspection of this plot shows that the PS composite has a relatively low  $I_{clear}^G / I_{agg}^G \sim 0.13$ , indicating poor SWNT spatial distribution. Upon increasing the AN content in the copolymer to 30 and 37 mol%, the value of  $I_{clear}^G / I_{agg}^G$  increases to  $\sim 0.2$ . As the amount of AN increases to 45 mol%, the magnitude of  $I_{clear}^G / I_{agg}^G$  increases to a maximum of  $\sim 0.6$ , a value that is double that of DMA30, the most well-dispersed MMA-*ran*-DMAEMA nanocomposite. The level of dispersion for SAN 49 decreases slightly, and dropped dramatically for SAN 56. The PAN composite also attains dispersion similar to that of the SAN45 composite. These results correlate well with the analysis of the D\* band of these nanocomposites, which reconfirms our hypothesis that good intermolecular interaction between SWNT and polymer matrix translates to optimum particle dispersion. They also clearly demonstrate that there exists an optimum amount of AN composition whereby polymer-nanotube interaction is optimal and translate to the best dispersion. In other words, merely increasing the amount of interacting moiety in the copolymer does not lead to a linear enhancement of the SWNT dispersion. In addition, this Raman mapping analysis has also demonstrated that electron withdrawing acrylonitrile is more effective than electron donating DMAEMA in the formation of EDA complex with the SWNT, as evidenced by an increase in the dispersion by a factor of  $\sim 2$ .

Because there do not exist visually obvious SWNT aggregates in the CNSt nanocomposites, we were not able to use this Raman mapping technique to quantify their dispersion, however the absence of visually identifiable aggregates itself indicates that the dispersion of SWNT in CNSt is superior to either the DMAEMA or SAN copolymers.

#### **4.4 Conclusion**

The experiments described in this chapter have shown that the level of dispersion is optimal when a minority of non-covalent interacting functional groups is present in a copolymer matrix. More specifically, optical microscopy and Raman mapping quantitatively indicate that DMA30 nanocomposite has the smallest bundle among its series. Qualitative observations from optical micrographs also indicate that SAN and St-CNSSt copolymers are better host matrices to disperse SWNTs relative to DMA. Additionally, Raman mapping for SAN45 and PAN nanocomposites shows that the dispersion of SWNT in these systems are better than the DMA series. This further affirms our conclusion that polymer chain connectivity governs the susceptibility of individual functional groups on a polymer chain to form electron donor-acceptor interactions with the SWNT and that the extent of this interaction translates to SWNT particle dispersion, and can be systematically controlled by varying copolymer composition.

## **CHAPTER 5: MORPHOLOGY OF POLYACRYLONITRILE NANOCOMPOSITES BY SMALL ANGLE NEUTRON SCATTERING**

### **5.1 Motivation**

As discussed in Chapters 3 and 4, optimized non-covalent electron donor-acceptor interactions between a copolymer matrix and anisotropic filler provide a method to reproducibly tune the nanoparticle dispersion in a polymer nanocomposite system. However, in order to optimize the property enhancement of the nanocomposite with respect to the neat polymer, a precise control of the dispersion and morphology of these nanoparticle entities is essential. Nevertheless, unraveling the nature of the spatial arrangement of the nanoparticles in the nanocomposites presents a challenge to material scientists since the overlap of features on many length scales increases the complexity of the interpretation of microstructural data.<sup>164</sup> A clear picture of the nanocomposite structure demands both sophisticated experiments and coordinated theoretical investigations.

Despite the significance and extensive use of electron microscopy in the elucidation of morphology and structure-property correlations in multi-component systems,<sup>165</sup> image analysis using this technique brings a number of challenges. Surface-based methods such as atomic force microscopy (AFM) or scanning electron microscopy (SEM) only shows the surface or a cross-section of the three-dimensional arrangement of the SWNTs in the polymer matrix.<sup>166</sup> Brintlinger et al. has also shown that the measured diameter of SWNT embedded in polymer matrix from SEM images are overestimated because the contrast stems from the differences in surface electrostatic potential between the conductive nanotube and insulating polymer matrix.<sup>167</sup> In transmission electron

microscopy (TEM), structure elucidation is a complex task due to the extremely low contrast between SWNT and polymer matrix<sup>78</sup> and the image contrast is also dependent on nonstructural factors such as sample thickness, lens aberrations and imaging conditions.<sup>74</sup> Although it is possible to get good TEM images by ultrathin sectioning of bulk samples by microtome, which is necessary to obtain morphology of “as-processed” samples, this process adds ambiguity to the interpretation of the 3-dimensional (3-D) organization of the filler in polymer matrix because the size of the 3-D structure exceeds the thickness of ultrathin sections.<sup>164,165,168</sup> In addition, Ajayan et al. have shown that the microtoming can produce aligned arrays of carbon nanotubes embedded in polymer matrix, therefore altering the actual spatial distribution of SWNT.<sup>169</sup> Therefore, we have utilized small angle neutron scattering to evaluate the morphology of carbon nanoparticles in polymer nanocomposites. In this chapter, we focus on this simple, unresolved question to provide insight into our understanding of the structure of these multi-component systems: How can material parameters be tuned to achieve thermodynamically miscible polymer nanocomposites? This will ultimately guide the synthesis and/or formulation of novel thermodynamically stable polymer nanocomposites and provide design rules that relate particle chemistry, size and polymer-particle interfacial interaction to the formation of miscible polymer nanocomposite systems.

## **5.2 Materials**

The molecular characteristic of polyacrylonitrile used in this study is listed in Table 3.2. Thick film polymer nanocomposite samples for neutron scattering experiments are prepared as outlined in Section 2.5.B.

### 5.3 Basics of Small Angle Neutron and X-ray Scattering

Small angle scattering is a unique technique to elucidate both the structure and dynamics of molecules. The underlying principles of x-ray and neutron scattering are very similar and the subtleties that exist between them are pointed out as deemed necessary in the discussion below. Figure 5.1 illustrates the basic principle of a scattering experiment. An incident beam of radiation with wavelength  $\lambda_o$  and wavevector  $k_o$  impinges upon a sample and is scattered with a final wavevector,  $k_f$ . The radiation is scattered isotropically from each scattering center. The term “scattering center” will be used throughout this chapter to refer to the particle that scatters x-rays or neutrons, usually an atom. The term  $\theta$  defines the angle between the scattered beam and the incident beam. The scattered radiation is detected by the detector, recording its intensity, which is the square of the amplitude of the scattered wave, as a function of scattering angle  $\theta$ . The wavevector change upon scattering, denoted by  $Q$  is given by:

$$Q = |k_f - k_i| = \frac{4\pi}{\lambda_o} \sin\left(\frac{\theta}{2}\right) \quad (\text{Equation 5.1})$$

$Q$  is the length scale of the scattering event and is the fundamental variable that correlates to the spatial properties of the scattering sample.  $Q$  is also inversely proportional to a real space length scale,  $d$  where<sup>170</sup>

$$Q = \frac{2\pi}{d} \quad (\text{Equation 5.2})$$



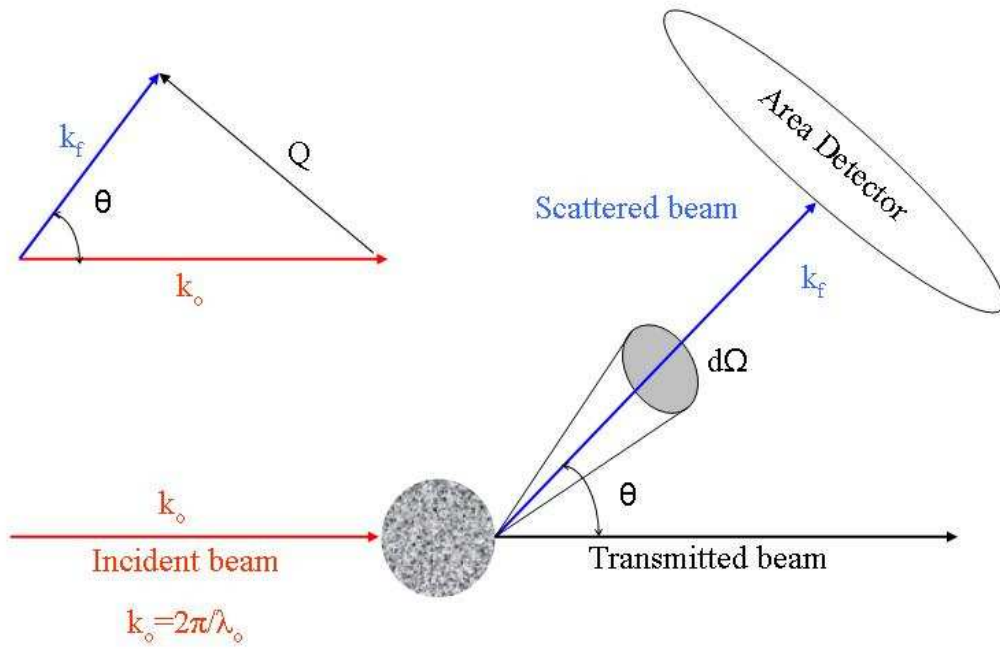


**Figure 5.1.** Illustration of scattering experiment and relationship between wavevectors and momentum transfers

Experimentally, the differential scattering cross section,  $(d\sigma/d\Omega)(Q)$ , is the dependent variable that is measured in a scattering experiment. For a neutron scattering experiment, this represents the number of neutrons scattered by the sample into a solid angle,  $d\Omega$ , as illustrated in Figure 5.1. The function  $d\sigma/d\Omega(Q)$  contains all the information on the size, shape, and interactions between the scattering centers in the sample.<sup>171</sup>

A generalized expression that relates differential scattering cross section to the structure of the sample is:<sup>171</sup>

$$\frac{d\sigma}{d\Omega}(Q) = NV^2(\Delta\rho)^2 P(Q)S(Q) + B \quad (\text{Equation 5.3})$$

where  $N$  is the number of scattering centers,  $V$  is the volume of one scattering center and  $B$  is the background signal. The contrast,  $(\Delta\rho)^2$ , form factor  $P(Q)$  and structure factor  $S(Q)$  also appear in this equation and will be discussed in the following discussion.

From Equation 5.3, one can deduce that the feasibility of extracting structural information from a neutron scattering experiment lies in the contrast that exists in the sample, from the  $(\Delta\rho)^2$  term.  $(\Delta\rho)^2$  quantifies the difference of the neutron scattering length density,  $\rho$  of the various components in the system studied, where:

$$\rho = \frac{\delta N_A}{M} \sum_i b_i \quad (\text{Equation 5.4})$$

For a polymeric system, in Equation 5.4, the parameter  $\delta$  denotes the bulk polymer density,  $N_A$  is Avagadro number,  $M$  is the monomer molar mass and  $b_i$  is the neutron scattering length of nuclei  $i$  within the monomer. A compilation of nuclei scattering length values can be found readily in the literature. Neutrons are especially suited to

study soft materials, which consist mostly of light atoms such as carbons and hydrogens. This is because  $b$  varies irregularly with nuclei, and more specifically, deuterium has a very different scattering length than hydrogen. This allows experimentalists to manipulate  $\rho$  by deuterium labeling, substituting hydrogen ( $b_H = -3.741 \times 10^{-15}$  m) with deuterium ( $b_D = +6.671 \times 10^{-15}$  m). This results in significant contrast between the protonated and deuterated components, resulting in higher scattering intensity. This is not feasible for x-rays as the x-ray scattering length is dependent upon the electron density of the sample and increases with atomic number. The scattering length density of an atom for x-rays is obtained by replacing the neutron  $b_i$  values in Equation 5.4 by  $Zr_e$ , where  $r_e = 2.81 \times 10^{-13}$  cm is the classical radius of the electron, and  $Z$  is the atomic number of the  $i^{\text{th}}$  atom.<sup>172</sup>

The term  $P(Q)$  in Equation 5.3 is the single object form factor, which is a dimensionless function that describes how  $d\sigma/d\Omega(Q)$  is modulated by interference effects between neutrons scattered by various parts of the same scattering object. This is commonly referred to as “intramolecular interference”, which provides the size and shape characteristics of the scattering object. Through manipulation of the contrast factor, for example, in a mixture of identical deuterated and protonated polymers with equal volume of scattering units that differ only by coherent scattering length  $b_H$  and  $b_D$ ,  $P(Q)$  can be obtained directly from scattering intensity,  $I(Q)$  and can be written as:<sup>170</sup>

$$I(Q) = (b_D - b_H)^2 x(1-x)Nz^2 P(Q) \quad (\text{Equation 5.5})$$

where  $N$  refers to the total number of molecules, with  $xN$  the fraction that are deuterated and  $(1-x)N$  the fraction that are protonated. It is also worth noting that coherent scattering

refers to scattering events that carry information about the structural arrangement within the sample. Incoherent scattering on the other hand carries no correlations between the positions in the sample of a nucleus and arises from random points in the sample, which cannot contribute to the constructive interference.

Expressions for  $P(Q)$  have been developed for various structures. Therefore, another method for data interpretation is to start from well-established models<sup>170</sup> and fitting the model scattering to the properly reduced  $d\sigma/d\Omega(Q)$  versus  $Q$ , the experimentally determined scattering curve. One of the most challenging aspects of small angle neutron scattering is the arsenal of data analysis procedure that are available to be directed at the data, depending on the region of the scattering curve. This is primarily because different regions of a scattering curve provide information about features on different lengths scales within the system under study. Recall from Equation 5.2 that  $Q$  is inversely proportional to the real space length scale. In general, in a dilute solution, zero angle scattering ( $I(Q)=0$ ) and analysis within the Guinier domain ( $Q \ll R_g^{-1}$ ) provides information on the molecular weight and radius of gyration ( $R_g$ ) of the scattering particle, respectively. If the scattering particle is a polymer chain, then the intermediate  $Q$  domain, where  $1/R_g < Q < 1/l$ , provides information on the statistical segment or persistence length of the polymer chain,  $l$ . If the polymer chain is beyond the dilute limit, and is in the semi-dilute or concentrated regime, the correlation length, which is the distance between contact points with other chains, may be obtained from the analysis of the intermediate  $Q$  regime. The high  $Q$  regime represents a length scale that approaches the length scale of chemical bonds, therefore giving information of the chain's local structure.

On the other hand, the interparticle structure factor,  $S(Q)$  in Equation 5.3 describes the interference effects between neutrons scattered by different scattering objects in the sample and therefore gives information on the relative positions of the scattering objects. This parameter is given by:

$$S(Q) = 1 + \frac{4\pi N}{QV_s} \int [g(r) - 1] r \sin(Qr) dr \quad (\text{Equation 5.6})$$

where  $g(r)$  is the density distribution of the scattering objects,  $r$  is the distance between scattering objects and  $V_s$  is the sample volume. The function  $g(r)$  gives the probability of finding two atoms separated by the distance,  $r$ . In other words, it provides a measure of the density distribution of the atoms in the scattering sample. The discussion presented in this section is meant to be an introduction to the important aspects of small angle scattering and not exhaustive. For a more thorough discussion, there exist excellent reviews and textbooks.<sup>170,171,173</sup>

#### **5.4 Results and Discussion: Real Space Structure and Scattering Patterns of Polyacrylonitrile (PAN) Composites**

Small angle neutron scattering was utilized to provide insight into the morphology of SWNTs in the PAN composite materials. In our work, small angle neutron and x-ray scattering curves of PAN/SWNT nanocomposites were obtained and show a peak that is reminiscent of the microphase-separation peak predicted by Schweizer et al. for polymer nanocomposites. Figure 5.2 shows the small-angle neutron scattering (SANS) patterns of polyacrylonitrile polymer and its SWNT nanocomposites containing 0.1, 0.2, 0.5, 1.0 and 2.0 wt% SWNT. The data was corrected for background scattering and detector

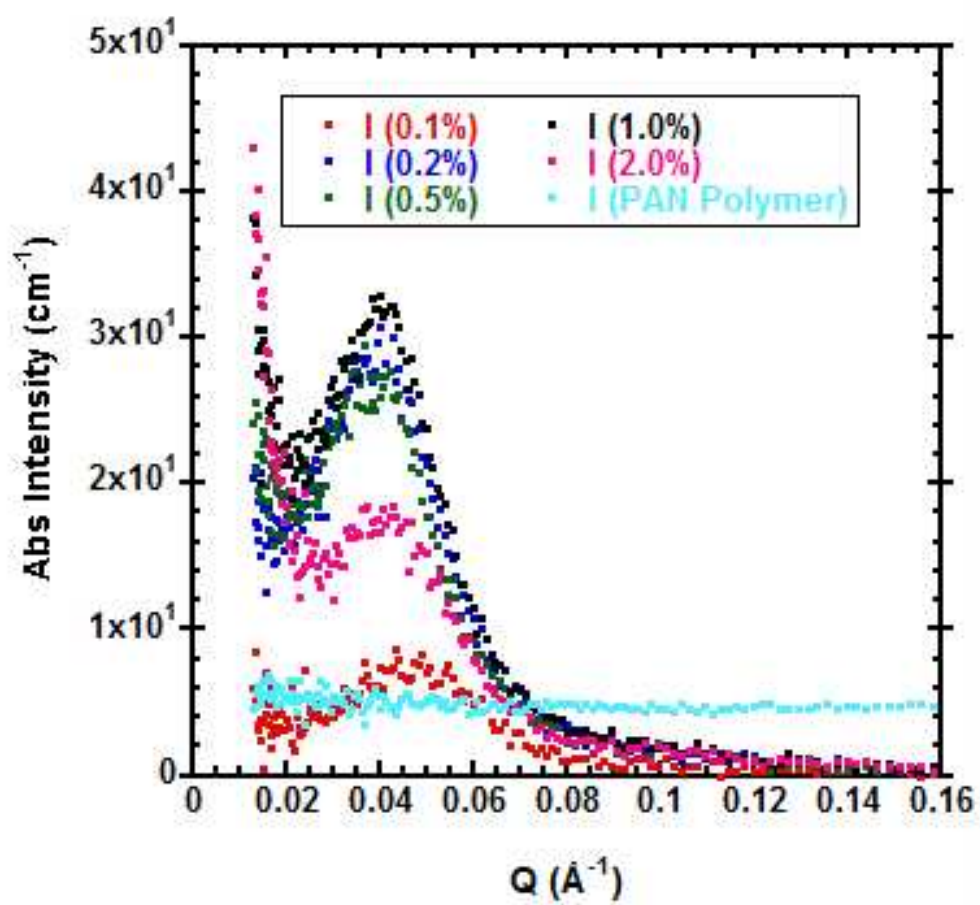


**Figure 5.2.** Small angle neutron scattering patterns of polyacrylonitrile thick film composite with varying SWNT loading, 0.1-2.0 wt% SWNT

efficiency, subtracted from polymer scattering contribution and converted to an absolute scale.

Interestingly, similar microphase separated-like peaks were not observed for any MMA-*ran*-DMAEMA or styrene-*ran*-acrylonitrile nanocomposites. As stated in Section 3.3.B, polyacrylonitrile shows anomalously good intermolecular interaction with SWNT and SWNT dispersion, as confirmed by Raman D\* band shift (Section 3.3.A.II) and Raman mapping (Section 4.3C.II). This is interpreted to indicate that the absence of the aromatic rings of the styrene in PAN, as opposed to SAN copolymers, leads to a significantly more flexible chain that can more easily wrap around the SWNT, creating more nitrile-SWNT EDA interactions. Therefore, the peaks observed in the scattering pattern of the polyacrylonitrile nanocomposite may be the manifestation of the formation of bound polymer layer wrapping around the carbon nanotubes (Figure 5.3).

These experimental results are initially interpreted by correlating to the theoretical work of Schweizer et al.<sup>174-177</sup> that uses the Polymer Reference Interaction Site Model (PRISM) to predict the thermodynamic phase behavior of polymer nanocomposites. In their work, they employed this microscopic polymer liquid state theory to determine the real space pair correlation function and calculate the collective scattering structure factors of melt polymer nanocomposites composed of hard spheres and homopolymers over length scales ranging from monomeric to macroscopic. This work has identified four general particle organizational behaviors (Figure 5.4), (I) contact aggregation, (II) steric stabilization (III) tight-particle bridging and (IV) longer range ‘tele-bridging’ attraction,

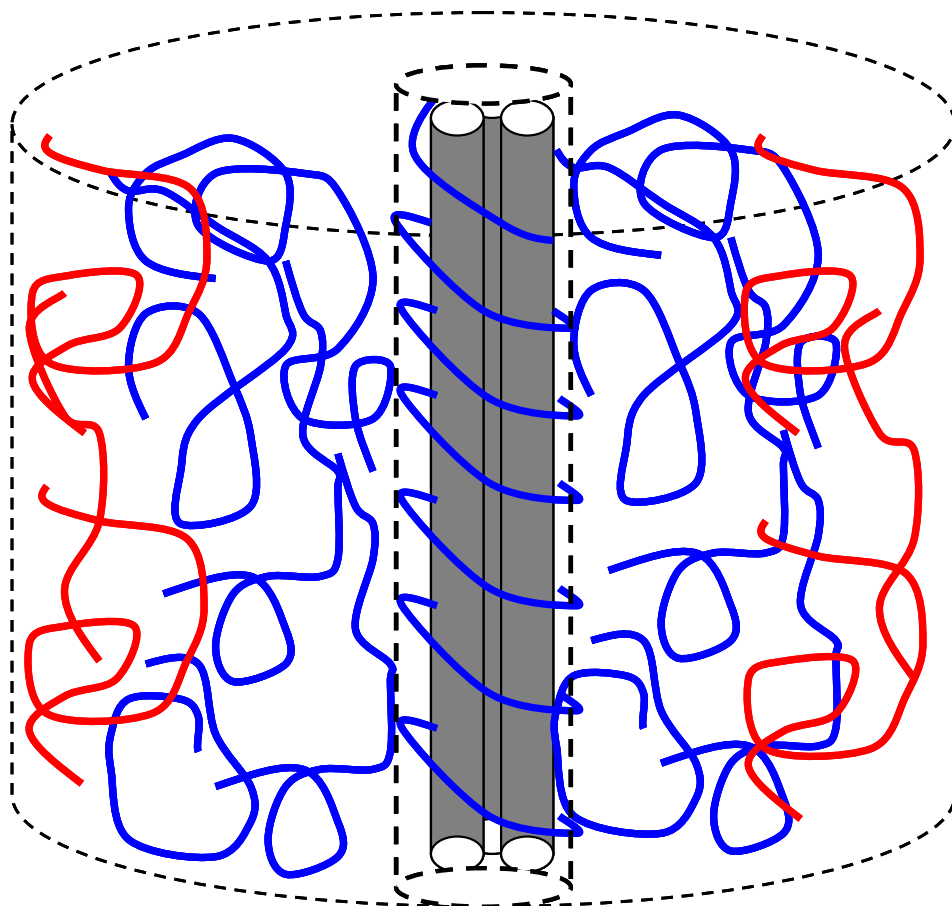


**Figure 5.3.** Schematic of the wrapping of a “bound-polymer” layer around SWNT aggregates. Red polymer chains correspond to bulk polymer matrix and blue chains correspond to polymers that participate in EDA interaction with SWNT



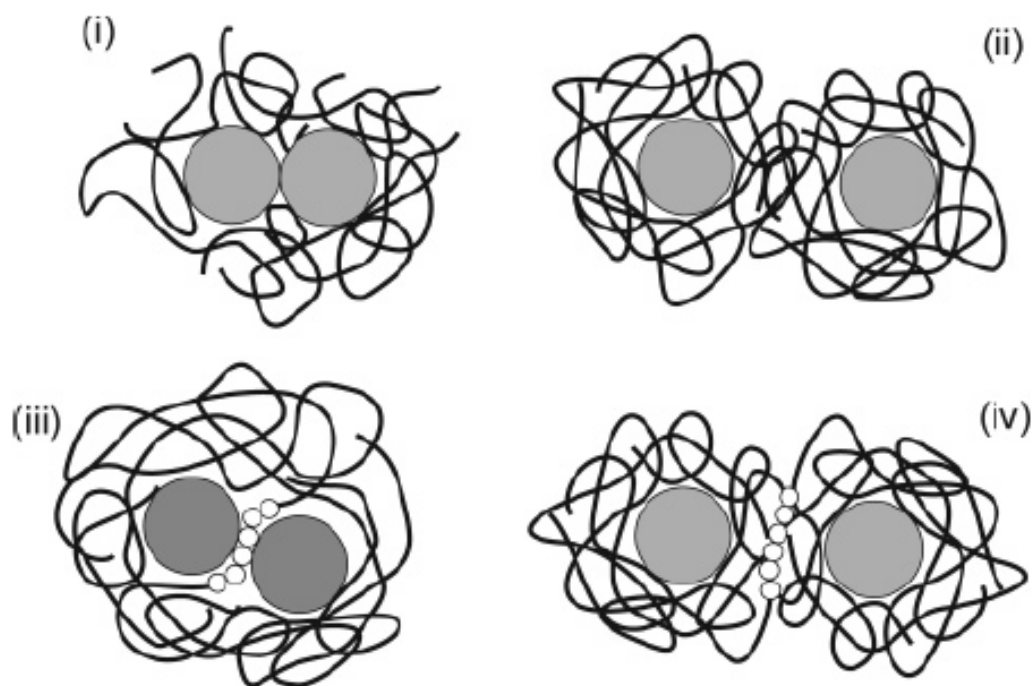


**Figure 5.4.** Illustrations of four states of particle organization in a dense polymer melt, (I) contact aggregation, (II) steric stabilization, (III) local bridging attraction, and (IV) longer range ‘tele-bridging’ attraction. Adapted from Schweizer et al.<sup>175</sup>

all of which are dependent upon the strength,  $\epsilon$  and spatial range,  $\alpha$  of the intermolecular attractions between the particle and polymer matrix.<sup>175</sup> At low polymer-nanoparticle interfacial interaction,  $\epsilon_{pc}$ , ( $\epsilon_{pc} < 0.3-0.5 k_B T$ ) the system adopts a direct nanoparticle contact or aggregation due to the extremely large depletion attraction between the particles, and is composed of polymer-rich and nanoparticle-rich phases (case I, Figure 5.4). The location of this demixing boundary is weakly sensitive to the particle-monomer size asymmetry ratio ( $D/d$ ) and interfacial attraction range,  $\alpha$ . The terms  $D$  and  $d$  denote the particle and monomer diameter respectively. When  $\epsilon_{pc}$  increases, the depletion attraction is eventually dominated by the enthalpy gain of placing polymer segments onto the particle surface. For moderate values of  $\alpha$ , the particles are bridged and can be enhanced with increasing chain length (case III, Figure 5.4). At larger  $\alpha$  but low  $\epsilon_{pc}$ , steric stabilization of the nanoparticles is realized, where thermodynamically stable adsorbed layers of polymers act as cushions between the particles (case II, Figure 5.4). At high  $\epsilon_{pc}$ , ( $\epsilon_{pc} < 2-3 k_B T$ ) the system exhibits a longer range “tele-bridged” configuration, which is similar to case II Figure 5.4, but has larger interparticle distances. This spinodal boundary is more sensitive to  $D/d$  and  $\alpha$  and increases of either parameter results in a narrowing of the miscibility window. In all cases, although the extent may vary, the miscibility window can ultimately disappear with the increase in nanoparticle size since the increase in particle size is directly proportional the magnitude of interparticle van der Waals attraction. Similarly, polymer chain length also has the same consequence due to finite size effect. As chains get larger and lose translational entropy, bridging between the nanoparticles is enhanced.

Schweizer and coworkers extended this theoretical characterization of the statistical structure of the polymer nanocomposite by calculating the corresponding partial structure factors of the composite to provide a direct correlation to the result of a scattering experiment.<sup>177</sup> The Fourier space structure factor of the sterically stabilized structure displays a microphase separation-like scattering peak, which is the result of a bound polymer layer around the fillers (Case II, Figure 5.4). The specific structure of this bound layer is dictated by (I) filler size, (II) filler volume fraction ( $\Phi$ ), (III) contact strength ( $\epsilon_{pc}$ ) and spatial range ( $\alpha$ ) of the interfacial cohesion. This thermodynamically stable “bound polymer layer” is a compromise state of organization, in which a polymer gains enough cohesive interaction energy to associate with a single filler, but not enough to give up the additional entropy required for bridging with multiple particles.<sup>177</sup>

The theory predicts specific changes in the structure factor,  $S_{cc}(k)$ , and thus changes in the bound layer, with increasing filler volume fraction. At a lower  $\epsilon_{pc}$  ( $\epsilon_{pc}=1$ ), and constant particle to monomer size asymmetry ratio,  $D/d$  and spatial attraction range,  $\alpha$ , the peak shifts to smaller wavevector as filler volume fraction,  $\Phi$  increases from 0.12 to 0.36. The authors postulate that this behavior could either be due to the expansion of the bound polymer layer or a larger filler effective radius. On the contrary, for a more attractive system ( $\epsilon_{pc}=2$ ), the structure factor peak shifts to higher wavevector, indicating a smaller mean nanoparticle separation, consistent with a tightly bridged configuration (case III, Figure 5.4).

The theory also predicts that the filler osmotic compressibility,  $S_{cc}(k=0)$ , will either increase or follow a non-monotonic dependence with particle volume fraction,  $\Phi$ , depending on the proximity of the mixture to the spinodal boundary. Qualitatively,

similar trends are observed in the osmotic compressibility,  $S_{cc}(k=0)$  and bound layer peak,  $S_{cc}(k)$  for both a low ( $\Phi=0.2$ ) and very high filler volume fraction ( $\Phi=0.4$ ). At lower  $\epsilon_{pc}$ , the bound layer peak is clearly present and as  $\epsilon_{pc}$  increases from 0.5 to 1.5, the scattering peak and  $S_{cc}(k=0)$  initially decreases in intensity. However, as  $\epsilon_{pc}$  reaches 2,  $S_{cc}(k=0)$  increases and the bound layer peak disappears. The authors proposed that the logical explanation for this trend is the evolution from a miscible structure with distinct bound layers to a tightly bridged conformation, where the adsorbed polymers are shared between multiple fillers, thereby masking the scattering signature of the bound layer.<sup>177</sup> From their work, it can be deduced that experimental realization of thermodynamic dispersion in a polymer nanocomposite system thus requires both an intermediate value of particle-monomer interfacial strength and spatial attraction range, and modest sized nanofillers and polymer.

In the scattering results shown in Figure 5.2, the filler size, strength and spatial range of the interfacial cohesion remains constant among the samples and the only variable is the SWNT volume fraction, which ranges from 0.00088 vol % (0.1 wt%) to 0.01765 vol % (2.0 wt%). Please note the difference in the convention used hereinafter, where the parameter  $k$  used in Schweizer's work, as explained above, is equivalent to  $Q$  in the following discussion. As shown in Figure 5.5, increasing filler volume fraction has a profound effect on the low angle scattering, which, for these samples is taken as the scattering intensity at the lowest measurable  $Q$ , denoted as  $I(Q_{low})$ . Based on Schweizer's work, the change in the filler osmotic compressibility,  $I(Q=0)$  correlates to the reorganization of the bulk polymer matrix, as schematically illustrated in Figure 5.5. If

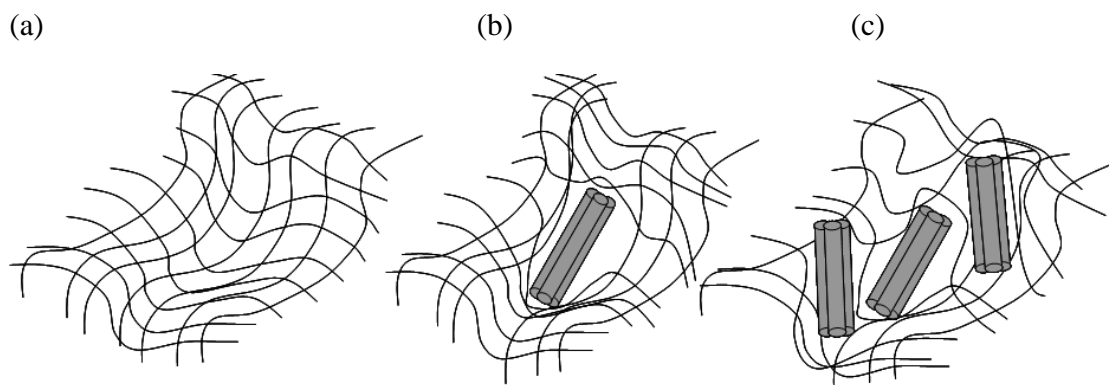


**Figure 5.5.** Schematic representation of structural changes that alter the dimensionless isothermal compressibility  $I(Q=0)$  for (a) unperturbed polymer chain (b) a nanocomposite with low filler concentration and (c) a nanocomposite with high filler volume fraction. As SWNT volume fraction increases, more voids are created to accommodate the presence of SWNTs.<sup>176</sup>

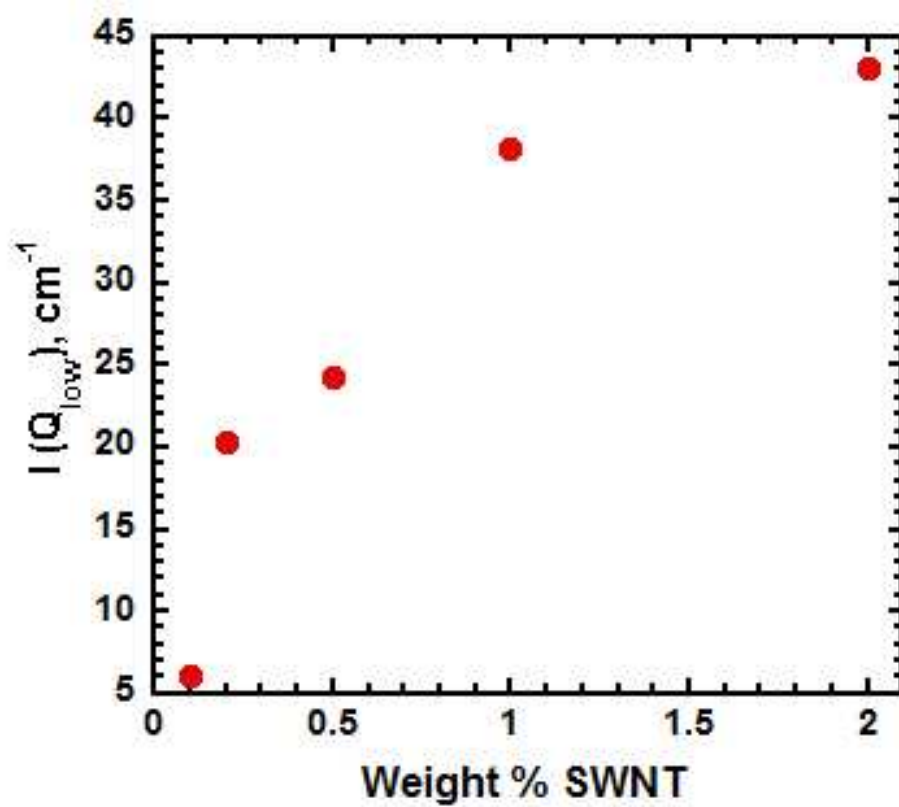


**Figure 5.6.** Scattering intensity at the lowest measurable  $Q$ ,  $I(Q_{low})$  as a function of mass % SWNT

we assume that  $I(Q_{\text{low}})$  maps to  $I(Q=0)$ , the dimensionless isothermal compressibility, the following discussion is valid. As shown in Figure 5.6,  $I(Q_{\text{low}})$  for a polymer matrix is the lowest ( $I(Q_{\text{low}}) = 4.53$ ), characteristic of an unperturbed polymer melt (case I, Figure 5.5). As the volume fraction of SWNT increases,  $I(Q_{\text{low}})$  increases, possibly due to the creation of voids in the polymer matrix by the inclusion of the SWNT, resulting in corresponding long-range (relative to the monomer scale) polymer concentration fluctuations.<sup>176,178</sup> One likely explanation for the observed upturn in the  $I(Q_{\text{low}})$  shown in the scattering patterns of PAN nanocomposites (Figure 5.2) is the onset of filler clustering, which is analogously observed in the scattering pattern of high particle volume fraction polymer nanocomposites, composed of hard spheres and homopolymers, described in Schweizer's theory.

Figure 5.7 shows the wavevector  $Q$  where the peak is a maximum,  $I(Q)_{\text{max}}$ , as a function of % SWNT in the polyacrylonitrile thick film composites. In Schweizer's theory,<sup>177</sup> the location of the peak in the scattering pattern is directly correlated to the bound polymer layer thickness,  $\Delta$  where  $Q$  scales roughly as  $2\pi/(D+\Delta)$  and  $D$  is the nanoparticle diameter. If we assume that the SWNT nanoparticle diameter  $D$  remains constant as SWNT volume fraction increases, the extent of bound polymer layer thickness among the PAN composites can be determined. Table 5.1 shows the value of  $D+\Delta$  for each sample from this calculation.

Theoretical investigations are underway to determine whether an increase from 0.5 wt% to 2.0 wt% SWNT is sufficient to alter the size of the nanoparticle bundle. However, with the current assumptions, this data indicates that as the % SWNT increases from 0.1 to 0.5 wt%, the shift of the correlation peak to lower wavevector implies that the bound

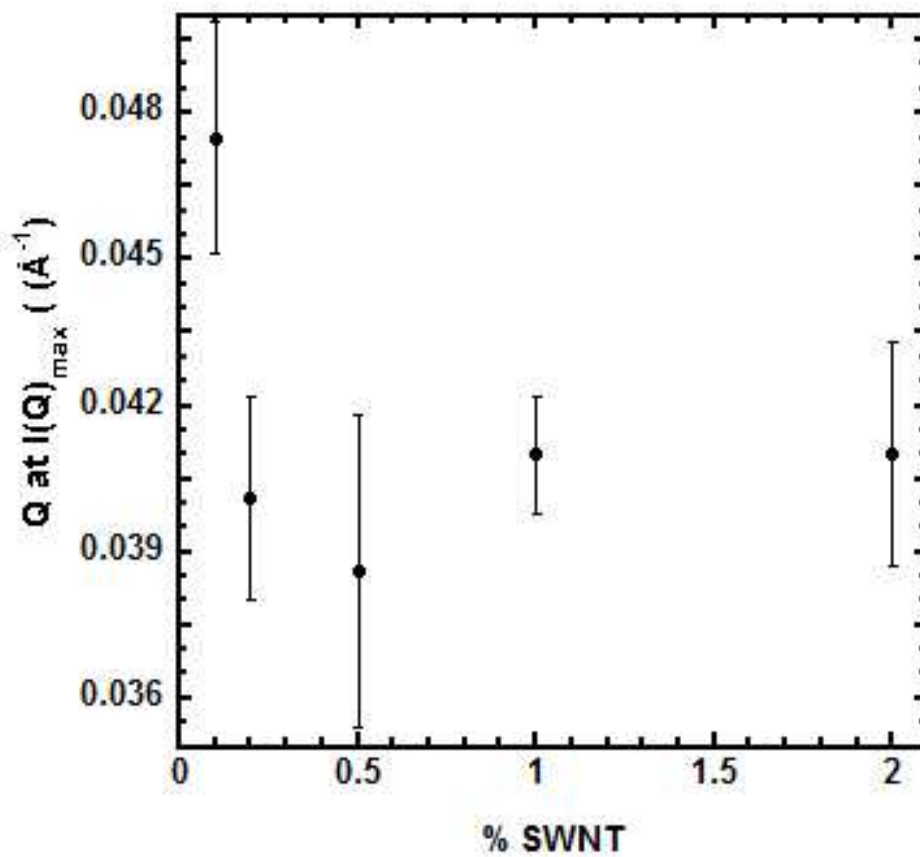


**Figure 5.7.**  $Q$  at  $I(Q)_{\max}$  as a function of % SWNT in polyacrylonitrile thick film composite



**Table 5.1.** Thickness of nanoparticle diameter and bound polymer layer thickness ( $D + \Delta$ ) for polyacrylonitrile composites containing 0.1 wt% to 2.0 wt% SWNT

% SWNT	$q$ ( $\text{\AA}^{-1}$ )	$D + \Delta$ (nm)
0.1	0.047447	13.2
0.2	0.040042	15.7
0.5	0.036502	17.2
1.0	0.040042	15.7
2.0	0.040664	15.5

polymer layer surrounding the nanofiller expands by ~30% (Figure 5.7). However, as the % SWNT increases further to 2.0 wt%, the shift to higher wavevector indicates that further increasing the concentration of nanotubes decreases the size of this bound layer, possibly forming a tightly bound configuration. This makes sense because as more SWNT is present in the system, a smaller mean nanoparticle separation is realized, thereby trapping the polymer layer between the nanoparticles.

The magnitude of the structure factor peak,  $I(Q_{\max})$ , depicted in Figure 5.8 as a function of SWNT concentration, is directly proportional to the amount of bound polymer layer. A non-monotonic dependence of  $I(Q)_{\max}$  on SWNT concentration is observed. As % SWNT increases to 1.0 wt%,  $I(Q)_{\max}$  increases, as does the thickness of the bound layer as determined from  $Q_{\max}$ , leading to a larger apparent volume of the nanoparticle. However, contrary to the predictions of Schweizer's theory,  $I(Q)_{\max}$  decreases for the 2.0 wt% SWNT nanocomposite. This may be due to a transition of this system into the regime where the higher volume fraction of SWNT induces a tight-particle bridging organization, resulting in a lower apparent volume of the nanoparticle.

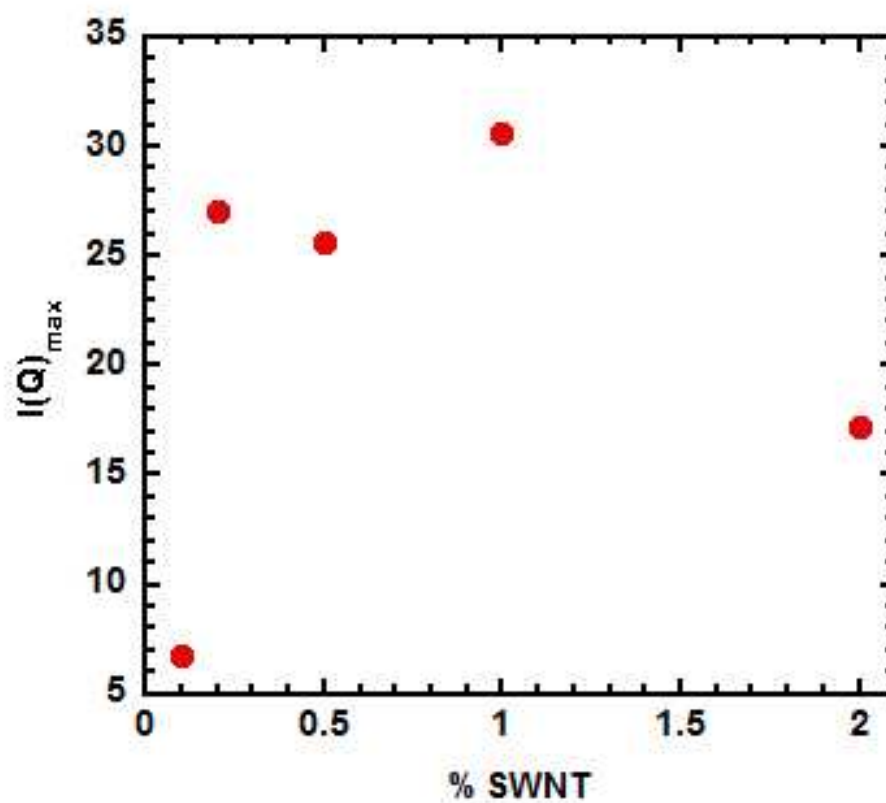


**Figure 5.8.** Maximum scattering intensity ( $I(Q)_{\max}$ ) at  $x_{\text{center}}$  of the observed correlation peak in the scattering of PAN nanocomposites

It is also possible that the presence of the microphase-separation like scattering peak is the manifestation SWNT-induced polymer crystallization. Polymer crystallization has also been shown to be induced by 2-dimensional (nanoplates/nanosheets), 1-dimensional (nanotubes/nanowires/nanorods) and 0-dimensional (nanoparticles) nanoparticles, creating a nanohybrid shish-kebab (NHSK), illustrated schematically in Figure 5.9 (a). In classical shish-kebab morphology of crystallization, polymer solutions/entangled melts undergo a coil-to-stretch transition under extensional flow. This transition was first postulated in a theory developed by de Gennes, where polymer chains undergo a sharp transition from a random coil to a fully extended-chain conformation in flow at a critical strain rate, without an intermediate stable chain conformation. For a chain larger than a critical molecular weight,  $M^*$ , the stretched chains aggregate to form chain fibrillar crystals and the remaining chain crystallize in a folded, periodic fashion. This mechanism is referred to as linear nucleation. In NHSK however, the nano fibrillar structure of CNT provide a 1-dimensional nucleation surface and shear is not needed in the particle-induced crystallization.<sup>179-182</sup>

This superstructure formation is based on previous studies that elucidated the formation of polymer crystal superstructures by crystallization during flow.<sup>183,184</sup> This superstructure is called ‘shish-kebab’ because it consists of a central threadlike fibril (shish) and multiple disc-shaped, folded-chain lamellae (kebabs). Simulations of flow-induced crystallization from a solution of short and long chains have shown that long chains stretch and form the shish core around the short chains aggregate in a kebab.<sup>185,186</sup> From small-angle neutron scattering patterns of deuterium-labeled isotactic polypropylene with different chain lengths, Kimata and coworkers confirmed the finding

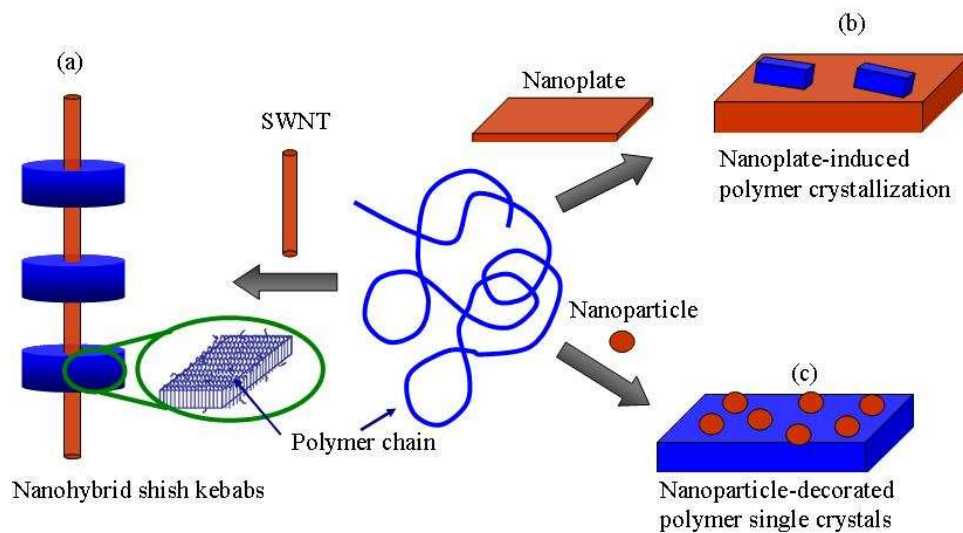


**Figure 5.9.** Schematic representation of three methods that the presence of a nanoparticle can induce/modify polymer crystallization. (a) nanohybrid shish kebabs (b) Nanoplate-induced polymer crystallization, (c) nanoparticle-decorated polymer single crystals

from those simulations.<sup>187</sup> In a general sense, the molecular structure and behavior of SWNTs are parallel with polymers, particularly rigid-rod polymers. Green et al. compared the properties and applications of SWNTs with those of lyotropic liquid-crystalline polymers (LCPs) and concluded that a SWNT meets the definition of a polymer as a large molecule of repeating, covalently bonded units.<sup>188</sup> This perspective therefore paved the way for the cross-application of theoretical and experimental frameworks originally developed for conventional polymers and applies it to SWNTs.

Li et al. have extensively investigated the crystallization of polyethylene (PE) on single-walled carbon nanotubes (SWNTs), multiwalled nanotubes (MWNTs) and vapor grown carbon nanofibers (CNFs). From wide-angle X-ray experiments, they found that the lateral dimension of the polyethylene kebab is ~50-80 nm whereas average MWNT periodicity is ~40-50 nm. They postulated that two factors affect the NISK growth that leads to the parallel orientation of polymer chains to the shish axis and orthogonal orientation between the lamellar surface and shish axis. First, strict crystallographic registry is needed between the polymer chain and the graphitic lattice and second is the geometric confinement by the CNT. Due to the small diameter of CNTs, they can be considered as rigid macromolecules and polymer chains prefer to align along the tube axis regardless of the lattice matching between the polymer chain and graphitic sheet, a mechanism referred to as 'soft epitaxy', whereby strict lattice matching is not required. In contrast, larger diameter fibers such as CNFs have small surface curvature and the polymer behaves as if it is on a flat surface, making lattice match and epitaxy the main growth mechanism. Therefore, geometric confinement becomes more pronounced as the fiber diameter decreases.

Additionally, Zheng and coworkers compared the morphology and crystallization behavior of polyethylene and poly(ethylene oxide) in SWNT nanocomposites by transmission electron microscopy, scanning electron microscopy, Fourier transform infrared spectroscopy, Raman spectroscopy, wide angle X-ray diffraction and differential scanning calorimetry. Based on their results, they hypothesized that the formation mechanism of PE on SWNT is as follows. Initially, the random-coiled PE chains coexist in the PE/SWNT suspension and are slowly adsorbed onto the SWNT surfaces. These adsorbed chains wraps along the SWNT surface and drag neighboring chains onto the nanotube cage. Thereafter, during polymer chain relaxation, a subglobule forms and acts as the crystal nucleus, which induces the epitaxial growth of PE chains into the lamellar structure. In order to decrease the interfacial energy, growth is realized perpendicular to the SWNT axis. In contrast, the less favorable interaction of PEO with SWNT causes the formation of an initial distorted helix structure around the SWNT and upon the increase in the amount of PEO wrapping, all the SWNT surface is wrapped with a thin homogenous coating of amorphous PEO. Therefore, the extent of intermolecular interaction between a polymer matrix and nanoparticle plays a major role in the propensity of a particle to portray nucleation effect.

Based on the discussion presented above, the observed small angle scattering peak may be the manifestation of polymer crystallization induced by the SWNT particles. In this case, the peak would correlate to the inter-kebab distance,  $\sim 16 \text{ nm}$  ( $2\pi/Q_{\text{max}}$ ). This unique hybrid structure has only recently been found<sup>179</sup> and numerous questions have yet to be answered. What is the role of CNT chirality on CNT induced crystallization? What

is the effect of particle curvature and surface chemistry on NBSK formation? And, what are the parameters that affect the periodicity of the inter-shish distance?

Although a definitive interpretation for the presence of the microphase separated peak in PAN nanocomposites has not been attained at this point, its presence indicates an ordering of the PAN polymer induced by the carbon nanotube cage. Whether this indicates the existence of a (I) thermodynamically bound layer around the SWNT or (II) the occurrence of SWNT-induced PAN crystallization is a subject of an ongoing research in our laboratory. In order to put these two possible phenomena into perspective, consider a typical polymer chain which has a radius of gyration of  $\sim 10$  nm.<sup>150</sup> As it diffuses near the surface of the filler, the diameter of the filler plays a critical role in the formation of an ordered structure or crystal. For a filler with diameter much larger than the polymer size,  $D^{\text{filler}} \gg D^{\text{polymer}}$ , the surface curvature is small and the polymer behaves as if it is on a flat surface, which requires strict lattice matching for the crystal growth. As the diameter of the filler reaches the order of the polymer size, the filler's surface is molecularly curvy. If the polymer obeys the strict lattice matching mechanism, this would lead to the formation of polymer crystals with distorted lattice, which is unstable. Therefore, for a filler possessing a diameter less than a certain critical diameter,  $D_{\text{crit}}$ , geometric confinement is the major factor that drives the crystalline formation mechanism and are exclusively parallel to the SWNT axis, disregarding its chirality. As a result, in our system, PAN lamellae would grow perpendicular to the nanotube axis and consequently form the nanoshish-kebab superstructure. If the case of  $D^{\text{filler}} \gg D^{\text{critical}}$  is realized on the other hand, the structure of the SWNT-polymer complex potentially mimics that of a thermodynamically bound layer wrapping around the carbon nanotube

cage. This postulation is made on the basis of Li's work,<sup>182</sup> where SEM micrographs of polyethylene (PE) crystallized on carbon nanofiber (CNF), with an outer diameter of 100-300 nm, generates randomly oriented PE lamellae on the CNF surface. In contrast, TEM micrographs of the crystallization of PE near periodically functionalized SWNTs and MWNTs with diameters that range from 0.8 to 30 nm show the clear formation of nanohybrid shish kebab superstructures.

Therefore, for larger diameter CNFs, where geometric confinement is weak, lattice matching dictates the overall orientation of the polymer chain wrapping around the carbon nanotube cage. Since SWNTs contain defects on its graphitic framework,<sup>189</sup> the polymer crystals may grow with varying orientations around the carbon nanotube cage, resulting in the formation of a thermodynamically bound polymer layer. At this point, since we are uncertain regarding the size of the SWNT bundles within the system and what the critical diameter that dictates the growth mechanism, we cannot be certain whether the microphase-separation like scattering peak originates from a bound polymer layer around the SWNT or the formation of a crystalline superstructure. However, experiments such as wide angle X-ray diffraction (WAXD) and differential scanning calorimetry (DSC) will provide additional information to clarify this uncertainty.

## **5.5 Conclusion**

We have shown that a combination of computational studies<sup>177</sup> and scattering experiment offers insight into elucidating the real space structure of a nanofiller in a polymer matrix. The emergence of microphase separated-like peaks in the small angle



scattering pattern of PAN nanocomposites may be the manifestation of the formation of a polymer bound layer or nanoparticle induced polymer crystallization.

First, Schweizer's theoretical work<sup>175-177</sup> predicts the formation of a thermodynamically stable bound polymer layer around the nanoparticle, which results in the appearance of a microphase separated like peak in the small angle scattering pattern. The location of the peak provides insight into the bound polymer layer thickness. In addition, increasing filler volume fraction also has a profound effect on the low angle scattering,  $(I(Q)_{\text{low}})$ , possibly due to the reorganization to the bulk polymer matrix or the onset of particle clustering. A second explanation that may explain the emergence of this peak is the occurrence of SWNT-induced polymer crystallization. The nano fibrillar structure of CNT provides a 1-dimensional nucleation surface and leads to the parallel orientation of polymer chains to the tube axis, resulting in the formation of lamellae that are oriented orthogonally to the tube surface. This investigation provides initial insight into the key chemical and physical variables that govern nanofiller dispersion and morphology, and are ongoing, with the ultimate goal of achieving rational control of nanoparticle dispersion in a polymer matrix.

## CHAPTER 6: DISSOLUTION OF SINGLE WALLED NANOTUBES BY POLYMERIC STERIC STABILIZATION

### 6.1 Introduction

The organization and interactions that occur during the nanocomposite preparation process are critical in developing a well-dispersed polymer nanocomposite. Therefore, an understanding and discussion of the nanocomposite preparation procedure, as is schematically presented in Figure 6.1, as well as the proposed mechanism for nanoparticle stabilization during the nanocomposite fabrication is needed. Initially, suspensions of single-walled carbon nanotubes (SWNTs) and the solvent dimethyl formamide (DMF) are sonicated for one hour to achieve homogenous nanoparticle dispersion (Stage A, Figure 6.1). After the addition of an appropriate amount of (co)polymer, the resulting suspension (Stage B, Figure 6.1) is further sonicated, concentrated and finally evaporated to produce the final, dry-state SWNT-polymer nanocomposite (Stage C, Figure 6.1). In the preceding chapters, the discussion has been limited to the thermodynamic behavior of this two-component system, i.e. SWNT-polymer charge transfer complex (Stage C), which consists of the free SWNT, SWNT-polymer complexes and non-interacting bulk polymer matrix. However, one underlying question that still pervades, and is the focus of this chapter is the thermodynamic behavior of the SWNT-polymer complex in solution during composite fabrication (Stage B, Figure 6.1). To study this complexation/stabilization process, schematically presented in Stage B, Figure 6.1, the solution is further centrifuged to remove the free SWNTs that do not participate in the formation of electron donor-acceptor interaction with the polymer matrix. The goal of this process is to isolate the SWNTs that have formed

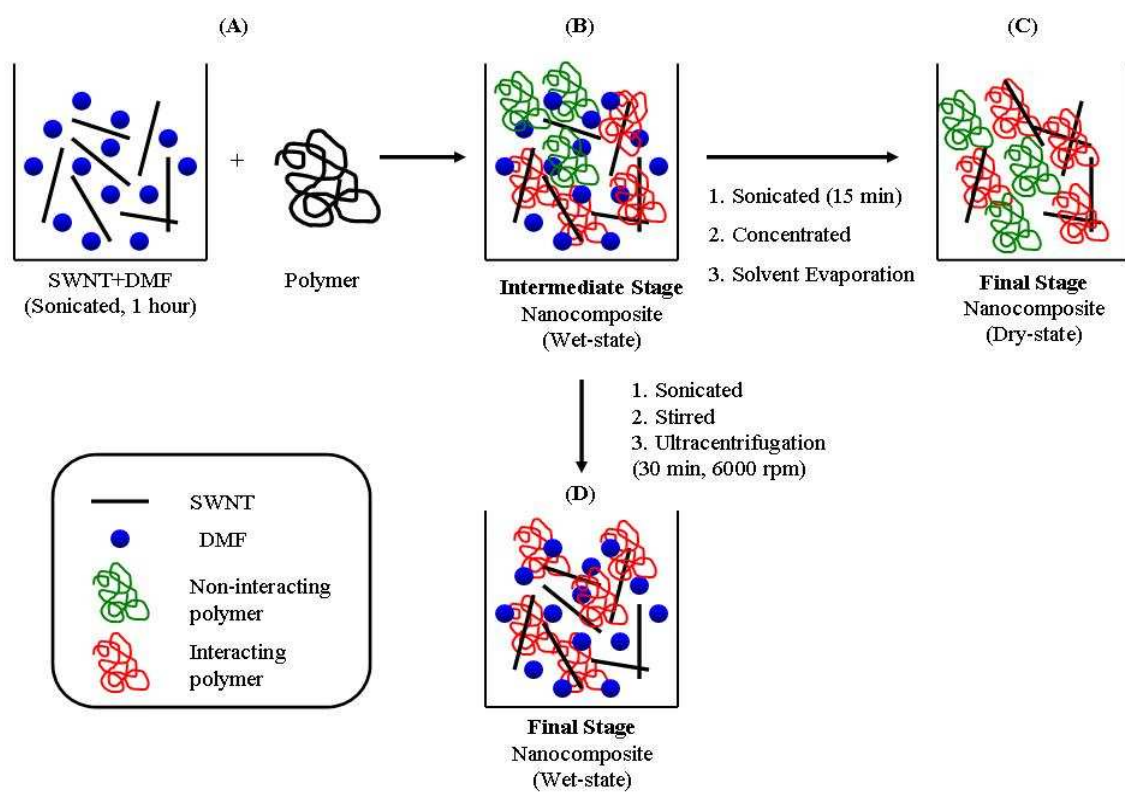


**Figure 6.1.** Schematic of sample preparation process for polymer nanocomposites

EDA interactions with the polymer for further analysis. Even with this extraction, this remains a complex system to be deciphered since interactions that impact the SWNT-polymer structure include the solvent-solvent, solvent-polymer, and solvent-SWNT interactions, in addition to the polymer-polymer, SWNT-SWNT and SWNT-polymer interactions that exist in a two-component system. Developing an understanding of the thermodynamics of polymer stabilized SWNT dispersions in a polymer solution is critical in order to unravel the most effective way to untangle SWNT bundles and attain control of the bundle-sizes embedded in polymer matrices by solution processing for optimal device performance in optical applications.<sup>190</sup> Clearly, the adsorption of the polymer onto the SWNT to stabilize the SWNT in solution is required to unbundle the SWNT and more effectively disperse the SWNT in the final polymer nanocomposite. Therefore, we must understand more thoroughly the polymer adsorption process in solution. Relevant questions become; Is the system thermodynamically stable? If not, what is the nature of the equilibrium state? Additionally, the solvent plays a double role, affecting the interactions between the adsorbate molecules (i.e. polymer) and determining the effective interaction between the surface (i.e. SWNT) and adsorbate. In this chapter, we seek to provide insight into the system parameters that govern polymer stabilized SWNT particle dispersion in suspension in the context of colloid science in order to begin to develop this level of understanding.

A colloidal dispersion consists of a dispersion medium (i.e. the continuous phase) where dispersed colloidal particles exist. The particles are called the dispersed phase and the particles are colloidal in character if they possess at least one dimension in the size range of 1 to  $10^3$  nm.<sup>191</sup> Colloidal stability is a universal event that occurs in many

biological and daily phenomena, from the properties of blood, antigen-antibody reactions, the nature of milk to even agricultural materials, where the degree of dispersion of the soil affects its crop bearing potential.<sup>192</sup> In science and technology, the stabilization of colloidal particles by nonionic macromolecules occurs in emulsion and suspension polymerizations, detergent action in washing, the formulation of paints, pharmaceutical emulsions and dispersions, the clarification of water residues and oil dispersants for use on crude oil spills. The domain of colloid science encompasses a broad range of systems where the particle can be in the form of micron-sized colloids, globular protein or self-assembled micelles or SWNT nanoparticles.<sup>50,191-195</sup>

The ability of a polymer in solution to act as either a stabilizer or a destabilizer of a particulate suspension has been known since ancient times. Gum Arabic, a natural gum made of the hardened sap taken from two species of the acacia tree, which is a complex mixture of polysaccharides and glycoproteins, has long been used for pigment particle stabilization in the food industry, painting and printmaking. The forces acting between colloidal particles in dispersed systems may be strongly modified by the adsorption of polymeric or macromolecular layers onto the particle surfaces. As an example, ancient Egyptians used the aqueous carbon-black (formed by combustion) dispersions stabilized by adsorbed layers of natural steric stabilizers such as gum Arabic, egg albumin or casein (from milk) to form stable ink.<sup>50</sup>

In this chapter, the questions posed in considering SWNT dispersion in the context of colloidal stability will be discussed under the following headings: First, what are the strategies that can be employed to promote particle stability? Second, once the strategy is established, what are the system parameters that affect the particle dispersion?

And finally, how do the polymer solution thermodynamics impact the stabilization phenomena?

## **6.2 Materials**

The characteristics of styrene-*ran*-acrylonitrile polymers used in this study are listed in Table 3.2 (Chapter 3). SWNT-polymer suspension samples for UV-Vis spectroscopy measurement (Section 2.6E) were prepared as outlined in Section 2.5C.

## **6.3 Basic Theory of Colloid Science**

### **A. Strategies for Imparting Colloidal Stability**

Understanding the nature of the interactions that imparts colloidal stability is imperative in understanding the parameters that induce particle dispersion and enable the fine-tuning of resulting material properties. There are two general ways of imparting colloid stability: (I) electrostatic stabilization and (II) polymeric stabilization.

Aerosols, a suspension of fine solid particles or liquid droplets in gas, are an example of a natural phenomenon that employs electrostatic stabilization. The Coulombic repulsion between the colloidal particles in aerosols (e.g. smog or fog) is of a long range character and can impart stability.<sup>191</sup> As shown in Figure 6.2, the mutual repulsion of the counterions in the dispersion medium surrounding the colloidal particles provides the stability in electrostatic stabilization. The surface potential of electrostatically stabilized dispersions may arise in a variety of ways, for example, by the adsorption of potential determining ions (e.g. anionic or cationic surfactants) or by ionization of ionogenic groups (e.g. carboxylic acid or sulfate half-ester groups) on the particle.<sup>192</sup> At room

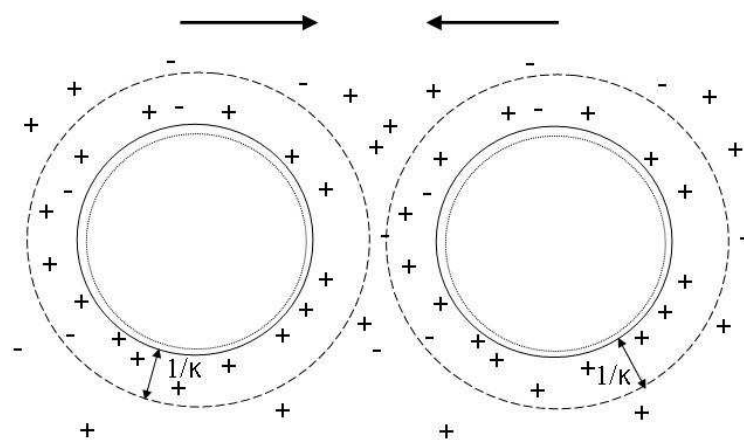


**Figure 6.2.** Diagram representing the origin of electrostatic stabilization for negatively charged particles.<sup>191</sup>

temperature, the spatial extension or thickness of the outer electrical layer ( $1/\kappa$ ) is a function of the ionic strength of the dispersion medium and can be written as follows:

$$1/\kappa = 0.33 \left( \frac{\epsilon}{I} \right)^{\frac{1}{2}} \quad (\text{Equation 6.1})$$

where  $\epsilon$  denotes the dielectric constant and  $I$  is the ionic strength of the dispersion medium. For a 1:1 electrolyte in water at 25°C,  $(1/\kappa)/\text{nm} \sim 0.3/c^{1/2}$  where  $c$  is the molar concentration.<sup>191</sup> It is therefore evident that in a dispersion medium of low ionic strength ( $c \leq 10^{-3}$  M,  $1/\kappa \geq 105$  nm), the thickness of the electrostatic layer exceeds the range of the van der Waals attraction, which is in the order of 5-10 nm, a value that has been previously determined by Hamaker and is valid for many colloidal systems.<sup>196</sup> By a similar token, ionic strengths greater than, say,  $10^{-1}$  M generates an electrostatic layer of less than 1 nm, in which case the electrostatic repulsion is of insufficient range to overcome the van der Waals attraction between the colloidal particles. This accounts for the occurrence of aggregation of electrostatically stabilized dispersions when the ionic strength of the dispersion medium is sufficiently high.

On the other hand, in polymeric stabilization, the spatial extension or thickness of the stabilizing layer of polymer molecules are greater than the range of the van der Waals attraction between colloidal particles.<sup>191</sup> This can be explained by the following argument. The root mean square (r.m.s.) end-to-end distance of linear polymers can be estimated to be a measure of their “diameter”. As briefly stated in Section 4.3C, the actual mean-square end-to-end distance of an unperturbed polymer chain,  $\langle h^2 \rangle_o$  is:<sup>150</sup>

$$\langle h^2 \rangle_o^{1/2} / \text{nm} \sim 0.06 M^{1/2} \quad (\text{Equation 6.2})$$



where  $M$  is the polymer molecular weight. Thus, for a polymer chain having molecular weight of  $10,000 \text{ g.mol}^{-1}$ , the r.m.s. end-to-end distance is 6 nm. Although the precise dimension of polymer chain can vary considerably depending on chain flexibility of the polymer,<sup>150</sup> it can be generally estimated that chains with molecular weight greater than  $\sim 10,000 \text{ g.mol}^{-1}$  have chain dimensions commensurable to or in excess of the range of van der Waals attraction between the colloidal particles. Therefore, adsorbed polymer molecules are excellent candidates for imparting colloidal stability as long as they can generate repulsion between the nanoparticles.

In polymeric stabilization, there are two mechanisms whereby macromolecules can impart colloidal stability: (I) depletion stabilization and (II) steric stabilization. Depletion stabilization is generated by polymer that is free in solution, in contrast to steric stabilization where the adsorbed or attached polymer (i.e. by grafting or physical adsorption) causes the repulsion between colloidal particles.<sup>191</sup> In addition, stabilization by the free polymer is an example of kinetic stability or thermodynamic metastability whereas steric stabilization is a phenomenon of thermodynamic stability. In depletion stabilization, stability arises from the depletion of free polymer between the surfaces of the particles when they are in close proximity and closer approach of the particles can only be achieved by a further depletion of the polymeric segment concentration between particles.<sup>197</sup> This type of stabilization occurs if the surface of the particle is inert or repulsive to the polymer, or if all adsorption sites are occupied.<sup>198</sup> A schematic of particles undergoing steric stabilization and depletion stabilization is diagrammatically presented in Figure 6.3.

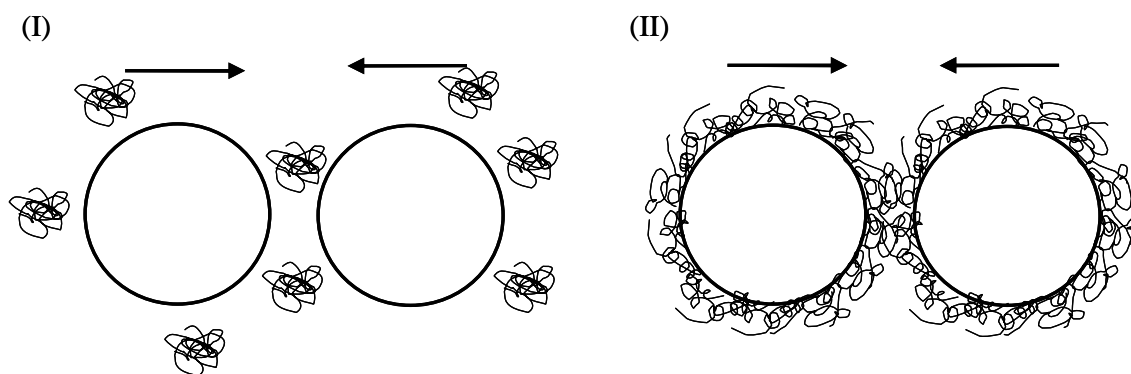


**Figure 6.3.** Schematic representation of (I) depletion and (II) steric stabilization

Steric stabilization offers several advantages over electrostatic stabilization. First, it is rather insensitive to the presence of electrolytes. As already mentioned above, in electrostatic stabilization, the addition of electrolyte compresses the spatial extension or thickness of the stabilizing layer. If the layer compresses to an extent that the electrostatic repulsion cannot overcome the van der Waals attraction, aggregation results. Polymer chains however, are of sufficient dimension to avoid such sensitivity. Only in the coil-globule transition region will the change of a flexible polymer chain from an extended coil in a good solvent to a collapsed dense globule in a poor solvent sufficiently collapse the polymer to impact its ability to sterically stabilize a colloidal particle. Second, steric stabilization is equally efficient in aqueous and non-aqueous dispersion media. As can be inferred from Equation 6.1 (i.e. the thickness of the electrostatic layer is directly proportional to the dispersion medium's dielectric constant) electrostatic stabilization is not as efficient in nonaqueous dispersion medium due to the low dielectric constant of most nonaqueous media. Third is the reversibility of flocculation in steric stabilization. Flocculation of particles can simply be induced by the introduction of an incompatible dispersion medium for the stabilizing moieties, and a mere dilution of the dispersion medium is sufficient to induce spontaneous redispersion.<sup>191</sup> The thermodynamic metastability of an electrostatically stabilized system means that the coagulated state is the lowest energy state and therefore can only be reversed if work is applied to the system.<sup>191</sup> For all these reasons, steric stabilization is commonly a preferred method of stabilization and is exploited both industrially and biologically.

## B. Polymer Solution Thermodynamics – Flory Huggins Theory

Steric stabilization is a generic term that encompasses all aspects of the stabilization of colloidal particles by nonionic macromolecules. On close approach of two sterically stabilized particles, the change in the free energy,  $\Delta G_F$ , at constant temperature and pressure can be written as:

$$\Delta G_F = \Delta H_F - T\Delta S_F \quad (\text{Equation 6.3})$$

where  $T$  is the temperature and  $\Delta H_F$  and  $\Delta S_F$  are the enthalpy and entropy of close approach or flocculation respectively. In order to impart particle stabilization,  $\Delta G_F$  needs to be positive and can be achieved in three ways, as summarized in Table 6.1.<sup>191,192,195</sup> In the first case, called enthalpic stabilization, both  $\Delta H_F$  and  $\Delta S_F$  are positive; which inherently means that the enthalpic component promotes stabilization and the entropic component disfavors it. Therefore, the contribution of the enthalpy term needs to exceed the entropic term in order to achieve positive  $\Delta G_F$ . The second case, termed entropic stabilization, has both  $\Delta H_F$  and  $\Delta S_F$  negative. In contrast to the first case, the enthalpy of close approach favors flocculation whereas the entropy term opposes it. As long as the entropic contribution exceeds the enthalpic term, particle stability can be attained. In the third mechanism, both the enthalpic and entropic component promotes stabilization. This is called combined enthalpic-entropic stabilization.

**Table 6.1.** Types of steric thermodynamic stabilization

$\Delta H_F$	$\Delta S_F$	$ \Delta H_F /T \Delta S_F $	$\Delta G_F$	Type
+	+	$>1$	+	enthalpic
-	-	$<1$	+	entropic
+	-	$\leq 1$ or $\geq 1$	+	combined enthalpic-entropic

## 6.4 Results and Discussion

Thus far, several investigations have reported SWNT dispersions in aqueous media with the aid of ionic and nonionic surfactants,<sup>199-201</sup> water soluble polymers<sup>202,203</sup> and DNA.<sup>204,205</sup> In aqueous media, SWNT aggregation is hampered by micelle formation of surfactants around the SWNTs.<sup>206</sup> In the case of polymers, dispersion is achieved through polymer wrapping around the nanotube sidewalls or  $\pi$ -interaction between the aromatic rings in the polymer matrix with the graphitic framework of SWNTs. In conjunction with these studies, the stability of sterically stabilized dispersions has also been extensively investigated in order to provide insight into the thermodynamic factors that control stability.<sup>207-209</sup> The dispersions are taken to the brink of instability and the factors that induce particle flocculation or aggregation are determined. More precisely, the regions where a one-phase solution is stable and where the mixture will undergo phase separation were examined. In the discussion that follows, the critical point on a phase boundary that separates a two phase region at high temperature from a one-phase region at low temperature is called upper critical flocculation temperature (UCFT) whereas a critical point on a phase boundary that separates a two-phase region at low temperature from a one-phase region at high temperature is called a lower critical flocculation temperature (LCFT).<sup>150</sup> In principle, the system parameters that influence the

critical flocculation point (CFPT) are (I) solvency of the dispersion medium, (II) particle number concentration, (III) the nature of the anchor polymer and nanoparticle, (IV) particle size and (V) molecular weight of the stabilizing moieties.<sup>191</sup> Each of these factors will be discussed accordingly in the following discussion.

Several investigations have utilized chemically modified<sup>210,211</sup> and unmodified SWNTs<sup>212-215</sup> with or without dispersants in different amide solvents in an attempt to achieve nanoparticle homogeneity. Amongst the amide solvents, pure N,N-dimethylformamide (DMF) and N-methyl-2-pyrrolidone (NMP) are promising candidates as solvents in which nanotubes are thermodynamically soluble (i.e. negative free energy of mixing), with a dispersion limit of 7 mg/L and 10 mg/L respectively.<sup>121,216</sup> It has been suggested that solvents possessing high electron pair donating ability, a low hydrogen bond donation parameter and high solvatochromic parameter are the characteristics of good nanotube dispersing solvents. These are necessary but not sufficient conditions since dimethylsulfoxide (DMSO), a poor SWNT solvent, meets the aforementioned criteria.<sup>217</sup> Although it is possible to prepare stable dispersions of unfunctionalized SWNTs in pure organic solvents, only low concentrations can be attained. In order to increase the SWNT loading in organic solvents, polymers such as polyimides<sup>36</sup> and PMMA<sup>16</sup> are codissolved in the solvent. Hasan et al. incorporated polyvinylpyrrolidone (PVP), a linear polymer, as a dispersant molecule to stabilize SWNTs by a thermodynamically driven wrapping process of SWNTs.<sup>190</sup> Even without further ultrasonic treatment, spontaneous debundling of SWNTs is observed upon the addition of PVP. This is evidenced by a significant increase in the photoluminescence intensity upon PVP addition. In contrast to the SWNT/NMP dispersions, which form obvious aggregates

after two months in solution, the SWNT/NMP polymer solutions are stable even after one year.<sup>218</sup> The effect of dispersion medium (i.e. solvent) on the extent of nanoparticle dispersion is rather complicated since the solvent's ability to adsorb strongly on the SWNT surface enables polymer displacement by competing for available surface sites.

Experimental works that both concur and contradict with the assumption that the CFPT depends significantly upon the number concentration of particles have been published.<sup>175,219,220</sup> Everett and Stageman investigated the dependence of both UCFT and LCFT on the particle number concentration for poly(methyl methacrylate) latex particles (~200 nm in diameter) stabilized by poly(dimethylsiloxane) (molecular weight ~7000 g.mol<sup>-1</sup>) in a range of normal alkanes.<sup>220</sup> It was found that the UCFT decreased with increasing particle concentration whereas the LCFT increased as a function of latex particle concentration. In a liquid state theoretical study of a dense mixture of hard nanoparticles and flexible polymer chains, Schweizer and coworkers found that the thermodynamically stable bound polymer layers exist in the dilute nanoparticle limit whereas phase separation occurs at higher volume fractions.<sup>174</sup> In contrast, Croucher and Hair did not observe a particle concentration dependence of the UCFT of polyacrylonitrile lattices sterically stabilized by polyisobutylene (PIB) in 2-methylbutane over the latex weight fraction range studied (0.002 to 0.02).<sup>219</sup> Note that in this experiment, the molecular weight of the stabilizing moiety, PIB, was high (i.e. 760,000 g.mol<sup>-1</sup>). It can therefore be deduced that CFPT is relatively insensitive to the particle number concentration for high molecular weight stabilizing chains.

The third and most important factor that affects the solubility of SWNT in a polymer suspension is the nature of the anchor polymer (Refer to Figure 6.4). Polymers

that are effective steric stabilizers by non-covalent functionalizations include amphiphatic block or graft copolymers. In these polymers, one of the blocks should be nominally insoluble in the dispersion medium to promote its adsorption to the particle surface, while the other block should be soluble in the dispersion medium. Homopolymers are also capable of imparting steric stabilization in SWNT dispersions, although its stability is inferior to amphiphatic block copolymers.<sup>191</sup> Random copolymers, as used in our studies, usually exhibit inferior stabilization relative to block or graft counterparts. However, the utilization of random copolymers to impart steric stabilization of nanoparticle remains important due to its cost effectiveness and practical application in industry due to its easy one-pot synthesis. For instance, Tadros et al. studied the enhanced steric stabilization of polystyrene lattices by partially hydrolysed (88%) poly(vinyl alcohol) containing on average 2 ester groups for every 18 alcohol groups.<sup>191,208</sup> The resultant polymer is an intermediate between a random and blocky structure. This work confirmed that it was possible to prepare PS dispersions in the presence of poly(vinyl alcohol) that were stable in 1 Molar KCl dispersion medium. On the other hand, Napper concluded that the anchor polymer does not affect the UCFT, from their investigation of five different poly(vinyl acetate) of varying hydrophobicity that is stabilized by poly(oxyethylene) of molecular weight 10,000 g.mol<sup>-1</sup> in 0.39 M MgSO<sub>4</sub>.<sup>221</sup> It can therefore be postulated that as long as the anchor polymer is attached sufficiently strongly to the colloidal particles, its chemical nature has minimal effect on the CFPT. In our charge transfer complex system (i.e. poly(styrene-*ran*-acrylonitrile)-SWNT system), the extent of interaction between the



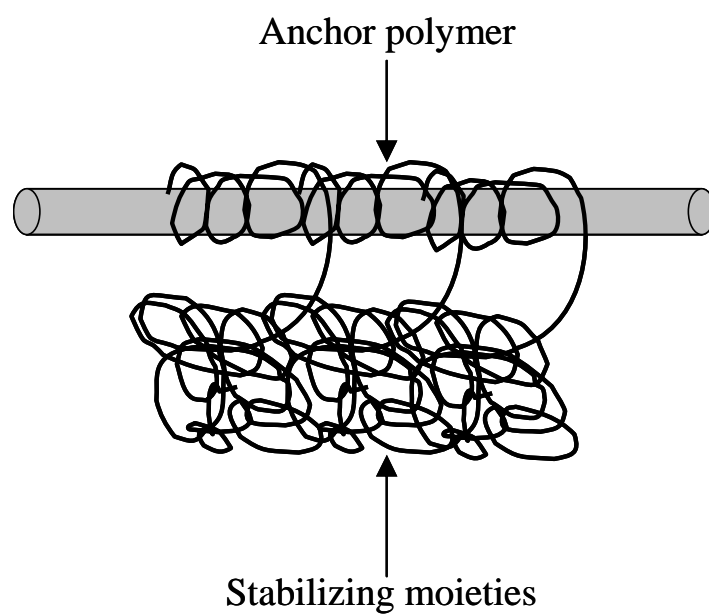


**Figure 6.4.** Schematic representation of the steric stabilization of a SWNT particle by an amphiphatic block copolymer

anchor polymers with nanoparticle is crucial in determining the extent of particle dispersion since it is a relatively weak noncovalent interaction. By the same token, the nature of the nanoparticle could also influence the onset of stability although this is not a concern in our experiment since it is a parameter that is held constant.

It is foreseeable that an increase in particle size results in the increase in van der Waals attraction between the particles, causing easier aggregation than for a smaller particle. It has been shown from computational studies by Schweizer et al. that the miscibility window narrows as the filler-monomer size asymmetry ratio grows.<sup>175</sup> However, if the stabilizing moieties are of sufficiently high molecular weight and the particle size is not too large, CFPT appears to be independent of the particle size. This has been shown by Dawkins and Taylor in their investigation of the LCFT of poly(methyl methacrylate) lattices stabilized by monodisperse poly(dimethylsiloxane) of molecular weight  $11,200 \text{ g.mol}^{-1}$  in n-heptane/ethanol (51/49 vol/vol) mixtures. The LCFT was independent of the particle size over the range of particle diameter studied (i.e. 96 nm to 480 nm).<sup>222</sup>

Finally, as mentioned previously (Section 6.3A), the CFPT is independent of molecular weight if the size of the stabilizing molecule is sufficiently high. For the sake of completion, it is restated that the chain dimension needs to be commensurable to or in excess of the range of van der Waals attraction between the colloidal particles to avoid the attraction between particles. The molecular weights of the polymers utilized in this study are greater than  $39,000 \text{ g.mol}^{-1}$ , which corresponds to r.m.s. end-to-end distance of 12 nm. This exceeds the range of the nanoparticle van der Waals attraction. Thus,

molecular weight variation can be discounted as one of the factors that affect the extent of intermolecular interaction in the sterically stabilized SWNTs studied here.

Recall that our main objectives are to develop strategies that can be employed to promote particle stability, understand the system parameters that govern the particle dispersion as well as comprehend the thermodynamics that impact the stabilization phenomena. In our effort to accomplish these goals, we have performed UV-Vis measurements (Refer to Section 2.5E for details of experiment) on the polymer nanocomposite in solution after centrifugation, bearing in mind that this process is designed to remove excess unstabilized SWNTs, which do not form intermolecular interaction with the polymer matrix. Figure 6.5 shows the optical absorbance at 500 nm of the SWNT-polymer-DMF suspensions as a function of mol% acrylonitrile in the random copolymer of styrene and acrylonitrile (SAN). The extinction coefficient,  $\epsilon$ , of SWNT in solution has been previously reported as  $0.0286 \text{ L.cm}^{-1}\text{mg}^{-1}$  at 500 nm.<sup>121</sup> With this knowledge of the extinction coefficient, Beers Law can be used to determine the concentration of SWNT that remains in solution. Figure 6.6 represents the SWNT concentration (mg/L) in suspension that participates in the formation of charge-transfer complex as a function of mol% acrylonitrile in the SAN copolymer. Since the specific chemical characteristics of the dispersion medium (i.e. DMF), particle number concentration (i.e. 1.0 wt%), nature of the nanoparticle (i.e. SWNT), and molecular weight of the stabilizing moieties ( $\sim 50,000 \text{ g.mol}^{-1}$ ) are held constant, the two system parameters that affect the extent of interaction between polymer and SWNT are the (I) nature of the anchor polymer and (II) the particle size.

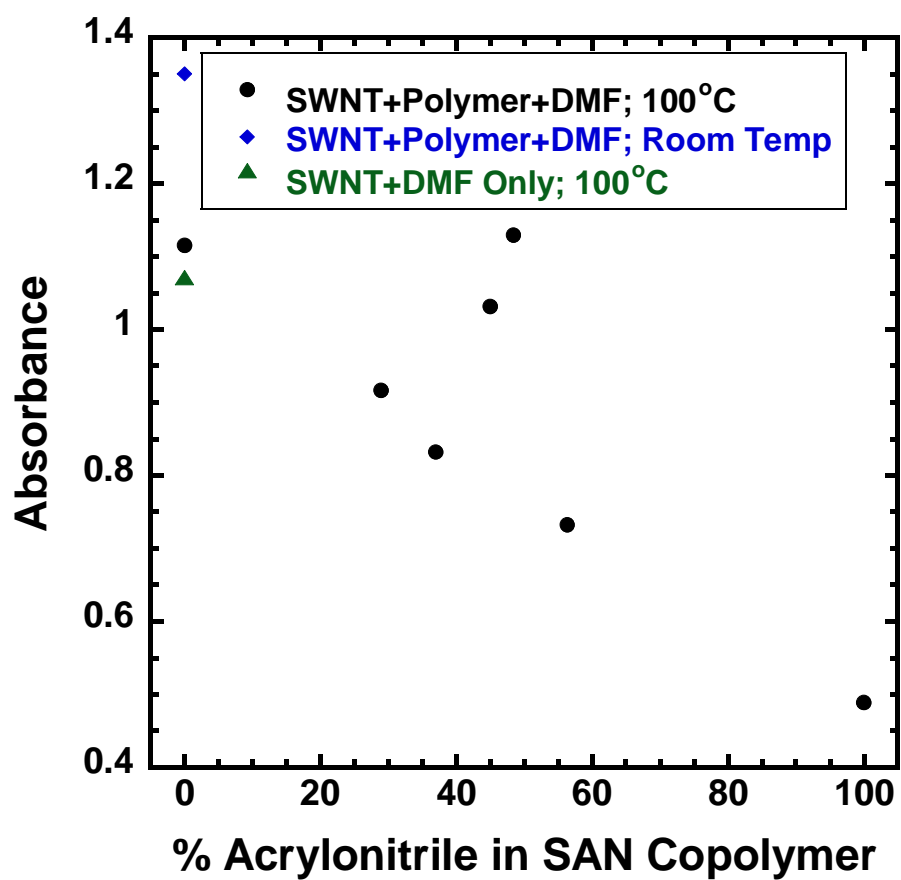


**Figure 6.5.** Absorbance at 500 nm of the SWNT material in suspension

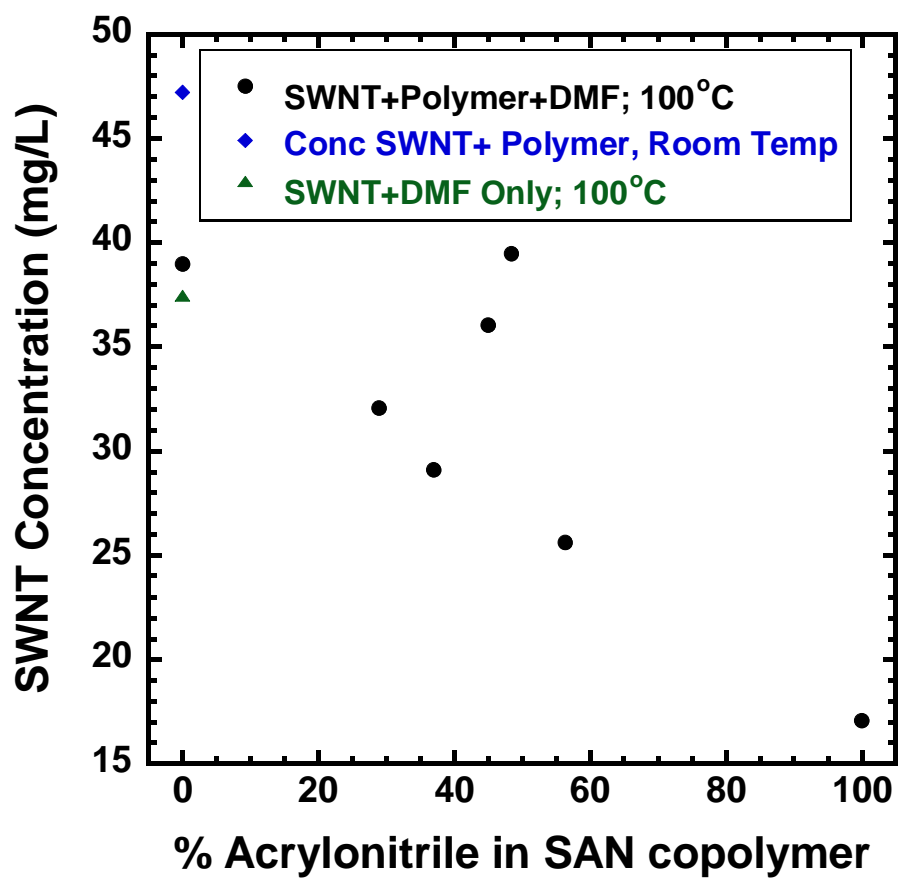


**Figure 6.6.** SWNT concentration (mg/L) in suspension after centrifugation

Initially, the absorbance of SWNT in DMF dispersion is measured as a control. As described in Section 2.5 C, all the polymer nanocomposite suspensions were subjected to heat (100 °C) during fabrication process. Additionally, one polystyrene nanocomposite sample was also prepared at room temperature. Interestingly enough, as shown in Figure 6.6, the PS nanocomposite shows that SWNT concentration increases from ~39 mg/L to ~47 mg/L when the temperature during composite preparation is decreased from 100 °C to room temperature. A more complete study is needed to more thoroughly document the impact of temperature on the ability of these polymers to sterically stabilize SWNTs, however, from these limited results, it can be inferred that it is worth constructing a phase diagram and locate the regions where the suspension is stable, and where the system undergoes nanoparticle aggregation.

At first glance, the results obtained in Figures 6.5 and 6.6, which show the optical absorbance at 500 nm and SWNT concentration, respectively, as a function of mol% acrylonitrile in the SAN copolymer, do not appear to completely agree with the optical microscopy and Raman spectroscopy data presented in Chapters 3 and 4 that document the dispersion of SWNTs in the SAN copolymers. One likely explanation for the discrepancy of the result obtained in Figures 6.5 and 6.6 with our optical microscopy and Raman spectroscopy data is that a correction factor is needed to normalize across particles of different size. The need for this correction factor stems from the fact that the extent of electron donor acceptor interaction that occurs between SWNT and polymer matrix varies depending on the amount of AN in the copolymer, thereby causing the portion of polymer matrix under influence of SWNT, called 'zone of influence' to differ. Even though we assume that the excess SWNTs have been removed by the centrifugation

process, it needs to be emphasized that due to the nature of the random copolymer, which possess both interacting and noninteracting functional groups, the adsorption of the polymer onto the SWNT occurs randomly. Strictly speaking, there exist some portion of the polymer chains that do not interact with the SWNT.

Depending on the amount of the polymer that participates in the intermolecular interaction with the SWNT or 'zone of influence', the effective sizes in the nanotube bundles or aggregates that are sterically stabilized by the polymer matrices will vary. There exist a number of parameters that can influence the effective sizes of the stabilized nanoparticles. For discussion purposes, consider sterically stabilized spherical particles, each of radius  $a$ , coated by polymer layers of thickness  $\delta$  (Figure 6.7). The overall nanoparticle-polymer complex diameter,  $H$ , is dependent upon the nature of the anchoring polymer. More specifically, as schematically illustrated in Figure 6.7 (a), if the anchor polymer interacts efficiently with the nanoparticle surface, the thickness of the sterically stabilized layer,  $\delta$  increases, and  $H$  increases. In contrast, poor intermolecular interaction between the particle and polymer matrix will cause the thickness of the bound polymer layer,  $\delta$ , to decrease, causing a decrease in the effective nanoparticle diameter,  $H$ . Recall from previous discussion that two critical factors that affect the extent of interaction in the system investigated are the (I) nature of the anchor polymer and (II) particle size. Therefore, correcting the data in Figure 6.6 for the variation in particle size, the nature of the anchor polymer becomes the dominant factor controlling the amount of SWNT that is stabilized by the charge transfer complex. Therefore, this analysis provides insight into the effectiveness of the SAN copolymers at stabilizing SWNT in solution, presumably by adsorbing onto the SWNT carbon cage.

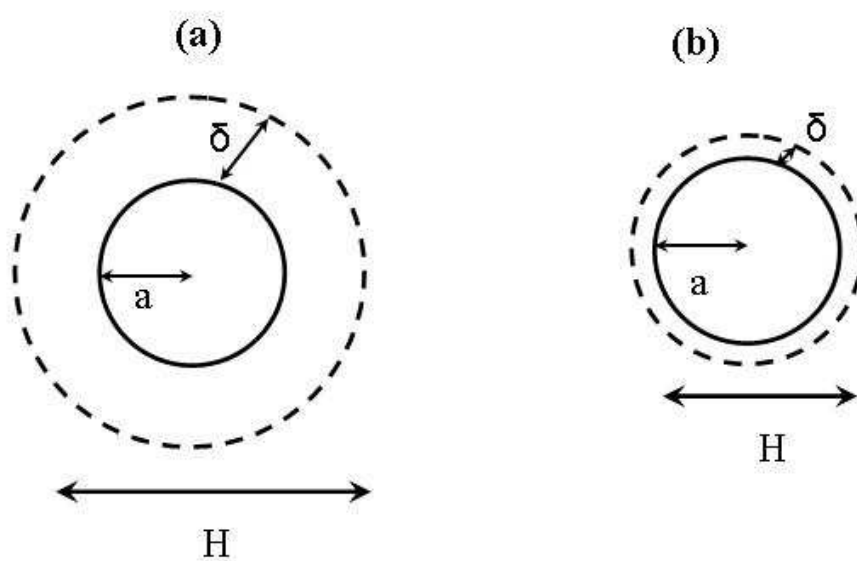


**Figure 6.7.** Schematic representation of two sterically stabilized particles with (a) thicker and (b) thinner bound polymer layers



Therefore, the next step in this investigation is to obtain the hydrodynamic diameter of the nanoparticles (in nm) that participate in EDA interaction with polymer matrix, using dynamic light scattering experiment and is shown in Figure 6.8 as a function of AN composition in the SAN copolymer. The results indicate that accounting for variation in dispersed nanoparticle size, the results more readily correlate to the measured dispersion in the resultant nanocomposites. For instance, the SWNTs that are stabilized by polystyrene, which is expected to be the weakest anchor polymer, has the smallest hydrodynamic diameter, presumably due to the formation of a very thin sterically stabilized layer around the nanoparticle and results in a small effective nanoparticle diameter,  $H$  (370 nm). The nanoparticle diameter increases as the % acrylonitrile in the copolymer increases, which can be attributed to an increase in the size of the bound layer. Polyacrylonitrile, which is expected to readily wrap around the nanotubes or its bundles, forms a larger thermodynamically stable bound layer which resists interpenetration or desorption. This causes an apparent increase in the effective nanoparticle diameter,  $H$ .

To correct for the variation in nanoparticle size, the concentration, in units of  $\text{mg}/\text{cm}^3$ , is multiplied by the hydrodynamic diameter, in units of cm, which is considered the correction factor, and the result gives the amount of SWNT participating in the polymer adsorption per unit area of the polymer under the 'zone of influence' in  $\text{mg}/\text{cm}^2$ . Figure 6.9 shows a plot of SWNT concentration x effective particle diameter as a function of percent acrylonitrile in SAN copolymer. After the treatment of the data by the correction factor, the polystyrene nanocomposite has the smallest effective concentration of SWNT in the suspension, which indicates its limited ability to efficiently stabilize the

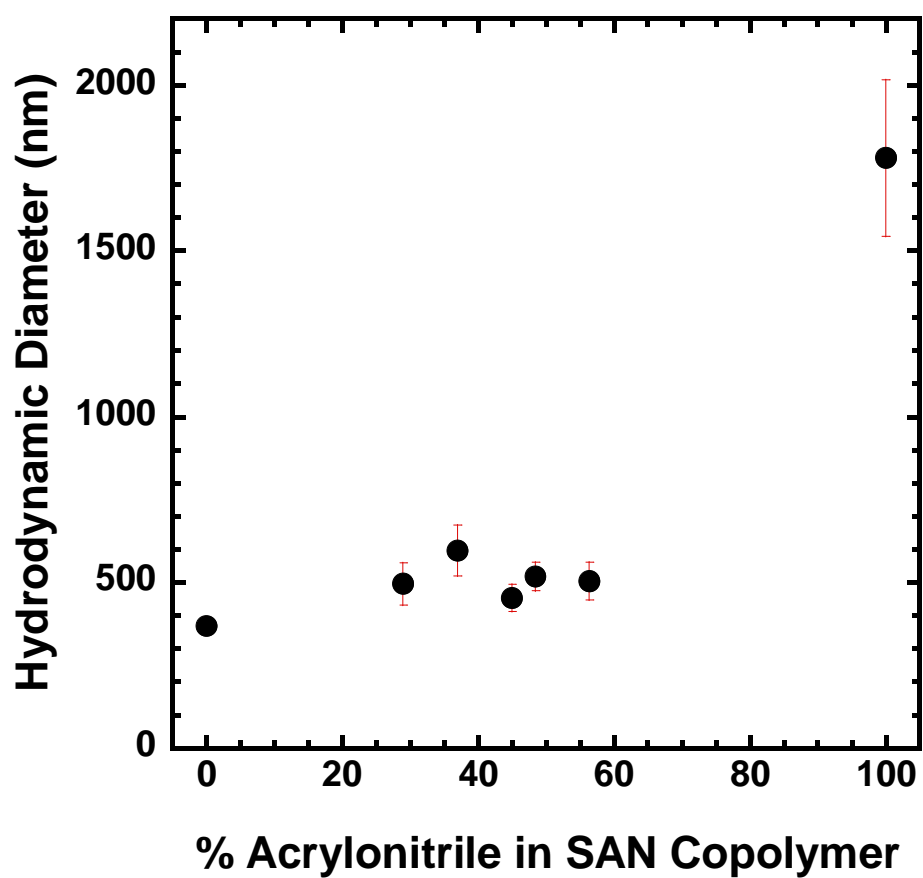


**Figure 6.8.** Effective nanoparticle diameter (in nanometer) in suspension from dynamic light scattering (DLS)

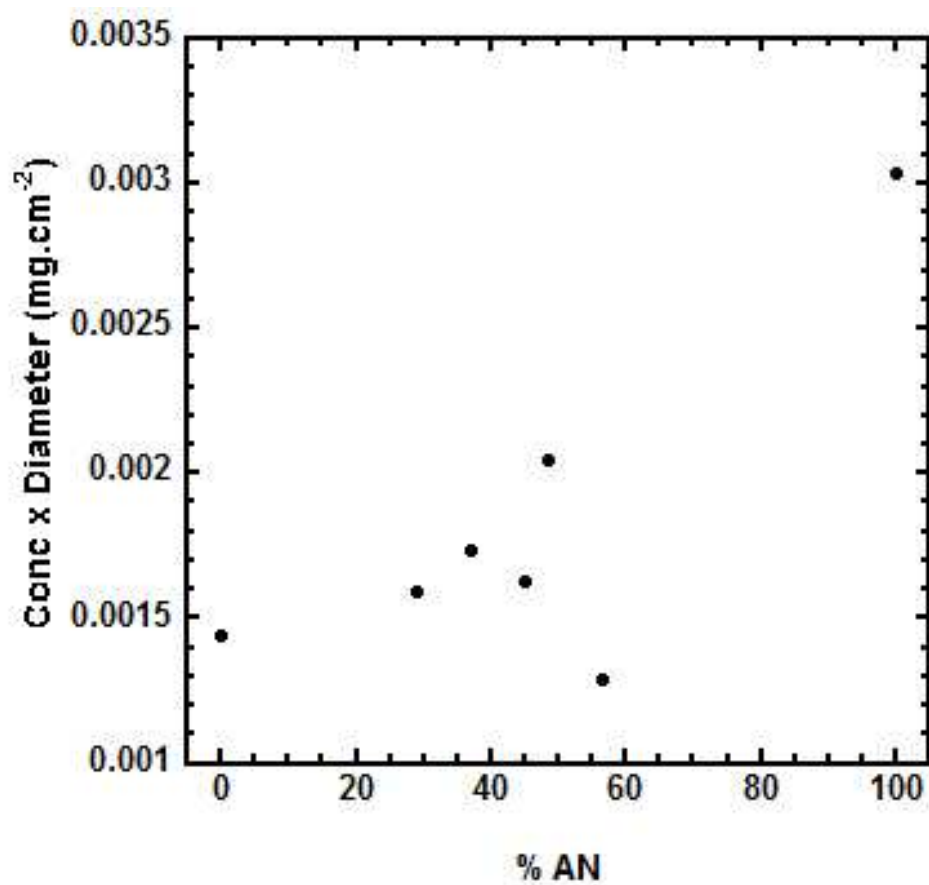


**Figure 6.9.** SWNT concentration x particle size in suspension as a function of percent acrylonitrile in SAN copolymer

nanoparticle, presumably due poor interaction with the SWNTs. This suggests that the weak  $\pi$ - $\pi$  interaction between the aromatic rings on polystyrene and the graphitic framework of SWNT do not readily overcome the strong van der Waals interparticle forces that exist between the SWNTs. At such a low extent of intermolecular attraction, the system experiences nanoparticle aggregation due to the large depletion attraction between the particles. As the mol% AN increases from 29 mol% to 48.5 mol%, the extent of attraction between SWNT and polymer increases, indicated by the increase in the amount of SWNT in the suspension. The depletion attraction now diminishes and steric stabilization is realized due to the enthalpic gain of polymer segments adsorbing onto the particle surface. However, further increasing the amount of acrylonitrile to 56 mol% results in a decrease in dispersed SWNT. This may be explained in that the entropic component of steric stabilization now dominates due to the close proximity between AN monomers along the polymer chain, thereby causing the hindrance of acrylonitrile accessibility in forming the charge transfer complex with the SWNT. The PAN composite very effectively sterically stabilizes the SWNT in solution. Due to its chain flexibility, wrapping of PAN polymer chains around the SWNT carbon cage is efficiently realized, resulting in the formation of a very thick sterically stabilized layer.

Without further experimental investigations and concrete evidence however, the above explanation serves merely as a conjecture to the physical events that take place in the multi-component system. Nevertheless, it sets a good platform for devising future experiments in an effort to more fully understand the mechanism by which intermolecular interaction in suspension forms and the underlying parameters that govern it. Gathering from the experiments that have been performed thus far, numerous questions can be

raised. What is the effect of the solubility parameter of the dispersion medium on the competition between solvent and polymer for available anchoring sites on the SWNT as well as the resulting dispersion of the nanoparticle in the suspension? Based on the findings from previous experiment,<sup>175,219,220</sup> we have also arrived upon the postulation that the critical flocculation point (CFPT) is relatively insensitive to the particle number concentration for sufficiently high molecular weight stabilizing chains. Therefore, what is the critical molecular weight that is commensurable to or in excess of the range of van der Waals attraction? Although a polymer chain molecular weight of roughly above  $\sim 10,000 \text{ g.mol}^{-1}$  has been estimated to be sufficient for imparting polymeric colloidal stability, this is contingent upon the ability of the polymer to generate repulsion between the nanoparticles. This leads to the need for the study of the effect of the polymer's surface chemistry and curvature of nanoparticle (e.g spherical fullerene and planar graphene) on the extent of charge-transfer complex formation and polymeric stabilization. It is also of great interest to investigate the molecular architecture effect on the thermodynamics of the polymer nanocomposite suspension. More specifically, will a blocky SAN copolymer exhibit better SWNT dispersion in DMF in comparison with a random copolymer? Although it is challenging to construct a phase diagram and relate it to the aforestated factors that induce the onset of flocculation, the utilization of both theoretical studies and experimental investigations is imperative in order to articulate the physical mechanism that occurs in the multi-component system.

## **6.5 Conclusion**

In this chapter, we have presented results that have begun the investigation of steric stabilization of SWNT in solution by copolymers that can form electron donor-

acceptor interactions with the SWNT. These results demonstrate that SWNT dispersions in pure N,N-dimethyl formamide (DMF) are stabilized by the adsorption of common commodity polymers such as styrene-*ran*-acrylonitrile and polyacrylonitrile onto the SWNTs. An interplay between the solvency of the dispersion medium, particle number concentration, the nature of anchor polymer and nanoparticle, particle size and molecular weight of the stabilizing moieties play a critical role in determining the SWNT nanoparticle stability. Previous work in this area has mostly focused on spherical polymeric fillers. The presented results provide a foundation from which a more complete understanding of the fabrication process of polymer nanocomposites from solution can be obtained. Ongoing research in our laboratory will expand this work to other copolymers and more complex fillers such as disks and deformable microgels.

## CHAPTER 7: CONCLUSIONS AND FUTURE WORK

### 7.1 Final Conclusion

The scientific literature devoted to polymer nanocomposites (PNC) is both immense and growing. However, due to difficulties in the characterization of these nanoscale fillers as a result of their structural heterogeneity, a complete understanding of the influence of particle-polymer intermolecular interactions on particle dispersion in PNC lags behind materials development. This leads to a proliferation of conflicting claims and little consensus on a global strategy for nanocomposite research or credible end-use targets. It is therefore our ultimate goal to minimize the gap between the fundamental understanding of PNC dispersion and structure and progress in materials development. Specifically, we are interested in developing a universal strategy to reproducibly tune the structure and material properties by control of the interfacial phenomenon in PNC, which dictate the ultimate characteristics of the material.

The extensive experimental and theoretical work<sup>142</sup> that is presented in this dissertation demonstrates that we have successfully developed a protocol for the optimization of a non-covalent (i.e. charge transfer) intermolecular interaction between polymer matrix and single-walled carbon nanotubes (SWNT), which serves to improve ultimate nanoparticle dispersion while still preserving the intrinsic properties of the pristine SWNTs. From the D\* band peak shift in Raman spectroscopy results presented in Chapter 3, it is clearly evident that the presence of a minority of interacting functional group (i.e. DMA30, SAN45, CNSt24) within a polymer chain leads to an optimum interfacial adhesion. In our results, an upshift in the D\* band is interpreted to originate

from compressive forces that are transferred from the polymer to the SWNTs while negative shifts indicate that the internal pressure within the carbon nanotube bundles is relieved by the formation of EDA complex between the polymer matrix and SWNT. The D\* band downshifts for nanocomposite samples that contain polymers with electron withdrawing acrylonitrile (AN) and cyanostyrene (CNSt) indicates that they are more effective in forming the electron-donor-acceptor complex relative to polymers containing the electron donating 2-(dimethylamino) ethyl methacrylate (DMAEMA), which shows D\* band upshifts. In contrast to homopolymers of polystyrene (PS), poly (methyl methacrylate) (PMMA) and polycyanostyrene (PCNSt), polyacrylonitrile (PAN) shows anomalously good intermolecular interaction with SWNT, attributed to its chain flexibility.

The aforementioned results led to the investigation of correlation of the extent of the SWNT-polymer intermolecular interaction and the nanoparticle dispersion in the polymer matrix. Does the optimum intermolecular interaction translate to enhanced SWNT dispersion? Qualitative experimental results by thick film composite visualization and optical microscopy as well as quantitative results by Raman mapping, indicate a direct correlation between the extent of intermolecular interaction and nanocomposite dispersion. Thick film composites composed of polymers that adhere weakly to the SWNT, such as PMMA and PS, show significant particle aggregation and opacity in comparison with composites containing polymers that have good adhesion with SWNT (e.g. DMA30, SAN45, CNSt24), which show homogeneity throughout the entire sample. Aggregate size analysis of the optical micrographs of the DMA series of nanocomposites also indicates that the DMA30 composite has the smallest aggregate size, signifying the best nanoparticle dispersion and further validates our claim that optimum intermolecular



interaction directly correlates to enhanced SWNT dispersion. Although quantitative results could not be obtained due to the resolution of optical microscopy, the optical micrographs of SAN and CNSt composites show minimal nanotube aggregates indicating that they are better dispersed than the DMA composites.

Raman imaging provides method to quantify the SWNT dispersion with slightly better resolution than optical microscopy ( $\sim 1\ \mu\text{m}$ ). This technique clearly demonstrates that the SWNTs in the SAN and CNSt are distributed throughout the sample, even in areas that appear optically clear. Utilizing this more robust Raman mapping method, the extent of SWNT dispersion is quantified by the ratio of the average-G band intensity in the clear region ( $I_{clear}^G$ ) of the composite to the average G-band intensity in the aggregated region ( $I_{agg}^G$ ). The level of dispersion obtained from this method directly correlates to the extent of SWNT-polymer interaction obtained from the D\* band shifts.

In order to provide additional insight into the formation of EDA interactions between monomers and SWNT, density functional theory (DFT) calculation was performed by our collaborator, Dr. Bobby Sumpter. The binding energies obtained from the DFT calculation corroborate well with our experimental results, where the binding energy with the SWNT orders as CNSt (10 kcal/mol), AN (4.5 kcal/mol), and DMAEMA (0.31 kcal/mol), in agreement with our experimental results that indicate that the CNSt moiety disperses the nanofiller best, followed by AN and DMAEMA. In addition, the optimized geometry of a cyanostyrene trimer as determined by DFT calculation illustrates how the polymer must adopt a conformation that differs from the monomer optimized geometry due to the effect of chain connectivity. In this system, only the

monomers at the ends contribute to the total binding energy in the system, whereas the middle cyanostyrene monomer does not interact with the SWNT.

All of these results indicate that geometric constraint is a critical entropic parameter that controls the formation of non-covalent interactions in PNC. To provide a physical view towards understanding this process, consider a polymer chain that has one functional group that participates in an intermolecular interaction with one SWNT. This EDA complex formation will consequently inhibit the propensity of an adjacent functional group on the chain to access and orient itself correctly to form an additional interfacial interaction. When functional groups are adequately spaced out along the polymer chain, the geometrical constraint effect is lessened because this creates a dynamically independent functional group and the formation of one intermolecular interaction does not inhibit the formation of an additional interaction with the SWNT. On the other end of the spectrum however, too large of a separation of functional groups in a polymer chain is also unfavorable since intermolecular interaction would be hindered by the limited amount of functional groups for an interaction to occur. In addition, polymer chain flexibility also plays a role in the formation of non-covalent interaction since this affects the ability of a polymer chain to conform itself favorably to the nanotube cage, which explains the observed beneficial intermolecular adhesion between polyacrylonitrile and SWNT. Therefore, the importance of polymer chain connectivity effects cannot be overlooked and this explains the occurrence of an optimal intermolecular interaction and particle dispersion when a moderate amount of functional groups exist along the polymer chain.

In our effort to obtain a precise understanding of and control over the morphology of these nanoparticle entities, we have also performed small-angle neutron and x-ray scattering on polyacrylonitrile (PAN) nanocomposites containing varying amount of SWNTs (Chapter 5). Although a definitive conclusion has not been attained at this point, the presence of microphase separation-like scattering peaks in the scattering patterns of PAN composite suggests an ordering of the PAN polymer around the carbon nanotube cage. Whether this indicates the existence of a thermodynamically bound layer around the SWNT or the occurrence of SWNT-induced PAN crystallization is a subject of an ongoing research in our laboratory.

The experimental results presented above focused on the final dry-state SWNT-polymer nanocomposite. However, the specific structure of the polymer-SWNT nanocomposite is certainly influenced by the preparation procedure, where the polymer and SWNT are initially both in solution. This stimulated our interest in studying the thermodynamic behavior of polymer stabilized nanoparticles in solution, where the interactions that influence the structure in solution include solvent-solvent, solvent-polymer, and solvent-SWNT interactions in addition to polymer-polymer, SWNT-SWNT and SWNT-polymer interactions that exist in a two-component system. UV-Vis spectroscopy measurement was performed to determine the SWNT concentrations that are stabilized by polymer adsorption in solution (Chapter 6). Initial experiments correlate reasonably well with the optical microscopy and Raman spectroscopy data. However, further experiments are required in order to gain a complete physical picture of the colloidal stabilization of the SWNT in solution by adsorbed polymer as well as to

develop a more complete understanding of the governing parameters that control nanoparticle dispersion in this fabrication process.

## 7.2 Future Work

Thus far, the series of experimental studies that were completed to drive the advancement of this PNC research has been discussed with the goal of highlighting the underlying physical principles and phenomena governing the polymer-SWNT interfacial behavior and the resulting nanoparticle dispersion. But, as with much scientific research, the results open new avenues of study as well as provide insight into controlling the polymer nanocomposite dispersion.

Of extreme importance in the field of polymer nanocomposites is the establishment of a quantitative understanding of the “nano” effect or surface to volume ratio of the filler as it relates to the change in specific material properties. Due to the small size and concurrently large surface area of nano-sized fillers, there exists a large fraction of polymers that are influenced by the nanoparticle interface, which is perturbed with respect to those in the bulk. Therefore, the magnitude of property change or control by the interfacial region is dictated by the total quantity of the interfacial area within a nanocomposite. Two critical factors that affect the surface-to-volume ratio and ultimately dictate the overall polymer nanocomposite properties are the (I) size and (II) shape of the nanofillers.<sup>39,223</sup> In order to illustrate the effect of nanofiller’s size, consider a spherical particle with radius  $r$ . The surface to volume ratio of the filler can be written as:

$$\frac{A_s}{V_s} = \frac{4\pi r^2}{4/3\pi r^3} \frac{3}{r} \quad (\text{Equation 7.1})$$

Equation 7.1 demonstrates that the available surface area ( $A_s$ ) per volume ( $V_s$ ) of filler increases as the spherical radius decreases. In a nanocomposite with filler volume fraction  $\phi$ , the total interfacial area-to-volume ratio scales linearly with  $\phi$ , where:

$$\frac{A_{i,total}}{V_{total}} = \frac{3\phi}{r} \quad (\text{Equation 7.2})$$

Equation 7.2 implies two possible scenarios. First, if  $\phi$  is held constant, the decrease in filler radius results in the increase in available surface area for intermolecular interactions. Second, this relationship demonstrates that two composites with identical surface areas can be fabricated with different filler sizes by the control of filler volume fraction.

In addition, shape also plays a role in the design of surface-to-volume ratios for nanocomposites. For a cylindrical filler of radius  $r$  and length  $L$ , the surface to volume ratio of the filler is:

$$\frac{A_c}{V_c} = \frac{2\pi r^2 + 2\pi rL}{\pi r^2 L} = \frac{2}{r} + \frac{2}{L} \quad (\text{Equation 7.3})$$

At equal volume fraction, the surface-to volume (SV) ratio for a spherical nanoparticle relative to a cylindrical nanoparticle scales as:

$$\frac{SV_s}{SV_c} = \frac{3}{2(1 + r/L)} \quad (\text{Equation 7.4})$$

This relationship demonstrates that for all plates ( $r > L$ ) and short rods ( $L < 2r$ ), the surface to volume ratio for cylindrical fillers is greater than the ratio for a spherical particle.

However, spherical fillers have greater surface to volume ratio compared to long fibers if  $L > 2r$ . Therefore, maximizing the quantity of interfacial region is a critical design factor for the development of optimal properties in filled nanocomposites.

Bearing the “nano” effect described above in mind, several questions or issues can be raised and pursued for future investigations:

1. What is the role of the size and shape of the nanoparticles on the intermolecular interaction between polymer and nanoparticle as well as the corresponding nanoparticle spatial dispersion? Preliminary density functional theory (DFT) calculation of the binding energy between a fullerene particle and monomer, performed by Dr. Bobby Sumpter, shows that the pentagon rings in  $C_{60}$ , a spherical nanoparticle, forms a considerably stronger interaction with the tertiary amino group in DMAEMA, relative to CNSt and AN monomers. This is clearly in contrast to the interaction formation of a SWNT, where DMAEMA is shown to form weak intermolecular interactions with SWNT, as evidenced both theoretically and experimentally. To examine this further, an ongoing research investigation in our group utilizes UV-Vis spectroscopy and x-ray diffraction to quantify the miscibility limit of  $C_{60}$  with the incorporation of electron donor-acceptor interactions between the polymer and fullerene.
2. We have also clearly established that optimal intermolecular interaction is directly correlated to particle spatial dispersion. However, does it translate to the attainment of enhanced mechanical, electrical and thermal properties of the PNC? In addition, what is the consequence of the “nano” effect on these properties? Therefore,

experiments such as tensile testing, direct current (DC) measurements and four-point probe resistance measurements are worth pursuing.

3. We have observed a microphase-separation like scattering peak in polyacrylonitrile nanocomposites. In order to provide further insight into the role of SWNTs on shaping the ordering of polyacrylonitrile, wide angle X-ray diffraction and differential scanning calorimetry measurements can be carried out. Once the origin of this peak has been determined, it is also worth investigating the effect of size and shape of the particle, filler volume fraction and surface chemistry on the particle structural arrangement in the multi-component system.
4. In Chapter 6, we have performed preliminary studies that set a good platform for further experiments to develop an understanding of the mechanism by which intermolecular interactions between polymers and SWNT form in solution, resulting in a sterically stabilized nanoparticle, and the underlying parameters that govern its formation. Devising experiments to determine the effect of the dispersion medium's solubility parameter, particle number concentration, molecular weight of polymer chain, size and shape of nanoparticle, surface chemistry and polymer molecular architecture on the intermolecular interaction formation and particle stabilization are worth pursuing in order to generate a phase diagram and relate it to the aforesaid factors that can be manipulated to control particle aggregation.

## REFERENCES



## REFERENCES:

- (1) Harris, P. J. F. *Carbon Nanotube Science: Synthesis, Properties and Applications*; Cambridge University Press: Cambridge, UK, 2009.
- (2) Dresselhaus, M. S.; Dresselhaus, G.; Avouris, P. *Carbon Nanotubes: Synthesis, Structure, Properties, and Applications*; Springer, 2000.
- (3) Moore, A. W.; et al. *British Journal of Applied Physics* **1962**, *13*, 393.
- (4) Ubbelohde, A. R. *Nature* **1968**, *220*, 434.
- (5) Blackman, L. C.; Ubbelohde, A. R.; Saunders, G. *Proceedings of the Royal Society of London Series A-Mathematical and Physical Sciences* **1961**, *264*, 19.
- (6) Oberlin, A.; Endo, M.; Koyama, T. *Carbon* **1976**, *14*, 133.
- (7) Oberlin, A.; Endo, M.; Koyama, T. *J. Cryst. Growth* **1976**, *32*, 335.
- (8) Kroto, H. W.; Heath, J. R.; O'Brien, S. C.; Curl, R. F.; Smalley, R. E. *Nature* **1985**, *318*, 162.
- (9) Heath, J. R. *ACS Symposium Series* **1992**, *481*, 1.
- (10) Iijima, S. *Nature* **1991**, *354*, 56.
- (11) Iijima, S. *Nature* **1991**, *354*, 56.
- (12) Iijima, S.; Ichihashi, T. *Nature* **1993**, *363*, 603.
- (13) Bethune, D. S.; Kiang, C. H.; Vries, M. S. d.; Gorman, G.; Savoy, R.; Vazquez, J.; Beyers, R. *Nature* **1993**, *363*, 605.
- (14) *Carbon Nanotubes: Science and Application*; Meyyappan, M., Ed.; CRC Press, 2005.
- (15) Loiseau, A.; Salvetat, J.-P.; Launois, P.; Petit, P.; Roch, S. *Understanding Carbon Nanotubes: From Basics to Applications*, 2006.
- (16) Winey, K. I.; Vaia, R. A. *MRS Bulletin* **2007**, *32*, 314.
- (17) Burghard, M. *Surface Science Reports* **2005**, *58*, 1.
- (18) Martel, R. *ACS Nano* **2008**, *2*, 2195.
- (19) Vivekchand, S. R. C.; Jayakanth, R.; Govindaraj, A.; Rao, C. N. R. *Small* **2005**, *1*, 920.

- (20) Ying, Y.; Saini, R. K.; Liang, F.; Sadana, A. K.; Billups, W. E. *Organic Letters* **2003**, *5*, 1471.
- (21) Bahr, J. L.; Tour, J. M. *Journal of Materials Chemistry* **2002**, *12*, 1952.
- (22) Huang, J.-E.; Li, X.-H.; Xu, J.-C.; Li, H.-L. *Carbon* **2003**, *41*, 2731.
- (23) Chen, J.; Liu, H.; Weimer, W. A.; Halls, M. D.; Waldeck, D. H.; Walker, G. C. *Journal of American Chemical Society* **2002**, *124*, 9034.
- (24) Baskaran, D.; Mays, J. W.; Bratcher, M. S. *Chem. Mat.* **2005**, *17*, 3389.
- (25) Mitchell, C. A.; Bahr, J. L.; Arepalli, S.; Tour, J. M.; Krishnamoorti, R. *Macromolecules* **2002**, *35*, 8825.
- (26) McIntosh, D.; Khabashesku, V. N.; Barrera, E. V. *Journal of Physical Chemistry C* **2007**, *111*, 1592.
- (27) Zhu, J.; Peng, H.; Rodriguez-Macias, F.; Margrave, J. L.; Khabashesku, V. N.; Imam, A. M.; Lozano, K.; Barrera, E. V. *Advanced Functional Materials* **2004**, *14*, 643.
- (28) Namilae, S.; Chandra, N.; Shet, C. *Chemical Physics Letters* **2004**, *387*, 247.
- (29) Bergeret, C.; Cousseau, J.; Fernandez, V.; Mevellec, J.-Y.; Lefrant, S. *Journal of Physical Chemistry C* **2008**, *112*, 16411.
- (30) Bahr, J. L.; Yang, J. P.; Kosynkin, D. V.; Bronikowski, M. J.; Smalley, R. E.; Tour, J. M. *Journal of the American Chemical Society* **2001**, *123*, 6536.
- (31) Georgakilas, V.; Kordatos, K.; Prato, M.; Guldi, D. M.; Holzinger, M.; Hirsch, A. *Journal of the American Chemical Society* **2002**, *124*, 760.
- (32) Strano, M. S.; Dyke, C. A.; Usrey, M. L.; Barone, P. W.; Allen, M. J.; Shan, H. W.; Kittrell, C.; Hauge, R. H.; Tour, J. M.; Smalley, R. E. *Science* **2003**, *301*, 1519.
- (33) Georgakilas, V.; Voulgaris, D.; Vazquez, E.; Prato, M.; Guldi, D. M.; Kukovecz, A.; Kuzmany, H. *Journal of the American Chemical Society* **2002**, *124*, 14318.
- (34) Kashiwagi, T.; Fagan, J.; Douglas, J. F.; Yamamoto, K.; Heckert, A. N.; Leigh, S. D.; Obrzut, J.; Du, F.; Lin-Gibson, S.; Mu, M.; Winey, K. I.; Haggenueller, R. *Polymer* **2007**, *48*, 4855.
- (35) Delozier, D. M.; Watson, K. A.; Smith, J. G.; Clancy, T. C.; Connell, J. W. *Macromolecules* **2006**, *39*, 1731.
- (36) Wise, K. E.; Park, C.; Siochi, E. J.; Harrison, J. S. *Chemical Physics Letters* **2004**, *391*, 207.

- (37) Liu, A.; Honma, I.; Ichihara, M.; Zhou, H. *Nanotechnology* **2006**, *17*, 2845.
- (38) Baskaran, D.; Mays, J. W.; Bratcher, M. S. *Polymer* **2005**, *46*, 5050.
- (39) Schadler, L. S.; Kumar, S. K.; Benicewicz, B. C.; Lewis, S. L.; Harton, S. E. *MRS Bulletin* **2007**, *32*, 335.
- (40) Barber, A. H.; Cohen, S. R.; Wagner, H. D. *Applied Physics Letters* **2003**, *82*, 4140.
- (41) Calleja, F. J. B.; Giri, L.; Asano, T.; Mieno, T.; Sakurai, S.; Ohnuma, M.; Sawatari, C. *J. Mater. Sci.* **1996**, *31*, 5153.
- (42) Chae, H. G.; Minus, M. L.; Kumar, S. *Polymer* **2006**, *47*, 3494.
- (43) Chang, T.-E.; Kisliuk, A.; Rhodes, S. M.; Brittain, W. J.; Sokolov, A. P. *Polymer* **2006**, *47*, 7740.
- (44) Chatterjee, T.; Yurekli, K.; Hadjiev, V. G.; Krishnamoorti, R. *Advanced Functional Materials* **2005**, *15*, 1832.
- (45) Ci, L.; Bai, J. *Composites Science and Technology* **2006**, *66*, 599.
- (46) Csempesz, F. *Colloid Journal* **1997**, *59*, 80.
- (47) Du, F.; Scogna, R. C.; Zhou, W.; Brand, S.; Fischer, J. E.; Winey, K. I. *Macromolecules* **2004**, *37*, 9048.
- (48) Duro, R.; Souto, C.; GÃmez-Amoza, J.; MartÃnez-Pacheco, R.; Concheiro, A. In *Drug Development & Industrial Pharmacy*; Taylor & Francis Ltd: 1999; Vol. 25, p 817.
- (49) Garg, A.; Sinnott, S. B. *Chemical Physics Letters* **1998**, *295*, 273.
- (50) *Polymer Adsorption and Dispersion Stability*; Goddard, E. D.; Vincent, B., Eds.; American Chemical Society: Washington D.C., 1984.
- (51) Rasheed, A.; Chae, h. G.; Kumar, S.; Dadmun, M. D. *Polymer* **2006**, *47*, 4734.
- (52) Rasheed, A.; Dadmun, M. D.; Ivanov, I.; Britt, P. F.; Geohegan, D. B. *Chem. Mat.* **2006**, *18*, 3513.
- (53) Panhuis, M. i. h.; Maiti, A.; Dalton, A. B.; Noort, A. v. d.; Coleman, J. N.; McCarthy, B.; Blau, W. J. *Journal of Physical Chemistry B* **2003**, *107*, 478.
- (54) McCarthy, B.; Coleman, J. N.; Czerw, R.; Dalton, A. B.; Panhuis, M. i. h.; Maiti, A.; Drury, A.; Bernier, P.; Nagy, J. B.; Lahr, B.; Byrne, H. J.; Carroll, D. L.; Blau, W. J. *Journal of Physical Chemistry B* **2002**, *106*, 2210.

- (55) Chen, H.; Xue, Q.; Zheng, Q.; Xie, J.; Yan, K. *Journal of Physical Chemistry C* **2008**, *112*, 16514.
- (56) Wagner, H. D.; Lourie, O.; Feldman, Y.; Tenne, R. *Applied Physics Letters* **1998**, *72*, 188.
- (57) Wagner, H. D. *Chemical Physics Letters* **2002**, *361*, 57.
- (58) Collins, P. G.; Bradley, K.; Ishigami, M.; Zettl, A. *Science* **2000**, *287*, 1801.
- (59) Kong, J.; Franklin, N. R.; Zhou, C.; Chapline, M. G.; Peng, S. *Science* **2000**, *287*, 622.
- (60) Claye, A.; Rahman, S.; Fischer, J. E.; Sirenko, A.; Sumanasekera, G. U.; Eklund, P. C. *Chemical Physics Letters* **2001**, *333*, 16.
- (61) Shim, M.; Ozel, T.; Gaur, A.; Wang, C. *Journal of American Chemical Society* **2006**, *128*, 7522.
- (62) Wood, J. R.; Frogley, M. D.; Meurs, E. R.; Prins, A. D.; Peijs, T.; Dunstan, D. J.; Wagner, H. D. *Journal of Physical Chemistry B* **1999**, *103*, 10388.
- (63) Wood, J. R.; Frogley, M. D.; Prins, A. D.; Dunstan, D. J.; Wagner, H. D. *High Pressure Research* **2000**, *18*, 153.
- (64) Wood, J. R.; Huang, Y.; Young, R. J.; Marom, G. *Composites Science and Technology* **1995**, *55*, 223.
- (65) Wood, J. R.; Wagner, H. D. *Applied Physics Letters* **2000**, *76*, 2883.
- (66) Wood, J. R.; Zhao, Q.; Frogley, M. D.; Meurs, E. R.; Prins, A. D.; Peijs, T.; Dunstan, D. J.; Wagner, H. D. *Physical Review B* **2000**, *62*, 7571.
- (67) Zhao, Q.; Wood, J. R.; Wagner, H. D. *Applied Physics Letters* **2001**, *78*, 1748.
- (68) Zhao, Q.; Wood, J. R.; Wagner, H. D. *Journal of Polymer Science: Part B: Polymer Physics* **2001**, *39*, 1492.
- (69) Lourie, O.; Wagner, H. D. *Journal of Materials Research* **1998**, *13*, 2418.
- (70) Barton, A. F. M. *Handbook of Solubility Parameters and Other Cohesion Parameters*; 2<sup>nd</sup> ed.; CRC Press: Boca Raton, 1991.
- (71) Petkov, V.; Billinge, S. J. L.; Vogt, T.; Ichimura, A. S.; Dye, J. L. *Physical Review Letters* **2002**, *89*, 075502.
- (72) Ichimura, A. S.; Dye, J. L.; Camblor, M. A.; Villaescusa, L. A. *Journal of the American Chemical Society* **2002**, *124*, 1170.

- (73) Bilc, D.; Mahanti, S. D.; Quarez, E.; Hsu, K.-F.; Pcionek, R.; Kanatzidis, M. G. *Physical Review Letters* **2004**, 93, 146403.
- (74) Billinge, S. J. L.; Levin, I. *Science* **2007**, 316, 561.
- (75) Brown, J. M.; Anderson, D. P.; Justice, R. S.; Lafdi, K.; Belfor, M.; Strong, K. L.; Schaefer, D. W. *Polymer* **2005**, 46, 10854.
- (76) Foster, J.; Singamameni, S.; Kattumenu, R.; Bliznyuk, V. *Journal of Colloid and Interface Science* **2005**, 287, 167.
- (77) Park, C.; Ounaies, Z.; Watson, K. A.; Crooks, R. E.; Jr., J. S.; Lowther, S. E.; Connell, J. W.; Siochi, E. J.; Harrison, J. S.; Clair, T. L. S. *Chemical Physics Letters* **2002**, 364, 303.
- (78) Reimer, L. *Transmission Electron Microscopy*; 4th Edition ed.; Springer New York, 1997.
- (79) Chen, Q.; Saltiel, C.; Manickavasagam, S.; Schadler, L. S.; Siegel, R. W.; Yang, H. *Journal of Colloid and Interface Science* **2004**, 280, 91.
- (80) Hough, L. A.; Islam, M. F.; Hammouda, B.; Yodh, A. G.; Heiney, P. A. *Nano Letters* **2006**, 6, 313.
- (81) Schaefer, D. W.; Zhao, J.; Brown, J. M.; Anderson, D. P.; Tomlin, D. W. *Chemical Physics Letters* **2003**, 375, 369.
- (82) Zhou, W.; Islam, M. F.; Wang, H.; Ho, D. L.; Yodh, A. G.; Winey, K. I.; Fisher, J. E. *Chemical Physics Letters* **2004**, 384, 185.
- (83) Beaucage, G.; Schaefer, D. W. *Journal of Non-Crystalline Solids* **1994**, 172-174, 797.
- (84) Hernández, J. J.; García-Gutiérrez, M. C.; Nogales, A.; Rueda, D. R.; Ezquerra, T. A. *Composites Science and Technology* **2006**, 66, 2629.
- (85) Xiao, Z.; Li, Y.; Akpalu, Y. A. *Polymer Composites* **2009**, 30, 559.
- (86) Beaucage, G. *Journal of Applied Crystallography* **1996**, 29, 134.
- (87) Martin, J. E.; Hurd, A. J. *Journal of Applied Crystallography* **1987**, 20, 61.
- (88) Schaefer, D. W. *Science* **1989**, 243, 1023.
- (89) Sinha, S. *Bulletin of Materials Science* **1985**, 7, 341.
- (90) Schaefer, D. W.; Brown, J. M.; Anderson, D. P.; Zhao, J.; Chokalingam, K.; Tomlin, D.; Ilavsky, J. *Journal of Applied Crystallography* **2003**, 36, 553.

- (91) Bellayer, S.; Gilman, J. W.; Eidelman, N.; Bourbigot, S.; Flambard, X.; Fox, D. M.; De Long, H. C.; Trulove, P. C. *Advanced Functional Materials* **2005**, *15*, 910.
- (92) Gaylord Norman, G. In *Copolymers, Polyblends, and Composites*; AMERICAN CHEMICAL SOCIETY: 1975; Vol. 142, p 76.
- (93) Xanthos, M. *Polymer Engineering & Science* **1988**, *28*, 1392.
- (94) Xanthos, M.; Dagli, S. S. *Polymer Engineering & Science* **1991**, *31*, 929.
- (95) Liu, N. C.; Baker, W. E. *Advances in Polymer Technology* **1992**, *11*, 249.
- (96) Koning, C.; Van Duin, M.; Pagnoulle, C.; Jerome, R. *Progress in Polymer Science* **1998**, *23*, 707.
- (97) Coleman, M. M.; Painter, P. C. *Progress in Polymer Science* **1995**, *20*, 1.
- (98) Coleman, M. M.; Pehlert, G. J.; Painter, P. C. *Macromolecules* **1996**, *29*, 6820.
- (99) Hu, Y.; Painter, P. C.; Coleman, M. M.; Butera, R. J. *Macromolecules* **1998**, *31*, 3394.
- (100) Pehlert, G. J.; Painter, P. C.; veytsman, B.; Coleman, M. M. *Macromolecules* **1997**, *30*, 3671.
- (101) Viswanathan, S.; Dadmun, M. D. *Journal of Polymer Science: part B: Polymer Physics* **2004**, *42*, 1010.
- (102) Neugebauer, D.; Matyjaszewski, K. *Macromolecules* **2003**, *36*, 2598.
- (103) Keller, R. N.; Wycoff, H. D. *Inorganic syntheses* **1946**, *2*, 1.
- (104) Coessens, V.; Pintauer, T.; Matyjaszewski, K. *Progress in Polymer Science* **2001**, *26*, 337.
- (105) Mao, B.; Gan, L.-H.; Gan, Y.-Y.; Li, X.; Ravi, P.; Tam, K.-C. *Journal of Polymer Science: Part A: Polymer Chemistry* **2004**, *42*, 5161.
- (106) Zhang, X.; Xia, J.; Matyjaszewski, K. *Macromolecules* **1998**, *31*, 5167.
- (107) Pietrasik, J.; Dong, H.; Matyjaszewski, K. *Macromolecules* **2006**, *39*, 6384.
- (108) Matyjaszewski, K.; Jo, S. M.; Paik, J.-j.; Shipp, D. A. *Macromolecules* **1999**, *1999*, 6431.
- (109) Odian, G. *Principles of Polymerization*; 4th Edition ed.; John Wiley & Sons: New Jersey, 2004.

- (110) Imoto, M.; Kinoshita, M.; Nishigaki, M. *Die Makromolekulare Chemie* **1965**, 86, 217.
- (111) Imoto, M.; Kinoshita, M.; Nishigaki, M. *Die Makromolekulare Chemie* **1966**, 94, 238.
- (112) Galbrecht, F.; Bunnagel, T. W.; Scherf, U.; Farrell, T. *Macromolecular Rapid Communications* **2007**, 28, 387.
- (113) Hayes, B. L. *Microwave synthesis: Chemistry at the speed of light*; CEM Publishing: Matthews, NC, 2002.
- (114) Hoogenboom, R.; Schubert, U. S. *Macromolecular Rapid Communications* **2007**, 28.
- (115) Stange, H.; Greiner, A. *Macromolecular Rapid Communications* **2007**, 28, 504.
- (116) Bogdal, D.; Penczek, P.; Pielichowski, J.; Prociak, A. *Advances in Polymer Science* **2003**, 163, 193.
- (117) Verneker, V. R. P.; Shaha, B. *Macromolecules* **1986**, 19, 1851.
- (118) *Polymer Handbook* 4th Edition ed.; Brandrup, J.; Immergut, E. H.; Grulke, E. A.; Abe, A.; Bloch, D. R., Eds.; John Wiley & Sons, 2005.
- (119) Zhang, Y.; Son, H.; Zhang, J.; Kong, J.; Liu, Z. *Journal of Physical Chemistry C* **2007**, 111, 1988.
- (120) Kao, C. C.; Young, R. J. *Composites Science and Technology* **2004**, 64, 2291.
- (121) Bahr, J. L.; Mickelson, E. T.; Bronikowski, M. J.; Smalley, R. E.; Tour, J. M. *Chemical Communications* **2001**, 193.
- (122) Driva, P.; Pickel, D. L.; Mays, J. W.; Baskaran, D. *Macromolecules* **2010**, 43, 6915.
- (123) Raman, C. V.; Krishnan, K. S. *Nature* **1928**, 121, 501.
- (124) Raman, C. V. *Nature* **1928**, 121, 619.
- (125) Ferraro, J. R.; Nakamoto, K.; Brown, C. W. *Introductory Raman Spectroscopy*; Second Edition ed.; Academic Press, 2003.
- (126) Skoog, D. A.; Holler, F. j.; Nieman, T. A. *Principles of Instrumental Analysis*; Fifth Edition ed.; Brooks/Cole, 1997.
- (127) Bethune, D. S.; Kiang, C. H.; Devries, M. S.; Gorman, G.; Savoy, R.; Vazquez, J.; Beyers, R. *Nature* **1993**, 363, 605.

- (128) Jorio, A.; Saito, R.; Dresselhaus, G.; Dresselhaus, M. S. *Phil. Trans. R. Soc. Lond. A* **2004**, 362, 2311.
- (129) Jorio, A.; Saito, R.; Hafner, J. H.; Lieber, C. M.; Hunter, M.; McClure, T.; Dresselhaus, G.; Dresselhaus, M. S. *Physical Review Letters* **2001**, 86, 1118.
- (130) Zhao, Q.; Wagner, H. D. *Phil. Trans. R. Soc. Lond. A* **2004**, 362, 2407.
- (131) Rao, A. M.; Richter, E.; Bandow, S.; Chase, B.; Eklund, P. C.; Williams, K. A.; Fang, S.; Subbaswamy, K. R.; Menon, M.; Thess, A.; Smalley, R. E.; Dresselhaus, G.; Dresselhaus, M. S. *Science* **1997**, 275, 187.
- (132) Pimenta, M. A.; Marucci, A.; Empedocles, S. A.; Bawendi, M. G.; Hanlon, E. B.; Rao, A. M.; Eklund, P. C.; Smalley, R. E.; Dresselhaus, G.; Dresselhaus, M. S. *Physical Review B* **1998**, 58, 16016.
- (133) Jorio, A.; Pimenta, M. A.; Filho, A. G. S.; Saito, R.; Dresselhaus, G.; Dresselhaus, M. S. *New Journal of Physics* **2003**, 5, 1.
- (134) Dresselhaus, M. S.; Gresselhaus, G.; Jorio, A.; Filho, A. G. S.; Saito, R. *Carbon* **2002**, 40, 2043.
- (135) Maciel, I. O.; Anderson, N.; Pimenta, M. A.; Hartschuh, A.; Qian, H.; Terrones, M.; Terrones, H.; Campos-Delgado, J.; Rao, A. M.; Novotny, L.; Jorio, A. *Nat Mater* **2008**, 7, 878.
- (136) Maciel, I. O.; Campos-Delgado, J.; Cruz-Silva, E.; Pimenta, M. A.; Sumpter, B. G.; Meunier, V.; López-Uribe, F.; Muñoz-Sandoval, E.; Terrones, H.; Terrones, M.; Jorio, A. *Nano Letters* **2009**, 9, 2267.
- (137) Krevelen, D. W. V.; Elsevier: Amsterdam, 1990, p 189.
- (138) Wagner, H. D. *Physical Review B* **1996**, 53, 5055.
- (139) Mu, M.; Winey, K. I. *Journal of Physical Chemistry C* **2007**, 111, 17923.
- (140) Shen, G. A.; Namila, S.; Chandra, N. *Materials Science and Engineering* **2006**, 429, 66.
- (141) Ajayan, P. M.; Schadler, L. S.; Giannaris, C.; Rubio, A. *Adv. Mater.* **2000**, 12, 750.
- (142) Linton, D.; Driva, P.; Sumpter, B.; Ivanov, I.; Geohegan, D.; Feigerle, C.; Dadmun, M. D. *Soft Matter* **2010**, 6, 2801.
- (143) Kendall, R. A.; Aprà, E.; Bernholdt, D. E.; Bylaska, E. J.; Dupuis, M.; Fann, G. I.; Harrison, R. J.; Ju, J.; Nichols, J. A.; Nieplocha, J.; Straatsma, T. P.; Windus, T. L.; Wong, A. T. *Computer Physics Communications* **2000**, 128, 260.



- (144) Binkley, J. S.; Pople, J. A.; Hehre, W. J. *Journal of the American Chemical Society* **1980**, *102*, 939.
- (145) Hehre, W. J.; Ditchfield, R.; Pople, J. A. *The Journal of Chemical Physics* **1972**, *56*, 2257.
- (146) Allinger, N. L.; Yuh, Y. H.; Lii, J. H. *Journal of the American Chemical Society* **1989**, *111*, 8551.
- (147) Sumpter, B. G.; Jiang, D. E.; Meunier, V. *Small* **2008**, *4*, 2035.
- (148) Yang, M.; Koutsos, V.; Zaiser, M. *Journal of Physical Chemistry B* **2005**, *109*, 10009.
- (149) Robeson, L. M. *Polymer Blends: A comprehensive review*; Hanser Publishers, Munich, 2007.
- (150) Hiemenz, P. C.; Lodge, T. P. *Polymer Chemistry*; 2nd Edition ed.; CRC Press, 2007.
- (151) Fetters, L. J.; Lohse, D. J.; Richter, D.; Witten, T. A.; Zirkel, A. *Macromolecules* **1994**, *27*, 4639.
- (152) Groot, R. D.; Warren, P. B. *Journal of Chemical Physics* **1997**, *107*, 4423.
- (153) Maiti, A.; Wescott, J.; Kung, P. *Molecular Simulation* **2005**, *31*, 143.
- (154) Usrey, M. L.; Chaffee, A.; Jeng, E. S.; Strano, M. S. *Journal of Physical Chemistry C* **2009**, *113*, 9532.
- (155) Dalton, A. B.; Stephan, C.; Coleman, J. N.; McCarthy, B.; Ajayan, P. M.; Lefrant, S.; Bernier, P.; Blau, W. J.; Byrne, H. J. *Journal of Physical Chemistry B* **2000**, *104*, 10012.
- (156) Coleman, M. M.; Painter, P. C. *Aust. J. Chem.* **2006**, *59*, 499.
- (157) Rasheed, A.; Dadmun, M. D.; Ivanov, I.; Britt, P. F.; Geohegan, D. B. *Chem. Mat.* **2006**, *18*, 3513.
- (158) Eastwood, E.; Viswanathan, S.; O'Brien, C. P.; Kumar, D.; Dadmun, M. D. *Polymer* **2005**, *46*, 3957.
- (159) Brown, S. D. M.; Jorio, A.; Corio, P.; Dresselhaus, M. S.; Dresselhaus, G.; Saito, R.; Kneipp, K. *Physical Review B* **2001**, *63*, 1.
- (160) Creton, C.; Kramer, E. J. *Macromolecules* **1991**, *24*, 1846.
- (161) Milner, S. T.; Xi, H. *Journal of Rheology* **1996**, *40*, 663.

- (162) Retsos, H.; Margiolaki, I.; Messaritaki, A.; Anastasiadis, S. H. *Macromolecules* **2001**, *34*, 5295.
- (163) Tan, N. C. B.; Tai, S.-K.; Briber, R. M. *Polymer* **1996**, *37*, 3509.
- (164) Beaucage, G.; Rane, S.; Schaefer, D. W.; Long, G.; Fischer, D. *Journal of Polymer Science: Part B: Polymer Physics* **1999**, *37*, 1105.
- (165) Adhikari, R.; Michler, G. H. *Polymer Reviews* **2009**, *49*, 141.
- (166) Loos, J.; Alexeev, A.; Grossiord, N.; Koning, C. E.; Regev, O. *Ultramicroscopy* **2005**, *104*, 160.
- (167) Brintlinger, T.; Chen, Y. F.; Durkop, T.; Cobas, E.; Fuhrer, M. S.; Barry, J. D.; Melngailis, J. *Applied Physics Letters* **2002**, *81*, 2454.
- (168) Pradhan, B.; Kohlmeyer, R. R.; Setyowati, K.; Owen, H. A.; Chen, J. *Carbon* **2009**, *47*, 1686.
- (169) Ajayan, P. M.; Stephan, O.; Colliex, C.; Trauth, D. *Science* **1994**, *265*, 1212.
- (170) Higgins, J. S.; Benoit, H. C. *Polymers and Neutron Scattering*; Oxford University Press: New York, 1994.
- (171) Pethrick, R. A.; Dawkins, J. V. *Modern Techniques for Polymer Characterisation*; Wiley 1999.
- (172) <http://www.ncnr.nist.gov/resources/sldcalc.html>.
- (173) Hammouda, B. *Journal of Macromolecular Science, Part C: Polymer Reviews* **2010**, *50*, 14.
- (174) Hall, L. M.; Schweizer, K. S. *The Journal of Chemical Physics* **2008**, *128*, 1.
- (175) Hooper, J. B.; Schweizer, K. S. *Macromolecules* **2005**, *38*, 8858.
- (176) Hooper, J. B.; Schweizer, K. S. *Macromolecules* **2006**, *39*, 5133.
- (177) Hooper, J. B.; Schweizer, K. S. *Macromolecules* **2007**, *40*, 6998.
- (178) Schelten, J.; Wignall, G. D.; Ballard, D. G. H.; Schmatz, W. *Colloid and Polymer Science* **1974**, *252*, 749.
- (179) Li, C. Y. *J. Polym. Sci. Pt. B-Polym. Phys.* **2009**, *47*, 2436.
- (180) Li, C. Y.; Li, L. Y.; Cai, W. W.; Kodjie, S. L.; Tenneti, K. K. *Adv. Mater.* **2005**, *17*, 1198.
- (181) Li, L.; Li, B.; Hood, M. A.; Li, C. Y. *Polymer* **2009**, *50*, 953.

- (182) Li, L. Y.; Li, C. Y.; Ni, C. Y. *Journal of the American Chemical Society* **2006**, *128*, 1692.
- (183) Kelarakis, A.; Yoon, K.; Sics, I.; Somani, R. H.; Hsiao, B. S.; Chu, B. *Polymer* **2005**, *46*, 5103.
- (184) Vaia, R. A.; Maguire, J. F. *Chem. Mat.* **2007**, *19*, 2736.
- (185) Dukovski, I.; Muthukumar, M. *Journal of Chemical Physics* **2003**, *118*, 6648.
- (186) Wang, M. X.; Hu, W. B.; Ma, Y.; Ma, Y. Q. *Macromolecules* **2005**, *38*, 2806.
- (187) Kimata, S.; Sakurai, T.; Nozue, Y.; Kasahara, T.; Yamaguchi, N.; Karino, T.; Shibayama, M.; Kornfield, J. A. *Science* **2007**, *316*, 1014.
- (188) Green, M. J.; Behabtu, N.; Pasquali, M.; Adams, W. W. *Polymer* **2009**, *50*, 4979.
- (189) Jorio, A.; Dresselhaus, G.; Dresselhaus, M. S. *Carbon nanotubes: Advanced Topics in the Synthesis, Structure, Properties and Applications*; Springer: New York, 2008.
- (190) Hasan, T.; Scardaci, V.; Tan, P. H.; Rozhin, A. G.; Milne, W. I.; Ferrari, A. C. *Physica E: Low-dimensional Systems and Nanostructures* **2008**, *40*, 2414.
- (191) Napper, D. H. *Polymeric Stabilization of Colloidal Dispersions*; Academic Press Inc: London, 1983.
- (192) Napper, D. H. *Industrial and Engineering Chemistry Product Research and Development* **1970**, *9*, 467.
- (193) *Polymer Interfaces and Emulsions*; Esumi, K., Ed.; Marcel Dekker, Inc: New York, 1999.
- (194) Morrison, I. D.; Ross, S. *Colloidal Dispersions*; John Wiley and Sons, Inc. : New York, 2002.
- (195) Napper, D. H. *Journal of Colloid and Interface Science* **1977**, *58*, 390.
- (196) Hamaker, H. C. *Physica* **1937**, *4*, 1058.
- (197) Feigin, R. I.; Napper, D. H. *Journal of Colloid and Interface Science* **1980**, *75*, 525.
- (198) Feigin, R. I.; Napper, D. H. *Journal of Colloid and Interface Science* **1980**, *74*, 567.
- (199) Islam, M. F.; Rojas, E.; Bergey, D. M.; Johnson, A. T.; Yodh, A. G. *Nano Letters* **2003**, *3*, 269.

- (200) Liu, J.; Rinzler, A. G.; Dai, H. J.; Hafner, J. H.; Bradley, R. K.; Boul, P. J.; Lu, A.; Iverson, T.; Shelimov, K.; Huffman, C. B.; Rodriguez-Macias, F.; Shon, Y. S.; Lee, T. R.; Colbert, D. T.; Smalley, R. E. *Science* **1998**, 280, 1253.
- (201) O'Connell, M. J.; Bachilo, S. M.; Huffman, C. B.; Moore, V. C.; Strano, M. S.; Haroz, E. H.; Rialon, K. L.; Boul, P. J.; Noon, W. H.; Kittrell, C.; Ma, J. P.; Hauge, R. H.; Weisman, R. B.; Smalley, R. E. *Science* **2002**, 297, 593.
- (202) Moore, V. C.; Strano, M. S.; Haroz, E. H.; Hauge, R. H.; Smalley, R. E.; Schmidt, J.; Talmon, Y. *Nano Letters* **2003**, 3, 1379.
- (203) O'Connell, M. J.; Boul, P.; Ericson, L. M.; Huffman, C.; Wang, Y. H.; Haroz, E.; Kuper, C.; Tour, J.; Ausman, K. D.; Smalley, R. E. *Chemical Physics Letters* **2001**, 342, 265.
- (204) Zheng, M.; Jagota, A.; Semke, E. D.; Diner, B. A.; McLean, R. S.; Lustig, S. R.; Richardson, R. E.; Tassi, N. G. *Nat. Mater.* **2003**, 2, 338.
- (205) Zheng, M.; Jagota, A.; Strano, M. S.; Santos, A. P.; Barone, P.; Chou, S. G.; Diner, B. A.; Dresselhaus, M. S.; McLean, R. S.; Onoa, G. B.; Samsonidze, G. G.; Semke, E. D.; Usrey, M.; Walls, D. J. *Science* **2003**, 302, 1545.
- (206) Wang, H. *Current Opinion in Colloid and Interface Science* **2009**, 14, 364.
- (207) Barker, M. C.; Garvey, M. J. *Journal of Colloid and Interface Science* **1980**, 74, 331.
- (208) Lambe, R.; Tadros, T. F.; Vincent, B. *Journal of Colloid and Interface Science* **1978**, 66, 77.
- (209) van den Boomgaard, T.; King, T. A.; Tadros, T. F.; Tang, H.; Vincent, B. *Journal of Colloid and Interface Science* **1978**, 66, 68.
- (210) Gao, J. B.; Zhao, B.; Itkis, M. E.; Bekyarova, E.; Hu, H.; Kranak, V.; Yu, A. P.; Haddon, R. C. *Journal of the American Chemical Society* **2006**, 128, 7492.
- (211) Niyogi, S.; Hamon, M. A.; Hu, H.; Zhao, B.; Bhowmik, P.; Sen, R.; Itkis, M. E.; Haddon, R. C. *Accounts Chem. Res.* **2002**, 35, 1105.
- (212) Bahr, J. L.; Yang, J.; Kosynkin, D. V.; Bronikowski, M. J.; Smalley, R. E.; Tour, J. M. *Journal of American Chemical Society* **2001**, 123, 6536.
- (213) Furtado, C. A.; Kim, U. J.; Gutierrez, H. R.; Pan, L.; Dickey, E. C.; Eklund, P. C. *Journal of the American Chemical Society* **2004**, 126, 6095.
- (214) Krupke, R.; Hennrich, F.; Hampe, O.; Kappes, M. M. *Journal of Physical Chemistry B* **2003**, 107, 5667.

- (215) Liu, J.; Casavant, M. J.; Cox, M.; Walters, D. A.; Boul, P.; Lu, W.; Rimberg, A. J.; Smith, K. A.; Colbert, D. T.; Smalley, R. E. *Chemical Physics Letters* **1999**, 303, 125.
- (216) Giordani, S.; Bergin, S. D.; Nicolosi, V.; Lebedkin, S.; Kappes, M. M.; Blau, W. J.; Coleman, J. N. *Journal of Physical Chemistry B* **2006**, 110, 15708.
- (217) Ausman, K. D.; Piner, R.; Lourie, O.; Ruoff, R. S.; Korobov, M. *Journal of Physical Chemistry B* **2000**, 104, 8911.
- (218) Hasan, T.; Tan, P. H.; Bonaccorso, F.; Rozhin, A. G.; Scardaci, V.; Milne, W. I.; Ferrari, A. C. *Journal of Physical Chemistry C* **2008**, 112, 20227.
- (219) Croucher, M. D.; Hair, M. L. *Journal of Colloid and Interface Science* **1981**, 81, 257.
- (220) Everett, D. H.; Stageman, J. F. *Colloid and Polymer Science* **1977**, 255, 293.
- (221) Napper, D. H. *Journal of Colloid and Interface Science* **1970**, 32, 106.
- (222) Dawkins, J. V.; Taylor, G. *Colloid and Polymer Science* **1980**, 258, 79.
- (223) Crosby, A. J.; Lee, J.-Y. *Polymer Reviews* **2007**, 47, 217.
- (224) Fetters, L.J.; Lohse, D.J.; Colby, R.H. *Physical Properties of Polymers Handbook*, 2<sup>nd</sup> ed; Springer-Verlag New York, 2007.
- (225) Kamide, K., Terakawa, T.; *Die Makromolekulare Chemie* 1972, 155, 25.

## **APPENDIX A**

### A.1. Effect of Chain Flexibility on the Formation of Charge Transfer Interactions

Density functional theory and free energy of mixing,  $\Delta G$ , calculations presented in Section 3.3.B. and 3.3.C, respectively, imply that polymer chain flexibility is a crucial factor that controls the extent of charge transfer interactions that exist between the polymer matrix and single-walled-nanotube (SWNT) and ultimately optimize the nanoparticle homogeneity. Strictly speaking, without this parameter, the homopolymers PDMAEMA and PCNSt could form the most intermolecular interactions with the SWNT due to the abundance of interacting functional groups along the polymer chains. In this section, we provide insight into the importance of chain flexibility of the polymer matrices in the formation of optimum SWNT-polymer interactions and correlate this information to the fact that the presence of a minority of interacting functional group (i.e. DMA30, SAN45 and CNSt24) in the copolymer matrix leads to the most efficient intermolecular interaction.

Flory defined the characteristic ratio,  $C_\infty$ , as a structure-specific parameter, which characterizes chain flexibility, describes the effect of local steric constraints on chain dimension and can be written as:

$$C_\infty = \frac{\langle h^2 \rangle_o}{nl^2} \quad (\text{Equation A.1})$$

where  $\langle h^2 \rangle_o$  is the actual unperturbed mean-square end-to-end distance of the polymer chain,  $n$  denotes the number of chemical bonds along the polymer backbone and  $l$  is the length of a backbone bond (i.e. 1.54 Å for C-C bond). For a high molecular weight polymer, the characteristic ratio,  $C_\infty$  approaches a constant value and can be written as:

$$C_{\infty} = m_b \frac{\langle h^2 \rangle}{l^2 M} \quad (\text{Equation A.2})$$

M denotes the polymer molecular weight and the parameter,  $m_b$ , represents the average molar mass per backbone bond and is calculated as follows:

$$m_b = \frac{M}{2 \times (M / x)} = \frac{x}{2} \quad (\text{Equation A.3})$$

where the number 2 represents the number of C-C bonds and  $x$  represents the monomer molar mass. The characteristic ratio,  $C_{\infty}$  of a homopolymer can then be calculated by the following equation:

$$C_{\infty} = \frac{x \times \langle h^2 \rangle_0}{2 \times l^2 \times M} \quad (\text{Equation A.4})$$

For common polymers such as PS and PMMA,  $\langle h^2 \rangle_0 / M$  can be readily obtained from the literature, where  $(\langle h^2 \rangle_0 / M)_{\text{PMMA}} = 0.39$  and  $(\langle h^2 \rangle_0 / M)_{\text{PS}} = 0.437$ .<sup>224</sup> Based on the similarity of structures, the values of  $\langle h^2 \rangle_0 / M$  for PCNSt is estimated to be similar to that of poly( $\alpha$ -methyl styrene) and  $\langle h^2 \rangle_0 / M$  for PDMAEMA is estimated to be similar to that of poly(ethyl butyl) methacrylate. The structures of PDMAEMA, poly (ethyl butyl) methacrylate, PCNSt and poly( $\alpha$ -methyl styrene) are depicted in Figure A.1. The characteristic ratio of polyacrylonitrile ( $C_{\infty}^{\text{PAN}} = 2.38$ ), an experimentally determined value reported by Kamide and coworkers is calculated by the following equation:<sup>225</sup>

$$C_{\infty} = \sqrt{\frac{(K / \Phi_o)^{2/3}}{M^{-1} l^2 (1 - \cos \Theta)(1 + \cos \Theta)^{-1}}} \quad (\text{Equation A.5})$$



K is the Mark-Houwink-Sakurada constant determined by intrinsic viscometry measurements and is characteristic of the polymer-solvent combination at a given temperature (K=2.9).  $\Phi_o$  denotes the Flory's viscosity parameter of a theta solvent ( $\Phi_o=2.87 \times 10^{-21}$ ) and  $\Theta$  represents the supplementary bond angle of the valence angle, where  $\Theta = \pi - 109^\circ 28'$ .

The characteristic ratio of the copolymers,  $C_\infty^{copolymer A-B}$  are calculated as follows:

$$C_\infty^{copolymer A-B} = C_\infty^A \times n_A + C_\infty^B \times n_B \quad (\text{Equation A.6})$$

where  $C_\infty^A$  and  $C_\infty^B$  denote the characteristic ratio of homopolymers A and B respectively, whereas  $n_A$  and  $n_B$  represent the mole percent of A or B chemical constituents in the copolymer chain. For example, from equation A.6, the characteristic ratio of CNSt50 is calculated as  $\frac{1}{2} \times C_\infty^{PS} + \frac{1}{2} \times C_\infty^{PCNSt}$ .

Tables A.1, A.2, and A.3 show the characteristic ratios of the MMA-*ran*-DMAEMA, styrene-*ran*-acrylonitrile and styrene-*ran*-cyanostyrene polymers used in this study. Even though PDMAEMA has an abundance of tertiary amino groups to form an efficient polymer-SWNT complex, the extent of intermolecular interaction and the dispersion of SWNT in the PDMAEMA nanocomposite is inferior to that in the nanocomposite containing 30 mol% DMAEMA, as evidenced by Raman spectroscopy and optical microscopy (Chapters 3 and 4). The calculated characteristic ratios of 11.0 for PDMAEMA and 9.38 for DMA30 provide one contribution to this experimental observation (Table A.1). Due to the greater flexibility of DMA30, as reflected by its lower characteristic ratio, the DMA30 polymer chain has a greater propensity to conform

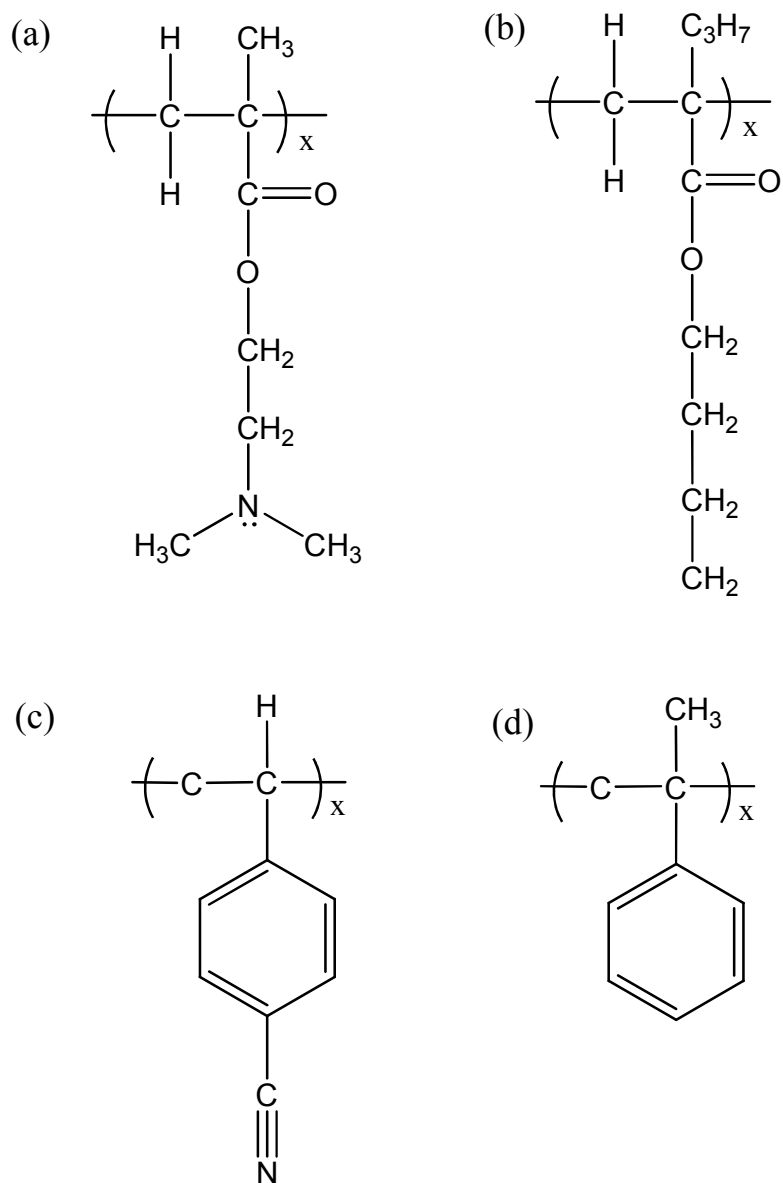


**Figure A.1.** Structures of (a) PDMAEMA, (b) poly(ethyl butyl) methacrylate, (c) PCNSt and (d) poly ( $\alpha$ -methyl styrene).

**Table A.1.** Characteristic ratio of PMMA, PDMAEMA and MMA-*ran*-DMAEMA polymers used in this study

Polymer	mol% DMAEMA	Characteristic Ratio
PMMA	0.00	8.68
DMA10	0.12	8.96
DMA20	0.26	9.29
DMA30	0.30	9.38
DMA50	0.49	9.82
PDMAEMA	1.00	11.00

**Table A.2.** Characteristic ratio of PS, PAN and styrene-*ran*-acrylonitrile polymers used in this study

Polymer	mol% AN	Characteristic Ratio
PS	0.00	10.11
SAN30	0.30	7.83
SAN37	0.37	7.26
SAN45	0.45	6.63
SAN49	0.49	6.33
SAN56	0.56	5.76
PAN	1.00	2.37

**Table A.3.** Characteristic ratio of PS, PCNSt and styrene-*ran*-cyanostyrene polymers used in this study

Polymer	mol% CNSt	Characteristic Ratio
PS	0.00	10.11
CNSt13	0.13	10.44
CNSt24	0.24	10.72
CNSt30	0.30	10.88
CNSt40	0.40	11.15
CNSt50	0.50	11.40
PCNSt	1.00	12.69

itself correctly to the carbon nanotube cage to form the electron donor-acceptor complex, whereas the more rigid PDMAEMA cannot. It needs to be re-emphasized however, that polymer chain flexibility parameter is not the lone factor in controlling the efficiency of

the formation of intermolecular interaction since PMMA, which has a characteristic ratio of 8.68, is the most flexible among this series, but does not achieve a good interaction with SWNT. Therefore, a balance between polymer chain flexibility and the presence of sufficient functional groups to form effective non-covalent interactions are required to achieve the most efficient interaction and nanoparticle dispersion.

By a similar token, PCNSt, which has a characteristic ratio of 12.69 is the most rigid polymer studied, and therefore cannot readily wrap around the carbon nanotube, thus achieving poor charge transfer interaction with SWNT in comparison with CNSt24 ( $C_{\infty} = 10.72$ ). Although polystyrene ( $C_{\infty} = 10.11$ ) is more flexible than CNSt24, the efficiency of the formation of charge-transfer complex and nanoparticle dispersion is still inferior in comparison with the less flexible CNSt 24 owing to the presence of the weaker  $\pi$ - $\pi$  interaction between the aromatic ring on the polystyrene chain and the graphitic framework of the SWNT.

For the styrene-*ran*-acrylonitrile series, it was found that SAN45 copolymer, which has a characteristic ratio of 6.63, forms the most efficient electron-donor acceptor complex with the SWNTs. Based on the chain flexibility factor alone, it is thus sensible that polystyrene ( $C_{\infty}^{\text{PS}} = 10.11$ ) does not interact as well with the SWNT. However, polyacrylonitrile shows anomalously good intermolecular interaction, and this is ascribed to the extensive flexibility of the polymer chain ( $C_{\infty} = 2.37$ ). The loss of the aromatic rings of the styrene leads to a significantly more flexible chain that can wrap more easily around the SWNT, creating more nitrile-SWNT EDA interactions.

In conclusion, the importance of polymer chain flexibility cannot be overlooked in understanding the factors that impact the ability of a polymer chain to form non-

covalent interactions with a nanoparticle. Furthermore, the analysis presented above verifies the role of flexibility in the occurrence of an optimal intermolecular interaction and particle dispersion when a moderate amount of functional groups exist along the polymer chain.

## VITA

Dias Linton was born on September 13<sup>th</sup> 1982 in Bintulu, Sarawak, East Malaysia. In December 1999, she graduated from Bintulu Secondary School and attended Kolej Tuanku Jaafar (in Negeri Sembilan, West Malaysia) briefly for her Advanced Level General Certificate of Education, the standard entry qualification for U.K. universities. Before completing the program, she decided to accept a scholarship by the Public Services Department of Malaysia and pursued her undergraduate studies at the University of Minnesota, Twin Cities in September 2001. In August 2005, after graduating with a Bachelor of Science in Chemistry, she moved to Knoxville, TN to continue her graduate career with a specialization in Polymer Chemistry, under the direction of Professor Mark Dadmun. She successfully defended her Ph.D. dissertation on September 20<sup>th</sup> 2010. On October 1<sup>st</sup> 2010, she became a postdoctoral research fellow in Professor Judit Puskas' research group at the Department of Polymer Science, University of Akron, Ohio.